

1-2018

Experimental and Model-based Terahertz Imaging and Spectroscopy for Mice, Human, and Phantom Breast Cancer Tissues

Tyler Bowman

University of Arkansas, Fayetteville

Follow this and additional works at: <http://scholarworks.uark.edu/etd>

 Part of the [Bioimaging and Biomedical Optics Commons](#), [Molecular, Cellular, and Tissue Engineering Commons](#), and the [Other Electrical and Computer Engineering Commons](#)

Recommended Citation

Bowman, Tyler, "Experimental and Model-based Terahertz Imaging and Spectroscopy for Mice, Human, and Phantom Breast Cancer Tissues" (2018). *Theses and Dissertations*. 2716.
<http://scholarworks.uark.edu/etd/2716>

This Dissertation is brought to you for free and open access by ScholarWorks@UARK. It has been accepted for inclusion in Theses and Dissertations by an authorized administrator of ScholarWorks@UARK. For more information, please contact scholar@uark.edu, ccmiddle@uark.edu.

Experimental and Model-based Terahertz Imaging and Spectroscopy for Mice, Human, and
Phantom Breast Cancer Tissues

A dissertation submitted in partial fulfillment
of the requirements for the degree of
Doctor of Philosophy in Engineering with a concentration in Electrical Engineering

by

Tyler Bowman
University of Arkansas
Bachelor of Science in Electrical Engineering, 2012
University of Arkansas
Master of Science in Electrical Engineering, 2014

May 2018
University of Arkansas

This dissertation is approved for recommendation to the Graduate Council.

Magda El-Shenawee, Ph.D.
Dissertation Director

Jingxian Wu, Ph.D.
Committee Member

Shui-Qing Yu, Ph.D.
Committee Member

Morgan Ware, Ph.D.
Committee Member

Jeffrey Wolchok, Ph.D.
Committee Member

Abstract

The goal of this work is to investigate terahertz technology for assessing the surgical margins of breast tumors through electromagnetic modeling and terahertz experiments. The measurements were conducted using a pulsed terahertz system that provides time and frequency domain signals. Three types of breast tissues were investigated in this work. The first was formalin-fixed, paraffin-embedded tissues from human infiltrating ductal and lobular carcinomas. The second was human tumors excised within 24-hours of lumpectomy or mastectomy surgeries. The third was xenograft and transgenic mice breast cancer tumors grown in a controlled laboratory environment to achieve more data for statistical analysis.

Experimental pulsed terahertz imaging first used thin sections (10-30 μm thick) of fixed breast cancer tissue on slides. Electromagnetic inverse scattering models, in transmission and reflection modes, were developed to retrieve the tissue refractive index and absorption coefficient. Terahertz spectroscopy was utilized to experimentally collect data from breast tissues for these models. The results demonstrated that transmission mode is suitable for lossless materials while the reflection model is more suitable for biological materials where the skin depth of terahertz waves does not exceed 100 μm . The reflection model was implemented to estimate the polarization of the incident terahertz signal of the system, which was shown to be a hybridization of TE and TM modes.

Terahertz imaging of three-dimensional human breast cancer blocks of tissue embedded in paraffin was achieved through the reflection model. The terahertz beam can be focused at depths inside the block to produce images in the x-y planes (z-scan). The time-of-flight analysis was applied to terahertz signals reflected at each depth demonstrating the margins of cancerous regions inside the block as validated with pathology images at each depth. In addition, phantom tissues

that mimic freshly excised infiltrating ductal carcinoma human tumors were developed with and without embedded carbon nanometer-scale onion-like carbon particles. These particles exhibited a strong terahertz signal interaction with tissue demonstrating a potential to greatly improve the image contrast.

The results presented in this work showed, in most cases, a significant differentiation in terahertz images between cancer and healthy tissue as validated with histopathology images.

Acknowledgements

I would like to acknowledge Dr. Magda El-Shenawee as the advisor and dissertation director of this work, without whom it would not have been possible. Her dedication and passion for the terahertz applications in breast cancer were the driving force for the work, and her standards for personal and professional excellence have inspired me as a student and as an engineer.

I would also like to thank the committee members of this dissertation, Dr. Jingxian Wu, Dr. Fisher Yu, Dr. Morgan Ware, and Dr. Jeffrey Wolchok, for their participation and contribution to this work. I also thank the faculty of the Biomedical Engineering Department of the University of Arkansas for advice and support throughout this work, with special thanks to Dr. Wolchok and Dr. Rajaram for the use of their lab space and equipment. I would like to thank Dr. Rajaram's students for their help in obtaining mice tumors in this work.

I would like to thank Dr. Keith Bailey with the Oklahoma Animal Disease Diagnostic Laboratory and Dr. Lucas Campbell with NWA Pathology and Associates for providing the histopathology assessment for the publications included in this work.

I would like to thank Dr. Phil Taday and Rebecca Goodall of TeraVIEW, Ltd. for THz system training and feedback, the Terahertz Spectroscopy and Imaging Laboratory members at the University of Arkansas for their support, and fellow members of the R15 NIH grant for their coordination in advancing this work to its current level. Finally, I thank all my family and friends whose patience and support made this work possible.

This work was supported by National Institute of Health (NIH) grant #R15CA208798, NSF/MRI award #1228958, NSF award #1408007, the Arkansas Biosciences Institute, and the Arkansas Breast Cancer Research Programs. In addition, direct funding was received through National Science Foundation Graduate Fellowship (NSF GRFP) award #DGE-1450079 from 2013

to 2016, National Science Foundation GK-12 Fellowship from 2012 to 2013, and the University of Arkansas Distinguished Doctoral Fellowship from 2013 to 2017.

Dedication

This work is dedicated to my wife Amanda, for her unending support.

Table of Contents

<u>Chapter 1: Introduction</u>	1
1. Motivation	1
2. Terahertz for Breast Cancer Applications	3
3. Terahertz Imaging and Spectroscopy System	6
4. Samples for Breast Cancer Spectroscopy and Imaging	9
5. Overview of Dissertation Chapters and Published Work	12
References	15
<u>Chapter 2: Terahertz Imaging of Excised Breast Tumor Tissue on Paraffin Sections</u>	24
Abstract	24
1. Introduction	24
2. System Set-Up and Methodology	30
2.1. Pulsed Terahertz System	30
2.2. Imaging Calibration	30
2.3. Tissue Preparation	32
3. Theoretical Model and Validation	33
3.1. Reflection Formulation in <i>TE/TM</i> Polarization	33
4. THz RIM Imaging Results	35
4.1. Imaging of 10 μm thickness tissue samples	35
4.2. Validation of THz reflected fields with theoretical model	40
4.3. Imaging of 20 and 30 μm thickness tissue samples	43
5. Discussion and Conclusions	45
Acknowledgments	46
Appendix A	46
References	47
<u>Chapter 3: Terahertz Transmission vs Reflection Imaging and Model-based Characterization for Excised Breast Carcinomas</u>	50
Abstract	50

1. Introduction	51
2. Methodology	54
2.1. Pulsed Terahertz System	54
2.2. Sample Preparation	55
2.3. Selection of slide materials	56
3. Propagation modeling	57
3.1. Transmission mode	57
3.2. Reflection mode	59
4. Validation of models	62
4.1. Animal tissue spectroscopy	63
4.2. Reflection imaging and calculation of tissue properties	64
5. Imaging of breast carcinoma	71
5.1. Case 1: Lobular carcinoma (LC)	71
5.1.1. Transmission and reflection images of LC	71
5.1.2. Calculation of refractive index and absorption coefficient of LC.....	79
5.2. Case 2: Infiltrating ductal carcinoma (IDC).....	82
5.2.1. Transmission and reflection images of IDC.....	82
5.2.2. Calculation of refractive index and absorption coefficient of IDC	87
6. Discussion and Conclusion	89
Appendix A	90
Funding	91
Acknowledgments	91
References	91
<u>Chapter 4: Terahertz Imaging of Three-Dimensional Dehydrated Breast Cancer Tumors</u>	<u>95</u>
Abstract	95
1. Introduction	95
2. Tissue Sample Preparation and THz Imaging System.....	98

3. Signal and Image Processing	100
3.1. Time of Flight Signal Analysis	100
3.2. Image processing techniques	102
3.2.1. Pre-processing	102
3.2.2. Intensity mapping	103
3.2.3. Edge sharpening	104
3.2.4. Edge detection	105
3.2.5. Region growing	106
4. Results.....	107
4.1. Image processing results	107
4.1.1. Sample preparation.....	107
4.1.2. Intensity mapping	107
4.1.3. Edge sharpening	108
4.1.4. Edge detection	109
4.1.5. Region growing	111
4.2. Three-dimensional imaging of breast cancer tissue blocks.....	112
4.2.1. Sample 1: Infiltrating ductal carcinoma (IDC).....	113
4.2.2. Sample 3: Lobular carcinoma (LC).....	119
5. Conclusions.....	123
Acknowledgments.....	124
References.....	124
<u>Chapter 5: A Phantom Study of Terahertz Spectroscopy and Imaging of Micro- and Nano-</u> <u>diamonds and Nano-onions as Contrast Agents for Breast Cancer</u>	128
Abstract.....	128
1. Introduction.....	129
2. Methodology and Materials	133
2.1. Terahertz Spectroscopy and Imaging Setup	133
2.2. Breast Cancer Phantom Tissue Development	136

2.3. Carbon-based Particle Preparation	137
2.4. THz Spectroscopy Process	138
3. Results of Particle Characterization.....	139
3.1. Particles in PDMS	139
3.2. Microdiamonds in Polyethylene.....	141
3.2.1. Effect of microdiamond size	141
3.2.2. Effect of microdiamond treatment	143
3.3. OLC in Polyethylene.....	144
3.4. Microdiamonds and OLC in IDC Phantom.....	146
4. Results of Breast Phantom Tumor Imaging with and without OLC Particles	148
5. Conclusions.....	152
Acknowledgments.....	153
References.....	153
<u>Chapter 6: Pulsed Terahertz Imaging of Breast Cancer in Freshly Excised Murine Tumors</u>	159
Abstract.....	159
1. Introduction.....	159
2. Methodology.....	162
2.1. Terahertz Imaging Setup	162
2.2. Mice Tumor Sample preparation.....	163
2.3. Correlation Process of THz and Pathology images.....	164
2.3.1. Pathology Morphing and Pathology Mask Generation	165
2.3.2. Statistical Bayesian Mixture Model	166
3. Experimental Results	170
3.1. Classification of samples with two tissue regions.....	170
3.2. Classification of samples with three tissue regions.....	177
4. Discussion and Conclusion.....	184
Disclosures.....	186

Acknowledgments.....	186
References.....	186
<u>Chapter 7: Conclusions</u>	191
References.....	194
Appendix A: Additional Published Work.....	196
Appendix B: MATLAB Codes.....	198

List of Published Papers

Chapter 2: T. C. Bowman, M. El-Shenawee, and L. K. Campbell. "Terahertz Imaging of Excised Breast Tumor Tissue on Paraffin Sections." *IEEE Transactions on Antennas and Propagation*, vol. 63, no. 5, pp. 2088-2097, 2015.

Chapter 3: T. Bowman, M. El-Shenawee, and L. K. Cambell, "Terahertz transmission vs reflection imaging and model-based characterization for excised breast carcinomas" *Biomed. Opt. Express* vol. 7, no. 9, pp. 3756-3783, 2016.

Chapter 4: T. Bowman, Y. Wu, J. Gauch, L. K. Campbell, and M. El-Shenawee, "Terahertz Imaging of Three-Dimensional Dehydrated Breast Cancer Tumors," *Journal of Infrared, Millimeter, and Terahertz Waves*, vol. 38, no. 6, pp. 766-786, 2017.

Chapter 5: T. Bowman, A. Walter, O. Shenderova, N. Nunn, G. McGuire, and M. El-Shenawee, "A Phantom Study of Terahertz Spectroscopy and Imaging of Micro- and Nano-diamonds and Nano-onions as Contrast Agents for Breast Cancer," *Biomedical Physics and Engineering Express*, vol. 3, no. 5, pp. 055001, 2017.

Chapter 6: T. Bowman, T. Chavez, K. Khan, J. Wu, A. Chakraborty, N. Rajaram, K. Bailey, and M. El-Shenawee, "Pulsed terahertz imaging of breast cancer in freshly excised murine tumors," *Journal of Biomedical Optics*, vol. 23, no. 2, pp. 026004, 2018.

Chapter 1: Introduction

1. Motivation

Breast cancer is a primary medical concern in the modern world, with an estimated one in eight women in the United States being diagnosed in their lifetime [1]. When breast cancer is diagnosed early enough, a more conservative lumpectomy procedure, which removes just the tumor and a small surgical margin of healthy tissue, is generally preferred over radical mastectomy, which removes the entire breast. Furthermore, it has been shown that successful lumpectomy procedures are just as effective at preventing cancer spread and recurrence as mastectomy [2]. As such, lumpectomy can provide equally effective removal of breast cancer with less cosmetic damage than mastectomy and stands to become more common as early cancer detection techniques improve. The primary surgical concern in these lumpectomy procedures is margin assessment, which determines whether cancer remains on the edge of the excised tissue, indicating remnant cancer in the surgical cavity. A positive margin denotes that there is cancer on the outside border of the removed tissue while a negative margin indicates that only healthy tissue is present at the surgical edge. Local recurrence of breast cancer occurs in the site of the original excision in 75-90% of cases, meaning that any positive margins must be addressed via additional excision to ensure patient health [3]. However, the amount of healthy tissue removed should be minimized to maintain the lumpectomy target of low cosmetic damage, meaning that sufficient but not excessive healthy margins is a key standard for these surgical procedures.

Recent guidelines from the American Society of Radiation Oncology have defined ‘no ink on tumor’ as the appropriate standard for a negative margin, meaning that any techniques for assessing the margins needs to only look at the very edge of the excised tissue [4]. The golden standard technique for this margin assessment is for a pathologist to fix the excised tumor in

formalin, then embed it in a paraffin block. This formalin-fixed, paraffin-embedded (FFPE) tissue is then further sectioned into 4-5 μm thick slices on microstrip slides and stained with hematoxylin and eosin (H&E) for pathologist examination under a microscope. However, the histopathology process can take from several days to weeks to go from freshly excised tissue to pathology assessment, meaning that any further excisions will require a second surgery that put additional strain on both patients and medical care providers [5]. While intraoperative techniques like radio frequency ablation and cavity shaving have shown to be effective in reducing positive margin rates, these techniques are generally undirected and can cause additional unnecessary damage without a method to isolate where any remaining cancer may be [6]. With a positive margin rate of 20-40% in conventional lumpectomy procedures, there is critical need for a fast intraoperative margin assessment tool [7].

Some techniques used to provide intraoperative margin assessment include rapid pathology processes like frozen section analysis (FSA) and touch-prep cytology. However, these techniques can lengthen the operation time, require a pathologist to be present in the operation room, and in the case of FSA can damage the excised tumor prior to full pathology [7], [8]. The most common technique currently in use that has been shown effective for intraoperative imaging is specimen radiography using x-ray [9]. However, there are limitations and low sensitivity of radiography mentioned in literature for detecting remnant tissue or small tumors [10]–[12]. Other investigated imaging techniques include microwave or infrared frequencies. However, microwave imaging was shown to have less than 10% differentiation between the properties of breast cancer and healthy fibrous tissue in a large-scale study from 0.5 to 30 GHz [13]. Infrared detection shows similar challenges and largely depends on fluorophores or contrast agents or on autofluorescence of

specific cellular structures [14]–[16]. As such, there remains a need for a rapid, accurate intraoperative margin assessment technique.

2. Terahertz for Breast Cancer Applications

The terahertz (THz) frequency range from 0.1 to 4 THz has been a growing area of interest for a variety of applications. While historically this band of frequencies has been difficult to access, the development of reliable THz sources has made research in the THz range accessible [17]. This includes a rapidly expanding field of biomedical imaging and spectroscopy both for cancer and noncancerous conditions [18]. This is primarily due to THz technology showing significant differentiation between various diseased and healthy tissues [19], [20]. THz radiation is relatively low-power and non-ionizing, making it biologically safe for both *in vivo* and excised tissues [21], [22]. Furthermore, THz frequencies have a greater imaging resolution than microwave techniques due to a shorter wavelength, and they have been shown to possess improved transmittance in fat tissues over infrared techniques [23]. General biomedical applications of THz imaging include the effects of liver cirrhosis [24], osseous tissue damage [25], cardiac tissue damage following myocardial infarction [26], and cell hydration sensing [27]. For cancer detection, THz imaging has been applied to a wide range of cancer types, starting with basal cell carcinoma in [28], [29] and cancer in the skin [30]–[32], liver [26], [33], colon [34], brain [35]–[37], and breast [38]–[44]. In all cases, THz has shown the ability to differentiate between cancer and healthy tissues. For breast cancer in particular, THz spectroscopy from 0.15 to 2 THz has shown distinct differentiation between cancer and healthy tissue at THz frequencies [45]. As a result, THz shows promise as a margin assessment tool.

For pulsed THz systems, two orientations of the sample under test are common: reflection or transmission. Transmission involves receiving the THz signal on the opposite side of a sample,

while reflection requires the THz emitter and detector to either be off-axis and at an oblique incidence or at a normal incidence with beamsplitters to isolate the incident and reflected signal. While THz signals have been seen to propagate through animal fat for effective imaging [23], most THz imaging of cancer to date has been conducted using reflection setups. This is primarily due to strong absorption of THz signals due to differences in water content between healthy and diseased or damaged tissues [46]. As a result, most transmission tissue imaging has been limited to either FFPE tissue or very thin slices of freshly excised tissue, where the absorption from water does not prevent imaging [26], [31], [47]. Furthermore, comparisons between transmission and reflection images of the same samples showed improved resolution of reflection setups due to a greater number of focusing elements [40]. In all cases, differentiation between healthy and cancerous tissue is expected to improve in healthy tissue when water content is a notable indicator of tissue health [35].

In addition to THz imaging, transmission and reflection models can be generated depending on sample orientation to calculate the refractive index and absorption coefficient from the THz image data [40]. This method of performing THz spectroscopy from imaging has been used in transmission setups for assessment of crystal formation in pharmaceuticals [48] and observing bone tissue degradation [25]. Meanwhile the use of THz reflection imaging to calculate material properties and system-dependent tomography setups are common in THz imaging applications [49]. Reflection spectroscopy has been used developed to detect water content in cells [27] and to characterize liver cirrhosis [24] and animal gastrointestinal tissues [50]. The investigation of spectroscopy models implemented into both transmission and reflection imaging setups were published in [40] and summarized below in Section 5.

Some other methods for quantifying the contrast in THz range include image processing and segmentation. The use of image processing tools like intensity windowing and histogram equalization has the potential to automate THz image visualization and reduce observer bias when viewing THz image results, while edge detection and region growing techniques can segment images into cancer and non-cancer regions [51], [52], [41]. Other algorithms can be applied to quantitatively compare THz images to digitized pathology to determine the imaging accuracy with a pixel-to-pixel comparison. Several classification methods have been investigated for FFPE tissue imaging and spectroscopy such as wavelet transformation [53], orthogonal signal correction and fuzzy rule-bending expert system [54], multispectral classification [55], and principal component analysis (PCA) [32], [56], [57]. For fresh tissue, PCA was shown to have 92% sensitivity and 87% specificity between dysplastic colon cancer and normal tissue while machine learning using a support vector machine (SVM) provided 96% sensitivity and 87% specificity for the same data [58]. SVM alone applied to 1.89 THz continuous wave imaging of breast cancer reported 72% discrimination [59]. Finally, SVM combined with PCA attained 92% accuracy for breast cancer [44]. Other than component analysis methods, statistical modeling using a Bayesian mixture method has been applied to murine breast cancer tissue as part of this dissertation work [43].

While image processing and classification can provide automated detection of cancer, further contrast in imaging is possible with the use of contrast agents. This can be used to avoid overlapping properties between tissue regions, such as a similar absorption coefficient between fibroglandular and breast cancer tissue in the THz range [45]. While contrast agents are well known in infrared, x-ray, and MRI technologies, their investigations in the THz range have been limited to date. One example is gold nano-rods (GNRs), which have been shown to increase the signal response of A431 epidermoid carcinoma cells in a petri dish by 20% under laser excitation [60].

Another example is superparamagnetic iron oxide nanoparticles (SPIOs) under magnetic excitation from MRI, which was shown to improve THz response in mouse ovarian cancer [61] and increase the reflected signal of water alone by 35% [62]. Other materials like gadolinium oxide and indium nitride have shown potential as contrast agents as well, but have yet to be implemented in THz imaging [63], [64]. One area of promising materials is carbon-based nanoparticles. Nanodiamonds (NDs) and onion-like carbon (OLC) can be functionalized to attach to cancer cells and have previously been combined with fluorophores for optical detection [65], [66]. NDs have been shown to have insignificant biological effects compared to nanoparticles of similar size [67]–[69]. While OLC has not been investigated as fully for toxicity, the few studies that have investigated it showed reduced inflammatory response and low genetic toxicity compared to carbon nanotubes [70], [71]. OLC has also been shown to have distinctly high broadband absorption from 20 Hz to 3 GHz, 8 to 53 GHz, 100 GHz to 3 THz, and 10 to 230 THz, which makes it viable as a contrast agent at THz frequencies without the need for additional fluorophores [72]–[74]. The investigation of these particles for THz imaging is detailed in [42] and summarized in Section 5.

3. Terahertz Imaging and Spectroscopy System

All experimental work in this dissertation was performed using the TPS Spectra 3000 (Teraview, Ltd.) THz imaging and spectroscopy system at the University of Arkansas. The system diagram is shown in Fig. 1. A Ti:Sapphire laser is used to excite the biased THz emitter antenna on a GaAs substrate. The THz signal generated by the antenna is then directed using mirrors to the sample space, with interchangeable modules used for reflection (Fig. 1a) or transmission (Fig. 1b) orientations. The generated THz time domain signal is shown in Fig. 1c, with a pulse width of ~280 fs for the maximum, ~587 fs for the first minimum, and ~287 fs for the second minimum.

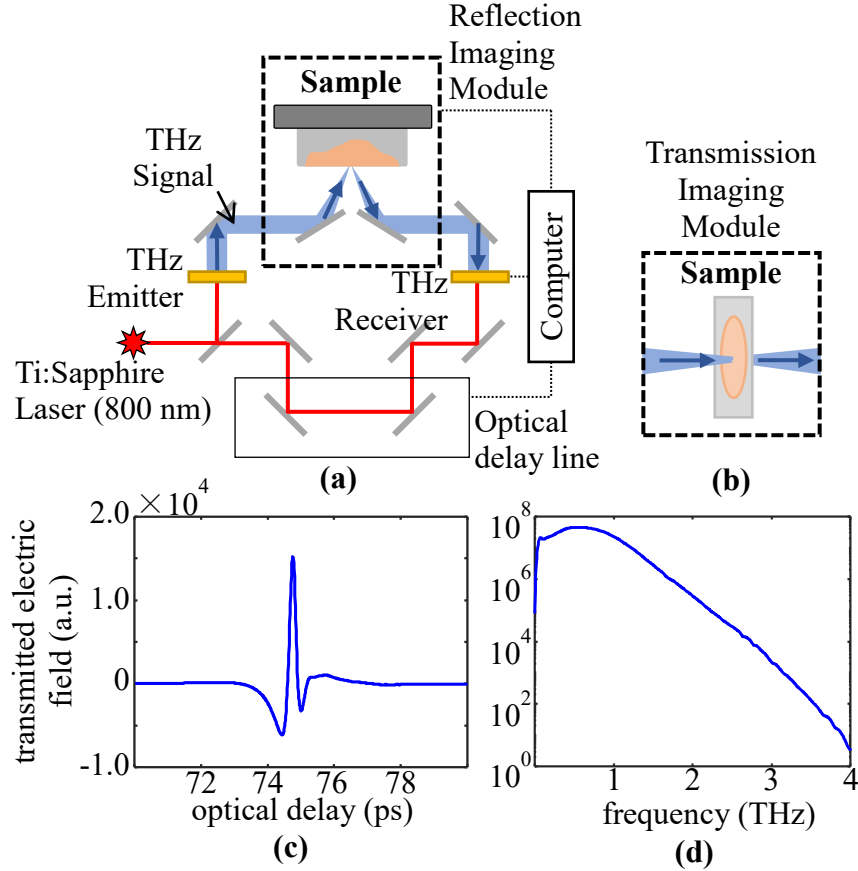


Figure 1. Diagram of THz imaging system with modules shown for (a) reflection imaging setup and (b) transmission setup.

The overall power of the system is $\sim 1 \mu\text{W}$. Performing Fourier transform on the time domain pulse results in the frequency domain spectrum from 0.1 to 4 THz seen in Fig. 1d.

The THz system consists of several modules that allow for transmission and spectroscopy under various conditions and orientations. The transmission modules are shown in Fig. 2, with the standard room temperature frame shown in Fig. 2a. Sample holders are used to mount materials in the THz signal path, with unique sample holders for pellets made of compressed powders or for liquid samples. The sample space is then purged with nitrogen gas to remove any effect from the water vapor presence in the chamber, and the sample measurement is taken as the average of many measurements (usually 1800) to decrease random system noise from the measurements. Fig. 2b shows the heated cell for pellet samples, which can perform spectroscopy up to 573 K. Meanwhile

the cryostat module in Fig. 2c allows for liquid helium to reach temperatures as low as 4 K. Thus, spectroscopy is possible across a wide range of temperatures. However, for the spectroscopy applications in this work only room temperature is considered.

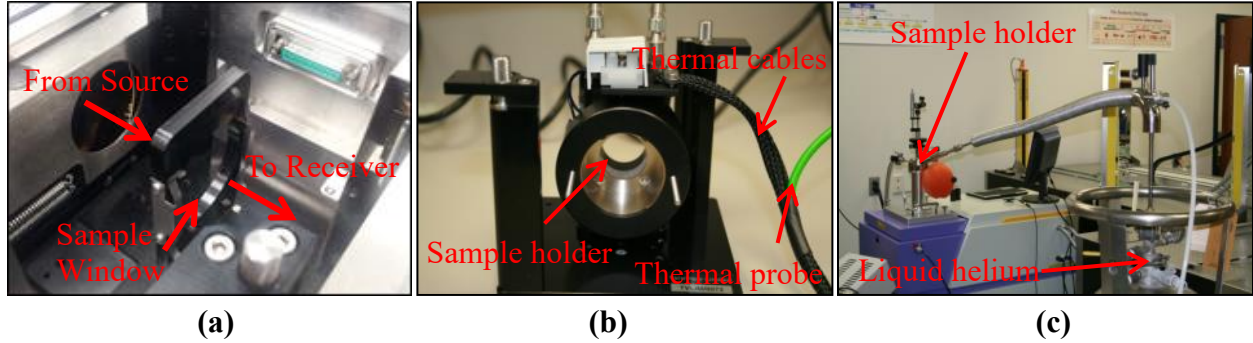


Figure 2. THz spectroscopy modules. (a) Standard module for room temperature measurements, (b) heated cell for temperatures up to 573 K, and (c) cryostat for temperatures down to 4 K.

THz imaging in the core system is performed using modules for either transmission or reflection orientations. The reflection imaging module in Fig. 3a sits above a mirror base that directs the THz signal upward to reflect off the sample and return to the detector below. A reflection stage controlled by step motors allows for step sizes as small as 50 μm , and the default imaging aperture has a diameter of 3.5 cm though removing it allows for a slightly larger scan area. For transmission imaging, the x-y mapper in Fig. 3b is used which has an imaging area of 2 cm \times 2 cm. In addition to the core system modules, the THz system also has a remote gantry system

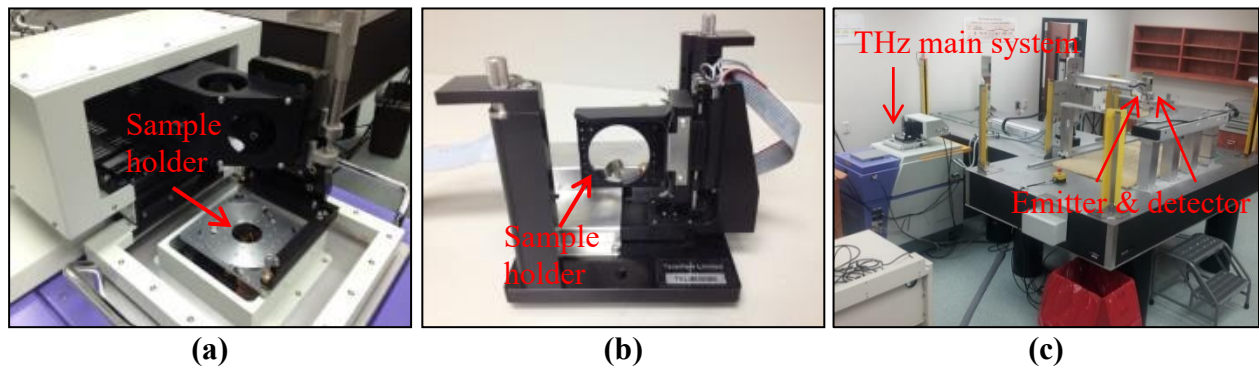


Figure 3. THz imaging modules. (a) Reflection imaging module, (b) transmission module (x-y mapper), and (c) external gantry system for samples up to 70 cm \times 70 cm.

that allows for large scale imaging in either reflection or transmission mode of up to 70 cm × 70 cm with a tradeoff of being in open air and therefore more subject to water vapor, though purging with nitrogen is still possible with a hood. For the works included in this dissertation all samples were small enough to use on the core system modules rather than the gantry. For mounting samples for transmission imaging, glass slides were found to be significantly attenuating at THz frequency, so low-loss polystyrene slides were eventually adopted instead [39], [40]. Likewise, polystyrene plates were implemented as windows to perform fresh tissue imaging due to their low loss and good signal transmission [43].

THz images are generated by scanning the sample in the beam path and measuring the reflected or transmitted THz signal at each point. Then, the THz signal is compared against a reference, generally the reflection from a gold mirror or a known material or transmission through an empty sample holder. From there, the THz image can be generated by taking the time domain peak or single frequency magnitude from the sample signal at each point [39]–[43], performing deconvolution of the reference signal [39], or applying a frequency domain spectral power integration [42], [43]. However, other features of the THz sample signal are being investigated as well.

4. Samples for Breast Cancer Spectroscopy and Imaging

Breast cancer tissue used in the published work for this dissertation was obtained from several sources. While results from every sample were not published, the full amount of samples will be described here. For human breast cancer, FFPE samples were purchased from tissue banks including the Cooperative Human Tissue Network (CHTN) and the National Disease Research Interchange (NDRI). 3 tissue samples were purchased from CHTN with the FFPE block already sectioned to provide 1 H&E slide and 11 slides of 10 μm thick unstained tissue on glass (3 H&E

slides and 33 10 μm slides total). A total of 3 FFPE tissue samples were purchased from NDRI as whole blocks with adjacent breast cancer and healthy tissue. Each block was scanned for THz imaging, then delivered to Northwest Arkansas Pathology Associates (NWA Pathology) for sectioning with alternating H&E and unstained slides. While the H&E slides maintained a standard thickness of 4-5 μm , the unstained slices followed a progression of 20, 30, and 40 μm to determine how thickness affected THz imaging and slide adhesion. All H&E slides were mounted on glass, while FFPE slices from the first sample were mounted on glass and the other two were mounted on polystyrene. A total of 48 H&E slides and 48 FFPE slices of tissue were generated from these samples. An additional 4 blocks of FFPE breast cancer tissue were supplied directly by NWA Pathology out of old surgical tissues set for discard. All four blocks underwent THz imaging, and then two were selected for additional sectioning. In these cases, a 20, 30, and 40 μm FFPE tissue slice was taken between every single pathology slice for imaging. All FFPE sections were mounted on polystyrene.

In addition to FFPE breast cancer tissue, three options have been investigated for experimentally validating THz imaging of freshly excised breast cancer tissue. The first is a series of breast cancer phantoms made using TX151 solidifying powder as a base along with varying amounts of water, oil, and surfactant to adjust the THz properties to align with that of fresh cancer or fibroglandular tissue and verified using THz spectroscopy [42], [75], [76]. Phantom tissues allow a high degree of control over the experimental setup and organization of cancer tissue with the surrounding healthy tissue. They also serve as a cost-effective means for developing imaging methodology and for examining the effects of contrast agents on the effective reflection from tissue [42].

The second method used to investigate fresh tissue is breast cancer tumors from mice, which are further divided into xenograft and transgenic tumors. Xenograft tumors are grown via cell injection of murine-derived E0771 breast adenocarcinoma cells. For this purpose, C57BL/6 black laboratory mice from The Jackson Laboratory were maintained on a high fat diet (D12492 from Research Diets, Inc.) until they reached a target weight of 35g [77]. The cells were then injected into the fatty deposits on each mouse's flank and the tumor was grown to a diameter of 1 cm before excision. Excised tumors were transferred in phosphate-buffered saline (PBS) to the THz system for imaging immediately after excision. Following THz imaging, tumors were immersed in formalin and shipped to the Oklahoma Animal Disease Diagnostic Laboratory (OADDL) for histopathology processing and pathology assessment. The resulting FFPE blocks were returned to the University of Arkansas for additional imaging and comparison. A total of 14 xenograft breast cancer samples obtained from 10 mice have been investigated, with some select results reported in [43]. On the other hand, transgenic mice tumors are naturally occurring due to selective breeding to eliminate a cancer suppressor gene. As such they represent a more natural tumor growth with associated structures and vasculature, making them better representations of human tissue than xenograft tumors. While some transgenic tumors have been excised from MMTV-PyMT mice from The Jackson Laboratory at this time, results from these samples have yet to be published and have only appeared in conferences to date [78].

The third option for imaging freshly excised breast cancer tissue is to obtain human surgical tissue directly through a biobank. This is being conducted currently with NDRI, where breast cancer and healthy breast tissues are taken directly from surgery and placed in in Dulbecco's Modified Eagle Medium (DMEM) to maintain tissue health with added penicillin streptomycin (PenStrep) to serve as an antibiotic. The samples are shipped overnight on wet ice to the University

of Arkansas, and THz imaging is performed within 24 hours of surgery. This is currently the fastest option to obtain freshly excised human without placing the THz system directly into a surgical setting. Since efforts using human surgical tissue are still underway, results have not yet been published. However, preliminary investigations have appeared in conferences [79]–[81].

5. Overview of Dissertation Chapters and Published Work

This dissertation follows the progression of THz imaging and spectroscopy of breast cancer at the University of Arkansas from computational modeling to experimental imaging and processing of fresh tissue. Chapter 1 has provided an overall introduction to the literature background, methods, and materials used throughout this work. Each subsequent chapter of this work corresponds to a single published paper in a peer-reviewed journal. The chapters and citations with their corresponding reference number for this chapter are as follows:

Chapter 2: [39] T. C. Bowman, M. El-Shenawee, and L. K. Campbell. “Terahertz Imaging of Excised Breast Tumor Tissue on Paraffin Sections.” *IEEE Transactions on Antennas and Propagation*, vol. 63, no. 5, pp. 2088-2097, 2015.

Chapter 3: [40] T. Bowman, M. El-Shenawee, and L. K. Cambell, “Terahertz transmission vs reflection imaging and model-based characterization for excised breast carcinomas” *Biomed. Opt. Express* vol. 7, no. 9, pp. 3756-3783, 2016.

Chapter 4: [41] T. Bowman, Y. Wu, J. Gauch, L. K. Campbell, and M. El-Shenawee, “Terahertz Imaging of Three-Dimensional Dehydrated Breast Cancer Tumors,” *Journal of Infrared, Millimeter, and Terahertz Waves*, vol. 38, no. 6, pp. 766-786, 2017.

Chapter 5: [42] T. Bowman, A. Walter, O. Shenderova, N. Nunn, G. McGuire, and M. El-Shenawee, “A Phantom Study of Terahertz Spectroscopy and Imaging of Micro- and Nano-diamonds and Nano-onions as Contrast Agents for Breast Cancer,” *Biomedical Physics and Engineering Express*, vol. 3, no. 5, pp. 055001, 2017.

Chapter 6: [43] T. Bowman, T. Chavez, K. Khan, J. Wu, A. Chakraborty, N. Rajaram, K. Bailey, and M. El-Shenawee, “Pulsed terahertz imaging of breast cancer in freshly excised murine tumors,” *Journal of Biomedical Optics*, vol. 23, no. 2, pp. 026004, 2018.

Lastly, Chapter 7 will provide overall concluding remarks and key challenges observed over the course of the dissertation. Further summaries of the included chapters are listed below.

In [39], THz reflection imaging and transmission spectroscopy were applied to FFPE slices of triple negative breast cancer tumors, notable for their high heterogeneity, to experimentally validate the differentiation between cancer and healthy tissue at THz frequencies. This work investigated three samples of infiltrating ductal carcinoma (IDC) in 10, 20, and 30 μm slices, showing clear differentiation between IDC and adjacent fibroglandular and fatty tissue and excellent correlation to pathology assessment performed on adjacent stained sections. Additionally, a transmission spectroscopy setup was used to calculate the refractive index and absorption coefficient of tissue on glass slides. These properties were then used to model the reflection of the FFPE tissue on glass, which showed close correlation to the experimental results. To the authors' knowledge, this was the first demonstrated differentiation between breast cancer and healthy tissue in FFPE sections, indicating an inherent contrast at the THz range independent of water presence in the tissue [39].

In [40], further investigation into different sample orientations and tissue characterization models were reported. This work compared transmission and reflection THz imaging for 20 and 30 μm FFPE slices of both lobular carcinoma (LC) and IDC. Imaging showed similar differentiation between cancer and healthy tissue for both tissue orientation. Spectroscopy models were calculated in reflection and transmission modes using impedance and reflection matching across multiple regions [82]–[84]. Furthermore, experimental techniques were used to approximate a linear orientation for an arbitrarily polarized THz beam at oblique incidence. The resulting spectroscopy showed a strong dependence of the solved properties on the sample phase, which is subject to the experimental setup and factors like microscope slide thickness and tissue adhesion to the slides. While only FFPE tissue was used for breast cancer in this work, the

characterization algorithms were also tested on bovine muscle and fat to represent fresh tissue and showed good correlation of spectroscopy results between the two methods [40].

Efforts toward automated image processing and segmentation for surgical applications, as well as investigation into three-dimensional tissue imaging, were reported in [41]. In this work intensity windowing and histogram equalization were employed to improve visualization of THz data with automated processes. Edge detection using Robert's Cross, Sobel, and Canny operators were effective in denoting the boundaries between cancer and healthy tissue, and region growing using the L2 norm of the reflected THz signal obtained reasonable estimations of the cancer regions from the THz images. Imaging of breast cancer tissue embedded in paraffin blocks showed secondary reflections different interfaces in the tissue, with the z-axis distance of the reflections calculated using a time of flight algorithm. From this THz Z-scan, the tissue images at depth were obtained without physically sectioning the block of tissue. The Z-scan images were then compared to pathology sections taken through the depth of the paraffin blocks, showing good detection of the cancer tissue edge and accurate depth estimation [41].

For additional improvement of THz imaging, carbon nanoparticles are investigated using breast cancer phantom models in [42]. Breast cancer phantoms were generated with a mixture of oil, water, surfactant, and a binding agent called TX151 with recipes developed to match the properties of freshly excised breast cancer [45], [75]. Micrometer-scale high-pressure, high-temperature (HPHT) diamond particles, NDs, and OLC embedded in PDMS and polyethylene tablets were investigated using transmission spectroscopy, showing increased scattering by micrometer-scale particles and high absorption by OLC at THz frequencies. The particles with the largest effect—100 μm diamond particles and 100 nm OLC—were further implemented into

cancer tissue phantoms, showing a distinct increase in refractive index and absorption coefficient when using OLC [42].

THz imaging was extended to fresh breast cancer tissue obtained from mice in [43]. Xenograft mouse tumors were grown in mice on a high fat diet, excised, and imaged immediately using THz reflection imaging. Additional imaging was performed following the histopathology process. An image morphing algorithm was implemented digitize pathology photographs, while a statistical Bayesian mixture model was used to classify regions of cancer, fat, and muscle for a point-to-point comparison. The results show excellent correlation of THz imaging of FFPE tissue to pathology and mostly effective comparison of fresh tissue imaging with clear challenges seen in removing excess fluid from the imaging plane and overlapping tissue properties [43].

References

- [1] American Cancer Society, “Cancer Facts and Figures 2015,” 2015. [Online]. Available: <http://www.cancer.org/acs/groups/content/@editorial/documents/document/acspc-044552.pdf>. [Accessed: 13-Jan-2016].
- [2] S. Glück and T. Mamounas, “Improving outcomes in early-stage breast cancer.,” *Oncology*, vol. 24, no. 11 Suppl 4, pp. 1–15, 2010.
- [3] V. S. Klimberg, J. Kepple, G. Shafirstein, L. Adkins, R. Henry-Tillman, E. Youssef, J. Brito, L. Talley, and S. Korourian, “eRFA: excision followed by RFA—a new technique to improve local control in breast cancer.,” *Ann. Surg. Oncol.*, vol. 13, no. 11, pp. 1422–33, 2006.
- [4] M. S. Moran, S. J. Schnitt, A. E. Giuliano, J. R. Harris, S. A. Khan, J. Horton, S. Klimberg, M. Chavez-MacGregor, G. Freedman, N. Houssami, P. L. Johnson, and M. Morrow, “Society of Surgical Oncology--American Society for Radiation Oncology Consensus Guideline on Margins for Breast-Conserving Surgery With Whole-Breast Irradiation in Stages I and II Invasive Breast Cancer,” *Int. J. Radiat. Oncol.*, vol. 88, no. 3, pp. 553–564, 2014.
- [5] L. Jacobs, “Positive margins: the challenge continues for breast surgeons.,” *Ann. Surg. Oncol.*, vol. 15, no. 5, pp. 1271–1272, 2008.

- [6] V. S. Klimberg, C. Boneti, L. L. Adkins, M. Smith, E. Siegel, V. Zharov, S. Ferguson, R. Henry-Tillman, B. Badgwell, and S. Korourian, “Feasibility of percutaneous excision followed by ablation for local control in breast cancer.,” *Ann. Surg. Oncol.*, vol. 18, no. 11, pp. 3079–87, 2011.
- [7] R. G. Pleijhuis, M. Graafland, J. de Vries, J. Bart, J. S. de Jong, and G. M. van Dam, “Obtaining adequate surgical margins in breast-conserving therapy for patients with early-stage breast cancer: current modalities and future directions.,” *Ann. Surg. Oncol.*, vol. 16, no. 10, pp. 2717–2730, 2009.
- [8] T. P. Olson, J. Harter, A. Muñoz, D. M. Mahvi, and T. M. Breslin, “Frozen section analysis for intraoperative margin assessment during breast-conserving surgery results in low rates of re-excision and local recurrence,” *Ann. Surg. Oncol.*, vol. 14, no. 10, pp. 2953–2960, 2007.
- [9] D. M. Layfield, D. J. May, R. I. Cutress, C. Richardson, A. Agrawal, M. Wise, and C. Yiangou, “The effect of introducing an in-theatre intra-operative specimen radiography (IOSR) system on the management of palpable breast cancer within a single unit,” *Breast*, vol. 21, no. 4, pp. 459–463, 2012.
- [10] L. Bathla, A. Harris, M. Davey, P. Sharma, and E. Silva, “High resolution intra-operative two-dimensional specimen mammography and its impact on second operation for re-excision of positive margins at final pathology after breast conservation surgery,” *Am. J. Surg.*, vol. 202, no. 4, pp. 387–394, 2011.
- [11] P. D. Britton, L. I. Sonoda, A. K. Yamamoto, B. Koo, E. Soh, and A. Goud, “Breast surgical specimen radiographs: how reliable are they?,” *Eur. J. Radiol.*, vol. 79, no. 2, pp. 45–49, 2011.
- [12] C. Rua, P. Lebas, P. Michenet, and I. Ouldamer, “Evaluation of lumpectomy surgical specimen radiographs in subclinical, in situ, and invasive breast cancer, and factors predicting positive margins,” *Diagn. Interv. Imaging*, vol. 93, no. 8, pp. 71–77, 2012.
- [13] M. Lazebnik, D. Popovic, L. McCartney, C. B. Watkins, M. J. Lindstrom, J. Harter, S. Sewall, T. Ogilvie, A. Magliocco, T. M. Breslin, W. Temple, M. Daphne, J. H. Booske, M. Okoniewski, and S. C. Hagness, “A large-scale study of the ultrawideband microwave dielectric properties of normal, benign and malignant breast tissues obtained from cancer surgeries,” *Phys. Med. Biol.*, vol. 52, no. 10, pp. 6093–6115, 2007.
- [14] Q. R. J. G. Tummers, F. P. R. Verbeek, B. E. Schaafsma, M. C. Boonstra, J. R. van der Vorst, G.-J. Liefers, C. J. H. van de Velde, J. V Frangioni, and A. L. Vahrmeijer, “Real-time intraoperative detection of breast cancer using near-infrared fluorescence imaging and Methylene Blue.,” *Eur. J. Surg. Oncol.*, vol. 40, no. 7, pp. 850–858, 2014.

- [15] S. Kumar, C. Desmedt, D. Larsimont, C. Sotiriou, and E. Goormaghtigh, “Change in the microenvironment of breast cancer studied by FTIR imaging,” *Analyst*, vol. 138, no. 14, pp. 4058–4065, 2013.
- [16] V. Sharma, S. Shivalingaiah, Y. Peng, D. Euhus, Z. Gryczynski, and H. Liu, “Auto-fluorescence lifetime and light reflectance spectroscopy for breast cancer diagnosis: potential tools for intraoperative margin detection,” *Biomed. Opt. Express*, vol. 3, no. 8, pp. 1825–1840, 2012.
- [17] P. U. Jepsen, D. G. Cooke, and M. Koch, “Terahertz spectroscopy and imaging - Modern techniques and applications,” *Laser Photon. Rev.*, vol. 5, no. 1, pp. 124–166, 2011.
- [18] S. Fan, Y. He, B. S. Ung, and E. Pickwell-MacPherson, “The growth of biomedical terahertz research,” *J. Phys. D. Appl. Phys.*, vol. 47, no. 37, p. 374009, 2014.
- [19] P. H. Siegel, “Terahertz technology in biology and medicine,” *IEEE Trans. Microw. Theory Tech.*, vol. 52, no. 10, pp. 2438–2447, 2004.
- [20] Y. Sun, M. Y. Sy, Y.-X. J. Wang, A. T. Ahuja, Y.-T. Zhang, and E. Pickwell-Macpherson, “A promising diagnostic method: Terahertz pulsed imaging and spectroscopy.,” *World J. Radiol.*, vol. 3, no. 3, pp. 55–65, 2011.
- [21] G. J. Wilmink and J. E. Grundt, “Invited Review Article: Current State of Research on Biological Effects of Terahertz Radiation,” *J. Infrared, Millimeter, Terahertz Waves*, vol. 32, no. 10, pp. 1074–1122, 2011.
- [22] S. W. Smye, J. M. Chamberlain, A. J. Fitzgerald, and E. Berry, “The interaction between Terahertz radiation and biological tissue.,” *Phys. Med. Biol.*, vol. 46, no. 9, pp. R101–R112, 2001.
- [23] P. Y. Han, G. C. Cho, and X. C. Zhang, “Time-domain transillumination of biological tissues with terahertz pulses.,” *Opt. Lett.*, vol. 25, no. 4, pp. 242–244, 2000.
- [24] S. Sy, S. Huang, Y.-X. J. Wang, J. Yu, A. T. Ahuja, Y.-T. Zhang, and E. Pickwell-MacPherson, “Terahertz spectroscopy of liver cirrhosis: investigating the origin of contrast.,” *Phys. Med. Biol.*, vol. 55, no. 24, pp. 7587–7596, 2010.
- [25] W. E. Baughman, H. Yokus, S. Balci, D. S. Wilbert, P. Kung, and S. M. Kim, “Observation of hydrofluoric acid burns on osseous tissues by means of terahertz spectroscopic imaging,” *IEEE J. Biomed. Heal. Informatics*, vol. 17, no. 4, pp. 798–805, 2013.
- [26] Y. Miura, A. Kamataki, M. Uzuki, T. Sasaki, J. Nishizawa, and T. Sawai, “Terahertz-wave spectroscopy for precise histopathological imaging of tumor and non-tumor lesions in paraffin sections.,” *Tohoku J. Exp. Med.*, vol. 223, pp. 291–296, 2011.

- [27] D. Y. S. Chau, A. R. Dennis, H. Lin, J. A. Zeitler, and A. Tunnacliffe, “Determination of Water Content in Dehydrated Mammalian Cells Using Terahertz Pulsed Imaging : A Feasibility Study,” *Curr. Pharm. Biotechnol.*, vol. 17, no. 2, pp. 200–207, 2016.
- [28] R. M. Woodward, V. P. Wallace, R. J. Pye, B. E. Cole, D. D. Arnone, E. H. Lin, and M. Pepper, “Terahertz Pulse Imaging of ex vivo Basal Cell Carcinoma,” *J. Invest. Dermatol.*, vol. 120, no. 1, pp. 72–78, 2003.
- [29] R. M. Woodward, B. E. Cole, V. P. Wallace, R. J. Pye, D. D. Arnone, E. H. Linfield, and M. Pepper, “Terahertz pulse imaging in reflection geometry of human skin cancer and skin tissue,” *Phys. Med. Biol.*, vol. 47, no. 21, p. 3853, 2002.
- [30] C. S. Joseph, R. Patel, V. A. Neel, R. H. Giles, and A. N. Yaroslavsky, “Imaging of ex vivo nonmelanoma skin cancers in the optical and terahertz spectral regions,” *J. Biophotonics*, vol. 7, no. 5, pp. 295–303, 2014.
- [31] C. S. Joseph, A. N. Yaroslavsky, V. A. Neel, T. M. Goyette, and R. H. Giles, “Continuous wave terahertz transmission imaging of nonmelanoma skin cancers,” *Lasers Surg. Med.*, vol. 43, no. 6, pp. 457–462, 2011.
- [32] K. I. Zaitsev, N. V. Chernomyrdin, K. G. Kudrin, I. V. Reshetov, and S. O. Yurchenko, “Terahertz Spectroscopy of Pigmentary Skin Nevi in Vivo,” *Opt. Spectrosc.*, vol. 119, no. 3, pp. 404–410, 2015.
- [33] P. Knobloch, C. Schildknecht, T. Kleine-Ostmann, M. Koch, S. Hoffmann, M. Hofmann, E. Rehberg, M. Sperling, K. Donhuijsen, G. Hein, and K. Pierz, “Medical THz imaging: an investigation of histo-pathological samples.,” *Phys. Med. Biol.*, vol. 47, no. 21, pp. 3875–84, 2002.
- [34] P. Doradla, K. Alavi, C. Joseph, and R. Giles, “Detection of colon cancer by continuous-wave terahertz polarization imaging technique,” *J. Biomed. Opt.*, vol. 18, no. 9, p. 90504, 2013.
- [35] S. J. Oh, S.-H. Kim, Y. Bin Ji, K. Jeong, Y. Park, J. Yang, D. W. Park, S. K. Noh, S.-G. Kang, Y.-M. Huh, J.-H. Son, and J.-S. Suh, “Study of freshly excised brain tissues using terahertz imaging,” *Biomed. Opt. Express*, vol. 5, no. 8, pp. 2837–42, 2014.
- [36] K. Meng, T. Chen, T. Chen, L. Zhu, Q. Liu, Z. Li, F. Li, S. Zhong, Z. Li, H. Feng, and J. Zhao, “Terahertz pulsed spectroscopy of paraffin-embedded brain glioma,” *J. Biomed. Opt.*, vol. 19, no. 7, p. 77001, 2014.
- [37] S. Yamaguchi, Y. Fukushi, O. Kubota, T. Itsuji, T. Ouchi, and S. Yamamoto, “Brain tumor imaging of rat fresh tissue using terahertz spectroscopy,” *Sci. Rep.*, vol. 6, no. 30124, pp. 1–6, 2016.

- [38] T. C. Bowman, A. M. Hassan, and M. El-Shenawee, "Imaging 2D Breast Cancer Tumor Margin at Terahertz Frequency using Numerical Field Data based on DDSCAT," *ACES J.*, vol. 28, no. 11, pp. 1017–1024, 2013.
- [39] T. C. Bowman, M. El-Shenawee, and L. K. Campbell, "Terahertz Imaging of Excised Breast Tumor Tissue on Paraffin Sections," *IEEE Trans. Antennas Propag.*, vol. 63, no. 5, pp. 2088–2097, 2015.
- [40] T. Bowman, M. El-Shenawee, and L. K. Campbell, "Terahertz transmission vs reflection imaging and model-based characterization for excised breast carcinomas," *Biomed. Opt. Express*, vol. 7, no. 9, 2016.
- [41] T. Bowman, Y. Wu, J. Gauch, L. K. Campbell, and M. El-Shenawee, "Terahertz Imaging of Three-Dimensional Dehydrated Breast Cancer Tumors," *J. Infrared, Millimeter, Terahertz Waves*, vol. 38, no. 6, pp. 766–786, 2017.
- [42] T. Bowman, A. Walter, O. Shenderova, N. Nunn, G. McGuire, and M. El-Shenawee, "A phantom study of terahertz spectroscopy and imaging of micro- and nano-diamonds and nano-onions as contrast agents for breast cancer," *Biomed. Phys. Eng. Express*, vol. 3, no. 5, p. 55001, 2017.
- [43] T. Bowman, T. Chavez, K. Khan, J. Wu, A. Chakraborty, N. Rajaram, K. Bailey, and M. El-Shenawee, "Pulsed terahertz imaging of breast cancer in freshly excised murine tumors," *J. Biomed. Opt.*, vol. 23, no. 2, 2018.
- [44] A. J. Fitzgerald, S. Pinder, A. D. Purushotham, P. O'Kelly, P. C. Ashworth, and V. P. Wallace, "Classification of terahertz-pulsed imaging data from excised breast tissue," *J. Biomed. Opt.*, vol. 17, no. 1, p. 16005, 2012.
- [45] P. C. Ashworth, E. Pickwell-MacPherson, E. Provenzano, S. E. Pinder, A. D. Purushotham, M. Pepper, and V. P. Wallace, "Terahertz pulsed spectroscopy of freshly excised human breast cancer," *Opt. Express*, vol. 17, no. 15, pp. 12444–12454, 2009.
- [46] A. J. Fitzgerald, E. Berry, N. N. Zinov'ev, S. Homer-Vanniasinkam, R. E. Miles, J. M. Chamberlain, and M. A. Smith, "Catalogue of human tissue optical properties at terahertz frequencies," *J. Biol. Phys.*, vol. 29, no. 2–3, pp. 123–128, 2003.
- [47] F. Wahaiia, G. Valusis, L. M. Bernardo, A. Almeida, J. A. Moreira, P. C. Lopes, J. Macutkevici, I. Kasalynas, D. Seliuta, R. Adomavicius, R. Henrique, and M. Lopes, "Detection of colon cancer by terahertz techniques," *J. Mol. Struct.*, vol. 1006, no. 1–3, pp. 77–82, 2011.
- [48] D. M. Charron, K. Ajito, J. Y. Kim, and Y. Ueno, "Chemical mapping of pharmaceutical cocrystals using terahertz spectroscopic imaging," *Anal. Chem.*, vol. 85, no. 4, pp. 1980–1984, 2013.

- [49] B. Recur, L. Frederique, B. Bousquet, L. Canioni, and P. Mounaix, "Review of Terahertz Tomography Techniques," *J. Infrared, Millimeter, Terahertz Waves*, vol. 35, no. 4, pp. 382–411, 2014.
- [50] Y. Bin Ji, S.-H. Kim, K. Jeong, Y. Choi, J.-H. Son, D. W. Park, S. K. Noh, T.-I. Jeon, Y.-M. Huh, S. Haam, S. K. Lee, S. J. Oh, and J.-S. Suh, "Terahertz spectroscopic imaging and properties of gastrointestinal tract in a rat model," *Biomed. Opt. Express*, vol. 5, no. 12, pp. 4162–4170, 2014.
- [51] R. C. Gonzalez and R. E. Woods, "Intensity Transformation and Spatial Filtering," in *Digital Image Processing*, 3rd ed., Upper Saddle River, NJ: Pearson Prentice Hall, 2008, pp. 120–144.
- [52] J. F. Canny, "A Computational Approach to Edge Detection," *IEEE Trans. Pattern Anal. Mach. Intell.*, vol. 8, no. 6, pp. 679–698, 1986.
- [53] D. Ng, F. T. Wong, W. Withayachumnankul, D. Findlay, B. Ferguson, and D. Abbott, "Classification of osteosarcoma T-ray responses using adaptive and rational wavelets for feature extraction," in *SPIE 6802, Complex Systems II*, 2007, vol. 6802, p. 680211.
- [54] N. Qi, Z. Zhang, Y. Xiang, Y. Yang, X. Liang, and P. D. B. Harrington, "Terahertz time-domain spectroscopy combined with support vector machines and partial least squares-discriminant analysis applied for the diagnosis of cervical carcinoma," *Anal. Methods*, vol. 7, no. 6, pp. 2333–2338, 2015.
- [55] E. Berry, J. W. Handley, A. J. Fitzgerald, W. J. Merchant, R. D. Boyle, N. N. Zinov'ev, R. E. Miles, J. M. Chamberlain, and M. A. Smith, "Multispectral classification techniques for terahertz pulsed imaging: An example in histopathology," *Med. Eng. Phys.*, vol. 26, no. 5, pp. 423–430, 2004.
- [56] F. Formanek, M.-A. Brun, and A. Yasuda, "Contrast improvement of terahertz images of thin histopathologic sections.," *Biomed. Opt. Express*, vol. 2, no. 1, pp. 58–64, 2010.
- [57] S. Nakajima, H. Hoshina, M. Yamashita, C. Otani, and N. Miyoshi, "Terahertz imaging diagnostics of cancer tissues with chemometrics technique," *Appl. Phys. Lett.*, vol. 90, p. 41102, 2007.
- [58] L. H. Eadie, C. B. Reid, A. J. Fitzgerald, and V. P. Wallace, "Optimizing multi-dimensional terahertz imaging analysis for colon cancer diagnosis," *Expert Syst. Appl.*, vol. 40, no. 6, pp. 2043–2050, 2013.
- [59] B. St. Peter, S. Yngvesson, P. Siqueira, P. Kelly, A. Khan, S. Glick, and A. Karellas, "Development and Testing of a Single Frequency Terahertz Imaging System for Breast Cancer Detection," *IEEE J. Biomed. Heal. Informatics*, vol. 17, no. 4, pp. 785–797, 2013.

- [60] S. J. Oh, J. Kang, I. Maeng, J.-S. Suh, Y. M. Huh, S. Haam, and J.-H. Son, “Nanoparticle-enabled terahertz imaging for cancer diagnosis,” *Opt. Express*, vol. 17, no. 5, pp. 3469–3475, 2009.
- [61] J. Y. Park, H. J. Choi, G. Nam, K. Cho, and J. Son, “In Vivo Dual-Modality Terahertz / Magnetic Resonance Imaging Using Superparamagnetic Iron Oxide Nanoparticles as a Dual Contrast Agent,” *IEEE Trans. Terahertz Sci. Technol.*, vol. 2, no. 1, pp. 93–98, 2012.
- [62] R. Zhang, L. Zhang, T. Wu, S. Zuo, R. Wang, J. Zhang, and J. Fang, “Contrast-enhanced continuous-terahertz-wave imaging based on superparamagnetic iron oxide nanoparticles for biomedical applications,” *Opt. Express*, vol. 24, no. 8, pp. 7915–7921, 2016.
- [63] D. K. Lee, H. Kim, T. Kim, B. Cho, K. Lee, and J. H. Son, “Characteristics of gadolinium oxide nanoparticles as contrast agents for terahertz imaging,” *J. Infrared, Millimeter, Terahertz Waves*, vol. 32, no. 4, pp. 506–512, 2011.
- [64] M. Ney and I. Abdulhalim, “Ultrahigh polarimetric image contrast enhancement for skin cancer diagnosis using InN plasmonic nanoparticles in the terahertz range,” *J. Biomed. Opt.*, vol. 20, no. 12, p. 125007, 2015.
- [65] Y. Y. Hui and H.-C. Chang, “Recent Developments and Applications of Nanodiamonds as Versatile Bioimaging Agents,” *J. Chinese Chem. Soc.*, vol. 61, pp. 67–76, 2014.
- [66] S. Giordani, J. Bartelmess, M. Frasconi, I. Biondi, S. Cheung, M. Grossi, D. Wu, L. Echegoyen, and D. F. O’Shea, “NIR fluorescence labelled carbon nano-onions: synthesis, analysis and cellular imaging,” *J. Mater. Chem. B*, vol. 2, pp. 7459–7463, 2014.
- [67] V. Vaijayanthimala, P.-Y. Cheng, S.-H. Yeh, K.-K. Liu, C.-H. Hsiao, J.-I. Chao, and H.-C. Chang, “The long-term stability and biocompatibility of fluorescent nanodiamond as an in vivo contrast agent,” *Biomaterials*, vol. 33, no. 31, pp. 7794–7802, 2012.
- [68] Y. Xing, W. Xiong, L. Zhu, E. Osawa, S. Hussin, and L. Dai, “DNA Damage in Embryonic Stem Cells Caused by Nanodiamonds,” *ACS Nano*, vol. 5, no. 3, pp. 2376–2384, 2011.
- [69] J. Bartelmess, S. J. Quinn, and S. Giordani, “Carbon nanomaterials: multi-functional agents for biomedical fluorescence and Raman imaging,” *Chem. Soc. Rev.*, vol. 44, pp. 4672–4698, 2014.
- [70] M. Yang, K. Flavin, I. Kopf, G. Radics, C. H. A. Hearnden, G. J. McManus, B. Moran, A. Villalta-Cerdas, L. A. Echegoyen, S. Giordani, and E. C. Lavelle, “Functionalization of Carbon Nanoparticles Modulates Inflammatory Cell Recruitment and NLRP3 Inflammasome Activation,” *Small*, vol. 9, no. 24, pp. 4194–4206, 2013.

- [71] L. Ding, J. Stilwell, T. Zhang, O. Elboudwarej, H. Jiang, J. P. Selegue, P. A. Cooke, J. W. Gray, and F. F. Chen, “Molecular Characterization of the Cytotoxic Mechanism of Multiwall Carbon Nanotubes and Nano-Onions on Human Skin Fibroblast,” *Nano Lett.*, vol. 5, no. 12, pp. 2448–2464, 2005.
- [72] J. Macutkevic, J. Banys, S. Moseenkov, V. Kuznetsov, N. Nunn, and O. Shenderova, “Dielectric Properties of Onion-Like Carbon and Detonation Nanodiamond / Polydimethylsiloxane Composites,” *Polym. Compos.*, pp. 1–9, 2014.
- [73] I. Kranauskaite, J. Macutkevic, J. Banys, E. Talik, V. Kuznetsov, N. Nunn, and O. Shenderova, “Synergy effects in the electrical conductivity behavior of onion-like carbon and multiwalled carbon nanotubes composites,” *Phys. Status Solidi B*, vol. 5, pp. 1–5, 2015.
- [74] O. Shenderova, V. Grishko, G. Cunningham, S. Moseenkov, G. McGuire, and V. Kuznetsov, “Onion-like carbon for terahertz electromagnetic shielding,” *Diam. Relat. Mater.*, vol. 17, pp. 462–466, 2008.
- [75] A. Walter, T. Bowman, and M. El-Shenawee, “Development of breast cancer tissue phantoms for terahertz imaging,” in *SPIE 9700, Design and Quality for Biomedical Technologies IX*, 2016, p. 970003.
- [76] A. Walter, “Development of Breast Tissue Phantoms for Enhanced Terahertz Imaging Utilizing Microdiamond and Nano-Onion Particles,” University of Arkansas, 2016.
- [77] S. K. Boi, C. M. Buchta, N. A. Pearson, M. B. Francis, D. K. Meyerholz, J. L. Grobe, and L. A. Norian, “Obesity alters immune and metabolic profiles: New insight from obese-resistant mice on high-fat diet,” *Obesity*, vol. 24, no. 10, pp. 2140–2149, 2016.
- [78] T. Bowman, N. Rajaram, K. Bailey, and M. El-Shenawee, “THz Imaging Comparison of Xenograft and Transgenic Murine Breast Cancer Tumors,” in *USNC-URSI 2018*, 2018.
- [79] T. Bowman, K. Bailey, and M. El-Shenawee, “Pulsed Terahertz Imaging of Fresh and Fixed Human Breast Cancer Tissue,” in *42nd International Conference on Infrared, Millimeter, and Terahertz Waves*, 2017.
- [80] M. El-Shenawee, T. Bowman, T. Chavez, K. Khan, J. Wu, A. Chakraborty, and K. Bailey, “Statistical Signal Processing for Quantitative Assessment of Pulsed Terahertz IMaging of Human Breast Tumors,” in *42nd International Conference on Infrared, Millimeter, and Terahertz Waves*, 2017.
- [81] T. Bowman, K. Bailey, and M. El-Shenawee, “Terahertz Imaging of Freshly Excised Invasive Ductal Carcinoma Breast Tumors,” in *2017 URSI General Assembly and Scientific Symposium*, 2017.

- [82] T. C. Bowman, “Experimental Terahertz Imaging and Spectroscopy for Ex-vivo Breast Cancer Tissue,” University of Arkansas, 2014.
- [83] C. T. A. Johnk, *Engineering Electromagnetic Fields and Waves*, 2nd ed. John Wiley & Sons, Inc., 1988.
- [84] S. J. Orfanidis, *Electromagnetic Waves and Antennas*. 2013.

Chapter 2: Terahertz Imaging of Excised Breast Tumor Tissue on Paraffin Sections

© 2015 IEEE. Reprinted, with permission, from T. C. Bowman, M. El-Shenawee, and L. K. Campbell. "Terahertz Imaging of Excised Breast Tumor Tissue on Paraffin Sections." *IEEE Transactions on Antennas and Propagation*, vol. 63, no. 5, pp. 2088-2097, May 2015. [doi: 10.1109/TAP.2015.2406893]

Abstract

This paper presents imaging and analysis of heterogeneous breast cancer tissue using pulsed terahertz imaging technology. The goal of this research is to validate and standardize a methodology for terahertz imaging capable of differentiating between heterogeneous regions of breast tumor. The specimens utilized here were obtained from breast tumors diagnosed as triple negative infiltrating ductal carcinoma. These tissues were fixed in formalin, embedded in paraffin, and cut into sections of three thicknesses: 10 μm , 20 μm , and 30 μm . All tissues were prepared on standard glass slides used in regular histopathology of hematoxylin and eosin stained sections. The terahertz pulsed system is used to scan the two dimensional tissue sections with step size of 400 μm , 200 μm , and 50 μm . The experimentally measured terahertz fields reflected from single pixels identified in each region of the tumor are validated with the Fresnel reflection coefficient formulation. A variety of signal normalization and processing methods are investigated. The images are also validated with the standard histopathology images. The obtained results of three different tumors demonstrate strong capability of terahertz reflection imaging mode to distinguish between the heterogeneous regions in the tumor.

1. Introduction

Breast cancer is a leading medical concern among women in the world today [1]. For breast cancer where the tumor is sufficiently small, the preferred method of treatment is for the patient to undergo breast conserving surgery (BCS), also called lumpectomy. This procedure seeks to remove the breast cancer via excision. Additionally, a minimal layer of surrounding normal tissue

known as the margin is removed to ensure that no more tumor tissue is left in the breast while maintaining the best cosmetic outcome for the patient. In order to meet both of these goals, it is critical to have a method for assessing the margin tissue that is reliable. In other words, there is a significant need to develop a reliable imaging technique capable of differentiating between cancer, healthy fibrous and glandular (fibroglandular) tissue that directly surrounds the tumor, and healthy fatty tissue of the breast.

The standard process for margin assessment is to prepare slices of the excised tumor tissue for evaluation by the pathologist, who will classify the margin tissue into one of three categories. A positive margin indicates that cancer exceeds the edge of the excised tumor, a negative margin denotes no cancer within 2 mm of the edge, and a close margin is assigned when there is cancer within 2 mm of the edge without exceeding the excision [2]. When a positive margin is detected, the patient is required to undergo a second surgery in order to remove all remaining cancerous tissue. The need for a second surgery creates strain on the time and resources of the medical provider and has negative financial, cosmetic, and emotional impacts on the patient [3].

With conventional lumpectomy procedures, 20-40% of excisions are found to have a positive margin [2]. Furthermore, when a new cancer growth also known as local recurrence does arise, 75-90% of cases involve cancerous tissue in the site of the primary surgery [4]. There are several concerns with the use of pathology alone in assessing the tissue for positive margins, as it is difficult to perform a frozen section on all of the margins at the time of surgery. Additionally, the final pathology report on the margin status takes several days to acquire. This delay in particular calls for the development of techniques that will more reliably detect the extent of the tumorous tissue prior to or at the time of surgery.

To date, many techniques have been developed to address the problem of positive margins in BCS. The most common technique for determining the shape and location of a tumor prior to the surgery is mammography, an imaging technique using X-rays. However, there are some limitations when attempting to map the full extent of a tumor with mammography alone, especially in younger women [2]. Magnetic resonance imaging (MRI) is another common method for detecting the extent of a tumor prior to surgery using magnetic coils and a contrast agent. However, the use of MRI in tumor detection does not demonstrate an improvement in the overall occurrence of positive margins and recurrence of cancer following surgery [5]. A number of intraoperative techniques are already in use for attempting to minimize the occurrence of positive margins such as wire-guided marking of the tumor edge, ultrasound and radio frequency detection, and cryoprobe methods to freeze the tumor bulk for better localization of the tumor being excised. However, tumor localization alone has not been found to fully address the problem of positive tumor margins [2], [6]. In addition to localization, other techniques attempt to provide assessment of the tumor margin during the surgery. Intraoperative specimen radiography evaluates the excised specimen using portable X-ray mammography, but the technique lacks the specificity to be reliable as a standalone method and requires a radiologist during the surgery [2]. For pathology assessment in the operating room, frozen section analysis (FSA) or touch prep cytology is used to perform rapid frozen pathology or pathology of the margin's surface cells, respectively [2], [7]. While FSA is relatively cheap overall, it increases the length of the operation, requires the services of a pathologist close to the operation room, and can require large amounts of tissue which could interfere with standard pathology diagnosis and tumor staging. Additionally, frozen artifacts in the tissue can make interpretation difficult [2]. Other methods such as shaving, radiofrequency

ablation, and local radiation therapy were proven effective in treating any detected cancerous tissue remaining in the lumpectomy cavity [8], [9].

Based on the above literature, there is a need to investigate new technologies capable of characterizing different regions of excised tumor tissue. The goal of this work is to apply terahertz (THz) imaging to this application. A comparable technology to terahertz is optical fluorescence imaging or chemical indicator sensing that have shown a potential for margin assessment [6], [10], [11]. However, experimental work in the literature demonstrated a significant enhancement in image contrast when using terahertz waves compared with near-infrared (NIR) [12]. This phenomenon is due to the longer wavelengths of THz waves compared with NIR and optical radiation. Scattering arises from spatial variations in the refractive index of the tissue, extracellular constituents, and mammalian cells. Photons are scattered most strongly by structures whose size matches the incident wavelength. Thus, scattering in biological materials is strong at visible and NIR wavelengths, and weak at longer wavelengths [13]. As a result, in biological tissue, Rayleigh scattering (i.e. weak scattering) is the major contributor to a THz pulse, whereas Mie scattering (i.e. strong scattering) becomes more important for an optical pulse. Thus the longer THz wavelength makes the scattering of waves in tissue much less than that of optical beams. In other words, biological scattering is particularly weak at THz wavelengths because THz waves are several orders of magnitude larger than most biological structures [13]. Due to this feature, THz tissue interactions are assumed to be an absorption-dominated case, which implies information at greater depth can be obtained with a THz beam [12], [13].

Another advantage is that THz radiation is non-ionizing and carries relatively little power. Therefore it poses little chance of damaging or changing the properties of tissue prior to the pathology diagnosis [14]-[17]. These studies showed promising results of THz time domain

images of freshly excised tumors. Also, it has been suggested in [14] that THz radiation is susceptible to several features of human tissues. In particular, the THz frequency range is known to respond to the density of tissue, the water content of the tissue, the protein structure as it differs between tissues, and the spin of certain diatomic compounds in the body. However, to the best of the authors' knowledge there has not been a thorough investigation into what specific components of cancer tissue compared to normal provide the differentiation in the THz range. While water content and density are key indicators of cancerous tissue, the work here will show differentiating contrast in THz imaging of fixed tissue where no water content was involved.

A recent study of single continuous frequency THz images was reported in [18]. Previous simulation and preliminary experimental work was presented in conferences by our group in [19], [20]. Other research on using THz radiation for different types of cancer and heart disease has also been reported, e.g. liver, lung, skin and heart tissue [21]-[23]. In all cases, THz imaging has been able to differentiate between cancerous and fibroglandular regions in the obtained images without the need to use contrast agents. This is a key characteristic in future efforts toward a fast and effective imaging technique for cancer margin assessment.

This work focuses on establishing and validating a THz reflection imaging methodology for differentiating between different regions in paraffin sections of fixed (dehydrated) cancerous breast tumors. As known, breast tumors can have significantly different morphology due to several factors, such as women's age, race, genetic profile, heterogeneity, cell density, etc. This work is also addressing the challenging issue of imaging triple negative tumors, known for their high heterogeneity. In addition, tumors from women of different age are considered here. The pulsed THz system used here provides a frequency range from 0.1 to 4 THz. Visual correlation between the obtained THz and histopathology images demonstrated good agreement, in addition to

validating experimentally measured THz fields with the theoretical reflection coefficient of multilayered sample. Although this research may overlap with some of the published work [14]-[17], it expanded the investigations to different venues that, to the best of our knowledge, were not investigated before. The novelty of this work is in demonstrating the contrast between cancer and normal tissue without the presence of water. The goal is to denote the distinction between the heterogeneous regions of triple negative breast tumors, investigate the effect of tissue section thickness on THz reflection imaging, and analyze experimental THz reflection data versus closed form expressions. The observation of the contrast in tumor tissue in the absence of water is of great significance to THz imaging technique.

It is important to emphasize that this work used formalin fixed, paraffin embedded breast cancer tissue, which can be purchased from biobanks, to allow for examining and developing the imaging technique without using valuable freshly excised tissue, which is much harder to obtain. It is well-known that the water content of the tissue does have a significant contribution to the electrical properties of the tissue in the THz range. In particular, the properties of fresh tissue up to 2 THz reported in [16] indicate somewhat higher refractive index and significantly higher absorption coefficients compared with those of fixed tissue [24], [25]. Thus any contrast seen in imaging fixed tissue to be shown in this work would be further strengthened when imaging freshly excised tumors in the THz frequency band.

In the future phase of this research, we will apply for Institutional Research Board protocol through collaboration with the local hospital to obtain freshly excised breast cancer tumor tissue.

This paper is organized as follows: the system set-up and methodology will be discussed in Section 2, theoretical model and validation with experimental data will be presented in Section

3, breast tissue imaging results and correlation with histopathology images will be presented in Section 4, and conclusions, discussion, and future work will be discussed in Section 5.

2. System Set-Up and Methodology

2.1. Pulsed Terahertz System

TPS Spectra 3000 model is used in this work. A simplified diagram of the system in the reflection mode is shown in Fig. 1. This system produces a signal using a Ti:sapphire femtosecond laser (800 nm) to excite a biased GaAs antenna, which subsequently emits a time-domain THz pulse. Upon taking the Fourier transform of this pulse, a frequency domain signal with a spectral range from 100 GHz to 4 THz is obtained as shown in Fig. 2. For the results presented in this work, the reflection imaging module (RIM) is utilized to scan $\sim 2 \text{ cm} \times 2 \text{ cm}$ two-dimensional (2D) tissue sections. Micro-motors on the module permit a variable step size with minimum value of $50 \mu\text{m}$ when raster scanning the sample.

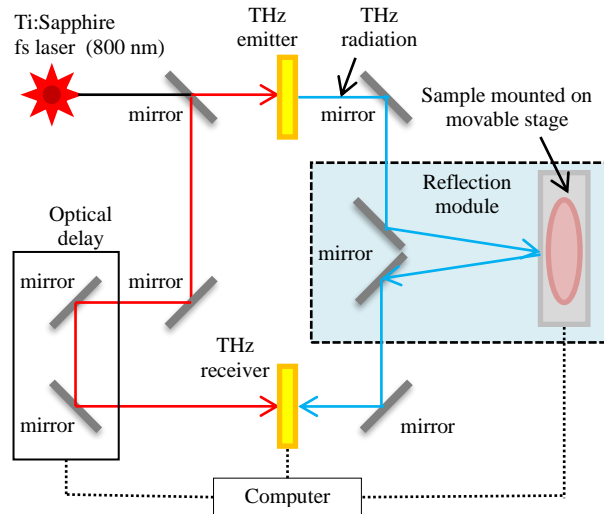


Figure 1. A diagram of the pulsed terahertz system in the reflection imaging mode.

2.2. Imaging Calibration

Prior to obtaining the image, a reference and baseline are selected. For the reflection mode, the reference could be either a gold mirror providing perfect reflection or a point on the same glass

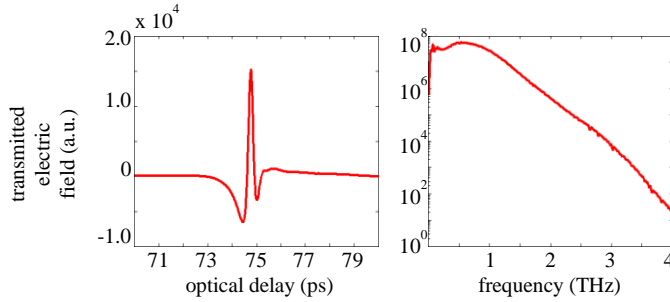


Figure 2. Standard unobstructed signal created by pulsed terahertz system in (a) time domain and (b) frequency domain. The optical delay is the time between the generation of the signal and when it is picked up by the receiver.

slide next to the tissue. The baseline is selected as air to provide the measurement of the system noise inside the compartment where the tissue samples are illuminated with the THz pulse. A flowchart of the standard calibration and signal processing for the time domain signal is shown in Fig. 3.

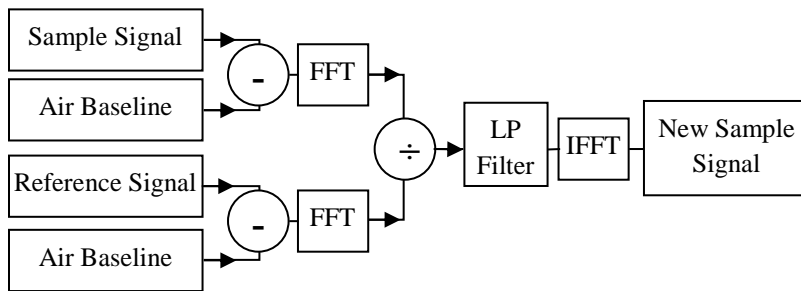


Figure 3. Flow diagram for post-processing deconvolution of the THz time domain signal using a reference signal that can be obtained from either a gold mirror or an empty glass slide. The air baseline indicates system noise when no sample (signal or reference) is present.

The focus point of the signal is set to provide a peak reflection at the surface of the sample in order to obtain the best resolution for the image. For thin tissue sections, no depth information can be obtained, but this functionality can be expanded upon using thicker tissue sections. A main condition in the available system is that the surface of the tissue needs to be perfectly flat. The RIM platform can be leveled to assure a horizontal flat surface such that the signal reaches all points of the surface at the same time, ensuring that the entire image is in focus. However, tissue

surfaces cannot be perfectly flat, so some errors are inherently introduced in the images due to surface roughness.

In order to obtain a THz image, the sample is raster scanned to measure the reflected waveform at each step in a defined 2D space (x - y). From the collected reflection measurements, the THz image is constructed from the values of the reflected time-domain pulse at each pixel of the sample. This pulse can also be normalized to the maximum value of the reference pulse (e.g. the mirror or the glass slide). Since the signal may be subject to effects from system noise and background reflections, a deconvolution process is utilized here as outlined in Fig. 3. This process can be employed with either the gold mirror reference or the glass slide reference in order to minimize both of these noise effects. Since this operation was performed in the frequency domain, a low-pass (LP) filter was implemented prior to obtaining the new sample signal in order to avoid low signal errors at higher frequencies of the reference. In comparing images obtained in this work via deconvolution using the mirror reference or the glass slide reference or just simple normalization, little overall difference was observed. However, using the deconvolution process provided slightly higher contrast between the different tissues. More advanced de-convolution techniques and regulated methods such as Tikhonov regularization and Wiener filtering could also be considered for further medical imaging enhancement [26], [27].

2.3. Tissue Preparation

The tissue samples used here were obtained from two different biobanks: the Cooperative Human Tissue Network (CHTN) division at the University of Alabama and the National Disease Research Interchange (NDRI). Uniformly flat tissue sections of 10 μm , 20 μm and 30 μm thickness were fixed in formalin and embedded in paraffin. Also, standard hematoxylin and eosin (H&E) stained pathology slides of 4-5 μm were cut from the same blocks in order to provide the

histopathology images for the purpose of validation. Three breast tumor blocks were obtained from patients at ages of 40, 46, and 54 years. The tumors of the first two patients were diagnosed as triple negative invasive ductal carcinoma, which indicates highly heterogeneous cancer adjacent to normal tissue. These two samples were obtained from Caucasian females who underwent mastectomy. The third block was obtained from black woman also using radical mastectomy.

We define these samples here as: Sample 1, 10 μm thickness obtained from 40 years old patient; Sample 2, 10 μm thickness obtained from 46 years old patient, and Sample 3, 20 μm and 30 μm thicknesses obtained from 54 years old patient. Samples 1 and 2 were provided by the CHTN while Sample 3 was provided by the NDRI. The histopathology images presented for all samples were provided by the Northwest Arkansas (NWA) Pathology Associates lab.

3. Theoretical Model and Validation

3.1. Reflection Formulation in TE/TM Polarization

As shown in Fig. 1, the RIM set-up is based on oblique incidence angle θ_1 , which is 30° in this system. An important step in making use of the reflection imaging is to validate the measured reflected THz signal at a single point with the well-known reflection coefficient of multilayered

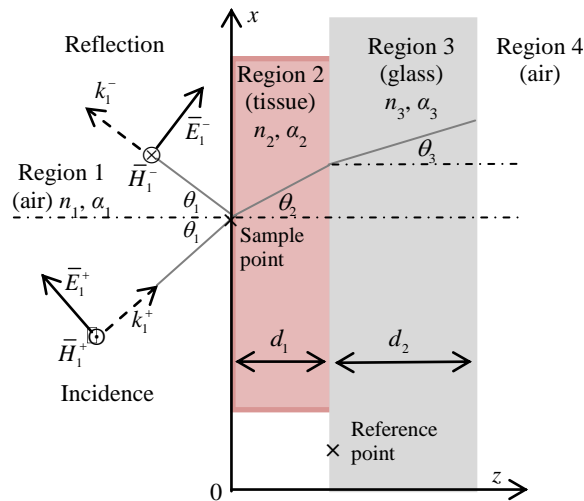


Figure 4. THz signal interaction at the boundary of tissue on glass for transverse magnetic field case (TM).

lossy media. The configuration shown in Fig. 4 shows the TM polarization (i.e. parallel, or p-polarization) case. While the TE case is also considered here but the configuration is not shown.

The reflection coefficient is obtained at single point on the tissue interface with air and also at a single point on the glass interface with air. Both points are marked by x in Fig. 4. The reflected field expressions are obtained following the procedure in [28] and [29].

Dividing the reflection coefficient from the tissue to that from the reference point obtains the following expression:

$$\frac{E_{sample}}{E_{ref}} = \left[\frac{\rho_{T,12} + \frac{\rho_{T,23} + \rho_{T,31} e^{-j2\tilde{k}_3 \cos \theta_3 d_2}}{1 + \rho_{T,23}\rho_{T,31} e^{-j2\tilde{k}_3 \cos \theta_3 d_2}} e^{-j2\tilde{k}_2 \cos \theta_2 d_1}}{1 + \rho_{T,12} \frac{\rho_{T,23} + \rho_{T,31} e^{-j2\tilde{k}_3 \cos \theta_3 d_2}}{1 + \rho_{T,23}\rho_{T,31} e^{-j2\tilde{k}_3 \cos \theta_3 d_2}} e^{-j2\tilde{k}_2 \cos \theta_2 d_1}} \right], \quad (1)$$

$$\times \left[\frac{1 + \rho_{T,13}\rho_{T,31} e^{-j2\tilde{k}_3 \cos \theta_3 d_2}}{\rho_{T,13} + \rho_{T,31} e^{-j2\tilde{k}_3 \cos \theta_3 d_2}} \right] e^{-j2\tilde{k}_1 \cos \theta_2 d_1}$$

in which E_{sample} and E_{ref} are the magnitudes of the electric fields reflected from the tissue interface and the reference point, respectively. The thickness of the tissue and glass are denoted by d_1 and d_2 , respectively, as shown in Fig. 4. The incident angles θ_1 and the transmitting angles in regions 2 and 3 (θ_2 and θ_3) are related through Snell's law (given in Appendix A). The symbols \tilde{n}_1 , \tilde{n}_2 , and \tilde{n}_3 are the complex index of refraction of regions 1, 2 and 3, with $\tilde{n}_1=1$ for air. The complex wavenumber \tilde{k}_1 , \tilde{k}_2 , and \tilde{k}_3 are given by $(\omega\tilde{n})/c$ where ω is the angular frequency and c is the speed of light.

The expressions $\rho_{T,ij}$ in (1) are given in Appendix A for the *TE* and *TM* cases, where i, j are the indices of the regions 1, 2, 3 or 4. Experimental THz measured electric fields will be compared with fields calculated using (1) and will be presented in Section 4.

4. THz RIM Imaging Results

4.1. *Imaging of 10 μm thickness tissue samples*

In this section the THz images of Sample 1 and Sample 2 are presented. Each of the two samples was imaged at a step size of 400 μm and 200 μm to obtain the initial and the final image, respectively. Scanning at a smaller step size of 50 μm is utilized to zoom in on interesting regions on the tissue section of Sample 1. These regions were based on the histopathology images, as will be discussed later in this section.

In this work, scanning 2 cm \times 2 cm sections using 400 μm step size requires an average of 4 minutes, while the raster scanning time increases in proportion to decreased step size depending on the scanned area. In addition to obtaining the THz images in the time domain, frequency domain images can be produced at any selected frequency in the band from 0.1 to 4 THz to possibly acquire better contrast at a single frequency. All experimental THz data here are collected using the system and then exported to MATLAB for post-processing as described in Section 2.

The THz images obtained using the reflection mode are shown in Figs. 5-8. In addition, the associated low power pathology images are shown in the same figures. In these figures, the color bar of the time domain images shows the electric field amplitude of the deconvolved pulse at each point on the sample. Additionally, for each sample THz frequency domain images are presented as well. The glass was used as a reference in all images. In these figures, all THz images are obtained using a step size of 200 μm .

The results of Fig. 5 show the images of Sample 1, taken from the 40 year old Caucasian woman via mastectomy. The post-surgery pathology report of this sample described the tumor as infiltrating ductal carcinoma (IDC). Furthermore, the cancer was defined to be poorly differentiated, indicating a low amount of distinction between cancerous and non-cancerous tissue

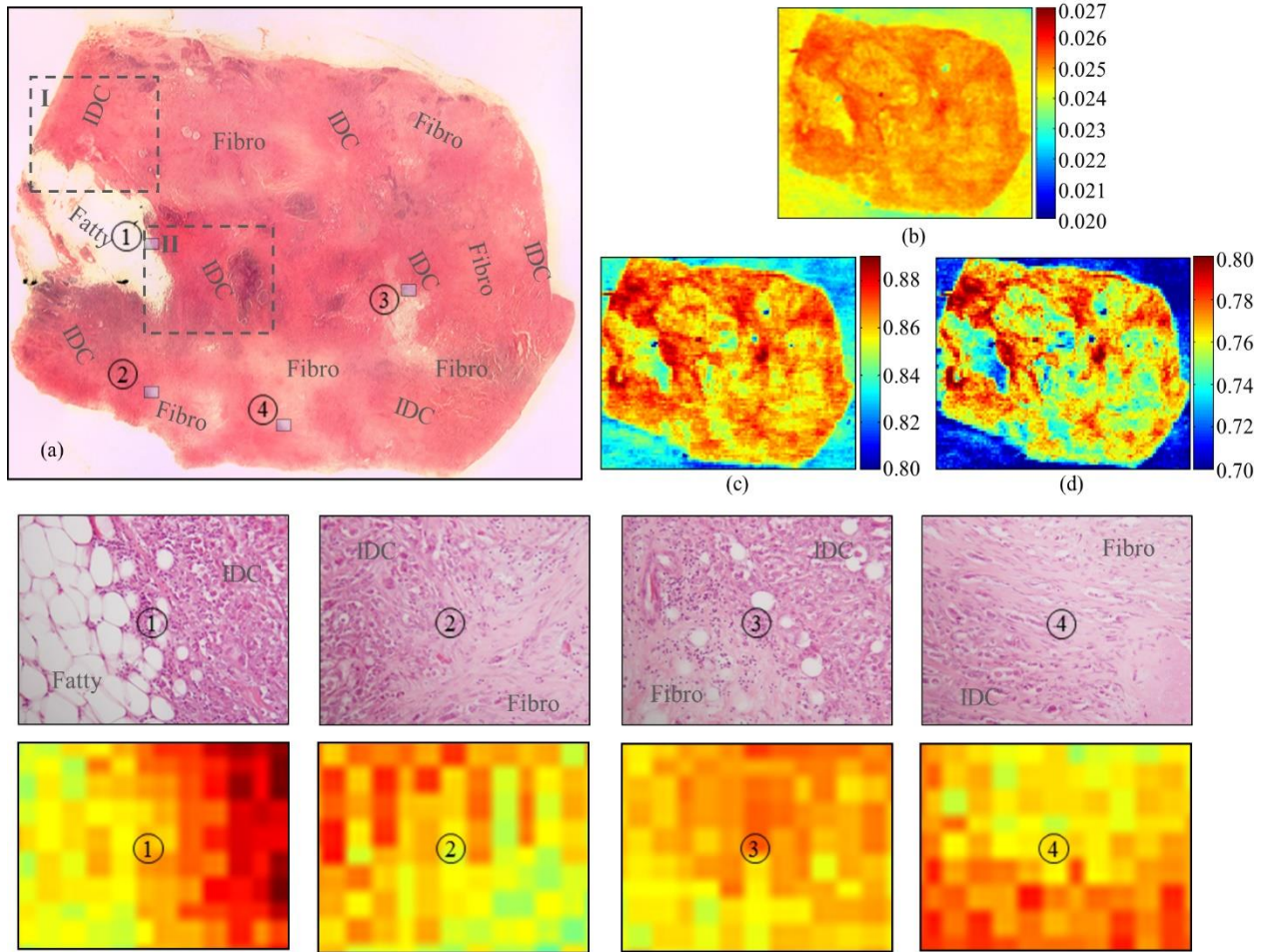


Figure 5. THz image of Sample 1, 40-year old Caucasian woman diagnosed with poorly-differentiated infiltrating ductal carcinoma (IDC). (a) Low power pathology image used for correlation. Selected locations of high power pathology of borders between regions are denoted by ① between Fatty and IDC and by ②, ③, and ④ between IDC and Fibro. (b) THz time-domain image, (c) THz frequency domain image at 1.5 THz, and (d) THz frequency domain image at 2.0 THz. THz images in (b), (c), and (d) are scanned at 200 μm . High power pathology images at 100X magnification are shown for ①, ②, ③, and ④ borders compared to the frequency-domain images at 1.5 THz using 50 μm scanning step size.

in the sample. A macroscopic low-power histopathology image obtained here is shown in Fig. 5a denoting the general regions of the tissue types observed in this sample using the stained slide. The image shows regions of IDC, fibroglandular (fibro), and fatty tissue.

It should be noted that the pathology examination used to define the regions in all tumor tissues utilized much more high-power pathology in order to examine the tissue on a cellular level

and define the different regions of the tissue. Due to space limitation, the high power pathology images will not be shown for all samples presented here. However, some critical border regions ①, ②, ③, and ④ (see to-scale rectangular markers in Fig. 5a) are demonstrated with high power images. It should be emphasized that the highly heterogeneous nature of the tissue in this sample and its small thickness of $\sim 10 \mu\text{m}$ make the regions more challenging to distinguish in Fig. 5b. However, the THz images obtained using the smallest scanning step size of the system ($50 \mu\text{m}$) for the border regions ①-④ are indeed highly correlated to the associated high power pathology images shown in Fig. 5.

In Fig. 5a, the fibroglandular tissue exhibits different levels of density, with the low-density tissue is defined by a mixture of fibro and fatty tissue. In particular, the darkest colors represent the IDC (cancer) regions, the lighter colors represent the healthy fibroglandular regions, and the almost white colors represent fatty tissue. Fig. 5b provides the time-domain THz image while Figs. 5c-d demonstrate the frequency domain images at 1.5 and 2 THz. The results also show that IDC regions reflected a higher magnitude of the electric field compared with the fatty or fibro regions. The IDC tissue appeared distinct as the high reflection indicated by dark red compared with the lower reflections fatty or fibro regions.

The results also agree with the original pathology report describing the tumor as poorly differentiated, as the contrast between adjacent regions of tissue is fairly low and there is a significant amount of mixed IDC and fibro tissue as well as low-density fibro tissue present in the sample.

In addition, two interesting regions in Fig. 5 are selected to be more closely investigated. The first region is located at the margin of the tissue section where the IDC tissue is denoted on the upper left side of the figure (labeled as I in Fig. 5a). The second region is selected where the

histopathology image in Fig. 5a shows a different tissue region to the three other regions defined in the pathology (labeled as II in Fig. 5a). This region is diagnosed by the pathologist as lymphoid aggregate surrounding carcinoma tissue in the core. Therefore, high resolution THz images are produced focused on these regions, I and II, as shown in Figs. 6a, b. In this case, the THz images are obtained upon scanning the regions using the smallest step size of 50 μm . The resulting images are presented in the frequency domain at 1.5 THz in Figs. 6a, b. These tissues appeared also well differentiated with the IDC tissue providing a higher reflection than the fibro and fatty tissues. In Fig. 6b, the lymphoid aggregate surrounding the carcinoma tissue is also clear in the THz image.

The observed smearing effect in the THz images in Figs. 6a and b is likely attributable to the interference in the reflected signal from the tissue interface and the glass slide below the tissue due to the small thickness of the tissue (10 μm). This problem is predicted to improve when thicker sections of tissue are used as will be shown later in this work. The high resolution results of Fig. 6 demonstrate the potential capability of THz imaging for differentiation between tissue regions at smaller scale without the need for a contrast agent. It should also be noted that high power pathology does offer much higher resolution than THz imaging.

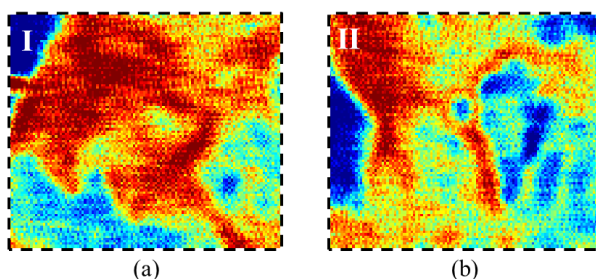


Figure 6. THz high resolution images using 50 μm step size for (a) region I and (b) region II, labeled in Fig. 5a.

The results for Sample 2 obtained from the 46 year old Caucasian woman via mastectomy are shown in Fig. 7. The pathology report of this section performed after surgery diagnosed the tumor with infiltrating ductal carcinoma. The low power pathology image of the H&E stained slide

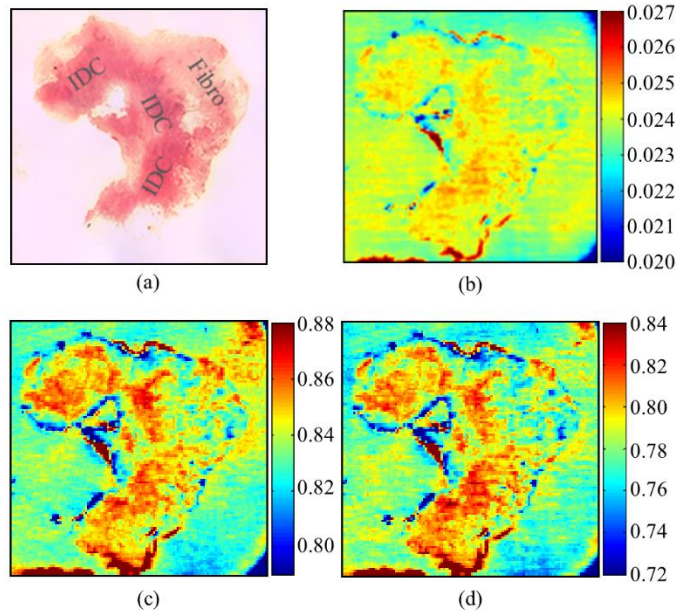


Figure 7. Sample 2 for 46-year old Caucasian woman diagnosed with infiltrating ductal carcinoma (IDC). (a) Low power pathology image used for correlation. (b) THz time-domain image of the sample. (c) Frequency domain image at 1.5 THz, and (d) Frequency domain image 1.75 THz.

is shown in Fig. 7a. This image further defines regions of IDC and fibro tissue that were identified by the pathologist. It is noted that the IDC region (cancer) almost occupies the whole left side of the tissue shown in Fig. 7a (dark color), while the healthy fibroglandular tissue occupies the right side (light color). The time-domain image is shown in Fig. 7b with a color bar scale of the deconvolved electric field amplitude ranging from 0.02 to 0.027. The THz frequency domain images at 1.5 and 1.75 THz are shown in Figs. 7c and d. As clearly shown in Fig. 7, the frequency domain images add more contrast to distinguish between IDC and fibro regions. This distinction was not as clear in the time-domain image of Fig. 7b. As mentioned earlier, the frequency domain images can be obtained in post-processing of collected data. The comparison between the histopathology image of Fig. 7a and the obtained THz images in Figs. 7c-d demonstrates a strong correlation. In these figures, the IDC cancerous region reflected the highest electric field in the tissue and is clearly distinct from fibro tissue region, consistent with the results of Fig. 5. The dark

red color at tissue boundaries observed in the THz images occurred at places where tissue is separated from the glass slide, indicating that the observed strong field is due to a high reflection from the glass itself beyond the range of values reflected by tissue. In Fig 7c, the high reflection observed in the upper right corner of the frame represents reflection from just paraffin on glass where no tissue is present.

While the 10 μm thickness of the tissue samples has rendered the THz imaging rather challenging, the strong correlation with pathology images is noticed. On the other hand, and in agreement with the literature [21], preparing thick tissue sections requires more elaborate procedures from the histopathology lab to assure uniform flat thick tissue sections that are well adhered to glass slides.

4.2. *Validation of THz reflected fields with theoretical model*

The samples used earlier to produce the THz images included 11 slides each. All slides were scanned producing similar images, but the results presented in Figs. 5-7 were for slide #3 in both samples. The experimentally measured electric fields reflected from the tissue interface normalized to that reflected from the reference point, as shown in Fig. 4, are compared with the theoretical model of (1). There are some assumptions made here to implement this comparison. The formulation of (1) is based on plane wave excitation to infinitely large flat homogeneous surface. However in the experimental measurements, the incident THz beam is a pulse and not a plane wave, and the single point on the tissue was identified inside a relatively small homogenous region. This assumption is more accurate at higher frequencies where the spatial spot size of the beam is smaller.

The fields in this model are calculated using the index of refraction \tilde{n} of glass and for different regions of tumor tissues as IDC, fibro, fat, etc. These values were obtained from

spectroscopy measurements reported in [24] and [25]. For consistency, this comparison is also made for slide #3 in Samples 1 and 2. The polarization of the experimentally collected THz signals using the system could not be confirmed due to the use of a complex mirror setup in the hardware as shown in Fig. 1. Although we can assume *TM* polarization here based on the normal incidence configuration of the spectroscopy module of the system [25], the comparison is conducted for both the *TM* and *TE* polarizations of the model in (1). Only the results for Sample 1 are shown in Fig. 8, but all comparison results similarly demonstrated good agreement.

The results of Fig. 8 show that the magnitude of E_{sample}/E_{ref} for *TE* and *TM* modes, calculated using (1), are almost the same due to the small incidence angle of the system (30°). The observed oscillations in the *TE* and *TM* mode plots can be explained by the multiple reflections in the glass slide that attenuate rapidly as the frequency increases. The glass slide has 1 mm thickness while the tissue section has much smaller thickness of 10 μm making the reflection from the configuration to be dominated by the glass. Therefore as observed in Fig. 8, the ratio E_{sample}/E_{ref} is

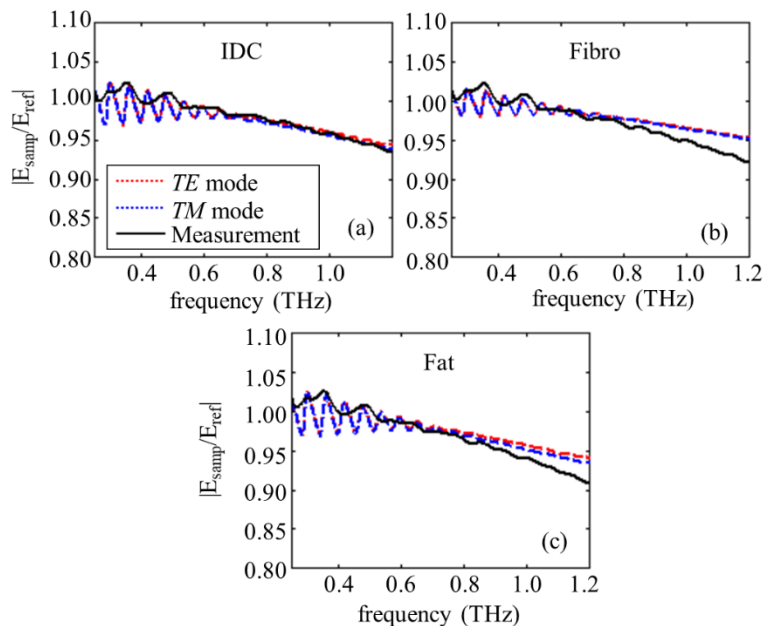


Figure 8. Validation of experimentally collected reflected THz fields vs. TE/TM theoretical model for (a) IDC region, (b) fibro region, and (c) fat region, all in tumor sections of slide #3 of Sample 1.

oscillating around a value of 1. By contrast, there are relatively small observed oscillations for the measurement plot due to the fact that the time domain signals collected using the system are time gated, leading to truncation of some of the multiple reflections. Depending on the frequency of the signal and the length of tissue sections, the edges of the tissue could create surface wave excitations that produce unpredictable oscillation patterns in the received signal. While it is known that the multiple reflections in the tissue and glass cause some oscillations, it should be noted that there is a possibility of some of the oscillations seen in Fig. 8 being due to the effect of these surface waves.

The experimental plot is the result of averaging over five single points on the tissue in the IDC, fat, and fibro regions. The experimental data demonstrate good agreement with the calculated *TE* and *TM* models throughout the range 0.25-1.3 THz. At frequencies higher than 1.3 THz, the glass becomes significantly attenuating to the THz signal making the measured spectroscopy data unreliable as reported in [24], [25]. Also it is observed that the measured data in Fig. 8 was not in good agreement with the model at frequencies lower than 0.25 THz. This disagreement is due to larger size of the spatial THz spot on the tissue at lower frequencies, while the incident signal in the model is assumed to be a plane wave at all frequencies. Fig. 8 shows that the model and experimental results differ in the fibro and also in the fatty tissue compared with the IDC results, where they are in very good agreement. This can be explained in that the electrical properties of the IDC, Fibro and fatty tissues were obtained using spectroscopy measurements based on averaging several points in each region. Due to the high heterogeneity of the tumor of Fig. 5, the electrical properties used in the models could be higher than the true values due to random inclusion of points from cancerous regions. This fact made the model results appear at higher values compared with the experimental data for both fibro and fatty regions. In all cases, these errors are ~ 2.7 - 5.4% . The measurements in Fig. 8 are raw data without using any type of filtering.

In general, the measurements and the model are in good agreement in all samples except at frequencies below 0.25 THz.

4.3. *Imaging of 20 and 30 μm thickness tissue samples*

In this example, the tumor presented in Fig. 9 is different from the previous examples. The tumor here has a well-circumscribed border where the IDC and the fibroglandular tissue have very little proliferation into each other.

In testing multiple tissue thicknesses, the adhesion of tissue of thickness more than 30 μm was a challenge leading to non-flat tissue surface on the glass slides. Therefore, in this section we present THz images of Sample 3 at two thicknesses 20 and 30 μm as shown in Fig. 9. The same scanning procedure used for Samples 1 and 2 is used here (i.e. 200 μm step size). Both the 20 and 30 μm sections were cut from the same tumor block, therefore, we present one histopathology image cut of thickness 3-4 μm and at a depth between these two sections. The pathology report identified two regions in this tumor as IDC and fibro as shown in Fig. 9a.

In this figure, the scattered spots within the fibroglandular tissue indicate benign lobular and ductal tissues of the breast that are not related to the region of cancer. The time domain THz images are shown in Fig. 9b for the 20 μm section and in Fig. 9c for the 30 μm section. In Figs. 9b-g the scattered spots in the THz 20 and 30 μm images are due to regions where the tissue was breaking (i.e. no tissue on glass) causing high reflection (red spots) or due to separation of tissue from the glass producing air pockets beneath the tissue causing low reflection (blue spots). Both cases are problems that arise from the lack of adhesion when working with thicker sections of tissue. In the THz images of the 20 μm section, the lobular tissue can be seen as dark colors indicating reflection similar to cancer, which is a false positive. However, the lobular tissue areas

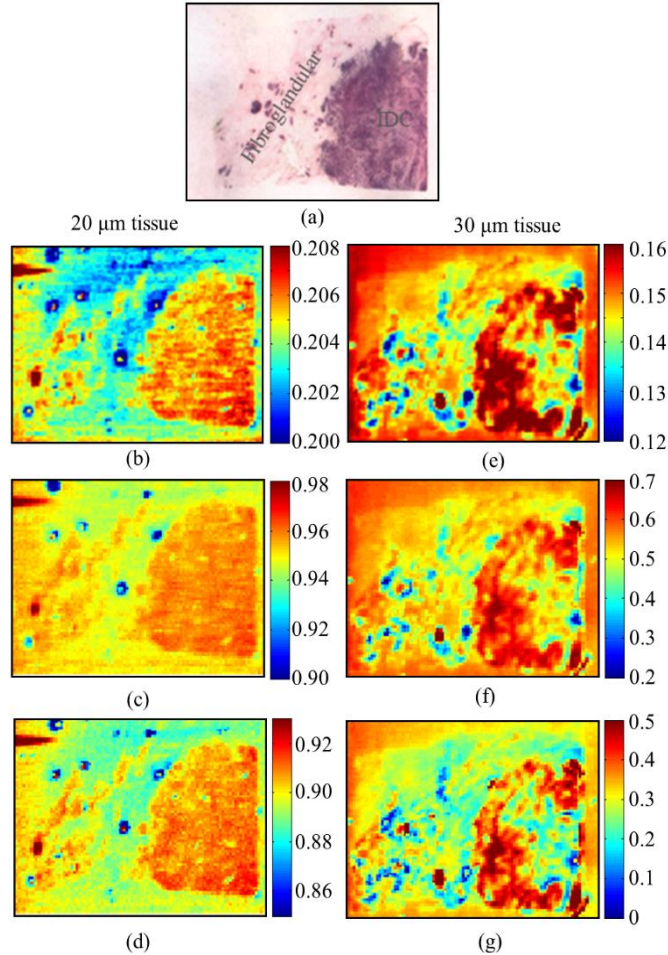


Figure 9. THz image of Sample 3, 54-year old black woman diagnosed with infiltrating ductal carcinoma (IDC). (a) Low power H&E pathology image used for correlation. THz images for the 20 μm as: (b) Time-domain image, (c) frequency domain image at 1THz, (d) frequency domain image at 1.25 THz. THz images for the 30 μm as: (e) Time-domain image, (f) frequency domain image at 1 THz, (g) frequency domain image at 1.25 THz.

are not seen as cancer in the 30 μm images, which shows the improvement of the imaging with the thicker tissue section.

Within the IDC region of Fig. 9a, a less pigmented central region (pink) can be seen on the right side of the image compared with a much darker pigmentation (purple) region near the border between the IDC and fibroglandular tissue. This pink region is most likely necrosis (dead tissue) or fibrosis (connective tissue formed by the tumor) that is typically found on the interior of reasonably large tumors. It is notable that the greatest distinction in the THz 30 μm images is seen

in the active cancer cells at the margin between the IDC and fibroglandular regions. The reason that this distinction exists in the 30 μm slice but not the 20 μm slice is likely due to the effect that increased thickness has on the reflected signal.

Upon comparing the THz images presented in Fig. 9 against those presented in Figs. 5 and 7, we can qualitatively conclude that the increased thickness in tissue sections has led to better contrast in the THz reflection mode images. However, one has to be cautious with this conclusion as it is not confirmed that the tumor of Sample 3 was triple negative as those of Samples 1 and 2.

5. Discussion and Conclusions

The results of this work demonstrate that THz reflection imaging successfully distinguished between cancer and non-cancer breast tissue even when the tissue section was heterogeneous and as thin as 10 μm . The presented THz images showed that cancerous regions are easily discerned from normal (fibroglandular and fatty) tissue in all three tumors considered here. Further comparison between the high power pathology and the THz images obtained using fine scanning steps of 50 μm demonstrated strong correlation even for heterogeneous thin section tissue. It is believed that this technology has a potential for tumor margin assessment in the future.

Ongoing research is to expand the THz imaging methodology to include the transmission mode. One of the goals is to identify which imaging module would provide better images. Also, imaging excised fresh tissue is a step further in this research. It is important to emphasize that obtaining excised tissue from lumpectomy is challenging due to the fact that these surgeries are conducted when the tumor is small in order to conserve the breast. As a result, most of the excised tissues are needed for diagnosis and staging the cancer, meaning that obtaining adequate samples will require the direct cooperation of pathologists and surgeons.

Acknowledgments

The Authors would like to thank Dr. Suzanne Klimberg, MD, professor of surgery and breast cancer oncology at the University of Arkansas for Medical Sciences (UAMS) for providing the medical insight on breast cancer lumpectomy and margins. Also the authors would like to thank Dr. S. G. Sharma with the Department of Pathology at UAMS for providing initial histopathology images. The Authors acknowledge the efforts of the staff in the histopathology lab at NWA Pathology Associates for preparing the thick tissue sections.

Funding for purchase and maintenance of the Pulsed Terahertz System is provided by NSF/MRI award #1228958. This work was supported by the NSF GRFP, the NSF award #1408007, and the Arkansas Biosciences Institute (ABI). This research was supported by a grant from the Arkansas Breast Cancer Research Programs. The University of Arkansas for Medical Sciences Translational Research Institute (CSTA Grant Award # UL1TR000039) provided resources during the review and selection process.

Appendix A

Snell's law is given as [28], [29]:

$$\tilde{n}_1 \sin \theta_1 = \tilde{n}_2 \sin \theta_2 = \tilde{n}_3 \sin \theta_3, \quad (\text{A1})$$

The expressions $\rho_{T,ij}$ in (1) are given here for the *TM* and *TE* cases, respectively, with i, j the indices of the regions 1, 2, 3 or 4 [24], [25].

$$\rho_{TM,ij} = \frac{\tilde{n}_i \cos \theta_j - \tilde{n}_j \cos \theta_i}{\tilde{n}_i \cos \theta_j + \tilde{n}_j \cos \theta_i} = \frac{\tilde{n}_i^2 \sqrt{\tilde{n}_j^2 - \sin^2 \theta_1} - \tilde{n}_j^2 \sqrt{\tilde{n}_i^2 - \sin^2 \theta_1}}{\tilde{n}_i^2 \sqrt{\tilde{n}_j^2 - \sin^2 \theta_1} + \tilde{n}_j^2 \sqrt{\tilde{n}_i^2 - \sin^2 \theta_1}} \quad (\text{A2})$$

$$\rho_{TE,ij} = \frac{\tilde{n}_i \cos \theta_i - \tilde{n}_j \cos \theta_j}{\tilde{n}_i \cos \theta_i + \tilde{n}_j \cos \theta_j} = \frac{\sqrt{\tilde{n}_i^2 - \sin^2 \theta_1} - \sqrt{\tilde{n}_j^2 - \sin^2 \theta_1}}{\sqrt{\tilde{n}_i^2 - \sin^2 \theta_1} + \sqrt{\tilde{n}_j^2 - \sin^2 \theta_1}} \quad (\text{A3})$$

References

- [1] “Breast Cancer.” American Cancer Society [Online]. Available: <http://www.cancer.org/acs/groups/cid/documents/webcontent/003090-pdf.pdf> Last revised 26 February 2013.
- [2] R. G. Pleijhuis, M. Graafland, J. de Vries, J. Bart, J. S. de Jong, and G. M. van Dam. “Obtaining Adequate Surgical Margins in Breast-Conserving Therapy for Patients with Early-Stage Breast Cancer: Current Modalities and Future Directions.” *Ann. Surg. Oncol.*, vol. 16, pp. 2717-2730, July 2009.
- [3] L. Jacobs, “Positive Margins: The Challenge Continues for Breast Surgeons,” *Ann. Surg. Oncol.*, vol. 15, no. 5, pp. 1271-1272, March 2008.
- [4] V. S. Klimberg, J. Kepple, G. Shafirstein, L. Adkins, R. Henry-Tillman, E. Youssef, J. Brito, L. Talley, and S. Korourian. “eRFA: Excision Followed by RFA—a New Technique to Improve Local Control in Breast Cancer.” *Ann. Surg. Oncol.*, vol. 13, no. 11, pp. 1422-1433, September 2006.
- [5] M. Morrow and G. Freedman. “A Clinical Oncology Perspective on the Use of Breast MR.” *Magn. Reson. Imaging. Clin. N. Am.*, vol 14, pp 363-378. August 2006.
- [6] S. Kennedy, J. Geradts, T. Bydlon, J. Q. Brown, J. Gallagher, M. Junker, W. Barry, N. Ramanujam, and L. Wilke. “Optical breast cancer margin assessment: an observational study of the effects of tissue heterogeneity on optical contrast.” *Breast Cancer Research*, vol. 12:R91, 2010.
- [7] T. P. Olsen, J. Harter, A. Muñoz, D. M. Mahvi, and TM. Breslin. “Frozen Section Analysis for Intraoperative Margin Assessment During Breast-Conserving Surgery Results in Low Rates of Re-excision and Local Recurrence.” *Ann. Surg. Oncol.*, vol. 14, no. 10, pp. 2953-2960, August 2007.
- [8] N. Cabioglu, K. K. Hunt, A. A. Sahin, H. M. Kuerer, G. V. Babiera, S. E. Singletary, G. J. Whitman, M. I. Ross, F. C. Ames, B. W. Feig, T. A. Buchholz, F. Meric-Bernstam. “Role for Intraoperative Margin Assessment in Patients Undergoing Breast-Conserving Surgery.” *Ann. of Surg. Oncol.*, vol. 14, no. 4, pp. 1458-1471,
- [9] V. S. Klimberg, C. Boneti, L. L. Adkins, M. Smith, E. Siegel, V. Zharov, S. Ferguson, R. Henry-Tillman, B. Badgwell, and S. Korourian. “Feasibility of Percutaneous Excision Followed by Ablation for Local Control in Breast Cancer.” *Ann. Surg. Oncol.* 28 January 2007.
- [10] V. Sharma, S. Shivalingaiah, Y. Peng, D. Euhus, Z. Gryczynski, and H. Liu. “Auto-fluorescence lifetime and light reflectance spectroscopy for breast cancer diagnosis: potential tools for intraoperative margin detection.” *Biomedical Optics Express*, vol. 3, no. 8, pp. 1825-1840. 9 July 2012.

- [11] J. Q. Brown, T. M. Bydlon, L. M. Richards, B. Yu, S. A. Kennedy, J. Geradts, L. G. Wilke, M. K. Junker, J. Gallagher, W. T. Barry, and M. Ramanujam, "Optical Assessment of Tumor Resection Margins in the Breast," *IEEE J. Selected Topics Quantum Electronics*, vol. 16, no. 3, pp. 530-544, May/June 2010.
- [12] P. Y. Han, G. C. Cho, and X.-C. Zhang, "Time-domain transillumination of biological tissues with terahertz pulses," *OPTICS LETTERS*, vol. 25, no. 4, 15 February 2000.
- [13] G. J. Wilmink and J. E. Grundt, "Current State of Research on Biological Effects of Terahertz Radiation," *J. Infrared Milli-Terahz Waves*, vol. 32, pp. 1074-1122, 2011.
- [14] P. H. Siegel, "Terahertz Technology in Biology and Medicine," *IEEE Trans. on Microwave Theory and Techniques*, vol. 53, no. 10, pp. 2438-2447, 2004.
- [15] A. J. Fitzgerald, V. P. Wallace, M. Jimenez-Linan, L. Bobrow, R. J. Pye, A. D. Purushotham, D. D. Arnone. "Terahertz Pulsed Imaging of Human Breast Tumors." *Radiology*, vol. 239, no. 2, pp. 533-540, May 2006.
- [16] P. C. Ashworth, E. Pickwell-Macpherson, E. Provenzano, S. E. Pinder, A. D. Purushotham, M. Pepper, and V. P. Wallace. "Terahertz pulsed spectroscopy of freshly excised human breast cancer." *Opt. Express.*, vol. 17, no. 15, pp. 12444-12454, 2009.
- [17] S. W. Smye, J. M. Champerlain, A. J. Fitzgerald, and E. Berry. "The interaction between Terahertz radiation and biological tissue." *Physics in Medicine and Biology*, vol. 46, no. 9, 22 August 2001.
- [18] St. Peter, B.; Yngvesson, S.; Siqueira, P.; Kelly, P.; Khan, A.; Glick, S.; Karellas, A., "Development and Testing of a Single Frequency Terahertz Imaging System for Breast Cancer Detection," *IEEE Journal of Biomedical and Health Informatics*, 17(4),785-797, (2013)
- [19] A. M. Hassan, D. C. Hufnagle, M. El-Shenawee, and G. E. Pacey, "Terahertz Imaging for Margin Assessment of Breast Cancer Tumors," *Proc. of 2012 IEEE MTT-S International Microwave Symposium Digest*, 17-22 June 2012.
- [20] T. C. Bowman, A. M. Hassan, and M. El-Shenawee, "Imaging 2D Breast Cancer Tumor Margin at Terahertz Frequency using Numerical Field Data based on DDSCAT," *Applied Computational Electromagnetics Society Journal*, vol. 28, no. 11, November 2013.
- [21] Y. Miura, A. Kamataki, M. Uzuki, T. Sasaki, J. Nishizawa, and T. Sawai. "Terahertz-Wave Spectroscopy for Precise Histopathological Imaging of Tumor and Non-tumor Lesions in Paraffin Sections." *Tohoku J. Exp. Med.*, vol. 223, no. 4, pp. 291-296, 17 March 2011.
- [22] S. Sy, S. Huang, Y. J. Wang, J. Yu, A. Ahuja, Y. Zhang, and E. Pickwell-MacPherson, "Terahertz spectroscopy of liver cirrhosis investigating the origin of contrast," *Phys. Med. Biol.*, vol. 55, pp. 7587-7596, 2010.

- [23] C. Reid, A. Fitzgerald, G. Reese, R. Goldin, P. Tekkis, P. O'Kelly, E. Pickwell-MacPherson, A. Gibson, and V. Wallace. "Terahertz pulsed imaging of freshly excised human colonic tissues," *Phys. Med. Biol.*, vol. 56, pp. 4333-4353, 2011.
- [24] T. Bowman and M. El-Shenawee, "Terahertz Spectroscopy for the Characterization of Excised Human Breast Tissue", *Proc. IEEE International Microwave Symposium (IMS)*, Tampa, FL, 2014.
- [25] T. C. Bowman, *Experimental Terahertz Imaging and Spectroscopy of Ex-vivo Breast Cancer Tissue*, M.S. thesis, Dept. Elect. Eng., Univ. Arkansas, 2014.
- [26] X. Zhang, E. Y. Lam, E. X. Wu, and K. K.Y. Wong. "Application of Tikhonov Regularization to Super-Resolution Reconstruction of Brain MRI Images." *Medical Imaging and Informatics: Lecture Notes in Computer Science*, vol. 4987, pp. 51-56, 2008.
- [27] M. Martin-Fernandez, C. Alberola-Lopez, J. Ruiz-Alzola, C.-F. Westin. "Sequential anisotropic Wiener filtering applied to 3D MRI data." *Magnetic Resonance Imaging*, vol. 25, pp. 278-292, 2007.
- [28] Carl T.A. Johnk. *Engineering Electromagnetic Fields and Waves*. 2nd ed. John Wiley & Sons, Inc. Copyright 1988.
- [29] S. J. Orfanidis. *Electromagnetic Waves and Antennas*. Copyright 1999-2013. Published online at www.ece.rutgers.edu/~orfanidi/ewa.

Chapter 3: Terahertz Transmission vs Reflection Imaging and Model-based Characterization for Excised Breast Carcinomas

© 2016 OSA. Reprinted, with permission, from T. Bowman, M. El-Shenawee, and L. K. Cambell, "Terahertz transmission vs reflection imaging and model-based characterization for excised breast carcinomas" *Biomedical Optics Express*, vol. 7, no. 9, pp. 3756-3783, 2016. [doi: 10.1364/BOE.7.003756]

Abstract

This work presents experimental and analytical comparison of terahertz transmission and reflection imaging modes for assessing breast carcinoma in excised paraffin-embedded human breast tissue. Modeling for both transmission and reflection imaging is developed. The refractive index and absorption coefficient of the tissue samples are obtained. The reflection measurements taken at the system's fixed oblique angle of 30° are shown to be a hybridization of TE and TM modes. The models are validated with transmission spectroscopy at fixed points on fresh bovine muscle and fat tissues. Images based on the calculated absorption coefficient and index of refraction of bovine tissue are successfully compared with the terahertz magnitude and phase measured in the reflection mode. The validated techniques are extended to 20 and 30 μm slices of fixed human lobular carcinoma and infiltrating ductal carcinoma mounted on polystyrene microscope slides in order to investigate the terahertz differentiation of the carcinoma with non-cancerous tissue. Both transmission and reflection imaging show clear differentiation in carcinoma versus healthy tissue. However, when using the reflection mode, in the calculation of the thin tissue properties, the absorption is shown to be sensitive to small phase variations that arise due to deviations in slide and tissue thickness and non-ideal tissue adhesion. On the other hand, the results show that the transmission mode is much less sensitive to these phase variations. The results also demonstrate that reflection imaging provides higher resolution and more clear margins between cancerous and fibroglandular regions, cancerous and fatty regions, and fibroglandular and

fatty tissue regions. In addition, more features consistent with high power pathology images are exhibited in the reflection mode images.

1. Introduction

Terahertz (THz) has been a greatly expanding field of research in recent years. While historically THz frequencies (0.1 to 4 THz) were difficult to access due to the gap between electronic and optical generation techniques, the advent of more reliable THz sources has opened up this range for a wide variety of potential applications [1]. Such areas include security and explosive detection [2], semiconductor characterization and carrier dynamics [3], and nondestructive evaluation of electronic devices [4].

One focus where THz has shown particular promise is in biomedical and pharmaceutical research, where the work in THz applications has grown rapidly, especially in the field of biomedical imaging [5]. This is in large part due to THz frequencies showing significant distinctions between many different kinds of diseased and healthy tissue [6], [7]. THz is particularly sensitive to water content in different types of tissue, which is a key contrast factor in many of its biomedical imaging applications [8]. As a result, THz imaging has shown promise in assessment of burns [9], liver cirrhosis [10], and tissue damage from myocardial infarction [11]. Most notably, THz imaging has been applied to detecting and assessing regions of cancer in healthy tissue for a wide range of cancers including cancer of the skin [12], [13], liver [11], colon [14], brain [15], and breast [16]-[18].

Generally, for THz biomedical imaging there are two common orientations of the sample under test: reflection or transmission. Standard transmission imaging involves the sample placed between plates of low-absorption material or standing free in a sample space. The incident signal generated by the THz system travels at a normal incident to the sample surface and the transmitted

signal is received on the other side. For THz reflection image, the reflected signal is measured on the same side as the incident signal. This is accomplished either by setting the incident and reflection signals at an oblique angle or by using a beamsplitter in order to separate the incident and reflected signals when both occur at normal incidence [14].

For biological applications, THz has been shown to propagate through several millimeters of animal fat tissue for effective imaging in transmission setups [19]. However, many bodily tissues possess significantly higher absorption in the THz range than fat due to the varying water content between healthy and diseased or damaged tissue [20]. Thus the use of THz transmission imaging for biological applications has been limited to date. Transmission imaging has been applied to thin (160-200 μm) sections of formalin-fixed heart and liver tissue [11], thicker (1.5 mm) sections of colon cancer embedded in paraffin [21], and thin (260 μm) frozen and thawed skin cancer tissue using continuous wave imaging at 1.4 and 1.6 THz [12]. In each case the sample preparation either relied on very thin tissue or on the dehydration of the sample through formalin fixing in order to maintain a reasonable transmitted signal. Because of this, reflection imaging is the more commonly used THz technique for in-vivo or fresh tissue studies. Investigations using a THz transmission setup have also shown the potential of applying spectroscopy across an imaging scan in order to perform regional solutions of the properties of the sample under test. This concept has been applied for assessment of crystal formations in pharmaceuticals [22] and in biomedical imaging for observing the degradation of bone tissue [23].

The use of imaging to obtain tissue properties has also been used in reflection orientations. The use of reflection imaging to calculate tissue characteristics is an established technique for THz applications, and various tomography techniques have also been developed for specific orientations of THz systems [24], [25]. Reflection spectroscopy has been applied to the detection

of water content in cells [8], assessment of liver cirrhosis [10], and in characterization of fresh animal gastrointestinal tissue [26]. A published study investigating THz interaction with DNAs, RNAs, proteins, biological liquids, and cellular structure or density demonstrated that THz contrast can be achieved without water presence [10], [27]. The THz contrast is expected to increase by four times with the water content in fresh tissue [15].

Previous work by our group has focused on the reflection imaging of infiltrating ductal carcinoma in flat sections [16], and preliminary results in reflection imaging of three-dimensional tissue embedded in paraffin blocks was reported [28], [29]. Preliminary work has investigated the THz transmission spectroscopy, but using only few point measurements taken from the same sample [30], [31].

The motivation for this work is to compare reflection and transmission imaging of human breast carcinomas and to address the advantages and disadvantages of each. To the author's knowledge, there is no previous work comparing THz imaging of biological tissue using both transmission and reflection orientation. While fresh tissue is highly absorbent to THz waves, which generally requires the use of reflection imaging [13], [18], dehydrated (fixed) cancer tissue can be imaged using reflection and/or transmission mode. Fixed tissue is more easily obtained than fresh tissue for this imaging as well and can be used to optimize the THz imaging and investigate the contrast of cancer independent of the water content. An additional focus of this work is the development of inversion algorithms to solve for the refractive index and absorption coefficient of biological tissues in the THz range. In contrast to previously published studies on the THz properties of breast tissue, this work seeks to address significant practical issues that can hinder the acquisition of these properties while developing the methods for an eventual clinical

application. The use of fresh bovine tissue is utilized in order to validate the calculation of fresh tissue refractive index and absorption coefficients.

The outline of the paper is as follows: Section 2 will address the methodology including the THz system and sample preparation; Section 3 will detail the propagation modeling; Section 4 will validate the modeling with property measurements of fresh bovine tissue; Section 5 will extend the imaging and characterization to excised human breast carcinomas; and Section 6 will address challenges and future work.

2. Methodology

2.1. Pulsed Terahertz System

The measurements in this work make use of the TPS 3000 pulsed terahertz imaging and spectroscopy system from TeraVIEW, Ltd. The system diagram can be seen in Fig. 1a. The incident terahertz pulse is directed by parabolic mirrors to the sample space for either transmission imaging (Fig. 1a) or reflection imaging (Fig. 1b). The system uses a Ti:Sapphire laser of ~100 mW to excite a GaAs antenna that generates the time domain terahertz pulse shown in Fig. 1c. The system has interchangeable modules that permit a transmission or reflection imaging setup. For transmission the sample is mounted in a motorized frame in the focal center of the incident beam and the transmitted signal is measured. Both the emitter and detector are positioned at normal angle to the sample under test. For reflection the sample is mounted on a motorized stage, and a parabolic mirror base directs the incident signal to focus at the surface of reflection. The reflected signal is then collected in the system. Both the emitter and detector are positioned at 30° oblique to the sample under test. In either case the signal is obtained by measuring the generated bias from a receiving antenna excited by the THz signal and an optically coherent laser pulse split from the original source. The sample space of the system is purged with dry nitrogen gas while in use in

order to reduce any absorption from water vapor in air. The THz signal generated in the system has an approximate beam width of 500 fs. The use of Fourier transform of the pulse provides an effective frequency range of 0.1 to 4 THz that can be seen in Fig. 1d. This allows for imaging or calculation of sample properties at several frequencies from a single time domain measurement. The output THz power of the system is approximately 1 μ W.

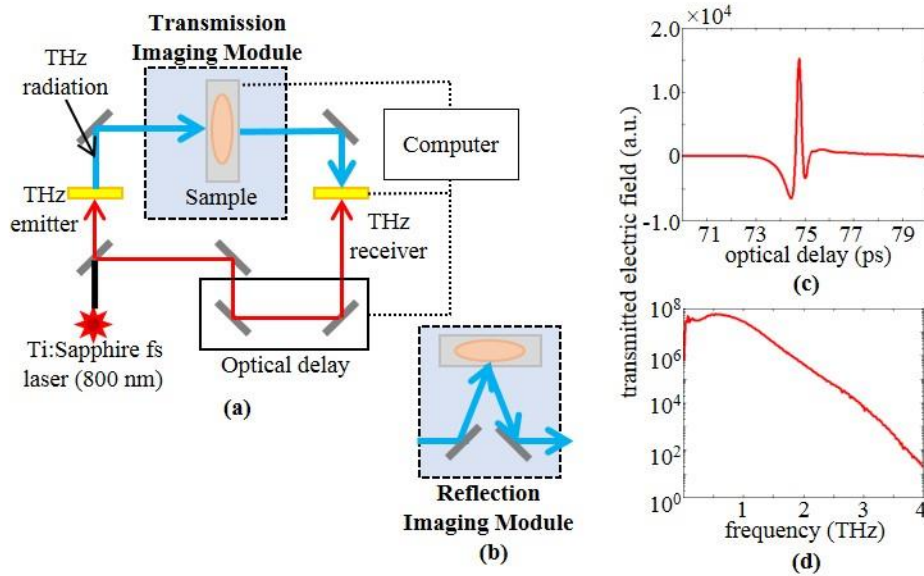


Figure 1. TPS Spectra 3000 (a) diagram with transmission imaging module, (b) reflection imaging module, (c) incident time domain signal, and (d) frequency domain signal obtained with Fourier transform.

2.2. Sample Preparation

The first excised breast cancer tissue sample used in this work was obtained through Northwest Arkansas Pathology Associates, P.A in collaboration with Dr. Lucas Campbell. The sample was obtained from a 69 year old patient diagnosed with stage II/III lobular carcinoma. Another sample was obtained through the National Disease Research Interchange (NDRI) from a 39 year old patient diagnosed with stage III/III infiltrating ductal carcinoma. The tissues were originally provided as formalin-fixed, paraffin-embedded (FFPE) blocks and were later sectioned into 20, 30, and 40 μ m thick tissue slices on polystyrene microscope slides. For the purpose of this

work, 20 and 30 μm sections are used. Between each tissue section, a 5 μm thick section is sliced, mounted on a standard glass microscope slide, and subjected to staining with hematoxylin and eosin (H&E) for the purpose of pathology assessment and correlation to the THz images. No staining or any contrast agents are applied to the sections used in THz imaging. The tissues selected in this work represent the two most common breast cancer types. Infiltrating ductal carcinoma accounts for approximately 8 out of every 10 invasive breast cancer diagnoses, while lobular carcinoma accounts for 1 of 10 [32].

2.3. Selection of slide materials

Previous work with FFPE tissue in our group dealt primarily with tissue on glass slides [16], [30]. However, this posed a significant problem with regards to the ability to perform transmission spectroscopy of the tissue due to the strong attenuation of glass in the THz range [30]. In order to have better transmission, polystyrene microscope slides of 3"×1" with an average thickness of 1 mm are selected due to their low absorption in the THz range compared to other standard polymers [33]. For imaging and validating the solution of the properties of fresh bovine tissue, a 1.2 mm thick polystyrene (Plaskolite) plate of 3cm×3cm was placed on the system to hold the fresh meat in the reflection setup, as will be detailed in Section 4. The properties of the two kinds of polystyrene are measured using a basic THz spectroscopy setup for a single material in

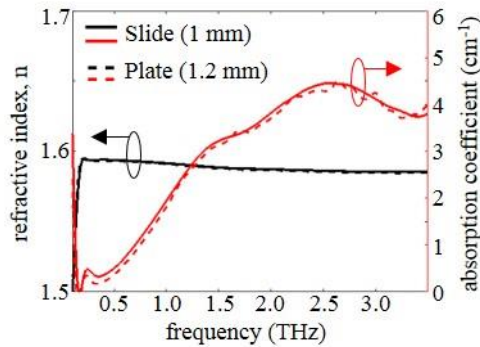


Figure 2. The refractive index (black) left scale and absorption coefficient (red) right scale of two polystyrene materials used in this work: a 1 mm thick microscope slide (solid line) and 1.2 mm thick polystyrene plate (dotted line).

air. The results are shown in Fig. 2. It can be clearly seen that the two types of polystyrene have very similar properties and relatively low absorption across the entire frequency range used in this work. Thus the material is suitable for both transmission and reflection imaging of tissue.

3. Propagation modeling

3.1. Transmission mode

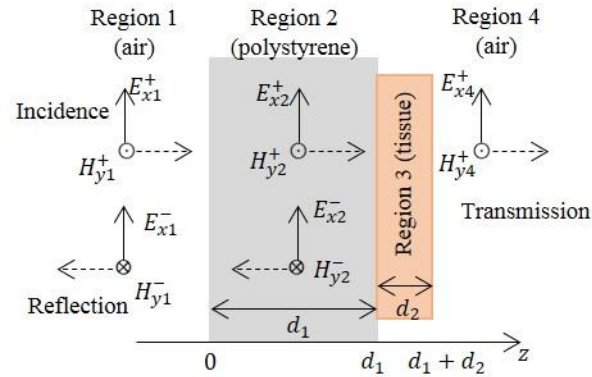


Figure 3. Transmission imaging setup.

In order to obtain the properties of the breast carcinomas in this work, modeling is set up to compare the theoretical propagation of the THz signal to the measured signal. The transmission setup for FFPE tissue mounted on a polystyrene slide can be seen in Fig. 3. In this measurement orientation the incident terahertz signal encounters the polystyrene first then the tissue before being collected at the receiver. While the sample measurement is selected as the transmission through both polystyrene slide and FFPE tissue, the reference signal can be taken from the transmission through air or the transmission through the polystyrene slide alone. Since the properties of the polystyrene can be measured separately as shown in Fig. 2, a blank slide serves as the reference in this case. The propagation of the signal through both the sample and reference points is calculated using well-established impedance and reflection interactions for multiple layers [34], [35]. The ratio of the sample to the reference signal takes the form

$$E_{smp}/E_{ref} = \tilde{\tau}e^{(\gamma_1-\gamma_3)d_2}, \quad (1)$$

where $\tilde{\tau}$ is the ratio between the transmission coefficients of the two measurements and $\gamma_i = j(\omega/c)\tilde{n}_i$ is the complex propagation coefficient of region $i = 1,2,3\dots$, with ω indicating the angular frequency, c is the speed of light in vacuum, and \tilde{n}_i as the complex refractive index of the region. This can be further expressed as $\tilde{n}_i = n - j\frac{c}{2\omega}\alpha_{abs}$, where the real refractive index n and the power absorption coefficient α_{abs} are the properties being calculated in this work. The term $\tilde{\tau}$ is given by

$$\tilde{\tau} = \left(\frac{2\tilde{n}_3(\tilde{n}_1 + \tilde{n}_2)}{(\tilde{n}_1 + \tilde{n}_3)(\tilde{n}_2 + \tilde{n}_3)} \right) \left(\frac{1 - \rho_{12}^2 e^{-2\gamma_2 d_1}}{1 + \rho_{23}\rho_{31} e^{-2\gamma_3 d_2}} \right) \left(1 + \rho_{12} \frac{\rho_{23} + \rho_{31} e^{-2\gamma_3 d_2}}{1 + \rho_{23}\rho_{31} e^{-2\gamma_3 d_2}} e^{-2\gamma_2 d_1} \right)^{-1}. \quad (2)$$

Here ρ_{ij} is the Fresnel reflection coefficient for normal incidence between regions i and j in the setup of Fig. 3, given by $\rho_{ij} = (\tilde{n}_i - \tilde{n}_j)/(\tilde{n}_i + \tilde{n}_j)$. The first term in the numerator is the ratio between the Fresnel transmission coefficients in the sample and the reference, while the remaining terms are all multiple reflection contributions of the Fabry-Perot effect in each region. For the case of carcinoma on a polystyrene slide, the thickness of the polystyrene is $d_1 = 1$ mm and the tissue thickness is $d_2 = 20\text{-}30$ μm . Although the absorption of the polystyrene is low and multiple reflections do exist in this layer, all second reflections are windowed out during measurements by adjusting the time scale in the system. In order to have consistency in the model with the measurements in this case, all $\exp[-2\gamma_2 d_1]$ terms in Eq. (2) are assumed zero. In order to obtain the properties of the tissue (region 3), Eq. (1) is numerically solved for a range of n_3 and $\alpha_{abs,3}$ and the error between both the magnitude and phase of the measured E_{samp}/E_{ref} and the calculated transmission is given by

$$err_{mag} = \left[\ln(|E_{samp}/E_{ref}|)_{meas} \right] - \left[\Re\{\ln(\tilde{\tau})\} + (\alpha_{abs,1} - \alpha_{abs,3})\frac{d_2}{2} \right], \text{ and} \quad (3)$$

$$err_{phase} = \left[\arg(E_{samp}/E_{ref})_{meas} \right] - \left[\Im\{\ln(\tilde{\tau})\} + \frac{\omega}{c}(n_1 - n_3)d_2 \right]. \quad (4)$$

The values of n_3 and $\alpha_{abs,3}$ for which the summed magnitudes of Eqs. (3) and (4) are simultaneously minimized are then considered to be the solutions. An inversion algorithm solves for the error between the measurement data and calculated transmission from a matrix of potential solutions using different values of the refractive index and absorption coefficient. The properties are then retrieved from the solution in the matrix with the lowest total error. To obtain a transmission image of the tissue properties, this technique is applied across every pixel in the scan for each desired frequency.

In order to reduce noise in the spectroscopy based image, two special considerations are accounted for in the measurements. In particular, the signal at the ends of the time domain measurement window is not necessarily zero, and the difference in values at this boundary can contribute high frequency noise to the measurements. To reduce this effect, a four-term Blackman-Harris filter is used to isolate the primary transmission peak in the reference and each measurement signal. Secondly, the optical delay between the reference and sample measurements is adjusted to have the peaks aligned to avoid any spectrum shifts based on the position of the peak in the time domain window. This optical delay shift is then applied to the time domain signal of the measurements when obtaining the measured magnitude and phase.

3.2. Reflection mode

The setup for the reflection mode can be oriented in several ways based on the positioning of the sample. The polarization of the beam with respect to the sample will affect the resulting reflection. This work investigates three different reflection setups, which are shown for the *TM* (parallel) mode in Fig. 4 [35]. In Fig. 4a, the incident THz signal encounters the tissue first then the polystyrene slide. Additional orientations shown in Fig. 4b and Fig. 4c are also investigated in this work. For the sake of space only the formulation for the setup in Fig. 4a will be given here,

while the expressions for the cases in Fig. 4a and 4b are slightly different. In all measurements here, secondary reflections are windowed out as explained in Section 3.1.

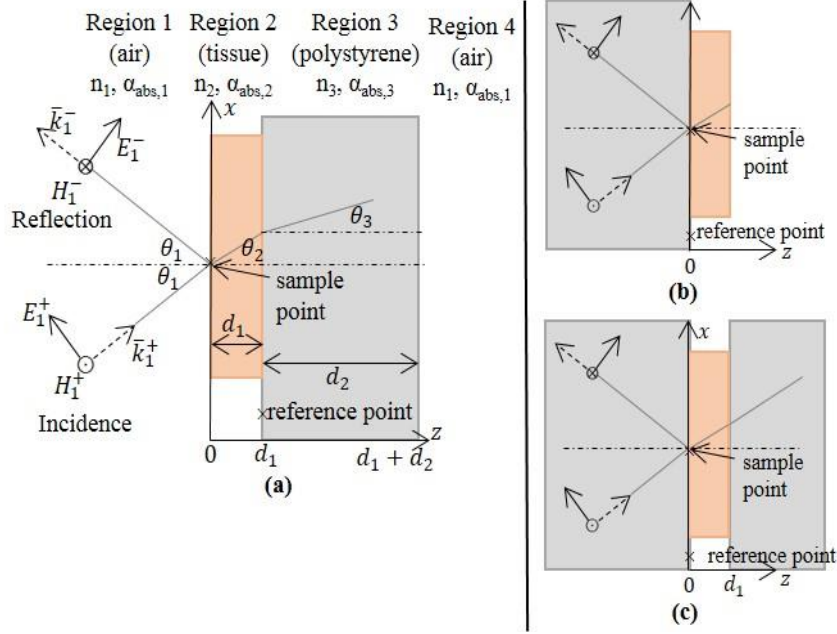


Figure. 4. Reflection imaging setups for tissue on polystyrene slides. (a) Air, tissue, polystyrene slide, air orientation. (b) air, slide, tissue, air orientation. (c) air, slide, tissue, slide, air setup. In all cases, the THz emitter and detector are located on the left side.

For the setup in Fig. 4a, the sample reflection is collected from the surface of the tissue, while the reference signal is collected from the same polystyrene slide with no tissue. The resulting ratio of the sample and reference signals is given by

$$\frac{E_{samp}}{E_{ref}} = \Gamma_T = \left(\frac{\rho_{T,12} + \rho_{T,23} e^{-j2\frac{\omega}{c}\tilde{n}_2 \cos \theta_2 d_1}}{1 + \rho_{T,12}\rho_{T,23} e^{-j2\frac{\omega}{c}\tilde{n}_2 \cos \theta_2 d_1}} \right) \frac{1}{\rho_{T,13} e^{-j2\frac{\omega}{c}\tilde{n}_1 \cos \theta_1 d_1}}, \quad (5)$$

Where $\rho_{T,ij}$ is the Fresnel reflection coefficient between regions i and j for the oblique incidence in the reflection mode where its expression depends on the polarization of the beam (see Appendix A). The difference in distance between the sample points on the tissue surface and the reference point on the polystyrene slide in Fig. 4a is accounted for through the phase term

($\exp\left(-j2\frac{\omega}{c}\tilde{n}_1\cos\theta_1d_1\right)$) in the denominator of Eq. (5). The angle of incidence in air is known ($\theta_i = 30^\circ$), so the angles of propagation in each region are defined using Snell's Law

$$\tilde{n}_1 \sin \theta_1 = \tilde{n}_2 \sin \theta_2 = \tilde{n}_3 \sin \theta_3. \quad (6)$$

In order to obtain a reflection image of tissue properties (i.e. the refractive index and absorption coefficient at each pixel), the polarization of the THz beam needs to be known (i.e. *TE* or *TM*). However, due to the parabolic mirrors used to orient the reflection beam in the measurement system, the polarization of the beam is believed to be a hybridization of *TE* and *TM* modes that could not be determined analytically. Instead, for this work the polarization of the detected signal is approximated experimentally by first measuring the electrical properties of an acrylic sheet using fixed point spectroscopy. Then the reflection from the acrylic is calculated for the *TE* and *TM* polarizations with accounting for potential rotations between the two polarizations from 0° to 90° as shown in Fig. 5. The calculated reflections at these rotation angles ψ and the measurement signal are compared versus frequency in Fig. 5.

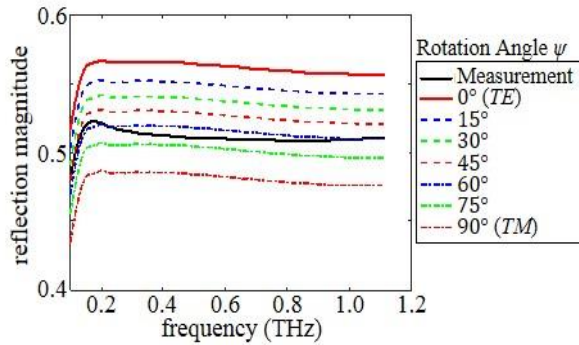


Figure 5. Calculated reflection signals at different rotation angle ψ between *TE* and *TM* modes versus the measurement signal for acrylic sheet.

From the comparison in Fig. 5, it becomes clear that while neither *TE* nor *TM* mode accurately models the reflection signal in the measurement system, a combined reflection with polarization rotation angle of $\psi = 60^\circ$ with respect to *TE* mode gives a good estimation of the received signal. The resulting calculated reflection ratio is expressed as

$$E_{samp}/E_{ref} = \Gamma = \sqrt{(\Gamma_{TE} \cos \psi)^2 + (\Gamma_{TM} \sin \psi)^2}. \quad (7)$$

Where Γ_{TE} and Γ_{TM} are the individual solutions to Eq. (5) for *TE* and *TM* polarizations (see Appendix A). Eq. (7) is used in all reflection images presented in this work. Finally the unknown properties of the tissue in region 2 in Fig. 4a are obtained by calculating the error for a range of n_2 and $\alpha_{abs,2}$ using

$$err_{mag} = \left[\ln(|E_{samp}/E_{ref}|)_{meas} \right] - [\Re\{\ln(\Gamma)\}], \text{ and} \quad (8)$$

$$err_{phase} = \left[\arg(E_{samp}/E_{ref})_{meas} \right] - [\Im\{\ln(\Gamma)\}]. \quad (9)$$

Unlike the transmission case in Eqs. (3) and (4), there are no explicit n_2 and $\alpha_{abs,2}$ in Eqs. (8) and (9) due to the absence of significant propagation in the polystyrene slide in the reflection mode compared to the transmission mode, but these unknowns are included in Γ . The solutions of the refractive index and absorption coefficient are obtained upon simultaneously minimizing the error expressions in Eqs. (8) and (9). For the other setups in Fig. 4b and Fig. 4c, similar equations to Eq. (5) are obtained accounting for different sequences of layers, and the additional phase term ($\exp\left(-j2\frac{\omega}{c}\tilde{n}_1 \cos \theta_1 d_1\right)$) in the denominator is absent since the tissue and reference points are at the same interface (expressions are not shown). The error equations (8) and (9) are the same in all setup cases of Fig. 4.

4. Validation of models

Fresh portions of bovine chuck steak are selected to validate the models of Section 3. However, because of the high absorption of THz signal in these tissues, only the reflection model can be validated. The transmission model was validated in previous work in comparison with published data of glass and polystyrene [30], [31].

4.1. Animal tissue spectroscopy

The diagram of the sample and reference setups and the results of the average properties are given in Fig. 6. Here the reference measurement through the quartz window and the sample transmission setup can be seen in Fig. 6a and Fig. 6b. The reference signal is collected as the transmission through the two quartz windows with no plate in between shown in Fig. 6a. The sample signal is collected from the fresh bovine tissue sliced very thin and placed in a liquid sample holder consisting of two 3 mm thick quartz plates (Fig. 6b). Pressure is applied to the outside of the plates in order to compress the tissue sample, and Teflon spacers around the outside edge are used to maintain a specific thickness of the tissue between the two plates. For the fat tissue a thickness of 500 μm is sufficiently thin to get a transmitted THz signal across the entire frequency range of the measurement system. However, for the more absorptive muscle tissue the thickness needed to be reduced to 100 μm . All single point spectroscopy measurements are averaged over 7200 time domain collected signals. Seven different samples are used for each tissue type. The properties of water are also measured here using the sample liquid holder in Fig. 6b with a

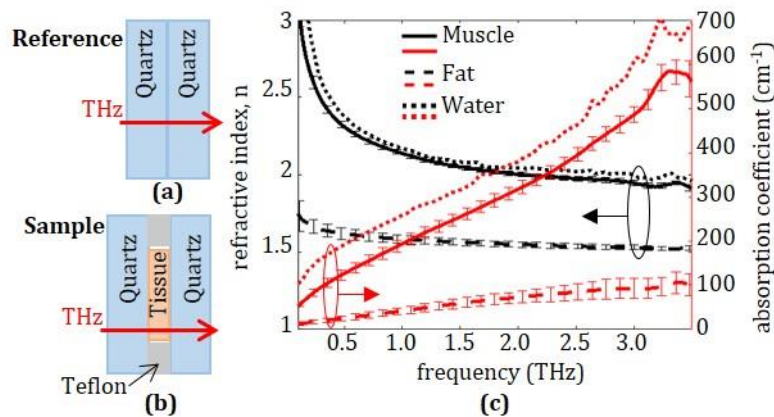


Figure 6. THz spectroscopy of fresh bovine tissue using (a) quartz window reference and (b) sample measurement of tissue in quartz holder (c) the mean calculated refractive index (black) and absorption coefficient (red) of the muscle (solid line) and fat (dashed line). Error bars indicate the standard deviation of the measurements. The measured properties of water (dotted line) are also shown for comparison.

separation of 100 μm . All spectroscopy measurements of bovine tissue and water were conducted at room temperature (295 K).

The results of the bovine tissue spectroscopy in Fig. 6c show a good differentiation between muscle and fat tissue for both refractive index and absorption coefficient. This is a well-known contrast between these tissue types in THz band as reported in the literature for human tissue [36]. These results will be used for validation of the reflection imaging models in Section 4.2. The standard deviations of the calculated values of refractive index and absorption coefficient for the muscle and fat are represented by the error bars on each plot. The same properties of water are also shown in Fig. 6 for comparison with the fresh bovine tissue. The results in Fig. 6 show the significant absorption of water that will be present in fresh tissue and will play a role in THz image contrast, in agreement with [8], [10], [15].

4.2. Reflection imaging and calculation of tissue properties

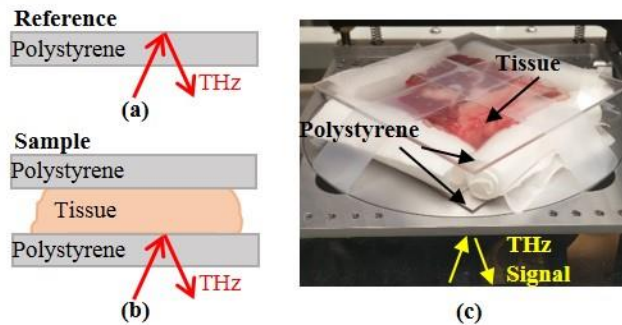


Figure 7. Reflection imaging setup where bovine tissue is held between two polystyrene plates. (a) The reference measurement, (b) the sample measurement, and (c) photo of the sample positioned on the system window. The THz emitter and detector are positioned below the window.

Fresh bovine tissue of size $\sim 3.5\text{ cm} \times 3.5\text{ cm} \times 2.5\text{ cm}$ is scanned to obtain peak time domain, magnitude, and phase THz images. Also the measured data are used to calculate the refractive indices and absorption coefficients at each pixel in the scan to produce tissue property images. The imaging setup can be seen in Fig. 7. In this setup a polystyrene plate is used to place the fresh

tissue on the imaging stage (window) and a second plate is placed on top of the tissue to apply pressure and enforce a flat surface at the focus of the THz beam. The setup is compressed manually until the tissue is flat and then held in place with tape. As a result, the tissue thickness is reduced to ~1 cm during the imaging process. Clean room wipes are placed between the plates surrounding the tissue, but outside of the scanning area, to prevent leaking of blood onto the system. The reference signal is collected from the reflection of an empty polystyrene plate (no tissue) as shown in Fig 7a. All sample measurements were aligned to the reference based on the reflection from the bottom of the polystyrene plate as shown in Fig. 7b. The model for the reflection setup in Fig. 4b is also investigated and the difference in solutions is found to be negligible due to the substantial thickness and high absorption of the bovine tissue.

The first bovine sample is shown in Fig. 8. The photograph of the tissue in Fig. 8a shows the two primary tissue types in this sample, with the white region primarily denoting fat and pink and red regions denoting muscle and blood. The image representing the peak of the time domain reflected signal at each pixel is shown in Fig. 8b, where the muscle and the fat can be clearly distinguished and compared against the photograph. Here the muscle shows a significant reflection compared to the fat tissue. This is an expected result due to the much higher contrast of the properties between the muscle and the polystyrene plate compared with those between the fat and polystyrene. It should be noted that all THz images presented in Figs. 8b-8j are obtained upon manually applying pressure to flatten the tissue while the photo in Fig. 8a was obtained before applying that pressure. As a result, the shape of the fat region appears more spread apart in the THz images compared with the original photo. This shape spreading could be accounted for by measuring the compression force and the elasticity of the tissue, but it is outside the scope of this work.

The Fourier transform is conducted on the time domain pulse at each pixel in the scan to obtain the magnitude and phase of the reflected signal taken against a blank polystyrene reference, as seen in Fig. 8. The magnitude images, normalized against the reference, can be seen at 1 THz in Fig. 8c and at 2 THz in Fig. 8d. Both frequency domain images show good distinction between the muscle and fat tissues. The reflected magnitude at 2 THz show lower values than that at 1 THz due to increased losses including higher absorption in the polystyrene plate at that frequency as well as lower refractive index in both tissues as the frequency increases in consistence with Fig. 6c.

The reflected phase images are shown at 1 THz in Fig. 8e and at 2 THz in Fig. 8f. While the general shape of the fat and muscle tissues can be seen in the phase image, the details of the tissue are not as clearly resolved as in the magnitude images. This is primarily due to the phase in the tissue region being entirely dependent on the phase shift from the reflection at the polystyrene/tissue interface rather than from any propagation in the tissue (tissue is highly absorbing). However, this also made the phase measurement highly sensitive to any curvature of the polystyrene plate, as small offsets in the position of the reflection peak are attributed to phase variations in the reflection. When necessary, small variation in the polystyrene position is corrected by shifting the measurement signal to align to the first reflection from the bottom of the polystyrene.

The magnitude and phase data are used to obtain the absorption coefficient and index of refraction of the tissue using the reflection model. The calculated refractive index images at 1 THz is shown in Fig. 8g and at 2 THz is shown in Fig. 8h. The absorption coefficient is shown at 1 THz in Fig. 8i and at 2 THz in Fig. 8j. The calculated properties show good agreement with the spectroscopy results in Fig. 6c, with the refractive index of the muscle being close to the average

value of 2.14 at 1 THz and decreasing to 2.0 at 2 THz. The refractive index of the fat shows a less significant reduction from 1.58 at 1 THz to 1.55 at 2 THz in the spectroscopy, which cannot be as clearly seen in the refractive index images. Likewise, the absorption coefficient can be seen

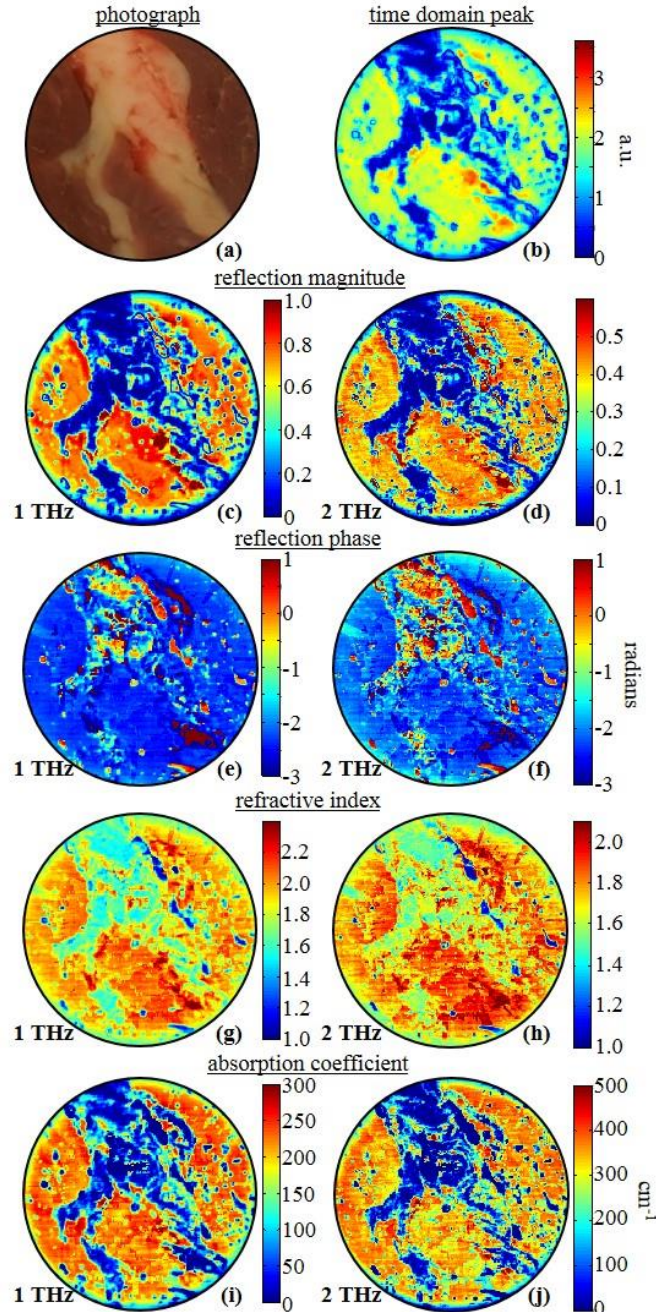


Figure 8. Reflection imaging and characterization of fresh bovine tissue. (a) Photograph of the sample. (b) THz time domain measured reflection from sample. Fourier transform used to obtain THz frequency domain reflected magnitude at (c) 1 THz and (d) 2 THz and reflected phase at (e) 1 THz and (f) 2 THz. The calculated refractive index at (g) 1 THz and (h) 2 THz and the calculated absorption coefficient at (i) 1 THz and (j) 2 THz.

increasing significantly as the frequency increases, and the results in the images are in good agreement with the measured transmission spectroscopy in Fig. 6c.

Few spots are observed in the solution images that do not look similar to the muscle or fat. Most notably, regions where the solved refractive index is 1 and absorption coefficient is 0, such as those on the top right edge of the fat tissue, indicate air gaps between the polystyrene and tissue that the applied pressure did not fully remove. Also, the large spots of higher refractive index seen around the bottom right area of the fat indicate that the blood from the tissue has pooled as evident by the slight difference with the muscle tissue.

The solution of the reflection imaging is further tested on a second sample of bovine tissue and compared across several frequencies in order to investigate the reconstruction algorithm. The results can be seen in Fig. 9 for the tissue photograph shown in Fig. 9a. The peak time domain reflection image can be seen in Fig. 9b. It should be noted that in this tissue sample there is a blood vessel in the center of the fat region that can be clearly seen in Fig. 9a and that subsequently appears in the THz image. Also, just below that blood vessel there is a region of connective tissue that appears white in the photograph but has no adipose tissue. As a result, the blood vessel and connective tissues areas appear, in all images in Fig 9, indistinguishable from the highly hydrated muscle tissue surrounding the fat. Overall the THz images sufficiently distinguish between muscle and fat regions. Rather than looking at magnitude and phase, the solution values of refractive index and absorption coefficient images are shown for several frequencies. While the 0.5 THz images in Fig. 9c and Fig. 9d do not possess as much spatial resolution, they provide significant contrast between the muscle and fat regions. The same observation can be seen for the solution images at 0.75 THz in Fig. 9e and Fig. 9f. As the frequency increases, the solution images become more subject to noise in the measurements. This most noticeably begins to arise in the images at 1 THz,

where the refractive index shown in Fig. 9g remains distinct between the fat and muscle, but the absorption coefficient in Fig. 9h starts to exhibit noise in the muscle region.

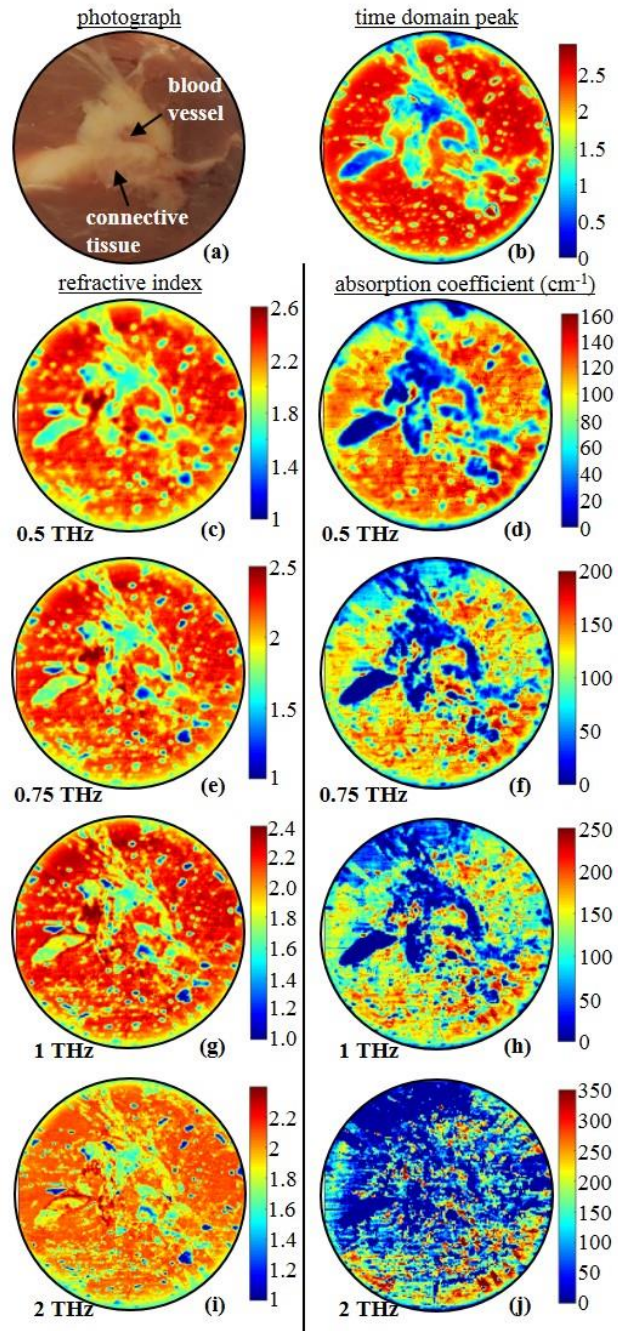


Figure 9. Reflection imaging and characterization of bovine tissue sample 2 represented by (a) photograph. (b) The time domain reflection image, (c) the refractive index, n , and (d) the absorption coefficient, α_{abs} , at 0.5 THz, (e) n and (f) α_{abs} at 0.75 THz, (g) n and (h) α_{abs} at 1 THz, and (i) n and (j) α_{abs} at 2 THz.

Of particular note is the slight blurring of the solution around the edges of the image shown in the top edge in Fig. 9h. This is primarily due to the slight shifting of the phase due to curvature of the polystyrene plate that could not be completely accounted for numerically. This time domain shift has a greater bearing on the phase and the subsequent solution as the frequency increases. The solution at 2 THz for both refractive index in Fig. 9i and absorption coefficient in Fig. 9j is subject to a greater amount of noise, particularly in the absorption coefficient image. This can be avoided in the future by performing signal averaging of the measurement at each point (no signal averaging is conducted here). Also, more selective windowing can be implemented to remove all measurement artifacts from early or late reflections, which can contribute high frequency noise to the solution. Nevertheless, in general the obtained properties show strong agreement with the spectroscopy in Fig. 6c.

In both of the bovine tissue samples presented here, the fat and muscle tissue showed clear contrast in both THz time and frequency domain images and in the reconstructed electrical properties. Thus the characterization using THz reflection mode has been shown to be effective for calculating the tissue properties. This methodology can also be applied to freshly excised breast cancer tissue in the future. Challenges seen from the animal tissue here include achieving full contact of the fresh tissue to the polystyrene plate. These gaps beneath the tissue can be filled with either blood or air, resulting in scattered spots of much higher or lower reflection in the imaging as seen in Figs. 8 and 9. While these effects can be improved by using some tool to apply uniform pressure to the back of the tissue, this comes as a tradeoff with distorting the tissue dimensions leading to larger THz images compared with the physical tissue. Additionally, while the high absorption of fresh tissue limits the capability for transmission imaging, the presence of water in the tissue can greatly improve the contrast in the resulting THz reflection images [10], [15].

In order to optimize the process for imaging of fresh breast cancer tissue, the primary adjustment to the methodology in this work is the development of a more standardized sample holder for mounting the tissue samples for THz imaging. While the fresh tissue imaging here used polystyrene plates and pressure was applied using tape, a clamp-based mount can be used to offer consistent pressure on the tissue. Additionally, a permanent sample holder can be outfitted with a suitable imaging window that can provide a uniformly flat surface so that the tissue properties can be more accurately obtained. Finally, this will allow for standardized reference measurements that can be used for effective differentiation of breast cancer from normal tissue in a clinical setting.

5. Imaging of breast carcinoma

In Section 5.1, the processes introduced in Secs. 3 and 4 will be employed on FFPE breast lobular carcinoma. Section 5.1.1 will detail THz transmission and reflection imaging, and Section 5.1.2 will show the refractive index and absorption coefficient solution images. The same details will be shown for FFPE infiltrating ductal carcinoma in Section 5.2.

5.1. Case 1: Lobular carcinoma (LC)

5.1.1. Transmission and reflection images of LC

All setups shown in Section 2 for imaging and calculation of tissue properties are implemented and compared for the lobular carcinoma samples. First, transmission and reflection imaging are investigated for two 30 μm thick samples taken from the same tumor block. For each sample a 5 μm section is also sliced and treated with standard pathology dyes hematoxylin and eosin (H&E). The low power pathology regions are defined for Sample 1 in Fig. 10a and Sample 2 in Fig. 10b. These two sample sections were sliced from the block at ~ 200 μm from each other. The lobular carcinoma of the sample is indicated by the dark purple H&E stain on the right, while the lighter pink region to the left indicates the fibroglandular tissue and the mostly clear areas

indicate a mixture of fatty/fibroglandular tissue. Six positions designated 1-6 are selected in Sample 2 for more thorough pathology assessment that will be discussed in Fig. 12.

The THz reflection images of the FFPE lobular tissue are shown in Fig. 10c for Sample 1 and Fig. 10d for Sample 2. The imaging used the setup with the signal encountering the tissue first as shown in Fig. 4a. It should be noted that the area outside of the tissue section in the THz images is paraffin. The same outlines from the pathology are applied to the THz images. The results in Figs. 10c and 10d show that the lobular carcinoma regions exhibit significantly higher reflection than the other regions. It is observed also that the mixture of fatty/fibroglandular tissue region exhibit reflection values between the carcinoma and fibroglandular. The fibroglandular tissue region exhibits the lowest reflection values. All reflection values represent electric fields in arbitrary units. In Fig. 10d, it is noted that the THz imaged tissue extends beyond the outlines established in the pathology images. This is primarily due to the slight difference in the tumor block structure where the pathology sections and THz sections were sliced. Depending on the technique used for slicing the tissue, as much as 100 μm of tissue could exist between the pathology and THz sections such that the tissue at lower extents in the block could be slightly larger. Regardless, the results of Figs. 10c and 10d show contrast between the carcinoma, fibroglandular and fatty/fibroglandular regions. However, there are some spots seen in the THz images that are not indicated in the pathology. For example, around the right edge of the carcinoma region, there is a dark blue area that is due to a raised edge of the tissue where it has separated from the slide. This occurs consistently in both samples in Figs. 10c and 10d.

The time domain transmission images are shown in Fig. 10e for Sample 1 and Fig. 10f for Sample 2. For the THz measurement system used in this work, the transmission stage is limited in its movement range such that this entire tissue could not be imaged. Thus while it is presented to

scale with the reflection images, there is a portion of the fibroglandular and fatty tissue regions that cannot be visualized. The difference in the size of Fig. 10e and Fig. 10f is due to a ~1 mm difference in positioning the tissue in the two scans. In the transmission mode the different regions of the tissue are clearly defined, with the lobular carcinoma showing the least transmission, followed by the fibroglandular and then the fatty/fibroglandular tissue. The area where the tissue has separated from the slide can be clearly seen as the region of dark blue on the right side of the carcinoma region. Of note is that the transmission image does not distinguish much between the

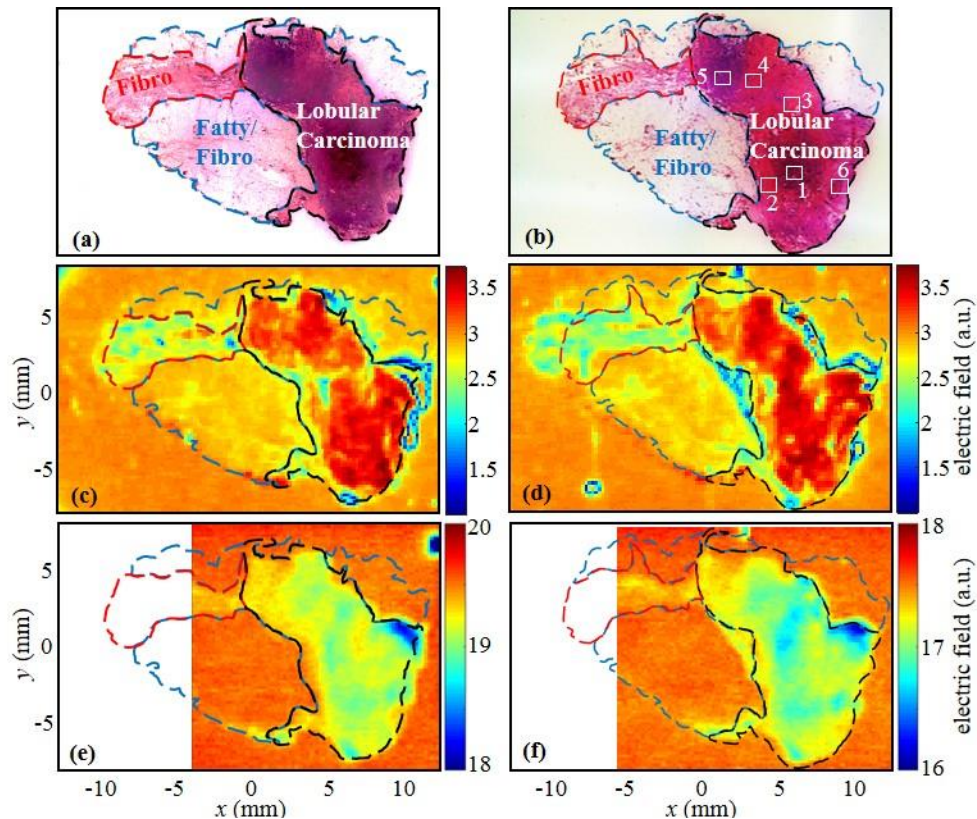


Figure 10. Reflection and Transmission images of lobular carcinoma samples obtained from 69-year-old woman. Pathology of (a) Sample 1 and (b) Sample 2 with regions designated by outlines for lobular carcinoma (black), fibroglandular (red), and fatty/fibroglandular (blue) tissue. Points 1-6 are indicated for high power pathology assessment to be shown in Fig. 12. Reflection peak time domain images are shown for (c) Sample 1 and (d) Sample 2. Transmission peak time domain images are shown for (e) Sample 1 and (d) Sample 2. Blank areas in the transmission images (e-f) represent the smaller scanning ranges (window size) in the transmission module in the measurement system used in this work, which is not the case for the reflection module in the system.

fatty/fibroglandular regions and the surrounding paraffin as shown in Figs. 10e and 10f. On the other hand, these two regions are clearly distinguished in the reflection images in Figs. 10c and 10d. In order to understand this issue, more thick tissue sections need to be investigated. In both samples the reflection mode demonstrate more clear contrast and higher resolution in the margins between regions compared with the transmission mode. All images are obtained using scanning step size of 200 μm . The transmission imaging used an average of 4 signals at each pixel while the reflection imaging used a single signal at each pixel.

In Fig. 11, the Fourier transform is used to obtain images at specific frequencies that can show additional details as reported in breast infiltrating ductal carcinoma [16]. In this case the areas of both transmission and reflection modes are truncated to the same size across all images for the purpose of comparison. The pathology is also shown at this scale for Sample 1 in Fig. 11a and for Sample 2 in Fig. 11b. For each imaging mode the frequency domain magnitude is shown at 1 and 2 THz. For transmission mode, the images at 1 THz are given in Fig. 11c and 11d for Sample 1 and 2 and the images at 2 THz are given in Fig. 11e and 11f. It can be seen that while increasing the frequency does provide a little more distinction of the margins of the tissue regions, this comes at the expense of increasing the noise at 2 THz. Also, neither of the frequency domain images in THz show any substantial details that were not shown in the time domain transmission images in Fig. 10e and Fig. 10f. Also, here the fatty/fibroglandular mixed tissue region still shows no differentiation from the paraffin region.

The reflection frequency domain images are shown at 1 THz for Sample 1 in Fig. 11g and Sample 2 in Fig. 11h. The images at 2 THz are shown for Sample 1 in Fig. 11i and for Sample 2 in Fig. 11j. While the time domain images in Fig. 10c and 10d exhibit the carcinoma as almost a homogeneous region, the reflection frequency domain images in Figs 11g-11j exhibit a

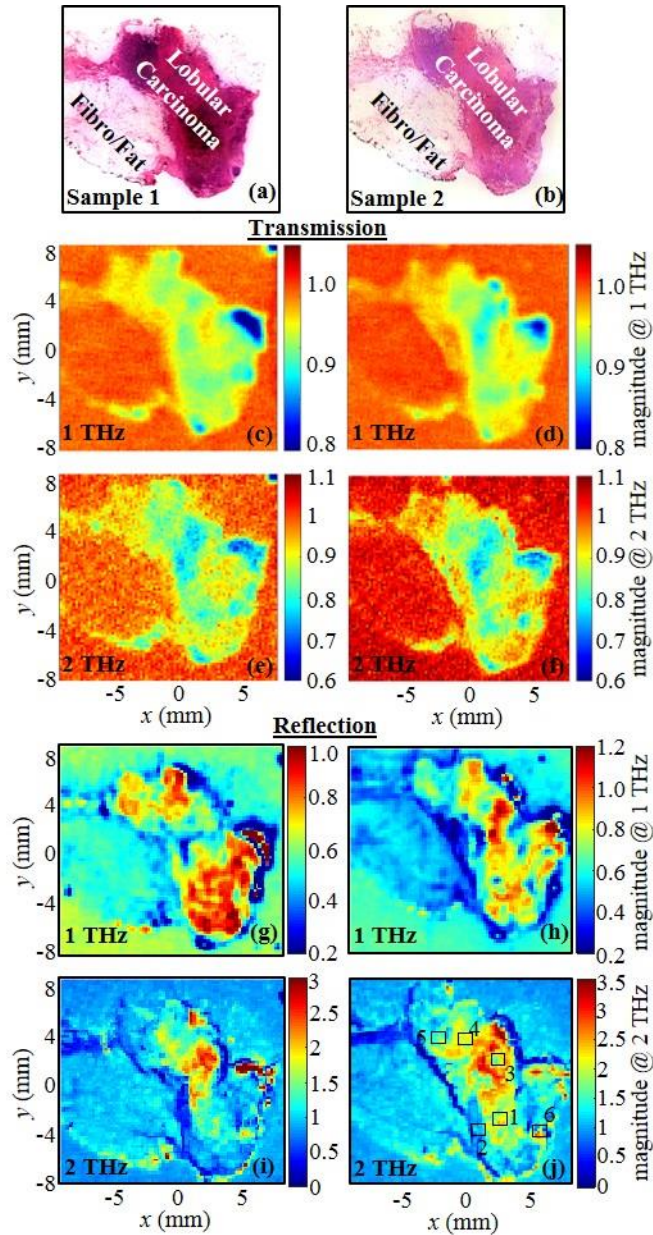


Figure 11. Frequency domain images of lobular carcinoma. Pathology given for (a) Sample 1 and (b) Sample 2. Transmission magnitude images at 1 THz for (c) Sample 1 and (d) Sample 2 and at 2 THz for (e) Sample 1 and (f) Sample 2 following the configuration in Fig. 3. Reflection magnitude images at 1 THz for (g) Sample 1 and (h) Sample 2 and at 2 THz for (i) Sample 1 and (j) Sample 2 following the configuration in Fig. 4a. Points labeled 1-6 in reflection images indicate features that are visible in the images compared with high power pathology in Fig. 12.

heterogeneous carcinoma region. In Fig. 11g, the 1 THz images show clear margins between all regions, although the reflection magnitude of the electric field from the fatty/fibroglanular mixed

region and mostly fibroglandular region seem similar, while the lobular carcinoma at this frequency shows higher reflection. However, of greater note is that the reflection within the lobular carcinoma itself shows heterogeneity exhibited at different positions in the region.

For Sample 1, the center of the lobular carcinoma shows much lower reflection at 1 THz than the upper and lower areas in Fig. 11g, while the center shows a higher reflection in Sample 2 in Fig. 11h. In the 2 THz images, the fibroglandular and fatty/fibroglandular mixed tissue regions are distinct, with the primarily fibroglandular region showing a lower reflection. The lobular carcinoma region once again shows the highest reflection, with the center area showing a consistently higher reflection than the rest of the carcinoma in Figs. 11i and 11j.

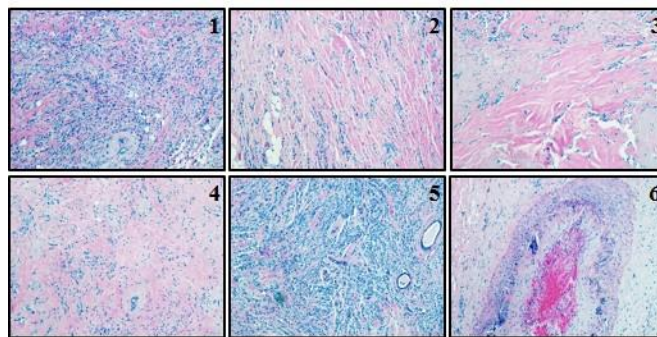


Figure 12. High power pathology (100X) of positions 1-6 indicated in Fig. 10b, showing neoplastic epithelial cells of varying density in positions 1-5 and a blood vessel in position 6.

In order to understand the areas of heterogeneity observed in the lobular carcinoma in the frequency domain reflection images, positions 1-6 are arbitrarily selected to obtain higher power pathology images (100X) in Sample 2. The higher power pathology images in Fig. 12 demonstrate that the tumor cells (i.e. the neoplastic epithelial component) are accompanied by varying amounts of mature collagen (the pink fibers). The tumor cells are small and blue-staining. In some areas, they are densely cellular, while in other areas they are overshadowed by the collagenous stroma. Positions 1-5 of the tumor contain neoplastic cells of varying cellular densities. In particular, positions 1 and 5 are more densely cellular as opposed to positions 2-4, which have more scant

cellularity with more stroma (dense pink material). Position 6 is a large blood vessel (artery) that appears to have patchy mineralization of the vascular wall and a poorly-organized thrombus (clot) in the lumen. The differences between these positions can be most clearly seen in the 2 THz reflection images in Figs. 11i and 11j, where positions 3 and 4 corresponding to the highly collagenous carcinoma show a much higher reflection than the densely cellular regions at positions 1 and 5. In both cases position 2 shows slightly lower reflection, which may indicate further difference, such as tissue adhesion to the slide, between the different areas of lower cellularity. The blood vessel at position 6 shows up as an isolated high reflection in both samples. These features were not observed in any significant sense in the transmission images in Fig. 11, indicating to another advantage of the reflection imaging of the sections used in this work.

For additional analysis of these heterogeneous areas inside the carcinoma region, the time domain reflection signals are collected at few points marked as A, B, and C shown in Fig. 13. The subsequent time domain comparison is given by Fig. 13a for Sample 1 and Fig. 13b for Sample 2. For Sample 1 the signal at point B is found to have an earlier peak position than the other two signals at A and C. Additionally, there is a secondary peak following the main peak that does not appear in the other signals. One possible explanation is a higher refractive index creating a separation in the reflected peaks of air with tissue and tissue with slide whereas generally these reflections are too close and overlap. Alternatively, there may be a physical separation between the tissue and the slide creating this secondary peak in signal B. This behavior of the measurement in the region of interest is even more pronounced in Sample 2, where the signal of point B in Fig. 13b occurs even earlier and the peaks are more pronounced.

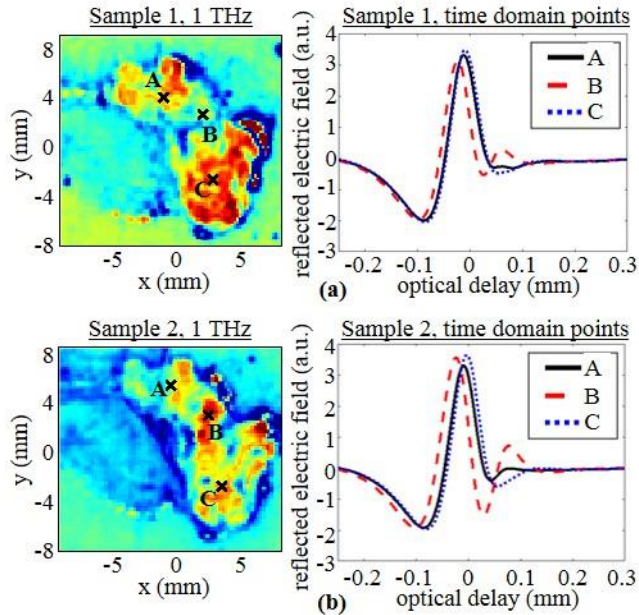


Figure 13. Single point reflection comparison for three selected points A, B, C in lobular carcinoma scans for (a) Sample 1 and (b) Sample 2.

In order to determine whether the adhesion of the tissue to the slide is the problem in the selected samples, in depth images referred to as the B-scan are obtained across different lines on the imaging scan with the optical delay serving as the vertical axis as shown in Fig. 14. From this view of the imaging it is possible to note the areas where the tissue has separated from the polystyrene slide. The B-scan images of the two samples are shown in Fig. 14a for Sample 1 and in Fig. 14b for Sample 2. Here the scan of each section is observed using an x - z axis cross-section taken at the indicated lines in the 1 THz frequency image of the reflection. In all B-scan images, the red interface indicates to the surface of the tissue with the air below. In looking at the B-scan images, Sample 1 only has two small noticeable spots where the surface of the tissue seems discontinuous in the third and fourth cross sections. However, these spots are at the far right edge of the lobular carcinoma where the separation of the tissue has also been observed in the time domain images of Fig. 10. For Sample 2 in Fig. 14b, the B-scan images show relatively larger discontinuous spots in the first and second cross-sections. However, the separation observed in the first cross section occurs at the edge of the tissue. On the other hand, the second cross section

shows potential separation of the tissue from the slide inside the carcinoma region. This corresponds to position 3 in the high power pathology in Fig. 12, where the collagenous tissue dominates, indicating to possible need for additional treatment of the sample prior to THz imaging.

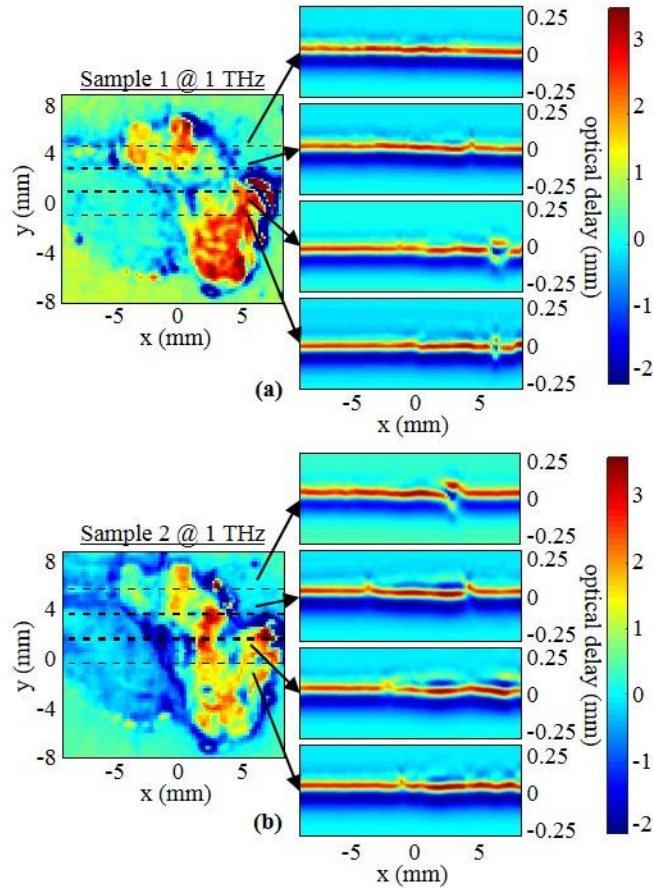


Figure 14. B-scan reflection imaging used to investigate tissue adhesion to polystyrene slides for (a) Sample 1 and (b) Sample 2 of lobular carcinoma. Color bars indicate electric fields in B-scan images on the right in arbitrary unit (a.u.).

5.1.2. Calculation of refractive index and absorption coefficient of LC

The absorption coefficient and refractive index of the lobular carcinoma samples are calculated for Sample 1 using three tissue experimental setups: the transmission in Fig. 3, the reflection in Fig. 4a where the THz incident signal interacts with the tissue first, and the reflection in Fig. 4b where the THz signal interacts with the polystyrene slide first. All images in Fig. 15 are

obtained at 1 THz. Fig. 15a and 15b show the results based on solving equations (3) and (4), the refractive index and absorption coefficient using the transmission setup. The results in Figs. 15c-d and Figs. 15e-f show the solution of equations (8) and (9) using the setups in Fig. 4a and Fig. 4b, respectively.

In order to solve for the properties of the lobular carcinoma using transmission, special consideration has to be taken for the nonuniform thickness of the polystyrene slide. This varying thickness across the slide, although in microns, causes a non-negligible phase variation in the measured signal that overwhelms the smaller phase differences from different tissue regions on the 30 μm tissue. In order to account for this artifact phase, the thickness of the polystyrene outside of the tissue is estimated using the phase shift in the polystyrene alone (without tissue) and is interpolated beneath the tissue. The solved refractive index in Fig. 15a shows consistently higher values in the lobular carcinoma than in the healthy tissue. The absorption coefficient in Fig. 15b shows expected low values in the lobular carcinoma and fibroglandular tissue regions due to the lack of water in the tissue while the absorption coefficient in the fatty/fibroglandular mixed tissue region is shown to be insignificant.

The solution of the refractive index using the first reflection orientation in Fig. 15c demonstrates the sensitivity of the solution to the reflection phase. In this instance the solved refractive index shifts from high values in the upper right to lower values on the bottom left of the image due to variations in the slide surface thickness. While the variation in phase in the transmission mode could be estimated and accounted for, the reflection mode is significantly more sensitive to this phase variation as shown in Fig. 15c compared with 15a. As a result, the absorption coefficient solution in Fig. 15d is also poor in this case. The solution in Fig. 15e using the second reflection setup in Fig. 4b shows better images compared with Figs. 15c-d. However, the solution

of the absorption coefficient in Fig. 15f shows the same issue as Figs. 15b and d. Similar results are obtained using Sample 2 in addition to using the sandwiched setup in Fig. 4c (not shown here). It should be noted that there are no reported properties of lobular carcinoma in this frequency range for either fresh or FFPE tissue to compare with.

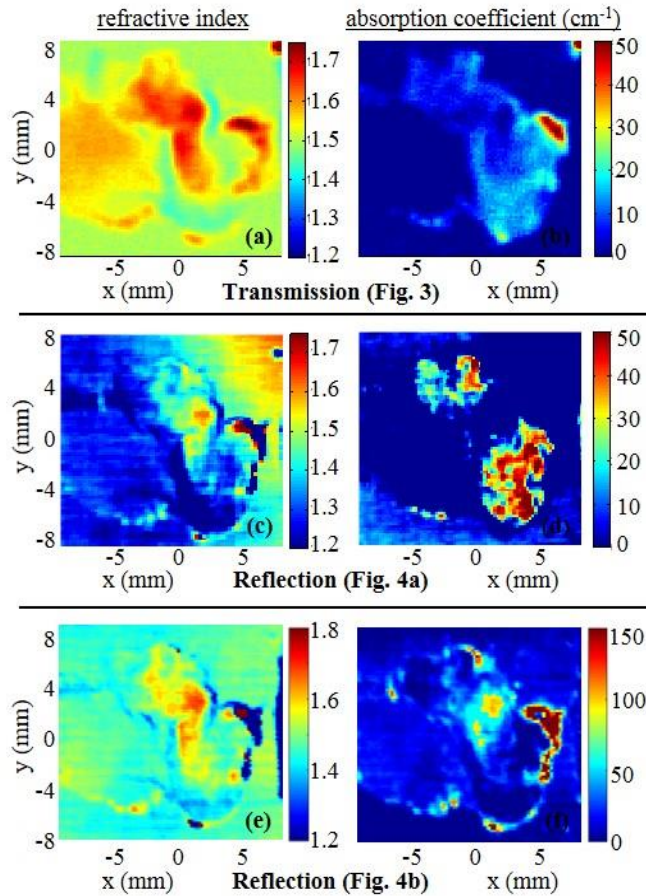


Figure 15. Comparison between transmission and reflection solutions for Sample 1 of lobular carcinoma using (a),(b) transmission imaging following configuration in Fig. 3, (c),(d) reflection imaging with tissue facing the incident signal following configuration in Fig. 4a, and (e),(f) reflection imaging with the polystyrene slide facing the incident signal following configuration in Fig. 4b. All frequency images are at 1 THz.

While the THz reflection and transmission images in Figs. 10 and 11 clearly demonstrate the contrast between lobular carcinoma and fibroglandular tissue regions in both time and frequency domains, the calculated solution images in Fig. 15 lack clear boundaries between the

two regions, especially in the absorption coefficient images. These poor results of the refractive index and absorption coefficients could be explained by the insufficient thickness of the tested tissue. It should be noted that the work published in [11] for THz imaging of dehydrated liver cancer tissue used slices of 200 μm thickness, and the work in [17] for THz imaging of freshly sliced breast tumors used 500 μm thickness. While the 30 μm tissue used in this work is sliced at the histology lab of NWA Pathology Associates using standard microtome, it is not a typical histopathology routine and has caused challenges in adhesion with the polystyrene slides as shown in Fig. 14. Slicing even thicker sections requires special equipment and special treatment of the slides to resolve the adhesion problem. Possible use of a vibratome for slicing thicker tissue up to 500 μm will be used in future work in addition to treating the slides with poly-L-lysine and ozone activation.

5.2. Case 2: Infiltrating ductal carcinoma (IDC)

5.2.1. Transmission and reflection images of IDC

Additional THz imaging was applied to 20 and 30 μm sections of the infiltrating ductal carcinoma (IDC) sample mounted on polystyrene slides. As with the sections of lobular carcinoma, 5 μm thick H&E stained slides were taken between each thick section. The histopathology and THz imaging results are shown in Fig. 16. Fig. 16a shows the pathology image of Sample 1, which corresponds to a 20 μm thick section, and Fig. 16b shows the pathology image of Sample 2 corresponding to a 30 μm section. The H&E slides are highly similar and indicate the IDC region with dark purple stain on the right, while the clear or pink stain on the left indicates healthy fatty/fibroglandular tissue. The more defined pink traces show areas of dense, fibrous collagen in the fatty tissue. It should be noted that the images of Fig. 16 are smaller than that of Fig. 10 due to the IDC sample being 2 cm \times 2 cm compared to the 1.5 cm \times 2.5 cm of the lobular carcinoma.

Several points designated 1-6 are selected in the histopathology of Section 2 shown in Fig. 16b for more detailed examination later in Fig. 18.

The time domain THz imaging of the samples in reflection mode can be seen in Fig. 16c for Sample 1 and Fig. 16d for Sample 2. As with the lobular carcinoma in Fig. 10, the carcinoma region in the pathology corresponds to a notably stronger reflection in the THz image. The contrast between the IDC and surrounding fatty/fibroglanular tissue is more apparent in the 30 μm section

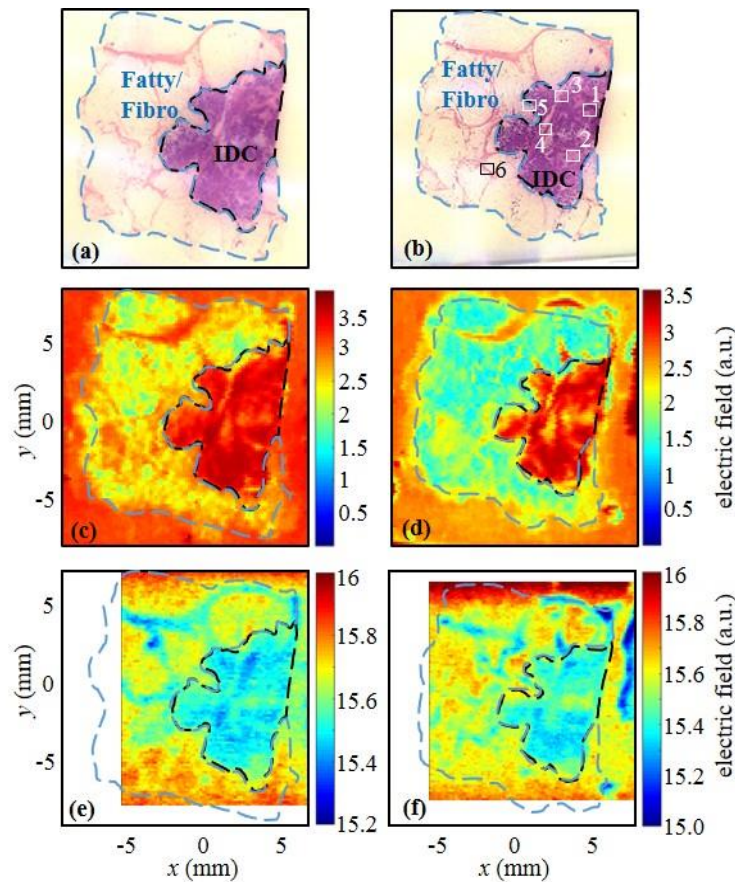


Figure 16. Reflection and Transmission images of infiltrating ductal carcinoma samples obtained from 39-year-old woman. Pathology of (a) Sample 1 and (b) Sample 2 with regions designated by outlines for infiltrating ductal carcinoma (black) and fatty/fibroglanular (blue) tissue. Points 1-6 are indicated for high power pathology assessment to be shown in Fig. 18. Reflection peak time domain images are shown for (c) Sample 1 and (d) Sample 2. Transmission peak time domain images are shown for (e) Sample 1 and (d) Sample 2. Blank areas in the transmission images (e-f) represent the smaller scanning ranges (window size) in the transmission module in the measurement system used in this work, which is not the case for the reflection module in the system.

in Fig. 16d compared to the 20 μm section in Fig. 16c, showing the improvement of the THz imaging as the thickness increases. THz imaging in the transmission mode is shown in Fig. 16e for Sample 1 and in Fig. 16f for Sample 2. Here the tissue shows lower transmission for the IDC compared to healthy tissue in agreement with the lobular carcinoma in Figs. 10e and 10f, although it lacks details apparent in the reflection imaging in Figs. 16c and 16d.

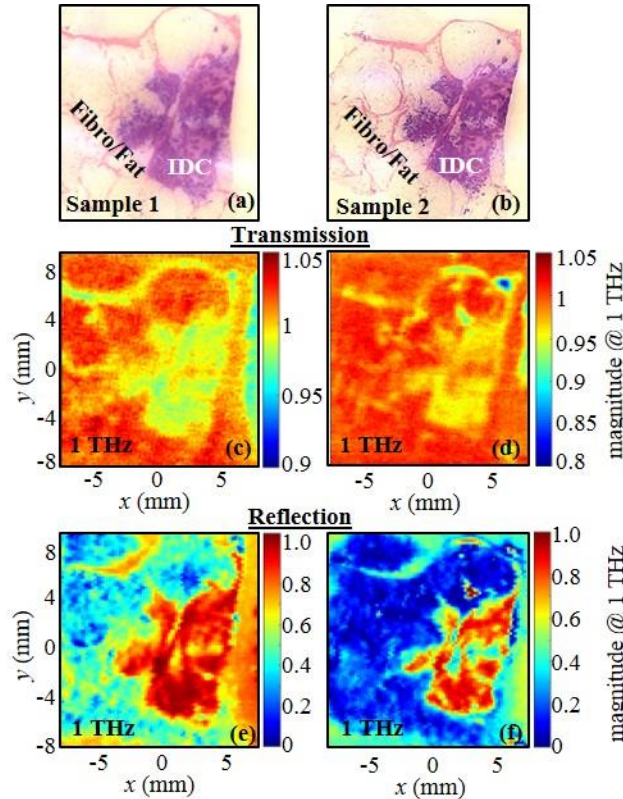


Figure 17. Frequency domain images of infiltrating ductal carcinoma. Pathology given for (a) Sample 1 and (b) Sample 2. Transmission magnitude images at 1 THz for (c) Sample 1 and (d) Sample 2 following the configuration in Fig. 3 and reflection magnitude images at 1 THz for (e) Sample 1 and (f) Sample 2 following the configuration in Fig. 4a.

Frequency domain images of the IDC sections are shown in Fig. 17. Unlike Fig. 11, only 1 THz images are shown here due to high frequency noise arising from multiple reflections in the slides used for these sections. Following the histopathology images in Figs. 17a and 17b, the 1 THz transmission image is shown for Sample 1 in Fig. 17c and Sample 2 in Fig. 17d. The region

of IDC can be seen more clearly than in the time-domain transmission images of Figs. 16e and 16f due to removing noise at higher frequencies. In particular, divisions in the IDC region become visible in the frequency domain in agreement with the pathology.

The transmission results show good consistency with the transmission through the lobular carcinoma in Figs. 11c-f. THz reflection images in Figs. 17e and Fig. 17f also show improved detail of the cancer edge as well as revealing interior details of the IDC region that can be seen in the pathology slides. The improved contrast and notable higher reflection is consistent with the lobular carcinoma in Figs. 11g-j.

In order to further examine the details of the interior of the IDC, high power pathology images were taken at the points indicated in Fig. 16b. The resulting 100X magnification images are shown in Fig. 18. Here the primary IDC region consists of the dark purple stained epithelial cancer cells seen in the top half of position 1. Pink streaks in the middle of the cancer indicate fibrous desmoplasia induced by the cancer, indicating a scirrhous tumor. Larger regions of lighter staining like in position 2 indicate mostly fibrous regions on the interior of the tumor. One notable feature in the histopathology of Fig. 16b and in the frequency domain images of Fig. 17f is the large split in the IDC region. This can be seen in position 3 where a blood vessel surrounded by

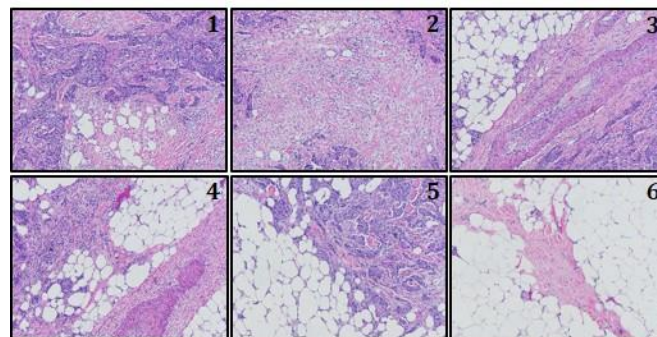


Figure 18. High power pathology (100X) of positions 1-6 indicated in Fig. 16b, showing neoplastic epithelial cells in position 1, interior fibrous tissue in position 2, blood vessels and fatty tissue dividing the IDC in positions 3-4, the edge of the epithelial cells with surrounding fat in position 5, and fibrous mature collagen in fatty tissue in position 6.

fibrous tissue in the center of the image divides the cancer in the lower right and fatty tissue in the upper left, and it is seen again in position 4 with the blood vessel in the lower right arising in the split, along with fatty tissue on both sides. While this split was not clear in the time domain images of Figs. 16c and 16d, the 1 THz images in Fig. 17f show the separation in IDC regions clearly that can be attributed to the blood vessel and fat. The edge of the IDC with the surrounding fat tissue is shown in position 5, which is clear in all THz images in Figs. 16 and 17. Finally the pink regions in the fatty/fibrogladular tissue are mature collagen, seen in position 6 and shown in the time domain image of Fig. 16d.

In the same manner that lobular carcinoma was examined for adhesion using the B-scan of the THz reflection image in Fig. 14, the two IDC samples are also investigated and presented in

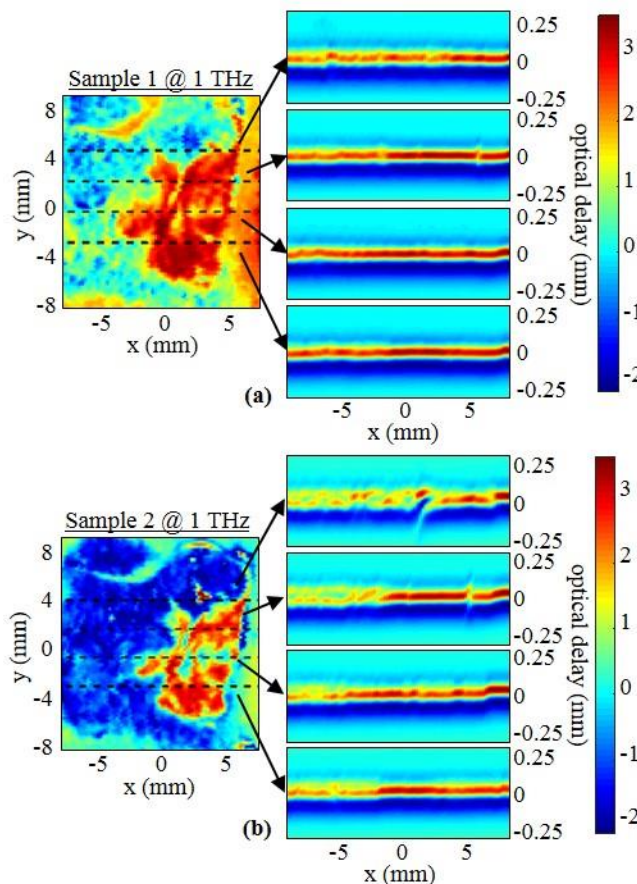


Figure 19. B-scan reflection imaging used to investigate tissue adhesion to polystyrene slides for (a) Sample 1 and (b) Sample 2 of infiltrating ductal carcinoma. Color bars indicate electric fields in B-scan images on the right in arbitrary units (a.u.).

Fig. 19. For the 20 μm section in Fig. 19a, the B-scan shows relatively little change in the surface reflection at the cross-sections indicated by the black dashed lines. Thus Sample 1 can be seen to have good adhesion that is consistent across the entire tissue section. For the 30 μm section in Fig. 19b, the first cross-section shows a clear separation of the tissue in the center, along with a small separation at the edge of the tissue on the right side that extends into the second cross-section. Additionally, the fatty/fibroglular tissue shows irregular reflections on the left side of all four cross-sections, but does not indicate any obvious separation of the tissue from the slide. This is likely due to small variations in adhesion of fibrous tissue in the fatty/fibroglular region, and it shows the difficulty in obtaining good adhesion in thicker sections as was already demonstrated for the lobular carcinoma in Fig. 14.

5.2.2. *Calculation of refractive index and absorption coefficient of IDC*

The absorption coefficient of the infiltrating ductal carcinoma samples are calculated for Sample 1 as shown in Fig. 20. The same experimental orientations of the tissue are used here similar to those used for the lobular carcinoma in Fig. 15. As observed in Figs. 15a, 15c, and 15e, the refractive index solutions in the IDC case did not demonstrate the region of IDC as distinct from the fatty/fibroglular tissue and are not presented here. This is likely due to inadequate tissue thickness and sensitivity to the polystyrene slide thickness that was often observed when the tissue thickness is comparable to the variation in slide thickness. The absorption coefficient solution shown in Figs. 20a and 20b seems to resolve the infiltrating ductal carcinoma, while the healthy tissue solution is too small to be fully resolved. This is consistent with the results seen in Figs. 15b and 15d, where the lobular carcinoma is the only tissue region that resolves the absorption. Finally the absorption coefficient calculated from the reflection experimental measurements using the orientation of Fig. 4b in Fig. 20c demonstrates the IDC region much better

than for the lobular carcinoma in Fig. 15f. However, it is noteworthy that the solution is overexpressed in regions where the adhesion of the tissue seen in the B-scan is in question in Fig. 14 for the lobular carcinoma and in Fig. 19 for the infiltrating ductal carcinoma. This is expressed in the center of the cancer in the lobular carcinoma in Figs. 15f and in the fatty/fibrogladular tissue of the infiltrating ductal carcinoma in Fig. 20c.

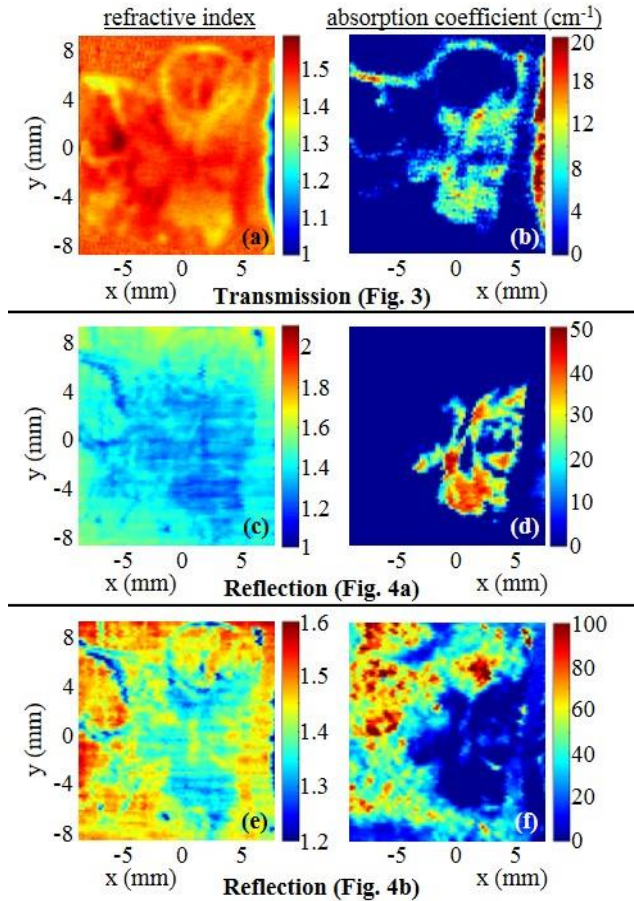


Figure 20. Comparison between transmission and reflection solutions of the absorption coefficient for Sample 1 of infiltrating ductal carcinoma using (a) transmission imaging following configuration in Fig. 3, (b) reflection imaging with tissue facing the incident signal following configuration in Fig. 4a, and (c) reflection imaging with the polystyrene slide facing the incident signal following configuration in Fig. 4b. All frequency images are at 1 THz.

Overall the conclusion based on results of the infiltrating ductal carcinoma show strong agreement with the results already seen in the lobular carcinoma. The carcinoma in both cases

shows strong contrast in the THz band against healthy tissue with higher reflection and more absorption in transmission mode. While the classification of the tissue remains subject to poor adhesion and sensitivity to slide thickness, THz imaging is shown to be effective for detecting the cancer even without the key contrast factor of the water content.

6. Discussion and Conclusion

The results demonstrated that THz imaging is capable of clearly differentiating the margins of both lobular carcinoma and infiltrating ductal carcinoma from surrounding fibroglandular and fatty tissue for the dehydrated tissues used in this work. THz imaging in both transmission and reflection modes proved successful with some key differences between the two modes. Although transmission imaging show less image resolution due to possessing fewer focusing elements in the THz beam path, the calculation of tissue properties in transmission mode showed less sensitivity to tissue adhesion that can cause variation in phase. By comparison, the reflection imaging showed a higher imaging resolution and is a more suitable mode for imaging fresh tissue, as has been seen in skin cancer imaging. [13] Additionally, the increased resolution and sensitivity of the THz reflection imaging allowed for better differentiation of heterogeneous areas inside the carcinoma that compared well with high power pathology images. Reflection imaging has shown the ability to distinguish not just the carcinoma from healthy tissue, but also to show contrast between different densities of cancer cells.

Identifying the polarization of the THz beam in the reflection mode was a challenge due to the use of multiple parabolic mirrors to direct and focus the beam. However, modeling the polarization angle of the beam and comparing against experimental data led to a good estimation of the hybrid polarization of TE and TM modes. This hybridized polarization was successfully validated on fresh bovine tissue.

Numerical challenges are observed in calculating the refractive index and absorption coefficient in the FFPE tumor cases due to the small thickness of the tissue compared with the polystyrene slide. Basically, the dehydrated tissue is considered a weak scatterer compared to the slide used to support the tissue leading to poor solutions. These problems could be resolved using thicker tissue sections and slide treatment to enhance tissue adhesion in future work.

While the current work does not address breast cancer margin assessment directly, it does represent a step forward in the methodology for eventual application while addressing some of the practical challenges in determining the origin of tissue contrast. Implementing the above techniques on freshly excised breast tumors requires moving the technology to the hospital similar to the work by Fitzgerald *et al.* [18]. Implementing the THz techniques into future clinical practice will require more research and clinical trials.

Appendix A

All modeling in this work is based on the impedance and reflection across a multiple layered system [34], [35]. This results in a term based on reflection coefficients at the interfaces ρ_{ij} and propagation terms through each region in the form of $\exp\left(-j2\frac{\omega}{c}\tilde{n}_1\cos\theta_1d_1\right)$, where i and j represent the layers across the interface as seen in equations (2) and (5). For the transmission mode the signal has a normal incidence $\theta_i = 0$, however, for oblique incidence at 30° , the reflection coefficients of each region rely on the polarization of the beam. In (5), where Γ_T uses the following expressions for the *TE* mode

$$\rho_{T,ij} = \rho_{TE,ij} = \frac{\tilde{n}_i \cos \theta_i - \tilde{n}_j \cos \theta_j}{\tilde{n}_i \cos \theta_i + \tilde{n}_j \cos \theta_j}, \quad (10)$$

and the following expression for the *TM* mode

$$\rho_{T,ij} = \rho_{TM,ij} = \frac{\tilde{n}_i \cos \theta_j - \tilde{n}_j \cos \theta_i}{\tilde{n}_i \cos \theta_j + \tilde{n}_j \cos \theta_i}. \quad (11)$$

Funding

National Science Foundation (NSF) (MRI 1228958, 1408007, DGE-1450079); University of Arkansas DDF.

Acknowledgments

The Authors would like to thank the staff at Northwest Arkansas Pathology Associates, P.A., for providing tissue and histopathology services for the carcinoma. The Authors would also like to thank Dr. Keith Bailey, Clinical Associate Professor and Comparative Pathologist at Oklahoma State University, for additional pathology assessment.

References

- [1] P. U. Jepsen, D. G. Cooke, and M. Koch, "Terahertz spectroscopy and imaging - Modern techniques and applications," *Laser Photon. Rev.* 5, 124–166 (2011).
- [2] Y. C. Shen, T. Lo, P. F. Taday, B. E. Cole, W. R. Tribe, and M. C. Kemp, "Detection and identification of explosives using terahertz pulsed spectroscopic imaging," *Appl. Phys. Lett.* 86, 1–3 (2005).
- [3] R. Ulbricht, E. Hendry, J. Shan, T. F. Heinz, and M. Bonn, "Carrier dynamics in semiconductors studied with time-resolved terahertz spectroscopy," *Rev. Mod. Phys.* 83, 543–586 (2011).
- [4] N. M. Burford, M. El-Shenawee, C. B. O’Neal, and K. J. Olejniczak, "Terahertz Imaging for Nondestructive Evaluation of Packaged Power Electronic Devices," *Int. J. Emerg. Technol. Adv. Eng.* 4, 395–401 (2014).
- [5] S. Fan, Y. He, B. S. Ung, and E. Pickwell-MacPherson, "The growth of biomedical terahertz research," *J. Phys. D. Appl. Phys.* 47, 374009 (2014).
- [6] P. H. Siegel, "Terahertz technology in biology and medicine," *IEEE Trans. Microw. Theory Tech.* 52, 2438–2447 (2004).
- [7] Y. Sun, M. Y. Sy, Y.-X. J. Wang, A. T. Ahuja, Y.-T. Zhang, and E. Pickwell-Macpherson, "A promising diagnostic method: Terahertz pulsed imaging and spectroscopy.," *World J. Radiol.* 3, 55–65 (2011).
- [8] D. Y. S. Chau, A. R. Dennis, H. Lin, J. A. Zeitler, and A. Tunnacliffe, "Determination of Water Content in Dehydrated Mammalian Cells Using Terahertz Pulsed Imaging: A Feasibility Study," *Curr. Pharm. Biotechnol.* 17, 200–207 (2016).

- [9] M. H. Arbab, D. P. Winebrenner, T. C. Dickey, A. Chen, M. B. Klein, and P. D. Mourad, "Terahertz spectroscopy for the assessment of burn injuries in vivo.," *J. Biomed. Opt.* 18, 077004 (2013).
- [10] S. Sy, S. Huang, Y.-X. J. Wang, J. Yu, A. T. Ahuja, Y.-T. Zhang, and E. Pickwell-MacPherson, "Terahertz spectroscopy of liver cirrhosis: investigating the origin of contrast.," *Phys. Med. Biol.* 55, 7587–7596 (2010).
- [11] Y. Miura, A. Kamataki, M. Uzuki, T. Sasaki, J. Nishizawa, and T. Sawai, "Terahertz-wave spectroscopy for precise histopathological imaging of tumor and non-tumor lesions in paraffin sections.," *Tohoku J. Exp. Med.* 223, 291–296 (2011).
- [12] C. S. Joseph, A. N. Yaroslavsky, V. A. Neel, T. M. Goyette, and R. H. Giles, "Continuous wave terahertz transmission imaging of nonmelanoma skin cancers," *Lasers Surg. Med.* 43, 457–462 (2011).
- [13] R.M. Woodward, B.E. Cole, V.P. Wallace, R.J. Pye, D.D. Arnone, E.H. Linfield, and M. Pepper, "Terahertz pulse imaging in reflection geometry of human skin cancer and skin tissue," *Phys. Med. Biol.*, vol. 47, no. 21, pp. 3853-3863, 17 October 2002.
- [14] P. Doradla, K. Alavi, C. Joseph, and R. Giles, "Detection of colon cancer by continuous-wave terahertz polarization imaging technique," *J. Biomed. Opt.* 18, 090504 (2014).
- [15] S. J. Oh, S.-H. Kim, Y. Bin Ji, K. Jeong, Y. Park, J. Yang, D. W. Park, S. K. Noh, S.-G. Kang, Y.-M. Huh, J.-H. Son, and J.-S. Suh, "Study of freshly excised brain tissues using terahertz imaging.," *Biomed. Opt. Express* 5, 2837–42 (2014).
- [16] T. C. Bowman, M. El-Shenawee, and L. K. Campbell, "Terahertz Imaging of Excised Breast Tumor Tissue on Paraffin Sections," *IEEE Trans. Antennas Propag.* 63, 2088–2097 (2015).
- [17] P. C. Ashworth, E. Pickwell-MacPherson, E. Provenzano, S. E. Pinder, A. D. Purushotham, M. Pepper, and V. P. Wallace, "Terahertz pulsed spectroscopy of freshly excised human breast cancer.," *Opt. Express* 17, 12444–12454 (2009).
- [18] A.J. Fitzgerald, V.P. Wallace, M. Jimenez-Linan, L. Bobrow, R.J. Pye, A.D. Purushotham, and D.D. Arnone, "Terahertz Pulsed Imaging of Human Breast Tumors," *Radiology*, vol. 239, no. 2, pp. 533-540, 2006
- [19] P. Y. Han, G. C. Cho, and X. C. Zhang, "Time-domain transillumination of biological tissues with terahertz pulses.," *Opt. Lett.* 25, 242–244 (2000).
- [20] A. J. Fitzgerald, E. Berry, N. N. Zinov'ev, S. Homer-Vanniasinkam, R. E. Miles, J. M. Chamberlain, and M. A. Smith, "Catalogue of human tissue optical properties at terahertz frequencies," *J. Biol. Phys.* 29, 123–128 (2003).
- [21] F. Wahaia, G. Valusis, L. M. Bernardo, A. Almeida, J. A. Moreira, P. C. Lopes, J. Macutkevicius, I. Kasalynas, D. Seliuta, R. Adomavicius, R. Henrique, and M. Lopes, "Detection of colon cancer by terahertz techniques," *J. Mol. Struct.* 1006, 77–82 (2011).

- [22] D. M. Charron, K. Ajito, J. Y. Kim, and Y. Ueno, "Chemical mapping of pharmaceutical cocrystals using terahertz spectroscopic imaging," *Anal. Chem.* 85, 1980–1984 (2013).
- [23] W. E. Baughman, H. Yokus, S. Balci, D. S. Wilbert, P. Kung, and S. M. Kim, "Observation of hydrofluoric acid burns on osseous tissues by means of terahertz spectroscopic imaging," *IEEE J. Biomed. Heal. Informatics* 17, 798–805 (2013).
- [24] S. Fan, E. P. J. Parrott, B. S.-Y. Ung, and E. Pickwell-MacPherson, "Improved Algorithm for Material Characterization by Terahertz Reflection Imaging," in *2015 40th International Conference on Infrared, Millimeter, and Terahertz Waves (IRMMW-THz)* (2015).
- [25] B. Recur, L. Frederique, B. Bousquet, L. Canioni, and P. Mounaix, "Review of Terahertz Tomography Techniques," *J. Infrared, Millimeter, Terahertz Waves* 35, 382–411 (2014).
- [26] Y. Bin Ji, S.-H. Kim, K. Jeong, Y. Choi, J.-H. Son, D. W. Park, S. K. Noh, T.-I. Jeon, Y.-M. Huh, S. Haam, S. K. Lee, S. J. Oh, and J.-S. Suh, "Terahertz spectroscopic imaging and properties of gastrointestinal tract in a rat model," *Biomed. Opt. Express* 5, 4162–4170 (2014).
- [27] J. H. Son, "Terahertz electromagnetic interactions with biological matter and their applications," *J. Appl. Phys.* 105, 102033 (2009).
- [28] T. C. Bowman, Y. Wu, A. Walter, J. Gauch, M. El-Shenawee, and L. K. Campbell, "Time of Flight THz Imaging of 3D Ex-Vivo Breast cancer Tumor Tissues," in *40th International Conference on Infrared, Millimeter, and Terahertz Waves* (2015).
- [29] T. Bowman, M. El-Shenawee, and L. K. Campbell, "Time of flight estimation for breast cancer margin thickness using embedded tumors," *Proc. SPIE* 9706, 97061V (2016).
- [30] T. C. Bowman, "Experimental Terahertz Imaging and Spectroscopy for Ex-vivo Breast Cancer Tissue," University of Arkansas (2014).
- [31] T. Bowman, M. El-Shenawee, and L. K. Campbell, "Regional spectroscopy of paraffin-embedded breast cancer tissue using pulsed terahertz transmission imaging," *Proc. SPIE* 9706, 97061W (2016).
- [32] "Breast Cancer." American Cancer Society [Online]. Available: <http://www.cancer.org/acs/groups/cid/documents/webcontent/003090-pdf.pdf> Last revised 4 May 2016.
- [33] R. Piesiewicz, C. Jansen, S. Wietzke, D. Mittleman, M. Koch, and T. Kürner, "Properties of building and plastic materials in the THz range," *Int. J. Infrared Millimeter Waves* 28, 363–371 (2007).
- [34] C. T. A. Johnk, *Engineering Electromagnetic Fields and Waves*, 2nd ed. (John Wiley & Sons, Inc., 1988).
- [35] S. J. Orfanidis, *Electromagnetic Waves and Antennas* (2013).

- [36] Z. D. Taylor, R. S. Singh, D. B. Bennett, P. Tewari, C. P. Kealey, N. Bajwa, M. O. Culjat, J. Hubschman, E. R. Brown, W. S. Grundfest, and H. Lee, "THz Medical Imaging : in vivo Hydration Sensing," *IEEE Trans. Terahertz Sci. Technol.* 1, 201–219 (2011).

Chapter 4: Terahertz Imaging of Three-Dimensional Dehydrated Breast Cancer Tumors

Reprinted by permission from Springer Customer Service Centre GmbH: Springer *Journal of Infrared, Millimeter, and Terahertz Waves* “Terahertz Imaging of Three-Dimensional Dehydrated Breast Cancer Tumors,” T. Bowman, Y. Wu, J. Gauch, L. K. Campbell, and M. El-Shenawee, © 2017. [doi: 10.1007/s10762-017-0377-y]

Abstract

This work presents the application of terahertz imaging to three-dimensional formalin fixed, paraffin embedded human breast cancer tumors. The results demonstrate the capability of terahertz for in-depth scanning to produce cross section images without the need to slice the tumor. Samples of tumors excised from women diagnosed with infiltrating ductal carcinoma and lobular carcinoma are investigated using a pulsed terahertz time domain imaging system. A time of flight estimation is used to obtain vertical and horizontal cross section images of tumor tissues embedded in paraffin block. Strong agreement is shown comparing the terahertz images obtained by electronically scanning the tumor in-depth in comparison with histopathology images. The detection of cancer tissue inside the block is found to be accurate to depths over 1 mm. Image processing techniques are applied to provide improved contrast and automation of the obtained terahertz images. In particular, unsharp masking and edge detection methods are found to be most effective for three-dimensional block imaging.

1. Introduction

Breast conservation surgery, also called lumpectomy, involves the excision of a breast cancer tumor with a margin of healthy tissue. The excised tumor is then processed by a pathologist, which could take several days, in order to determine whether there is any cancer remaining on the surgical edge, denoting a positive margin [1]. Once positive margins are detected, a second surgery is required to remove the remaining cancerous tissues. Even with modern techniques, positive margin rates are reported to be as high as 20-40% [2]. To minimize the need for second surgery, it

is necessary to develop a rapid and accurate intraoperative method for margin assessment [3]. Terahertz (THz) imaging is proposed here to investigate the margins of excised tumors.

While THz imaging has proven potential providing contrast between breast cancer and healthy tissue in both fresh and formalin-fixed, paraffin-embedded (FFPE) tumors [4]-[7], all published work was performed on flat sections of the tumor. While the ultimate goal is to investigate the margins of freshly excised tumors, here we focus on excised dehydrated tumors fixed in formalin and embedded in paraffin. To the authors' knowledge, this is the first investigation for in-depth imaging of breast tumors using THz to approach the problem of margin assessment. In addition, the investigation of paraffin tissue blocks could provide useful information for pathologists to determine the position and extent of the embedded tissue prior to the histopathology sectioning. Some of our preliminary results were presented in conference papers [8], [9]. Ongoing research is investigating THz imaging of freshly excised tumors grown in mice.

Terahertz (THz) imaging technology has been a rapidly expanding field of research for biomedical applications in recent years [10]. THz imaging and spectroscopy applications have expanded rapidly with the development of THz sources and systems [11], and research in the 0.1 to 4 THz range has been applied to a wide variety of medical conditions, showing clear contrast in assessment of liver cirrhosis [12], myocardial infarction [13], burn wounds [14], and cancer diagnosis [15]. THz is an attractive approach for biomedical applications due to having higher resolution than microwave frequencies while being shown to penetrate over a millimeter in fat [16] and through several millimeters in fixed tissue [17]. Additionally, THz imaging is sensitive to water content in tissue [18] and uses non-ionizing radiation such that it is biologically safe for in-vivo applications [19]. THz imaging has been successfully applied to cancer of the liver [13, 17],

colon [20], brain [21], skin [22], and breast [4], [5]. While the THz sensitivity to water content is one source of contrast between different kinds of cancer and adjacent healthy tissue, several investigations have shown clear differentiation of dehydrated tissues as well, showing the strong potential of THz in assessment of cancer [4], [17], [21].

In addition, image processing techniques are implemented to enhance the THz images. Within an intraoperative setting, the use of automated image generation and signal-based cancer detection will reduce both staff training needed to use the THz imager and observer bias in determining the status of the margins. Basic image processing techniques can greatly improve the visualization of THz images using intensity windowing and histogram manipulation [23], [24]. For example, the use of edge detection and region growing techniques are implemented to segment images into regions of cancer and healthy tissue [23], [25]. One automated approach for distinguishing breast cancer tissue from normal tissue region makes use of data reduction techniques together with support vector machine (SVM) classification with radial basis functions to distinguish tumor from normal tissue in excised breast tissue samples [5]. Several methods for data reduction were explored. The first utilized ten heuristic parameters that characterized time domain and frequency domain properties of the THz signals, the second made use of principal component analysis (PCA) of the THz pulses, and the third made use of the PCA of the ten heuristic parameters. The authors found that SVM classification of the top 10 principal components of yielded 92% tissue classification accuracy for the 51 tissue samples in their study. This is a very strong result given the amount of data reduction performed (from 512 time samples of the THz signal down to 10 PCA coefficients) [5]. Our group has performed preliminary work on image processing applied to THz images of breast cancer tissue to aid in the visibility of important image features such as the boundaries of cancer tissue and normal tissue [26]. In this

work, we explore additional image enhancement, edge detection, and image segmentation methods for THz images to aid in automated tissue classification.

The layout of this work will be as follows: Section 2 will address tissue sample preparation, and a description of the THz system, Section 3 will discuss signal processing used in THz images, Section 4 will present results of THz images and image processing, and Section 5 will include concluding remarks and future investigations.

2. Tissue Sample Preparation and THz Imaging System

The breast cancer tissue samples used in this work were purchased from the biobank at the National Disease Research Interchange (NDRI) or obtained from Northwest Arkansas (NWA) Pathology Associates, P.A. Samples were obtained as three-dimensional bulk FFPE tissue embedded in paraffin blocks. Following THz scanning of the tissue in blocks, the samples were sectioned at NWA Pathology into 30 μm thick slices and were mounted on glass or polystyrene slides. Histopathology assessment was performed on 5 μm thick sections sliced between each thicker sections of 30 μm and stained with hematoxylin and eosin (H&E) for validation of THz images. The tissue sections used here will be classified as follows: Sample 1 was obtained from a 54 year old patient diagnosed with Grade III/III infiltrating ductal carcinoma (IDC), Sample 2 was obtained from a 39 year old patient diagnosed with Grade III/III IDC, and Sample 3 was obtained from a 69 year old patient diagnosed with Grade II/III lobular carcinoma (LC). Samples 1 and 2 were provided by NDRI and Sample 3 was provided by NWA Pathology Associates. Histopathology images of the samples will be compared with THz images.

The THz images presented in this work were obtained by scanning the tissue using the TPS Spectra 3000 pulsed THz imaging and spectroscopy system developed by TeraView, Ltd. A

simplified diagram of the system can be seen in Fig. 1a, where an incident 800 nm laser pulse is produced by a Ti:Sapphire laser and used to excite a biased GaAs antenna. This in turn generates the time-domain THz pulse seen in Fig. 1b. In the reflection mode, the pulse is directed through a system of mirrors to focus onto the tissue sample at an incident angle of 30° , and the reflected signal is measured at a second GaAs antenna positioned at the same angle and gated by a coherent laser pulse split from the same excitation pulse. An adjustable optical delay line is used to window the measurement time domain range around the reflected signal while a rapid scan delay line is used to measure inside of that range. The tissue samples in this work are mounted on a motor-controlled imaging stage so that the reflection measurement is taken at each step in a scan. A motor step size of $200\ \mu\text{m}$ is used in this work. The generated THz signal of the system has a width of $\sim 500\ \text{fs}$ and generated output THz power of $\sim 1\ \mu\text{W}$.

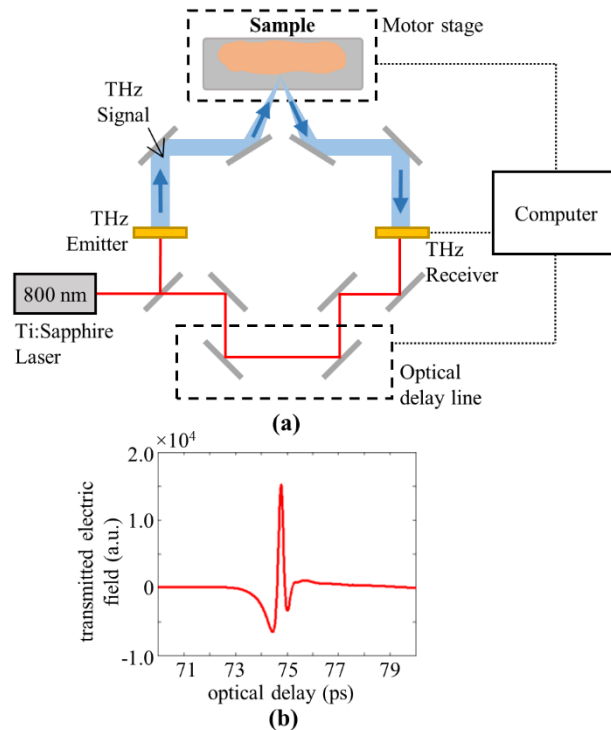


Figure 1. TPS Spectra 3000 (a) pulsed THz system diagram. (b) Generated THz time domain signal.

3. Signal and Image Processing

3.1. Time of Flight Signal Analysis

In order to quantify the ability of THz to penetrate into three-dimensional tissue, the time domain THz signal can be used to estimate the depth of features inside the block using a time of flight analysis. This is done by considering the optical path of the signal as shown in Fig. 2. The time of flight analysis is a unique capability of time domain systems for finding the thickness of multiple layers, such as the top and bottom surfaces of tissue embedded in a paraffin block. Each interface between two different regions produces a reflection peak. In this case, the primary surface reflection occurs between the air and the paraffin block, while a second reflection arises at the tissue surface at some distance z_{depth} below the surface. The measured reflection peaks are then separated by a distance of Δd on the optical delay line. This can be alternately expressed by a time delay Δt between the received reflections from the two interfaces. The time delay is proportional to double the depth of the second reflection such that

$$k\Delta t = 2z_{depth} , \quad (1)$$

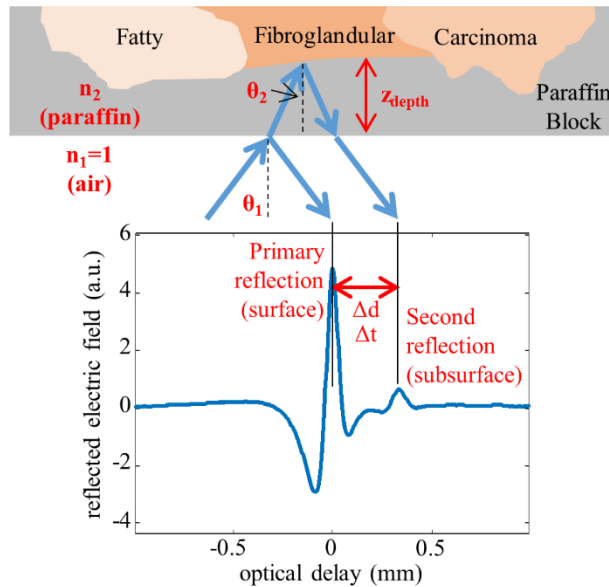


Figure 2. Multiple reflection peaks for determining feature depth in time of flight analysis.

where k is some factor accounting for the effective propagation angle $\theta_{2,eff}$ and signal velocity relating the time delay to the distance traveled in the block. Both of these factors require knowledge of the effective refractive index of the tissue block $n_{2,eff}$. While for individual materials THz spectroscopy can be used to get accurate signal properties (complex index of refraction), for unknown tissue block properties the value can be estimated by using measurements and the Fresnel reflection coefficient. The reflected signal from a mirror reference is measured to obtain the incident field E_{inc} and the reflected signal from the tissue block E_{refl} is measured and the ratio is expressed as

$$\frac{E_{refl}}{E_{inc}} = \frac{n_1 - n_{2,eff}}{n_1 + n_{2,eff}}, \quad (2a)$$

$$n_{2,eff} = n_1 \frac{(1 - E_{refl}/E_{inc})}{(1 + E_{refl}/E_{inc})}, \quad (2b)$$

where n_1 and $n_{2,eff}$ are the refractive index of air and the effective refractive index of the tissue block, respectively. Here, the measurement of the reflected signal from the tissue block (E_{refl}) is based on the peak value of the primary reflection from the surface. Depending on the depth of the tumor tissue, the value of $n_{2,eff}$ could be biased towards the refractive index of paraffin or some average of the refractive indices of paraffin, carcinoma, fibroglandular (healthy) and fatty tissues. The effective velocity of the signal in the tissue block can be calculated using $v_p = c/n_{2,eff}$, where c is the speed of light in a vacuum. Multiplying the velocity with the time delay between peaks gives an estimate of the overall signal path length. Since the signal travels at an oblique incidence, the z_{depth} at each pixel is related to the effective propagation angle $\theta_{2,eff}$ in the tissue block using Snell's Law

$$n_1 \sin \theta_1 = n_{2,eff} \sin \theta_{2,eff}. \quad (3)$$

The depth, z_{depth} , of the tissue at any given pixel can be estimated as

$$z_{depth} \cong \frac{1}{2}v_p \Delta t \cos \theta_{2,eff}. \quad (4a)$$

It should be noted that the reflected THz time domain signal is different at each pixel in the x - y cross section of the block. However, in the above discussion, all pixels are assumed to have the same $\theta_{2,eff}$ and $n_{2,eff}$ while the difference in depths is due to Δt at each pixel. This method can produce an image in the x - z or y - z cross sections. To obtain an x - y cross section image, the depth z of this cross section can be selected and the associated time t can be obtained using the following expression

$$t = \frac{2z}{v_p \cos \theta_{2,eff}} + t_0, \quad (4b)$$

where t_0 is the location of the primary peak of the reflected signal at each pixel.

The estimation of (4) relies on measuring a secondary peak and hence the time distance Δt as shown in Fig. 2. In the event that one of the tumor regions (i.e. carcinoma, fatty, or fibroglandular) is very close to the paraffin surface, the secondary signal from that particular region could be merged into the primary peak, which make estimating the depth of that particular region not possible. Also, as will be presented in the results of Section 4, the secondary reflection will not be seen at pixels located inside the same tissue region inside the tumor, however, once the tissue region changes the secondary reflection can be seen in the measurements indicating to a change in the tissue type.

3.2. Image processing techniques

3.2.1. Pre-processing

The image processing in this work converts time domain THz signals from the measurement system's file format (TeraView's TVL) to three-dimensional RAW image files so they can be visualized using the open source software package *MeVisLab* [27]. Since the TPS Spectra 3000 THz system uses step motors without encoders when collecting time domain signals,

there is some horizontal alignment error between even and odd rows of the obtained images. To remove these alignment errors, we shifted odd rows in the image by minimizing the mean squared error (MSE) between the time domain signals of each odd row and its two adjacent even rows. This aligned image is then used for further image processing.

3.2.2. Intensity mapping

One of the principal image processing techniques needed for clear scan visualization is windowing the range of image intensity values [23]. While normally this intensity range can be manually set to provide the best contrast between regions, this is a highly subjective process and can vary depending on the signal strength of the system at the time of imaging. In order to automate this process to obtain consistently high contrast between differing regions in the scan, automated intensity windowing or histogram equalization can be used [23, 24]. For automated windowing, the distribution function of the intensities in the image is calculated and the window is set to a small range of intensities centered at the main distribution peak. For histogram equalization, first the cumulative distribution function (*cdf*) of the image is calculated for L discrete intensities using

$$cdf(r_k) = \frac{1}{MN} \sum_{j=0}^k n^j, \quad (5)$$

Where $k = 1, 2, 3, \dots, (L - 1)$, L is the selected number of total intensity values in the image, $M \times N$ are the dimensions of the image, and n^j is the number of pixels with intensity r_j , or the intensity distribution at point j . The *cdf* is then remapped to a new intensity distribution with the equation

$$s_k = (L - 1) cdf(r_k). \quad (6)$$

The result of this transformation is that intensity values with fewer points in the image (less relevance) are grouped together and intensity values with more points in the image (greater

relevance) are distributed across the intensity range, providing greater contrast when the difference between tissue regions is relatively small.

One other method used in this work for visualization of the three-dimensional scans is uniform scaling. Rather than perform a histogram equalization, the intensity of the x - y cross-section at each time domain point is considered individually and rescaled from 0 to 1 based on the local maximum and minimum. Since secondary reflections inside of the tissue block are likely to be reduced from the transmission and reflection losses of the signal, this gives equal consideration to primary surface reflections and later secondary reflections in the visualization of the scan.

3.2.3. Edge sharpening

Another method for improving the visualization in THz imaging is the use of edge sharpening [23]. This is done by adding a secondary mask to the original image for all three dimensions of the scan such that $output(x, y, t) = input(x, y, t) + \alpha * mask(x, y, t)$, where α is an adjustable control variable. The mask itself is obtained by subtracting a blurred image from the input, $mask(x, y, t) = input(x, y, t) - blurred(x, y, t)$, where the blurred image is obtained by performing neighborhood averaging of the $N \times N \times N$ points centered around the position being solved. Gaussian averaging can also be used for this purpose, but was not found to show any significant difference from neighborhood averaging in this work. Edge sharpening using the blurred image to create the mask is referred to as unsharp masking.

An alternate method for calculating the mask is to apply a 3x3 Laplacian kernel, as shown in Fig. 3, to the input image. The Laplacian can be applied with (Fig. 3a) or without (Fig. 3b) the diagonal points considered in the mask, though for this work the difference between the two was found to be negligible. The resulting mask is then applied in the same manner as the unsharp masking.

0	-1	0
-1	4	-1
0	-1	0

(a)

-1	-1	-1
-1	8	-1
-1	-1	-1

(b)

Figure 3. Laplacian kernels to calculate edge sharpening mask (a) without diagonal points and (b) with diagonal points.

3.2.4. Edge detection

In addition to automated techniques for improving the visualization of the THz imaging of cancer, methods for the detection of cancer are also needed for developing accurate margin assessment. Several different edge detection techniques can be used to show clear distinction between regions for this assessment [23]. Straightforward edge detection can be performed using kernels such as Robert's Cross and Sobel operators seen in Fig. 4. The Robert's Cross operators in Fig. 4a detect differences along diagonals while the Sobel operators in Fig. 4b detect differences along the x -axis or y -axis. In both cases, the final image is obtained by taking the magnitude of the two component images created by the operators along different axes. A small amount of Gaussian smoothing prior to performing edge detection has also been shown to improve the resulting edge detection calculations.

0	-1	1	0
1	0	0	-1

(a)

-1	-2	-1	-1	0	1
0	0	0	-2	0	2
1	2	1	-1	0	1

(b)

Figure 4. Edge detection operators for (a) Robert's Cross and (b) Sobel methods.

Another robust method for performing edge detection is a classic technique known as Canny edge detection [25]. This technique works by smoothing the input image using a Gaussian filter and then finding the zero crossings of the second derivative along the gradient direction, which correspond to the maxima/minima of the first derivative. Non-maxima suppression is then

used to remove zero crossings corresponding to minima of the first derivative. Next, the gradient magnitude of the image is calculated using the Sobel operator. Any gradient value greater than an assigned threshold denotes a strong edge, while any points adjacent to a strong edge that meet a lower threshold are considered a weak edge. Finally, connectivity analysis is used to connect any strong and weak edges found in the same 3×3 neighborhood of points. Existing Canny edge detection algorithms were implemented to obtain the images in this work [28].

3.2.5. *Region growing*

Edge detection is useful for visualizing the outlines of objects in images, but in some cases there are weak or broken edges in an image, and these outlines do not fully enclose objects of interest in an image. In these cases, image segmentation techniques that focus on pixel similarity are often more effective. One classic segmentation algorithm is region growing, which starts with one or more seed points in the image defined to be cancer or healthy tissue. Then adjacent points in the image are compared to the seed points and added to the region for the defined tissue if they are found to be similar enough to the original points based on a predefined threshold or other criteria [23]. For our THz images, we have 1024 time domain samples at each (x,y) location. There are three natural choices for comparing these sample vectors: to calculate their correlation (inner product), to calculate the $L1$ norm (sum of absolute differences), or to calculate the $L2$ norm (sum of square differences). A fourth option is to compare the intensities of the peak value in each THz signal. In our experiments, the $L2$ norm was found to be most successful in growing regions corresponding to cancer or healthy tissue.

4. Results

4.1. Image processing results

4.1.1. Sample preparation

The above discussed image processing techniques are first tested on tissue sections of 30 μm thickness taken from Sample 1 and Sample 2 and mounted on microscope slides. The section from Sample 1 is mounted on glass, while the section for Sample 2 is mounted on polystyrene. THz x - y reflection imaging is taken for both samples and the resulting images are used in testing the improvement of image processing techniques. The H&E stained slides are also taken adjacent to these 30 μm sections to obtain histopathology images for validation. For the imaging performed in this work, the original THz scan of the samples took approximately 35 minutes at a step size of 200 μm . All additional processing of the dataset took less than a minute.

4.1.2. Intensity mapping

For visualizing the THz scan of the sample, histogram equalization is found to be the most effective technique for automatically scaling the intensity of the THz image. This process is shown for Sample 1 in Fig. 5. The histopathology image is shown in Fig. 5a, where the darker purple staining on the right corresponds to the region of infiltrating ductal carcinoma (IDC), while the light pink staining on the left corresponds to the healthy fibroglandular tissue. The original THz reflection image of the 30 μm is shown with inherent scaling in Fig. 5b, which shows little difference in the reflection intensities of the cancer and fibroglandular tissue. The distribution of intensities in the original image can be seen in Fig. 5c, where points are mostly grouped around the tissue reflection in the center of the intensity range with small distributions at the low and high ends of the scale primarily corresponding to the reflection from the round imaging frame and the glass slide, respectively. The use of histogram equalization significantly increases the contrast

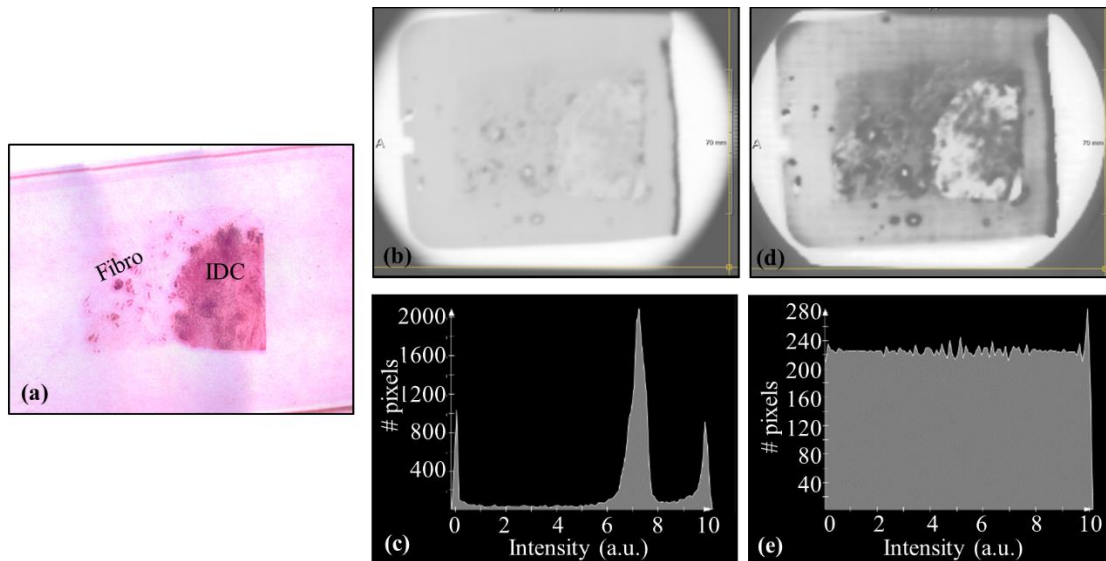


Figure 5. Histogram equalization of Sample 1 with (a) the histopathology image, (b) the original THz image, (c) the original intensity distribution, (d) THz image after equalization, and (e) intensity distribution after equalization.

between the two regions in Fig. 5d. From this process the intensity distribution has spread out to fill the entire range more evenly as shown in Fig. 5e, such that the points too close for clear contrast are given more distinction. The use of histogram equalization in scaling the intensity values of the THz image provides an automatic method for observing the contrast in between the cancer and healthy fibroglandular tissue. This effective automated technique for intensity scaling in the THz image will be useful for future imaging applications for reducing observer bias in the results.

4.1.3. Edge sharpening

In addition to histogram equalization, the scan of Sample 1 is further enhanced by edge sharpening techniques. The resulting images are shown in Fig. 6. The original histogram equalized image is shown in Fig. 6a. Unsharp masking is performed with a mask size of $5 \times 5 \times 5$ pixels and different values of α in order to obtain more clearly defined edges between regions. The results of the unsharp masking are given in Fig. 6b for $\alpha = 0.6$ and in Fig. 6c for $\alpha = 1.5$. Additionally, the Laplacian in Fig. 3b is applied in Fig. 6d for $\alpha = 0.4$ and Fig. 6e for $\alpha = 0.8$. From the results of the edge sharpening, the cancer tissue edge with the healthy tissue is seen to increase in resolution

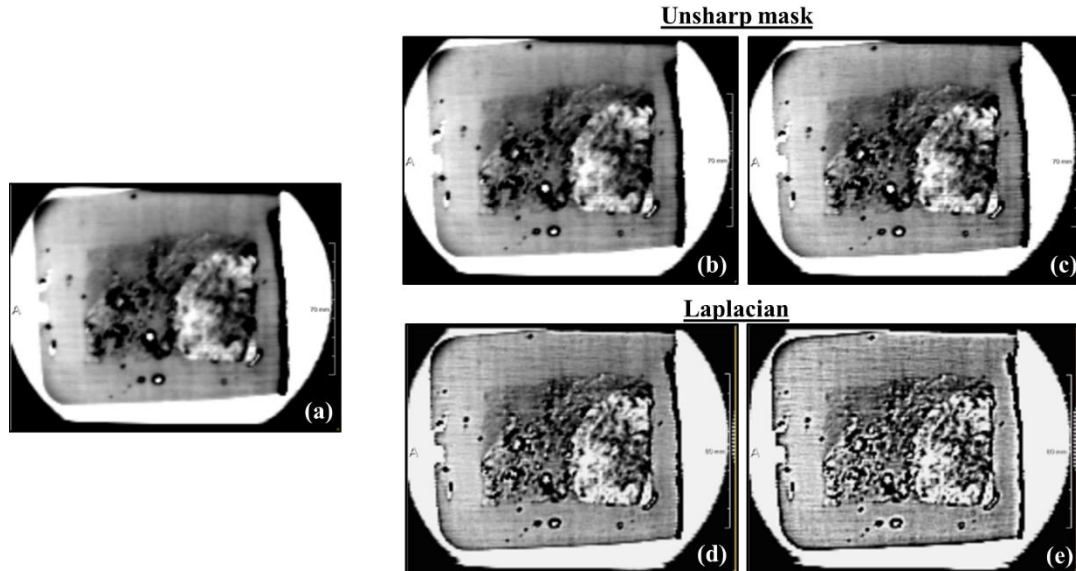


Figure 6. Unsharp masking applied to (a) original image after histogram equalization of Sample 1. (b) Unsharp masking using a factor of $\alpha = 0.6$ and (c) $\alpha = 1.5$. (d) The Laplacian mask using $\alpha = 0.4$ and (e) $\alpha = 0.8$.

in all cases. For the unsharp mask method in Fig. 6b and Fig. 6c this increase is less pronounced but provides more clear definition across the entire region. The Laplacian mask sharpening in Fig. 6d shows a more pronounced definition in the edges of the tissue regions, but has some noise starting to arise in the fibroglandular tissue. This noise begins to increase as the factor α applied to the mask increases from 0.4 to 0.8, as the resulting image in Fig. 6e shows. Due to the noise in the fibroglandular tissue it becomes difficult to differentiate between the cancer and fibroglandular regions. Thus, edge sharpening has shown to be effective in providing better definition of the edges of the tissue regions; however, care must be taken when selecting α values for this enhancement technique to avoid excessive noise amplification.

4.1.4. Edge detection

Following the image enhancement using automated methods, detection methods for differentiating breast cancer from healthy tissue are investigated. Edge detection using Robert's Cross, Sobel, and Canny methods are all shown in Fig. 7 for Sample 2. The histopathology images using 5 μm sections sliced adjacent to the 30 μm section is shown in Fig. 7a. The IDC region of

this sample can be clearly seen on the right side, while the left is primarily fibroglandular tissue. It should be noted that Sample 2 lacks the well-circumscribed border shown in Sample 1, and thus is selected here to show the effectiveness of the edge detection. The original THz image of the 30 μm section is shown using manual intensity scaling in Fig. 7b. The edge detection of the THz image using the Robert's Cross method is given in Fig. 7c. It can be seen that the area of infiltrating ductal carcinoma is clearly outlined in the THz image. Additionally, there are some edges detected on the interior of the fibroglandular region due to the difference between primarily fibroglandular or primarily fatty areas of the tissue (denoted by pink and clear areas in the pathology, respectively). However, there is no clear estimation of the edge of the fibroglandular tissue from the surrounding paraffin. The Sobel method in Fig. 7d shows similarly good definition of the edge of the IDC region, as well as showing reasonable edges around the fibroglandular region. While there are some faint edges visible within the fibroglandular region, the method accurately shows the most distinct edges at the boundaries of the tissue. The more robust Canny detection technique

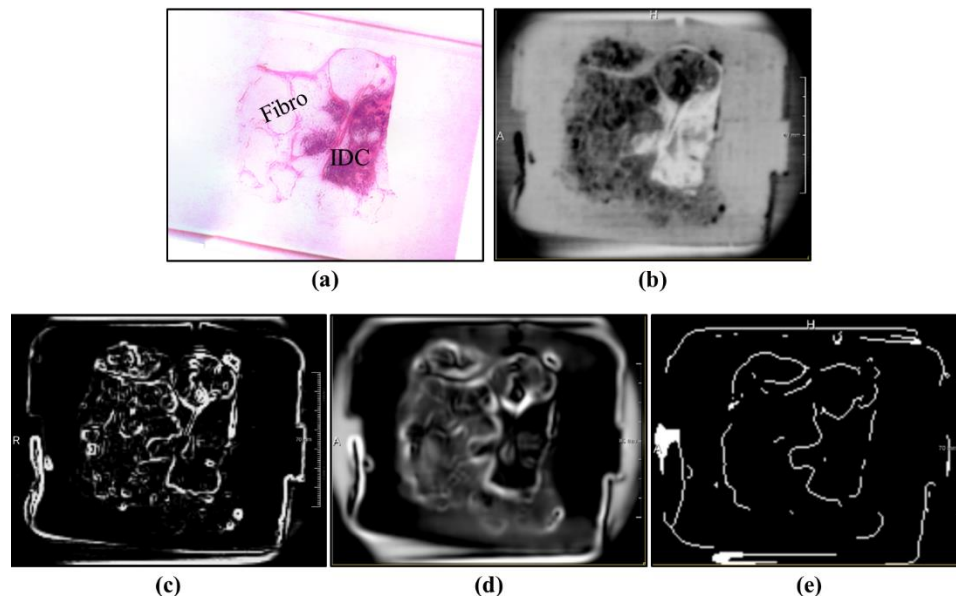


Figure 7. Edge detection of the THz reflection of Sample 2 based on (a) the sample histopathology image and (b) the THz reflection image, where the edge detection techniques are (c) Robert's Cross method, (d) Sobel method, and (e) the Canny method.

in Fig. 7e is less sensitive to features on the interior of the tissue regions and mostly outlines both the IDC and fibroglandular regions of the tissue. In this case a closed edge is not detected around the entire regions, and so it is not sufficient for an automated detection technique. However, it does provide a good visual approximation of the tissue boundaries. These results show that the edge detection techniques possess some effectiveness in distinguishing between the different regions of tissue, especially between the cancer and healthy tissue regions. Neither the Robert's Cross nor Canny edge detection showed complete borders around the fibroglandular tissue, while the Sobel operator showed good region borders with some sensitivity to edges on the interior of the fibroglandular region. It is anticipated that when fresh tissue is used, the increased contrast between cancerous and healthy tissues will improve the edge detection of the image.

4.1.5. *Region growing*

An alternative method for detection of IDC in THz images is the use of region growing. The methods discussed in Section 3.2.5 based on the peak intensity alone or the $L2$ norm of the entire THz signal are implemented for the IDC samples used in this work. The results are shown in Fig. 8. The histopathology image of Sample 1 is once again shown in Fig. 8a. The THz reflection image in Fig. 8b is overlaid with a pink region corresponding to the region growth solution based on the reflection intensity alone, while the white area in Fig. 8c shows the region grown by taking the threshold of the $L2$ norm. Here both region growing techniques provide a good detection of the edge of the cancer tissue but do not solve for the center of the IDC region. This is due to a significant amount of necrosis in the center of the IDC (based on the pathology report) that can also be seen as bright pink in the histopathology image rather than the darker purple stain of the cancer. Thus the IDC in Sample 1 is resolved well.

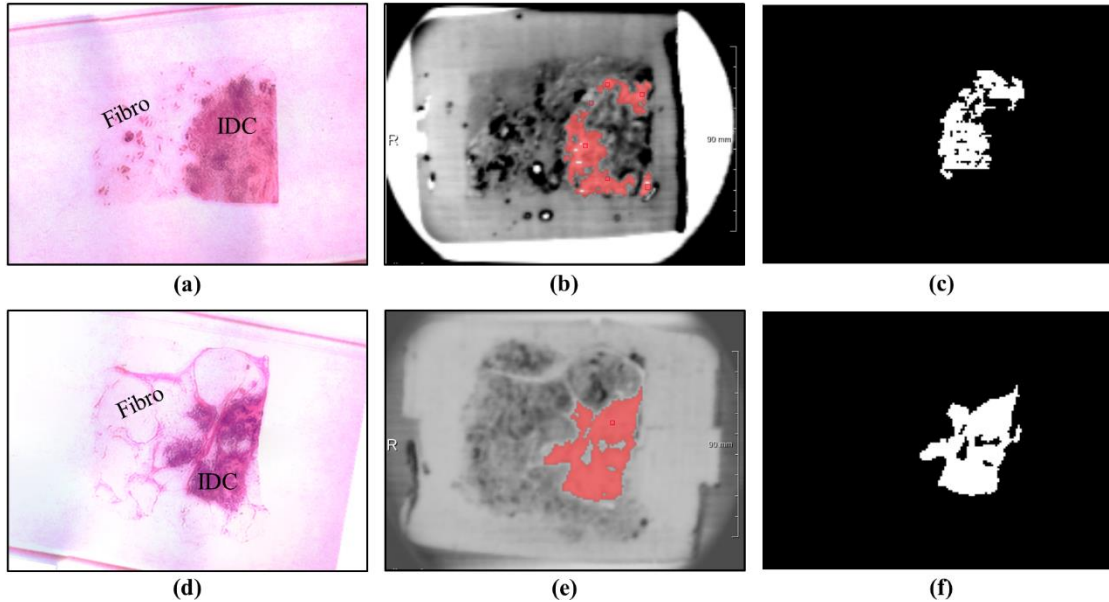


Figure 8. (a) Histopathology image of Sample 1, with (b) THz reflection image overlaid with intensity-based region growing and (c) region grown using $L2$ norm threshold. (d) Histopathology image of Sample 2, with (e) THz reflection image overlaid with intensity-based region growing and (f) region grown using $L2$ norm threshold.

The histopathology image of Sample 2 is shown in Fig. 8d. Here the region grown from the intensity peak in Fig. 8e as well as the region obtained from $L2$ mapping in Fig. 8f both show very good detection of the cancer region in these areas. These grown regions even account for the necrosis region at the center of the IDC and show a high level of accuracy against the histopathology. Therefore, while some edge detection techniques were unable to reliably resolve the boundaries of the tissue regions, a region growth method has proven effective at obtaining accurate regions that can be ascribed to the cancer in the tissue.

4.2. *Three-dimensional imaging of breast cancer tissue blocks*

The three-dimensional (3D) imaging in this work is performed on two different tissue blocks. The imaging setup can be seen in Fig. 9. Here a three-dimensional tissue block can be seen in Fig. 9a, while the sample on the scanning stage is shown in Fig. 9b. The signal from the THz system is incident from below and reflected back into the receiver. The three samples used in this work all had similar sizes prior to THz imaging ($3\text{cm} \times 2\text{cm} \times \sim 0.6\text{cm}$). However, the tumor

tissue in Sample 2 extended to the mounting cassette rather than being fully embedded. Therefore, results from only Sample 1 and Sample 3 are shown here.

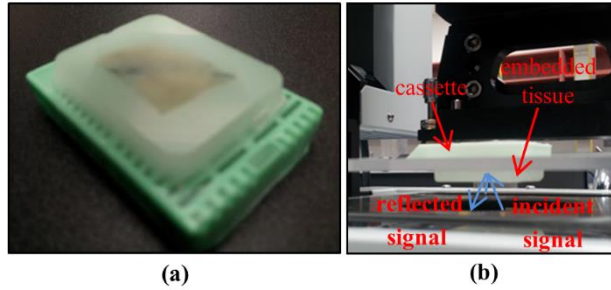


Figure 9. (a) Three-dimensional tissue block mounted on pathology cassette. (b) Tissue block mounted in THz system.

4.2.1. Sample 1: Infiltrating ductal carcinoma (IDC)

The 3D THz scan is performed on a tumor obtained from a 54 year old patient diagnosed with stage III/III infiltrating ductal carcinoma (IDC). The pathology report described the tumor as being well-circumscribed. The THz scan is performed on the tissue block both before and after facing off the block to expose the tissue. The generated 3D datasets consist of the reflected electric field measurement in the time domain (as seen in Fig. 2) at each x - y position in the scan. The time of flight estimation is used to convert the time domain values to z -axis positions. THz images are then produced by either taking the peak reflection signal at each x - y position or by showing a cross-section image for a single x -axis, y -axis, or z -axis value. The results are presented in Fig. 10. The H&E histopathology image is shown in Fig. 10a, showing the main two tissue regions of IDC indicated by the darker pink on the right and the fibroglandular region indicated by the light pink on the left of the image. Small spots of dark pink stain are shown in the fibroglandular tissue indicating to healthy lobular tissue (according to the pathology report). Before shaving the paraffin from the top of the block, $n_{2,eff}$ is calculated to be 1.512 based on (2) which represents the effective refractive index of paraffin, carcinoma, fibro, and fatty tissues. The individual refractive indices of tumor tissues were measured in our separate work [29] to be ~ 1.67 for infiltrating ductal

carcinoma, 1.52 for fibroglandular, and 1.36 for fatty tissue, and the refractive index of paraffin has been reported as 1.495 [30]. The angle of incidence in air for the THz system used in this work is fixed at $\theta_1 = 30^\circ$, and the effective angle $\theta_{2,eff}$ is calculated to be 19.3° .

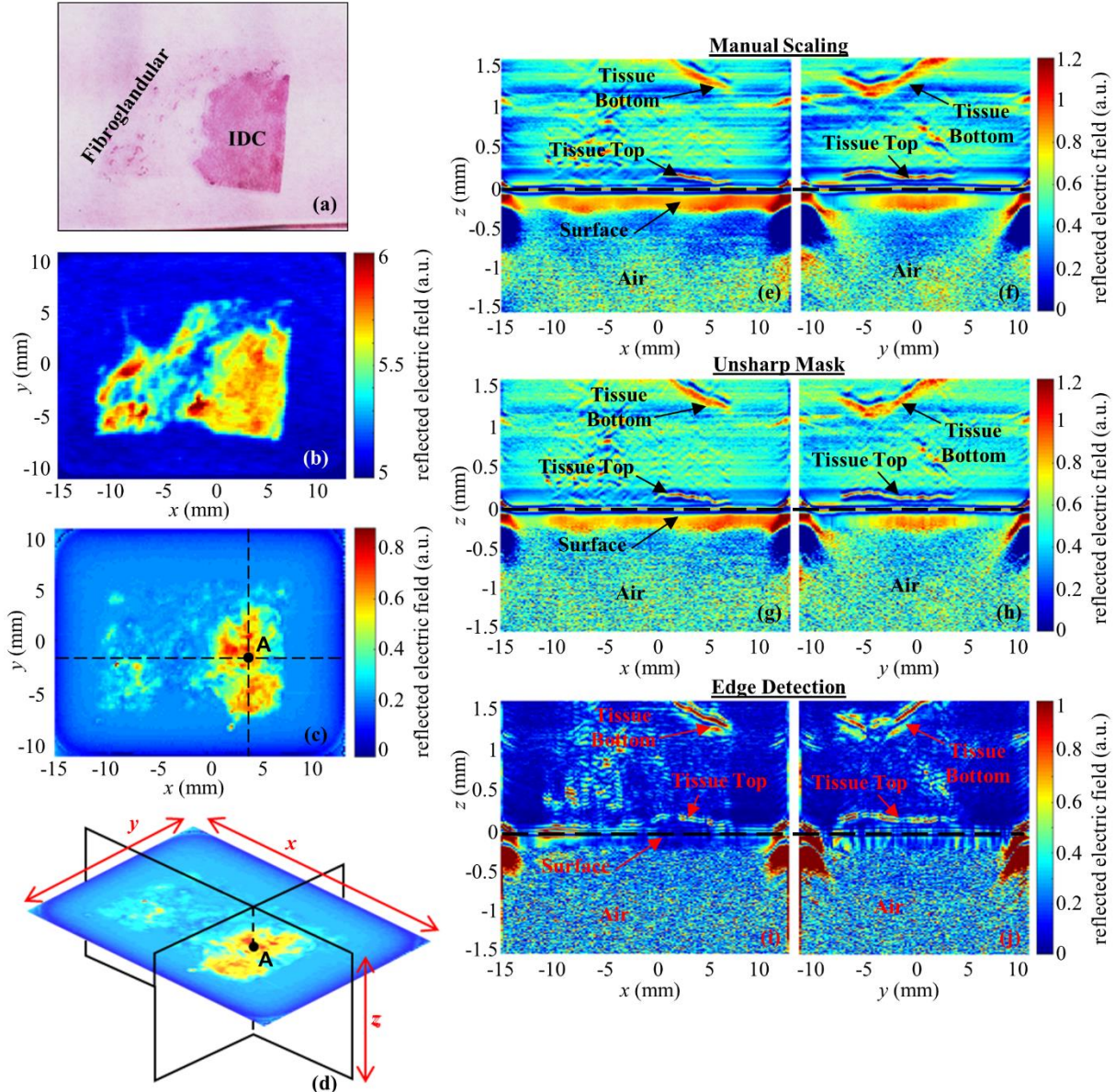


Figure 10. Imaging of Sample 1 obtained from 54 year old women with infiltrating ductal carcinoma (IDC) and embedded in paraffin block. (a) Histopathology image. (b) THz x-y cross-section image of the tumor surface from the faced-off tissue block, and (c) from the block prior to being faced off. (d) 3D diagram of z-axis cross-sections indicated by dashed lines in (c) and aligned at point A. (e) THz x-z cross-section image at the x-direction in (d). (f) THz y-z cross-section image at the y-direction indicated in (d). The x-z and y-z cross-sections are repeated using (g)-(h) unsharp mask enhancement of the THz scan and (i)-(j) edge detection of the THz scan using the Sobel operator.

Fig. 10b shows reflected signal from the surface of the faced off block with the tissue exposed in order to correlate the tissue regions to the histopathology. Here the tissue regions are clearly defined, with the IDC on the right and the fibroglandular on the left. In the faced-off block the two regions are not distinct at the surface, but the outside border of the tissue is clear. From the THz scan with the paraffin covering the tissue, the reflected peak from the surface of the tissue inside the block is shown in Fig. 10c. This image is obtained using the values of the secondary peak of the signal at each pixel in the image as discussed in Section 2. Here a significant reflection can be seen over the area of IDC on the right consistent with the histopathology image in Fig. 10a, though the full extent of the region is not as clearly outlined as in Fig. 10b. Additionally, the carcinoma shows clear contrast compared to the region of fibroglandular tissue on the left, which shows smaller reflection values. This layer can be more clearly visualized by making use of cross-section images into the depth of the block by observing the x - z or y - z planes of the scan, with the z -axis corresponding to the time domain of the measured reflection signals using the time of flight estimation technique in (5) to provide an approximation of feature depth beneath the surface of the block. This scan with the estimated z -axis depth will be referred to as the Z-scan. The dashed lines intersecting at point A in Fig. 10c show the positions where the cross-section images are taken, and further clarification is given in Fig. 10d, which shows a 3D diagram of the scan (i.e. x - z and y - z planes). Since the THz Z-scan produces a 3D dataset, these additional cross-section images take no additional time to acquire. The x - z cross-section image is shown in Fig. 10e and the y - z cross-section image is shown in Fig. 10f. The figures are oriented in the same direction as the experimental setup, with the signal coming from below to reflect off the sample such that the tissue is above the air-paraffin interface. These images make use of uniform scaling at each depth in order to highlight the secondary reflections. However, the uniform scaling increases the noise in

the air in Figs. 10e-j due to the very low signal in this region, and there is some degree of noise in the paraffin block away from the tissue interfaces as well. Reflections arise when an interface between tissue regions or between tissue and the paraffin block is encountered by the THz signal moving in the z-direction. In both cross-section views, the reflection from the block surface, from the top of the tissue, and from the bottom of the tissue are all clearly visible for the tumor, while the side walls of the tissue are at a more oblique angle with the THz signal and do not appear. The interface between paraffin and the top of the tumor is estimated using (4) to be between 150 and 200 μm , while the bottom of the tissue has a range between 1 mm and 1.5 mm. In contrast, the fibroglandular tissue region shows some distributed scattering but no clearly defined reflections outlining the entire region. This is likely due to a high similarity of the dehydrated fibroglandular tissue to the surrounding paraffin.

In order to investigate enhancement and automation of the THz imaging processing, unsharp masking and edge detection are applied to the THz scan due to their effectiveness in the imaging of tissue sections. It should be noted that while region growing is shown to be effective for tissue sections in Fig. 8, it is not found to resolve the three-dimensional block imaging well and requires more work to be implemented. The results of the unsharp mask method can be seen for the x - z and y - z cross-sections in Figs. 10g and 10h, respectively. Here the reflections from the tissue top and bottom are defined more clearly, and many of the horizontal effects in the block not corresponding to the tissue reflections are diminished. Thus the unsharp mask shows good clarification of the tissue boundaries while decreasing other effects in the signal. This effect can be seen more clearly using the automated Sobel operator as seen for the x - z and y - z cross-sections in Figs. 10i and 10j. It can be seen that any signal in the block aside from the tissue reflections is suppressed, leaving the clear reflections from the top and bottom of the tissue. This technique also

highlights the scattered reflections through the depth of the fibroglandular tissue, as seen on the left side of Fig. 10i. As a result, the boundaries and margin of the infiltrating ductal carcinoma are clearly determined in the 3D THz scan of the paraffin block in Fig. 10, and image processing shows good results in improving the visibility of the tissue at depth.

Upon facing off the tissue block, we present THz x - y cross section images in Fig.11 at a variety of estimated depths and without slicing the block. The THz images were obtained by taking the electric field value at each point for a specified z -axis value and applying uniform scaling across the image. For histopathology images, the tissue block is physically sliced to obtain 5 μm sections at each depth ($z = 0$ to 850 μm) as shown in Fig. 11. While a total of 15 histopathology sections are sliced from the block, only 4 are presented here for space limitations. The histopathology images can be seen at $z = 0$ μm in Fig. 11a, $z = 180$ μm in Fig. 11e, $z = 695$ μm in Fig. 11i, and $z = 850$ μm in Fig. 11m. In all these images the IDC is shown in darker purple staining on the right and the fibroglandular in light pink on the left. Notice in all THz images in Fig.11, only those in the first row at $z = 0$ show full distinction between the IDC and fibroglandular tissues consistent with the histopathology image in Fig. 11a. All the other THz images are produced at cross sections inside the tumor using the z -scan (without slicing), where no or little distinction between regions are observed. The reason is that at these depths, away from the surface, there are no interfaces inside the tumor and hence no reflections that would show different tissue regions in the THz images. At depths of 695 μm and 850 μm , the histopathology images start to show a decrease in the cancer regions approaching the bottom of the tumor. THz images at these depths also show the receding edge of the cancer region consistent with the histopathology images.

The unsharp mask and edge detection processing techniques are implemented on the THz data as shown in Fig. 11 in the third and fourth columns. The unsharp mask image in Fig. 11c shows

sharper details with better contrast in the tissue reflections compared with Fig. 11b. The edge detection using the Sobel operator in Fig. 11d clearly outlines the region of IDC at the surface of the tissue and provides edges of the more scattered fibroglandular tissue. Since there is no significant reflection at $z = 180 \mu\text{m}$ in the THz image in Fig. 11f, there is likewise no significant effect of the image processing in Figs. 11g-h. As the bottom reflection becomes visible in Fig. 11j, the unsharp mask method in Fig. 11k shows some improvement in the details of the bottom reflection, while the edge detection in Fig. 11l shows excellent definition of the tumor edge as the

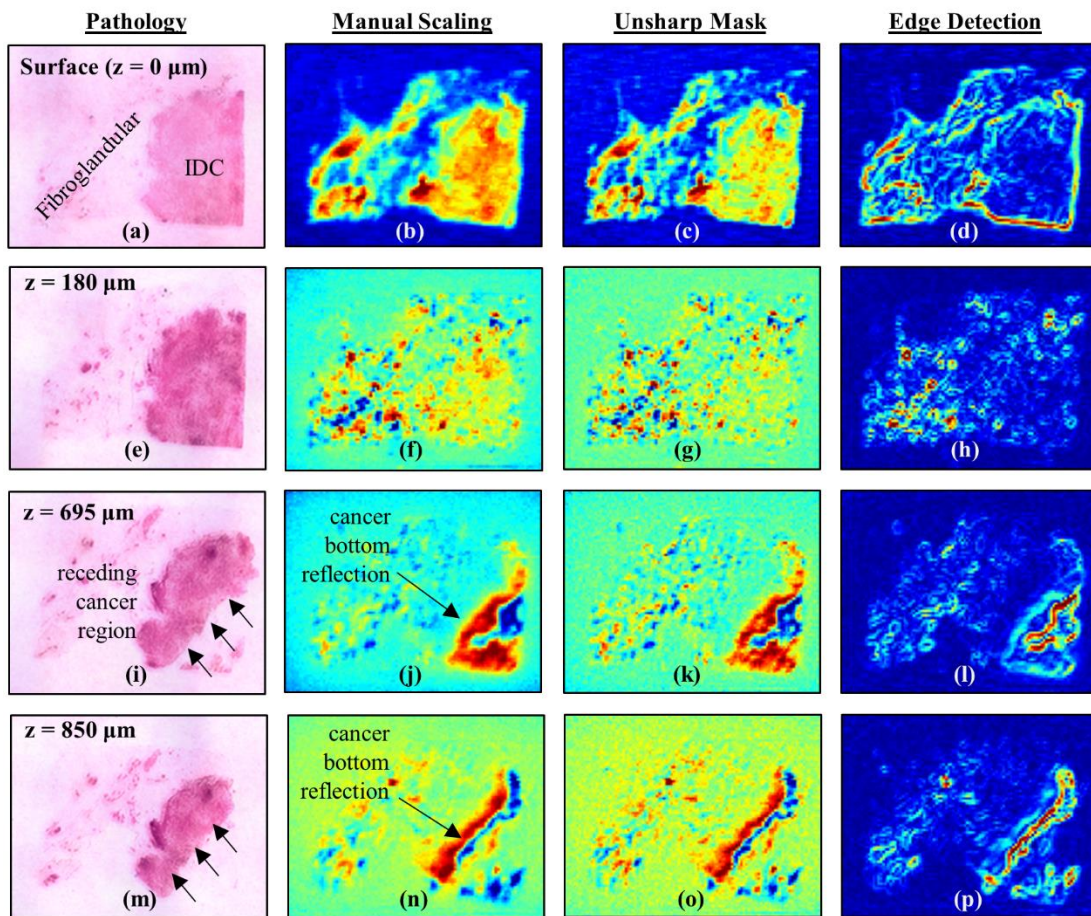


Figure 11. Comparison of histopathology images, THz Z-scan images, unsharp mask THz images, and edge detection of THz images of Sample 1. From the surface of the block where $z = 0 \mu\text{m}$, (a) the histopathology image and Z-scan images (b) with manual scaling, (c) with unsharp mask enhancement, and (d) with edge detection using the Sobel operator. This sequence is repeated at different depths (e)-(h) at $z = 180 \mu\text{m}$, (i)-(l) at $z = 695 \mu\text{m}$, (m)-(p) at $z = 850 \mu\text{m}$. All histopathology images are stained as shown in pink while all THz images are not stained and are obtained without physically slicing the tumor.

dark red line. The image processing shows similar improvement at $z = 850 \mu\text{m}$, where the unsharp mask results in Fig. 11o show improved feature resolution over the standard THz image in Fig. 11n, and the edge detection in Fig. 11p accurately defines the bottom edge of the receding tumor.

The results of Fig. 11 show the effectiveness of THz in detecting the boundaries of cancerous tissues buried in the paraffin block. These 3D THz images provide insight into the interaction of the THz signal with the heterogeneous tumor tissues.

4.2.2. Sample 3: Lobular carcinoma (LC)

The 3D THz imaging is applied Sample 3 that was obtained from a 69 year old patient diagnosed with Grade II/III lobular carcinoma (LC). The size of the block is $3\text{cm} \times 2\text{cm} \times 0.6\text{cm}$, and the block was faced off prior to THz imaging. For the time of flight estimation, $n_{z,eff}$ is calculated to be 1.488 and the angle $\theta_{z,eff}$ is calculated to be 19.64° . The results of Sample 3 are shown in Fig. 12. The histopathology image in Fig. 12a shows the clearly separate regions of the LC as the dark purple stained region on the right, the primarily fibroglandular tissue as the pink stained region on lower right part of the tissue, and fibroglandular/fatty tissue as the clear region in the top right.

The surface reflection from the tissue in the paraffin block is given in Fig. 12b, where the lobular carcinoma shows a distinctly higher reflection from the rest of the tissue, with the fibroglandular showing slightly lower reflection and the more fatty tissue appearing only slightly different from the surrounding paraffin block. The dashed lines intersecting at point A indicate the cross sections selected for looking at the tissue in-depth, which is further clarified in the 3D diagram in Fig. 12c. The in-depth cross sections of the block can be seen in in Fig. 12d for the x - z view and Fig. 12e for the y - z view of the dashed lines in Fig. 12b and imaging planes in Fig. 12c. Since the block was faced off prior to scanning, the cancer tissue is already present, the tissue

surface reflection is aligned with the block reflection. The reflection from the bottom of the tissue is estimated to be between 1.5 mm and 2 mm, though part of the reflection is seen to extend beyond the range of the Z-scan. The reflection from the bottom of the tissue is broader along the z-axis than the reflections in Sample 1 due to the increased depth of the signal in the paraffin block. The

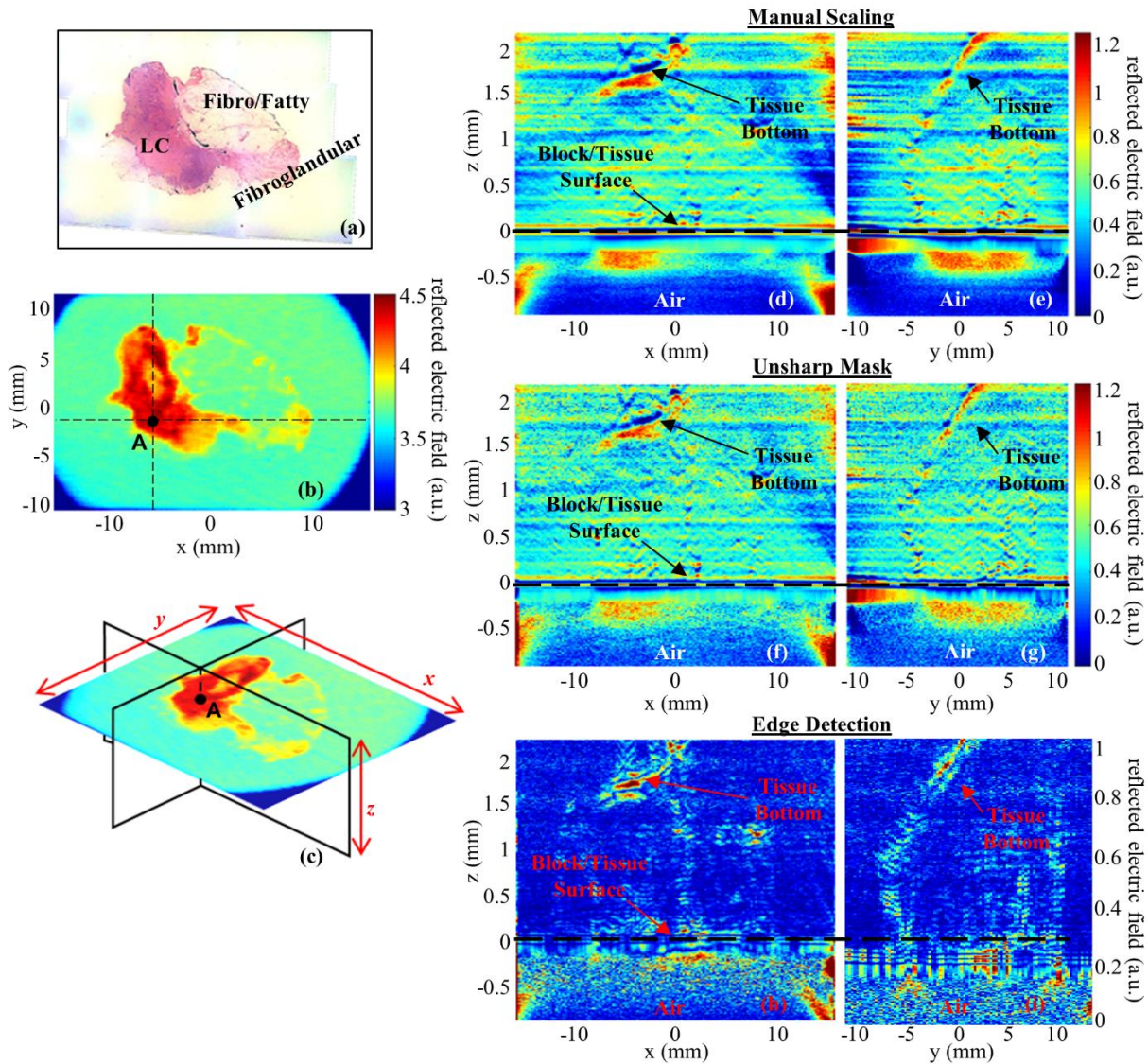


Figure 12. Imaging of Sample 3 obtained from 69 year old patient diagnosed with lobular carcinoma (LC) and embedded in faced-off paraffin block. (a) Histopathology image. (b) THz x-y cross section image from tissue surface. (c) 3D diagram of z-axis cross-sections indicated by dashed lines in (b) and aligned at point A. (d) THz x-z cross-section image at the x-direction indicated by the dashed line in (c). (e) THz y-z cross-section image at the y-direction indicated by the dashed line in (c). The x-z and y-z cross-sections are repeated using (f)-(g) unsharp mask enhancement of the THz scan and (h)-(i) edge detection of the THz scan using the Sobel operator.

use of unsharp mask enhancement in Figs. 12f and 12g shows some resolution improvement of the tissue reflection with decreased horizontal smearing but slightly increased noise. Similarly, the automated edge detection in Figs. 12h and 12i shows clear definitions of the boundary, including the very slowly receding edge of the IDC in 12i. In all cases the boundary of the cancer tissue is clearly defined at depth, with image processing showing greater clarity.

In order to correlate the THz images of the cancer boundaries deep in the block, the Z-scan of Sample 3 is compared to histopathology images taken from at several depths as shown in Fig. 13. The histopathology images are shown in Figs. 13a ($z = 0 \mu\text{m}$), 13e ($z = 1050 \mu\text{m}$), 13i ($z = 1620 \mu\text{m}$), and 13m ($z = 2000 \mu\text{m}$), which show lobular carcinoma in the dark stain region on the left, the fibroglandular tissue in the light stained region on the bottom right, and low density fibro/fatty tissue in the upper right. As with the results in Fig. 11, only the THz images in the first row of Fig. 13, which corresponds to the block surface ($z = 0 \mu\text{m}$), show the tissue regions consistent with the histopathology in Fig. 13a. The remainder of the THz images are produced at cross-sections where the signal is inside of the breast cancer tissue and show little distinction between tissue regions. This is due to the significant distance that the tissue extends into the paraffin block with no interfaces present inside the tumor, as seen by the pathology at 1050 μm . The bottom edge of the lobular carcinoma is shown in the histopathology at 1620 μm and 2000 μm as the cancer region recedes. The THz images at these depths show the same receding edge of the carcinoma, demonstrating good agreement with the histopathology. In this case the reflection is not seen as clearly as in Sample 1 due to the reflection being much deeper in the block and due to the steepness of the bottom of the tissue, which can also be seen in Figs. 12d and 12e compared to Fig. 10.

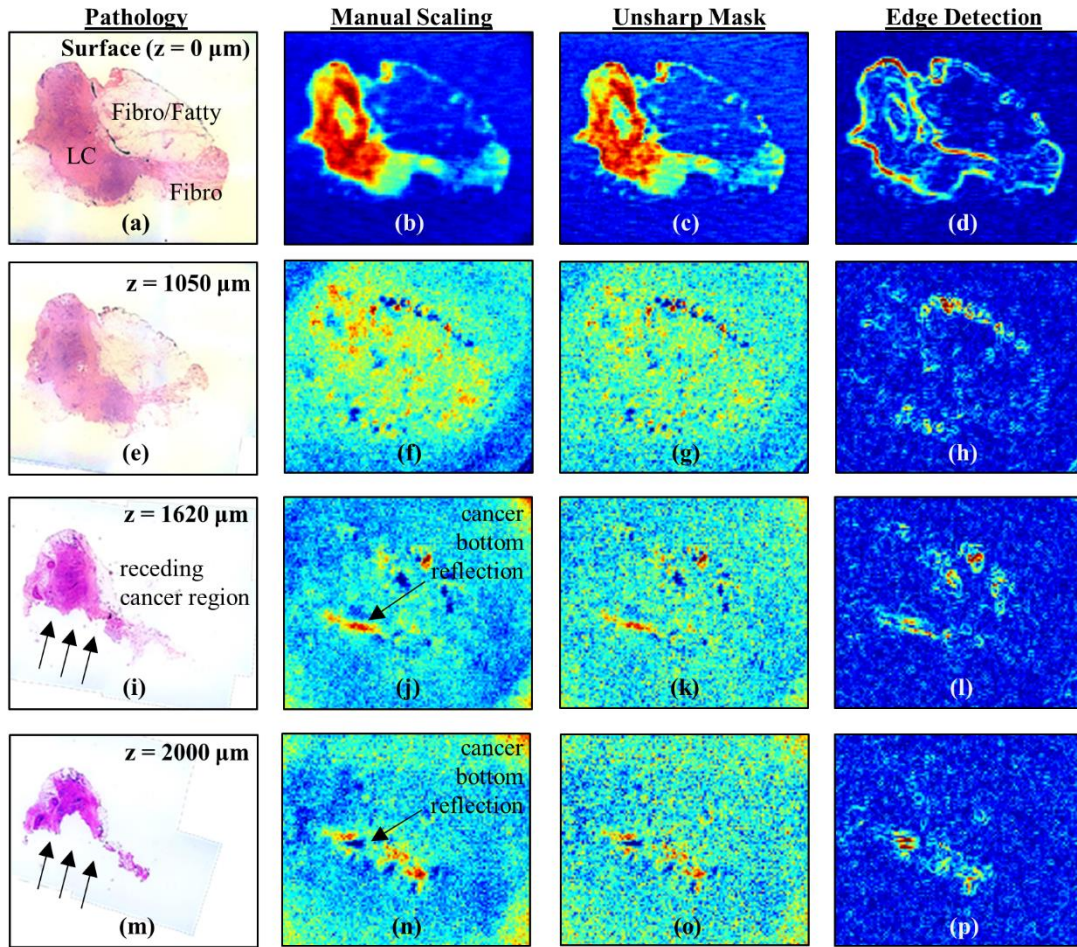


Figure 13. Comparison of histopathology images, THz Z-scan images of Sample 3 in the paraffin block. From the surface of the block where $z = 0 \mu\text{m}$, (a) the histopathology Z-scan images (b) with manual scaling, (c) with unsharp mask enhancement, and (d) with edge detection using the Sobel operator are shown. This sequence is repeated at different depths (e)-(h) at $z = 1050 \mu\text{m}$, (i)-(l) at $z = 1620 \mu\text{m}$, and (m)-(p) at $z = 2000 \mu\text{m}$. All histopathology images are stained as shown in pink while all THz images are not stained and are obtained without physically slicing the tumor.

The unsharp masking and edge detection methods applied to the THz data of Sample 3 are shown in the third and fourth columns of Fig. 13, respectively. Unsharp masking in Fig. 13c shows enhanced features compared to the THz image in Fig. 13b, with sharper edges and even some definition for the fibrous streaks in the fibro/fatty tissue region. Edge detection using the Sobel operator is shown to clearly define the outline of the tissue in Fig. 13d, as well as defining the border between lobular carcinoma and the fibro/fatty tissue. Since there are only small reflections

at $z = 1050 \mu\text{m}$ in Fig. 13f, the unsharp mask in Fig. 13g shows relatively little improvement in the imaging. Edge detection in Fig. 13h shows clear definition of the edge of the fibro/fatty region along with some faint resolution of the other tissue boundaries. At $z = 1620 \mu\text{m}$, the use of unsharp masking in Fig. 13k shows slight improvements in the visualization of the reflection in Fig. 13j but also increases the noise surrounding the tissue. The edge detection in Fig. 13l clearly distinguishes the reflection from the bottom of the tissue. It should be noted that there are some additional reflections from the edge of the fibro/fatty region with the paraffin block that continue to arise in these images and are clarified by the automated edge detection. As the depth increases to $z = 2000 \mu\text{m}$, slight improvement of the reflection edge can be seen using the unsharp mask in Fig. 13o, though due to the scattered nature of the reflection the increased noise in the surrounding block becomes a problem in resolving the reflection. Likewise, Fig. 13p shows noise around the final reflection but clearly resolves the tissue bottom.

The results in Fig. 12 and Fig. 13 show the effectiveness of THz for imaging lobular carcinoma and demonstrate a penetration depth of at least 2 mm. Thus the potential of THz imaging for various pathologies of breast cancer is clearly demonstrated.

5. Conclusions

This work showed the successful application of THz imaging to both infiltrating ductal carcinoma and lobular carcinoma embedded in paraffin blocks. THz imaging showed clear definition of the upper and lower boundaries of cancer in the block, which was correlated in 3D with histopathology sections sliced throughout the blocks. While the histopathology images showed the tumors through at any section throughout the block, THz imaging highlighted the boundaries of the cancer only when a change in tissue type occurred. Furthermore, the 3D imaging of the blocks could be segmented into x - y , x - z , and y - z cross-section images in order to visualize

these boundaries electronically without the need for slicing the tissue. These results show the effectiveness of THz imaging for the assessment of tumor margins, where cancer tissue is near the edge of the surgical excision.

Image processing techniques were shown to be effective for THz images of tissue sections and three-dimensional tissue embedded in paraffin blocks. Several methods showed image improvement mostly for flat sections of breast cancer tissue. However, unsharp masking and edge detection techniques were shown to be effective for the images of the three-dimensional tissue in blocks. In particular, edge detection using a Sobel operator showed very good definition of the cancer boundaries. The overall enhancement provided by these techniques is not significant, indicating that the manual methods were successful at the expense of training and time by a system operator. The image processing techniques critically provide automation for THz imaging without the need for training the operator. These techniques lend the THz imaging to be used within an intraoperative setting.

Acknowledgments

The Authors would like to thank the pathology staff at the Northwest Arkansas Pathology Associates, P.A., for providing histopathology services for the tissue used in this work. This work was funded by NSF-MRI #1228958, NSF awards #1408007 and #DGE-1450079, and the University of Arkansas Distinguished Doctoral Fellowship program.

References

- [1] L. Jacobs, "Positive margins: the challenge continues for breast surgeons.," *Ann. Surg. Oncol.* vol. 15, no. 5, pp. 1271–1272 (2008).
- [2] R. G. Pleijhuis, M. Graafland, J. de Vries, J. Bart, J. S. de Jong, and G. M. van Dam, "Obtaining adequate surgical margins in breast-conserving therapy for patients with early-stage breast cancer: current modalities and future directions.," *Ann. Surg. Oncol.* vol. 16, no. 10, pp. 2717–2730 (2009).

- [3] N. Cabioglu, K. K. Hunt, A. A. Sahin, H. M. Kuerer, G. V. Babiera, S. E. Singletary, G. J. Whitman, M. I. Ross, F. C. Ames, B. W. Feig, T. A. Buchholz, and F. Meric-Bernstam, "Role for Intraoperative Margin Assessment in Patients Undergoing Breast-Conserving Surgery," *Ann. Surg. Oncol.* vol. 14, no. 4, pp. 1458–1471 (2007).
- [4] T. C. Bowman, M. El-Shenawee, and L. K. Campbell, "Terahertz Imaging of Excised Breast Tumor Tissue on Paraffin Sections," *IEEE Trans. Antennas Propag.* vol. 63, no. 5, pp. 2088–2097 (2015).
- [5] A. J. Fitzgerald, S. Pinder, A. D. Purushotham, P. O'Kelly, P. C. Ashworth, and V. P. Wallace, "Classification of terahertz-pulsed imaging data from excised breast tissue," *J. Biomed. Opt.* vol. 17, no. 1, pp. 16005 (2012).
- [6] T. C. Bowman, "Experimental Terahertz Imaging and Spectroscopy for Ex-vivo Breast Cancer Tissue," University of Arkansas (2014).
- [7] P. C. Ashworth, E. Pickwell-MacPherson, E. Provenzano, S. E. Pinder, A. D. Purushotham, M. Pepper, and V. P. Wallace, "Terahertz pulsed spectroscopy of freshly excised human breast cancer.," *Opt. Express* vol. 17, no. 15, pp. 12444–12454 (2009).
- [8] T. Bowman, M. El-Shenawee, and L. K. Campbell, "Time of flight estimation for breast cancer margin thickness using embedded tumors," in *SPIE 9706, Optical Interactions with Tissue and Cells XXVII* (2016), p. 97061V. doi: 10.1117/12.2211167.
- [9] T. C. Bowman, Y. Wu, A. Walter, J. Gauch, M. El-Shenawee, and L. K. Campbell, "Time of Flight THz Imaging of 3D Ex-Vivo Breast cancer Tumor Tissues," in *40th International Conference on Infrared, Millimeter, and Terahertz Waves* (2015). doi: 10.1109/IRMMW-THz.2015.7327416.
- [10] S. Fan, Y. He, B. S. Ung, and E. Pickwell-MacPherson, "The growth of biomedical terahertz research," *J. Phys. D. Appl. Phys.* vol. 47, no. 37, pp. 374009 (2014).
- [11] P. U. Jepsen, D. G. Cooke, and M. Koch, "Terahertz spectroscopy and imaging - Modern techniques and applications," *Laser Photon. Rev.* vol. 5, no. 1, pp. 124–166 (2011).
- [12] S. Sy, S. Huang, Y.-X. J. Wang, J. Yu, A. T. Ahuja, Y.-T. Zhang, and E. Pickwell-MacPherson, "Terahertz spectroscopy of liver cirrhosis: investigating the origin of contrast.," *Phys. Med. Biol.* vol. 55, no. 24, pp. 7587–7596 (2010).
- [13] Y. Miura, A. Kamataki, M. Uzuki, T. Sasaki, J. Nishizawa, and T. Sawai, "Terahertz-wave spectroscopy for precise histopathological imaging of tumor and non-tumor lesions in paraffin sections.," *Tohoku J. Exp. Med.* vol. 223, pp. 291–296 (2011).
- [14] M. H. Arbab, D. P. Winebrenner, T. C. Dickey, A. Chen, M. B. Klein, and P. D. Mourad, "Terahertz spectroscopy for the assessment of burn injuries in vivo.," *J. Biomed. Opt.* vol. 18, no. 7, pp. 77004 (2013).

- [15] C. Yu, S. Fan, Y. Sun, and E. Pickwell-Macpherson, "The potential of terahertz imaging for cancer diagnosis: A review of investigations to date," *Quant. Imaging Med. Surg.* vol. 2, no. 1, pp. 33–45 (2012).
- [16] P. Y. Han, G. C. Cho, and X. C. Zhang, "Time-domain transillumination of biological tissues with terahertz pulses.," *Opt. Lett.* vol. 25, no. 4, pp. 242–244 (2000).
- [17] P. Knobloch, C. Schildknecht, T. Kleine-Ostmann, M. Koch, S. Hoffmann, M. Hofmann, E. Rehberg, M. Sperling, K. Donhuijsen, G. Hein, and K. Pierz, "Medical THz imaging: an investigation of histo-pathological samples.," *Phys. Med. Biol.* vol. 47, no. 21, pp. 3875–84 (2002).
- [18] Z. D. Taylor, R. S. Singh, D. B. Bennett, P. Tewari, C. P. Kealey, N. Bajwa, M. O. Culjat, J. Hubschman, E. R. Brown, W. S. Grundfest, and H. Lee, "THz Medical Imaging : in vivo Hydration Sensing," *IEEE Trans. Terahertz Sci. Technol.* vol. 1, no. 1, pp. 201–219 (2011).
- [19] G. J. Wilmink and J. E. Grundt, "Invited Review Article: Current State of Research on Biological Effects of Terahertz Radiation," *J. Infrared, Millimeter, Terahertz Waves* vol. 32, no. 10, pp. 1074–1122 (2011).
- [20] P. Doradla, K. Alavi, C. Joseph, and R. Giles, "Detection of colon cancer by continuous-wave terahertz polarization imaging technique," *J. Biomed. Opt.* vol. 18, no. 9, pp. 90504 (2013).
- [21] S. J. Oh, S.-H. Kim, Y. Bin Ji, K. Jeong, Y. Park, J. Yang, D. W. Park, S. K. Noh, S.-G. Kang, Y.-M. Huh, J.-H. Son, and J.-S. Suh, "Study of freshly excised brain tissues using terahertz imaging," *Biomed. Opt. Express* vol. 5, no. 8, pp. 2837–42 (2014).
- [22] I. C. S. Joseph, A. N. Yaroslavsky, V. A. Neel, T. M. Goyette, and R. H. Giles, "Continuous wave terahertz transmission imaging of nonmelanoma skin cancers," *Lasers Surg. Med.* vol. 43, no. 6, pp. 457–462 (2011).
- [23] R.C. Gonzalez, R.E. Woods, *Digital Image Processing*, 3rd edn. (Pearson Prentice Hall, NJ, 2008), pp. 120-144, 689-794.
- [24] W. K. Pratt, *Digital Image Processing*, 4th edn. (John Wiley & Sons, NJ, 2007), pp. 288-291.
- [25] J. F. Canny, "A Computational Approach to Edge Detection," *IEEE Trans. Pattern Anal. Mach. Intell.* vol. 8, no. 6, pp. 679–698 (1986).
- [26] Y. Wu, T. Bowman, J. Gauch, and M. El-Shenawee, "Adaptive Enhancement and Visualization Techniques for 3D Terahertz Images of Breast Cancer Tumors," in *SPIE 9706, Optical Interactions with Tissue and Cells XXVII* (2016), p. 970602. doi: 10.1117/12.2209706.
- [27] MeVisLab official website. (2015). Available: <http://www.mevislab.de/>

- [28] Detect Edges with Canny Edge Detection Filter (ITK, 2015) <http://itk.org/ITKExamples/src/Filtering/ImageFeature/DetectEdgesWithCannyFilter/Documentation.html> (accessed 26 August 2016).
- [29] T. Bowman, M. El-Shenawee, and S. G. Sharma, "Terahertz spectroscopy for the characterization of excised human breast tissue," in IEEE MTT-S International Microwave Symposium Digest (2014). doi: 10.1109/MWSYM.2014.6848538.
- [30] M. Naftaly, Terahertz Metrology, 1st edn. (Artech House, MA, 2015).

Chapter 5: A Phantom Study of Terahertz Spectroscopy and Imaging of Micro- and Nano-diamonds and Nano-onions as Contrast Agents for Breast Cancer

© 2017 IOP Publishing. Reprinted from T. Bowman, A. Walter, O. Shenderova, N. Nunn, G. McGuire, and M. El-Shenawee, "A Phantom Study of Terahertz Spectroscopy and Imaging of Micro- and Nano-diamonds and Nano-onions as Contrast Agents for Breast Cancer," *Biomedical Physics and Engineering Express*, vol. 3, no. 5, pp. 055001, 2017. This is the Accepted Manuscript version of an article accepted for publication in *Biomedical Physics & Engineering Express*. IOP Publishing Ltd is not responsible for any errors or omissions in this version of the manuscript or any version derived from it. The Version of Record is available online at [doi: 10.1088/2057-1976/aa87c2].

Abstract

THz imaging is effective in distinguishing between cancerous, healthy, and fatty tissues in breast tumors, but a challenge remains in the contrast between cancerous and fibroglandular (healthy) tissues. This work investigates carbon-based nanoparticles as potential contrast agents for terahertz imaging of breast cancer. Microdiamonds, nanodiamonds, and nanometer-scale onion-like carbon are characterized with terahertz transmission spectroscopy in low-absorption backgrounds of polydimethylsiloxane or polyethylene. The refractive index and absorption coefficients are calculated based on the measured electric fields. Nanodiamonds show little effect on the terahertz signal, microdiamonds express resonance-like, size-dependent absorption peaks, and onion-like carbon provides a uniform increase in the optical properties even at low concentration. Due to its strong interaction with terahertz frequencies and ability to be activated for selective binding to cancer cells, onion-like carbon is implemented into engineered three-dimensional breast tumor models composed of phantom tissue mimicking infiltrating ductal carcinoma surrounded by a phantom mimicking healthy fibroglandular tissue. This model is imaged using the terahertz reflection mode to examine the effectiveness of contrast agents for differentiation between the two tissue types. In both spectroscopy and imaging, a 10% concentration of onion-like carbon shows the strongest impact on the terahertz signal and holds promise as a terahertz contrast agent.

1. Introduction

Electromagnetic detection of breast cancer encompasses a wide field of frequency ranges and techniques [1]. In addition to well-known screening and treatments in X-ray technology, magnetic resonance imaging, and radiation therapy, investigations into the properties of breast tissues have spanned a broad range of frequencies in the electromagnetic spectrum. Early investigations found clear distinctions in the dielectric permittivity and conductivity between tumors, tumor-adjacent tissue, and healthy breast tissue from 20 kHz (very low frequency, VLF) to 100 MHz (very high frequency, VHF) [2], between malignant and healthy tissue from 50 MHz (VHF) to 900 MHz (microwave) [3], and between breast cancer metastasis in lymph nodes compared to normal lymph nodes from 0.5 GHz to 30 GHz [4]. However, a study at 3.2 GHz showed significant overlap in permittivity and conductivity between fibrous, benign, and malignant tumors [5], and two large-scale studies from 0.5 to 30 GHz showed wide permittivity variations in healthy fibrous tissue depending on the fat concentration [6], and that the permittivity of malignant breast cancer and densely fibrous tissue (little to no fat) differs by less than 10% [7]. This lack of contrast represents a key challenge in microwave detection of cancer.

At the visible and infrared frequencies, investigation of the properties of breast cancer showed similar challenges as in the microwave range [8], [9]. As a result, most modern implementations of optical frequencies for breast cancer detection depend on fluorescence using fluorophores and contrast agents or on auto-fluorescence of specific cellular structures [10]-[12]. These fluorescence imaging applications are mostly focused on intraoperative (i.e. in an operation room) differentiation between malignant and healthy tissue, which is a primary medical concern in breast cancer surgeries. Intraoperative differentiation between cancer and healthy tissues as a complementary process to pathology was also investigated using x-ray imaging of surgically

removed tumors (specimen radiography). Radiography for tumor margin assessment was shown to be effective [13], but several studies have reported that it can miss remnant cancer when compared to pathology [14], suffers from size and accuracy in smaller tumors [15], and has low sensitivity [16]. Thus, there is still a need to develop techniques for accurate intraoperative assessment of breast tumor boundaries following a surgical procedure.

The terahertz (THz) frequency band is currently being investigated as an alternative method for intraoperative assessment of breast cancer. THz frequencies were reported to be nonionizing and safe for biological applications [17] with higher image resolution compared to the microwave band. A comparison between optics and THz imaging for freshly excised tissues, favoring THz imaging, was reported in [18]. Furthermore, THz imaging was successfully applied to a wide range of cancer applications of freshly excised tissues of the breast [19]-[20], skin [21], and brain [22], and for fixed tissues of the breast [23]-[25] and liver [26]. Reported THz spectroscopy of freshly excised breast cancer tissue from 0.15 to 2 THz showed distinction between the refractive index of cancer, fibroglandular, and fat tissues [19]. Likewise, THz pulsed imaging of human breast cancer has shown clear distinctions between these tissue types in both fresh and formalin-fixed, paraffin-embedded (FFPE) tumors [20], [23]-[25]. While THz for detecting cancer margins has shown a potential, it is not meant for use in patient diagnosis, screening, or replacing the pathology assessment of surgical tissues. If successful, THz imaging has a potential to provide a rapid intraoperative assessment of excised tumors.

However, the reported THz works of freshly excised tissues [19] showed a relatively little difference in the absorption of cancer and fibroglandular tissues. The idea here is to implement contrast agents to improve the distinction between cancerous and healthy tissues in THz imaging. For example, gold nano-rods (GNRs) were shown to provide an approximate 20% increase in the

THz response of A431 epidermoid carcinoma cells in a petri dish when activated with an infrared laser [27]. Likewise, superparamagnetic iron oxide nanoparticles (SPIOs) were utilized in conjunction with localized magnetic fields and MRI to increase THz contrast by an unreported amount in pulsed time-domain imaging of mouse ovarian cancer [28] and by 35% for 0.2 THz continuous wave imaging of water [29]. However, both GNRs and SPIOs require the use of an external non-THz source to generate the contrast improvement in the particles. Gadolinium oxide has also shown potential for contrast enhancement in THz spectroscopy [30], and indium nitride was investigated in modeling of skin cancer [31], but neither particle was tested in THz imaging.

This work investigates the use of carbon-based particles with dimensions on the micrometer and nanometer scale as potential THz contrast agents for imaging breast tumors. Fluorescent high pressure high temperature (HPHT) nanometer-scale diamonds (nanodiamonds, NDs) containing color centers and onion-like carbon (OLC, also called carbon nano-onions) conjugated with a fluorophore were previously utilized for fluorescence in optical frequencies [32], [33]. NDs were shown to be biologically safe for extended times using injections of 100 nm functionalized particles over a period of 5 months in mice [34]. Additionally, small NDs in the 5 nm range induced relatively little genetic toxicity compared to other nanoparticles [35], and in general NDs have shown insignificant toxicity in all studies [36]. Meanwhile, OLC was shown to have distinctly high absorption at frequencies from 20 Hz to 3 THz, excluding the frequency ranges from 3 GHz to 8 GHz and 53 GHz to 100 GHz [37], [38]. OLC was also shown to be an effective absorber in low quantities at infrared frequencies from 10 to 230 THz [39]. OLC can be functionalized to selectively bind the surface of cancer cells [40], [41] and was shown to induce less inflammatory response and cell toxicity than carbon nanotubes with similar functionalization [41], [42]. OLC of size 30 nm in concentrations of 0.6 mg/L and 6 mg/L was reported to have far

less genetic toxicity in human fibroblasts than carbon-nanotubes in one tenth of the concentration [42]. Similar results were seen for 5 nm OLC in concentrations of 30, 300, and 3000 $\mu\text{g/mL}$ in rat fibroblasts with minimal loss of cell viability (15% at the highest concentration) [43], and additional studies of OLC at lower concentrations showed insignificant toxicity when tested with different kinds of functionalization [44]. In addition to having low toxicity, these carbon-based particles cost less than organic dyes or quantum dots used for nanoparticle functionalization by an order of magnitude [36]. However, these particles have yet to be investigated for effectiveness in tissue at THz frequencies.

In this work, microdiamonds, nanodiamonds, and OLC are investigated as potential image contrast factors by first using THz spectroscopy to examine the optical properties of each particle type with multiple sizes, preparations, and concentrations while distributed in polydimethylsiloxane (PDMS) or polyethylene. These polymers have relatively low absorption compared to fresh tissues and allow for characterization of the particles without significant signal loss in the surrounding medium. The particles providing the greatest impact on the THz signal are then examined in breast cancer phantom tissues. Phantom tissues are used here for their highly-controlled nature, ease in implementing the particles in different concentrations, and low cost.

Phantoms were utilized for some time in microwave frequency modeling of breast cancer and other tissue types [45], [46]. However, the use of phantoms for THz applications in the literature so far was limited to solid phantoms with limited ability to mimic tissue properties [47] or highly tunable non-solid oil-water emulsions [48]. This work makes use of highly tunable solid phantoms for breast cancer tissues recently developed by the authors as reported in [49] and [50]. To the best of our knowledge, the current paper is the first work to demonstrate OLC and other carbon-based particles immersed in breast phantom tumors as potential THz image contrast agents.

This work is organized as follows: methodology and materials in Section 2; results of particle characterization in Section 3; results of breast phantom tumor imaging with and without OLC particles in Section 4; and discussion and concluding remarks in Section 5.

2. Methodology and Materials

2.1. Terahertz Spectroscopy and Imaging Setup

This work was conducted using the TPS Spectra 3000 pulsed THz imaging and spectroscopy system (purchased from TeraView Ltd., UK) at the University of Arkansas. The diagram of the system can be seen in Fig. 1. An 800 nm pulse from a Ti:Sapphire laser is used to excite a biased THz emitter consisting of a photoconductive antenna on a GaAs substrate. The resulting THz signal is either transmitted through a sample placed in the system as seen in Fig. 1a or directed using mirrors to reflect off the sample as seen in Fig. 1b and is then collected at a THz receiver with the same structure as the emitter. The unobstructed THz pulse is given in Fig. 1c, while the Fourier transform of the pulse is given in Fig. 1d. The width of the time-domain pulse is ~ 280 fs at $1/\sqrt{2}$ from the positive peak of the electric field signal, ~ 587 fs at $1/\sqrt{2}$ from the first negative peak of the electric field signal, and ~ 287 fs from the second negative part of the signal, which corresponds to a frequency range of 100 GHz to 4 THz as seen in Fig. 1. The output power of the THz system (~ 1 μ W) used in this work and the short time of exposure make it biologically safe and provides negligible heating even in high-absorption samples [17]. In all measurements, the sample chamber is purged with dry nitrogen gas for at least 15 minutes to eliminate absorption by water vapor.

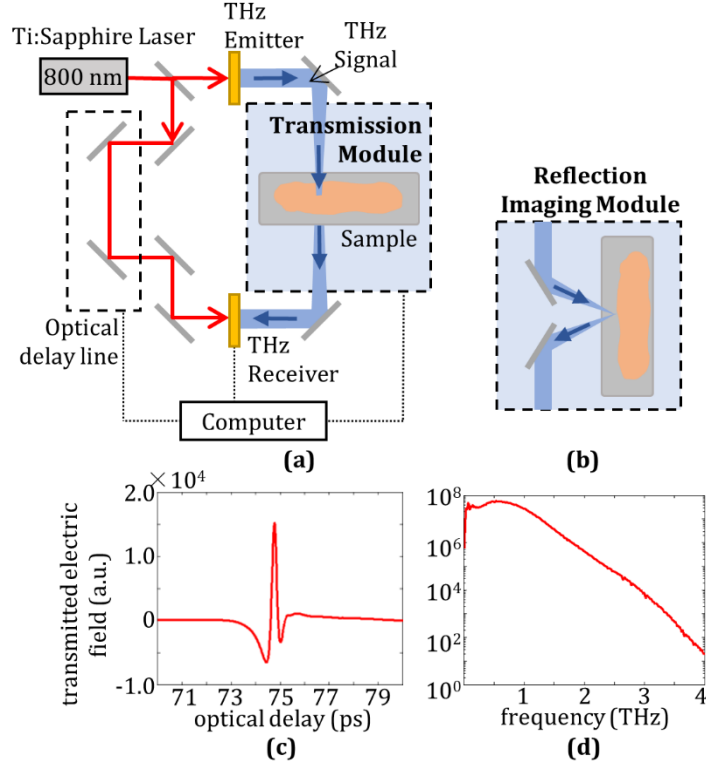


Figure 1. (a) Terahertz system diagram with transmission spectroscopy module and (b) reflection imaging module. (c) Generated time-domain THz signal and (d) frequency-domain spectrum after Fourier transform.

THz spectroscopy is used to calculate the complex refractive index of the carbon-based particles embedded in polymer and of tissue phantoms with and without contrast agents. This complex refractive index is defined by:

$$\tilde{n} = n - i\kappa = n - i \frac{c}{\omega} \frac{\alpha_{abs}}{2} \quad (1)$$

Where \tilde{n} is the complex refractive index, n is the real part of the refractive index (referred to here as just refractive index), κ is the imaginary part of the refractive index or extinction coefficient, c is the speed of light, ω is the angular frequency, and α_{abs} is the absorption coefficient. In this work the standard optical properties of refractive index and absorption coefficient are presented. The sample setup for spectroscopy can be seen in Fig. 2. For particles embedded in polymers, the background media are rigid and free-standing so the transmitted signal through the sample can be

measured directly as seen in Fig. 2a. The Fourier transform of the transmitted signal is then compared to the signal transmitted through the empty sample holder based on the following equation [23]:

$$E_{samp}/E_{ref} = \tilde{\tau}e^{(\gamma_1-\gamma_2)d} \quad (2)$$

Where E_{samp} is the transmitted electric field signal through the sample, E_{ref} is the transmitted reference signal, γ_1 and γ_2 are the complex propagation constants defined by $\gamma = i\frac{\omega}{c}\tilde{n}$ for the background medium (air) and the sample respectively, d is the sample thickness, and $\tilde{\tau}$ is the ratio of the Fresnel transmission terms for the sample and reference setups. A range of refractive index and absorption coefficient values are inserted into equation (2) and compared against the measurement data to find the pair of values with the lowest total mean square error at each frequency. It is important to note that the refractive indices and absorption coefficients calculated in this work are for both the particles and the background medium. The standard practice is to suspend or mix these particles with another medium such as PDMS or polyethylene, though it is possible to extract the optical properties of the particles alone as reported in [51]. More detailed equations for calculating the refractive index and absorption coefficient from transmitted signals were published in [23].

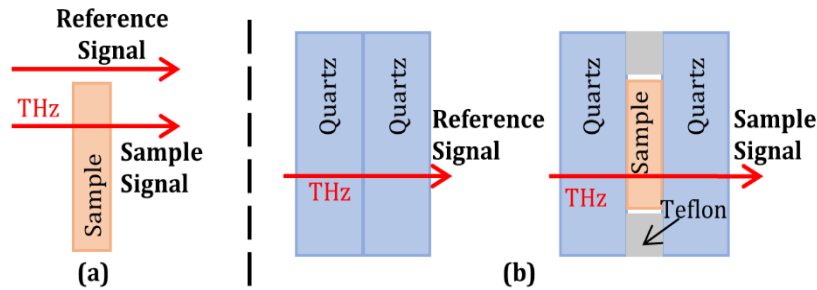


Figure 2. THz transmission spectroscopy setups with (a) air reference and single-layer sample transmission for polymer-embedded samples and (b) quartz window reference and multi-layer sample transmission for phantom samples.

For phantoms, the samples are not rigid and are instead mounted between quartz windows with a spacer to ensure consistent sample thickness, as seen in Fig. 2b. In this setup, the reference measurement is taken from the transmitted signal through two quartz windows without the phantom (Fig, 2b), and the solution of the refractive index and absorption coefficient follow the same form as equation (2). All spectroscopy measurements use an average of 1800 transmitted signals. All phantom samples used in the spectroscopy measurements between the two quartz windows in this work are 200 μm thick.

2.2. *Breast Cancer Phantom Tissue Development*

The development of phantom materials in THz band was reported in the literature [47,48]. We developed phantom materials with THz properties similar to that of freshly excised tissue using TX151 solidifying powder (obtained from Oil Center Research, Inc.) mixed with agar and an emulsion of water, olive oil, and a surfactant [49,50]. An effective dielectric permittivity equation is used to obtain the first estimate for how much oil should be incorporated to approach the desired THz material properties. Due to oil and water emulsions forming small, spherical micelles when mixed, this estimate is made for spherical packing using Bottcher's equation [52]:

$$v_2 = \frac{(\tilde{\epsilon} - \tilde{\epsilon}_1)(2\tilde{\epsilon} + \tilde{\epsilon}_2)}{3\tilde{\epsilon}(\tilde{\epsilon}_2 - \tilde{\epsilon}_1)}. \quad (3)$$

Here $\tilde{\epsilon}$ is the effective complex permittivity of the combined mixture, while $\tilde{\epsilon}_1$ and $\tilde{\epsilon}_2$ are the complex permittivity of the host medium (water-surfactant-TX151) and the permeating material (oil), respectively. The permittivity of the individual components and resulting phantom are obtained using THz spectroscopy. Then these values are used to calculate v_2 , the volume packing fraction. While v_2 is not inherently known for the mixture, it can be directly related to the volume percentage of oil if the dispersion of oil is assumed to be consistent. The permittivity of a

phantom mixture for a given volume percentage can also be estimated by changing the equation to its quadratic form as follows:

$$0 = 2\tilde{\epsilon}^2 + (3v_2(\tilde{\epsilon}_1 - \tilde{\epsilon}_2) + \tilde{\epsilon}_2 - 2\tilde{\epsilon}_1)\tilde{\epsilon} - \tilde{\epsilon}_1\tilde{\epsilon}_2 . \quad (4)$$

The phantoms for this work are detailed in [49,50] and were tuned to the refractive index and absorption coefficient of infiltrating ductal carcinoma (IDC) and healthy fibroglandular tissues reported in the literature [19]. The developed recipe for the IDC phantom by percent weight is 66% water, 12% oil, 6% surfactant, 14% TX151, and 2% agar, and the developed recipe for the fibroglandular phantom is 56% water, 18% oil, 10% surfactant, 14% TX151, 2% agar [49,50].

2.3. Carbon-based Particle Preparation

The microdiamonds, nanodiamonds (NDs), and nanometer-scale OLC used in this work were provided by Adámas Nanotechnologies in two different media. The first set of particles was embedded in PDMS while subsequent samples were received as a powder. All nanometer-scale properties were evenly distributed in the PDMS composites while the microdiamonds were too heavy to remain in suspension and sedimented into a single layer before the PDMS was cured. While a single layer of microdiamonds in PDMS does not fully model the distributed particles that would be present in a biomedical application, it is still useful to observe the THz signal interaction with the particles. Additional details on the fabrication of particles and sample preparation were previously reported in other works [32], [37], [39], [53].

Four types and concentrations (by weight) of PDMS-nanoparticle composites were investigated: 1% 100 nm diameter OLC, 1% 100 nm diameter NDs, 2% 100 nm diameter NDs, and 1% 40 nm diameter NDs. For microdiamonds in a single layer in PDMS, three particle types and treatments were investigated: 10% 100 μm diameter pristine microdiamonds, 5% 150 μm

diameter irradiated (Irr) microdiamonds, and 10% 150 μm diameter irradiated and annealed (Irr-Ann) microdiamonds containing NV centers.

2.4. THz Spectroscopy Process

Following an initial investigation of the different particle types in PDMS, the particles that showed potential as THz image contrast agents were investigated individually by embedding the particles in polyethylene tablets. Microscope photos of a few selected powders are shown in Fig. 3. Fig. 3a shows 100 μm microdiamonds at 100X magnification, with the yellow hue being typical of these samples due to the lattice size. The same is seen in the 20 μm microdiamonds at 200X magnification in Fig. 3b, which shows consistent structure and coloration of the particles across different scales and discrete separation of particles. This consistency persists down to the nanodiamond scale as well, though only microdiamonds were received as powder. Fig. 3c shows 200 nm OLC at 400X magnification. Both individual particles and larger clusters and aggregates can be seen at this scale. This grouping together of particles is often attributed as the reason for the broad frequency response of OLC [37],[39], though it should disperse in aqueous solutions.

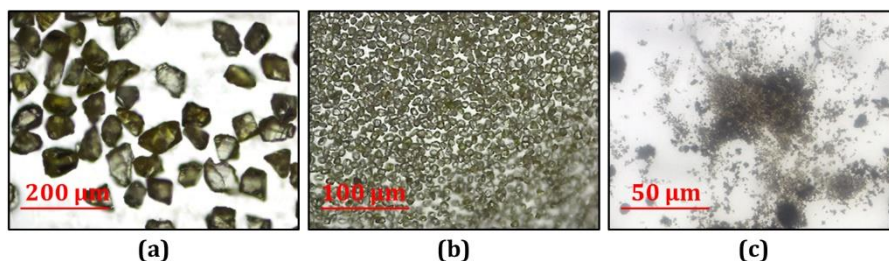


Figure 3. Microscope images of powders used in work. (a) 100 μm microdiamond at 100X magnification, (b) 20 μm microdiamond at 200X magnification, and (c) 200 nm OLC at 400X magnification.

The polyethylene tablets with the samples are generated by mixing polyethylene powder and particles in a mortar, then compressing them into tablets using a five-ton hydraulic press. The particles are mixed at a 1% or 10% concentration in polyethylene to examine the degree of interaction the particles have with the THz signal. For the larger microdiamonds, the diameters of

some of the particles are comparable with THz wavelengths and result in some scattering as will be shown in Section 3. Therefore, in order to obtain reliable characterization of these particles, all particle-embedded tablets are measured at two different rotations, then broken down and remade multiple times to provide averaged properties with reduced scattering effects. This process is also extended to the nanometer-scale particles to maintain a consistent measurement process for all samples. Spectroscopy of the particles in PDMS and polyethylene is conducted using the single-layer transmission setup with an air reference seen in Fig. 2a.

Following individual characterization, the particles most suitable to providing image contrast are implemented into the developed IDC (cancer) phantom tissues and characterized using the spectroscopy setup in Fig. 2b. Then the particles in the phantoms are used for THz imaging to simulate the contrast agent binding to the surface of excised breast cancer tumors.

3. Results of Particle Characterization

3.1. Particles in PDMS

The first set of particles examined are embedded in PDMS and investigated separately as nanometer-scale particles and micrometer-scale particles. THz spectroscopy of the four PDMS-nanoparticle composite samples and a pure PDMS sample, as a reference, is shown in Fig. 4. The optical properties of bulk diamond from [54] are reported in Figs. 4-9 for comparison.

All the nanometer-scale particles show an increase in the refractive index compared to the PDMS without particles in Fig. 4a. The use of PDMS as a reference serves as a relatively low absorption background to observe the THz interaction with each particle type. It is clearly seen that the increase provided by the NDs is relatively small while the shift provided by OLC is more significant. A similar change in properties is seen in the absorption coefficient in Fig. 4b. Here the NDs provide no noticeable increase in absorption, which agrees with the low absorption of bulk

diamond, while the OLC significantly increases the absorption coefficient of the overall sample. Therefore, for particles in the nanometer size range, only the OLC shows a significant promise as a THz contrast agent.

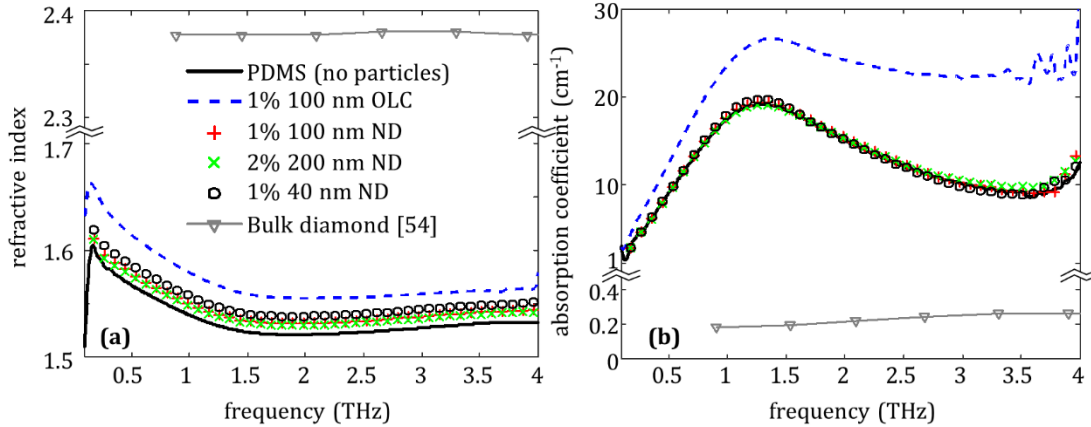


Figure 4. The (a) refractive index and (b) absorption coefficient of nanodiamond (ND) and onion-like carbon (OLC) particles embedded in PDMS.

The THz spectroscopy results of the four PDMS-microdiamond composites are displayed in Fig. 5, with the refractive index shown in Fig. 5a and the absorption coefficient in Fig. 5b. All three particle types provide an increased refractive index and absorption coefficient over the entire measurement range. The results of Fig. 5 outline the different variables of the particles that are examined in this work. Most notably, the 150 μm diameter particles demonstrate an increase at lower frequencies compared to pure PDMS and have an absorption coefficient peak around 1.5 THz. Meanwhile the 100 μm diameter particles show a more notable increase at higher frequencies and an absorption peak around 2.75 THz. In both cases the absorption peak most likely indicates a resonance due to the particle sizes coinciding with THz wavelengths. Between the two 150 μm diameter samples, the difference in the properties is due to different particle concentrations. Both OLC and microdiamonds show significant properties in the THz frequency range, but additional spectroscopy is needed to determine the effect of particle size and microdiamond treatment. Since

NDs show insignificant reaction to THz signals, they are not considered for subsequent measurements.

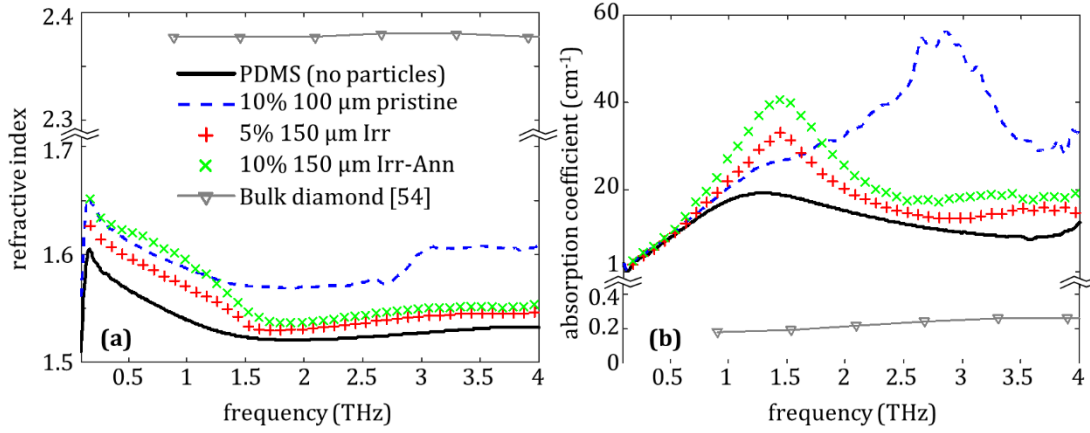


Figure 5. The (a) refractive index and (b) absorption coefficient of microdiamonds embedded in PDMS.

3.2. Microdiamonds in Polyethylene

The second round of particles consists of different sizes of OLC and microdiamonds left in powdered form, which are characterized by polyethylene embedding as described in Section 2. The microdiamonds are investigated in diameters of 1, 20, 40, 100, and 150 μm. They are also examined for a variety of treatments based on availability as follows: 1-40 μm particles in pristine, irradiated, and irradiated-annealed states, 100 μm particles in pristine and irradiated states only, and 150 μm particles in irradiated and irradiated-annealed states.

3.2.1. Effect of microdiamond size

Polyethylene tablets are made for each pristine microdiamond ranging from 1 μm to 100 μm with a 10% concentration and measured using the process described in Section 2. The average properties across three tablets for each particle size are presented in Fig. 6.

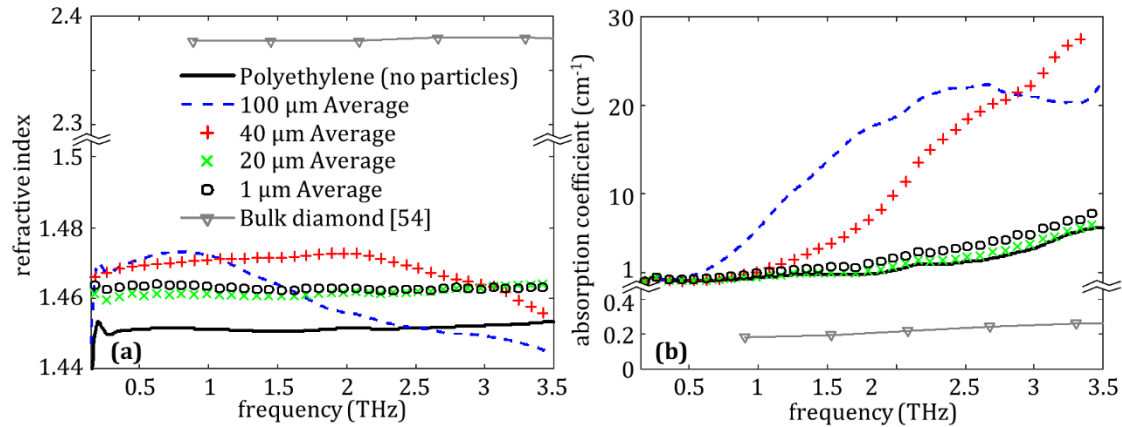


Figure 6. The average (a) refractive index and (b) absorption coefficient for polyethylene tablets containing 10% pristine 100 μm diamond, 40 μm diamond, 20 μm diamond or 1 μm diamond.

The results for microdiamonds are shown in Fig. 6, where they demonstrate a noticeable increase in the refractive index for all sizes. The 100 μm particles primarily provide enhancement at lower THz frequencies, while the 40 μm particles show a significant increase across most of the measured frequency range, only dropping back toward the value of polyethylene as the frequency approaches 3.5 THz. Meanwhile the 20 μm and 1 μm particles demonstrate a comparable and uniform increase in the refractive index. The changes to the absorption coefficient in Fig. 6b provide more clarity to the changes in the THz properties of the samples seen previously. For the 100 μm microdiamonds, an absorption peak can be seen around 2.5 THz. This is similar to the size-dependent resonance peak seen for the same particles in the PDMS in Fig. 5, but it is broader and at a slightly lower frequency due to a more even distribution of the particles in polyethylene. This size-dependent scattering is supported by the steadily increasing absorption of the 40 μm particles, which appear to possibly have a peak outside of the frequency range achievable by the system. However, the 1 and 20 μm particles show only a small, uniform increase in the absorption. This discrepancy is most likely due to these particles being too small to scatter the THz signal, leaving the attenuation of the transmitted signal as the only contribution to the calculated

absorption. This agrees with the slightly higher shifts in properties created by the 1 μm particles, as they would be present at a higher density in the sample for the same weight concentration.

From the results in Fig. 6, it is seen that either 40 μm or 100 μm particles could potentially increase the contrast of a region in a THz imaging setup. While the 1 μm and 20 μm particles do show some small increase in the refractive index of the material, they provide insignificant changes to the absorption coefficient even in a low-absorption material. For the larger particles, 40 μm microdiamonds show a more broadband shift in the refractive index and absorption coefficient compared to the polyethylene alone, but the 100 μm particles exhibit more significant changes in properties at lower frequencies where most of the power of the THz pulse is present (as seen in the signal spectrum in Fig. 1d). Thus the selection between these two particles is dependent on what is most suitable for the imaging application.

3.2.2. *Effect of microdiamond treatment*

Since the characterization of microdiamonds embedded in PDMS did not address the effect of different particle treatments on the THz properties, three samples were prepared with the 40 μm microdiamond in pristine, irradiated, and irradiated-annealed states at 10% concentration and measured following the process in Section 2. The results of this characterization are given in Fig. 7 with the polyethylene and average properties from the 100 μm samples as references.

It can be seen in Fig. 7a that the microdiamond treatments have little change to the refractive index from the pristine microdiamond particles. This is also seen in Fig. 7b, where there is a negligible difference between the absorption of the pristine and treated particles. This process was repeated for the 1 μm and 20 μm particles with similar results not shown here, demonstrating that treatment type of the microdiamond particles has no effect on the THz properties of the

particles in this case. It is safe to assume that any effect between the different particles is going to be primarily dependent on the size, as seen in Fig. 6, or the concentration, as seen in Fig. 5.

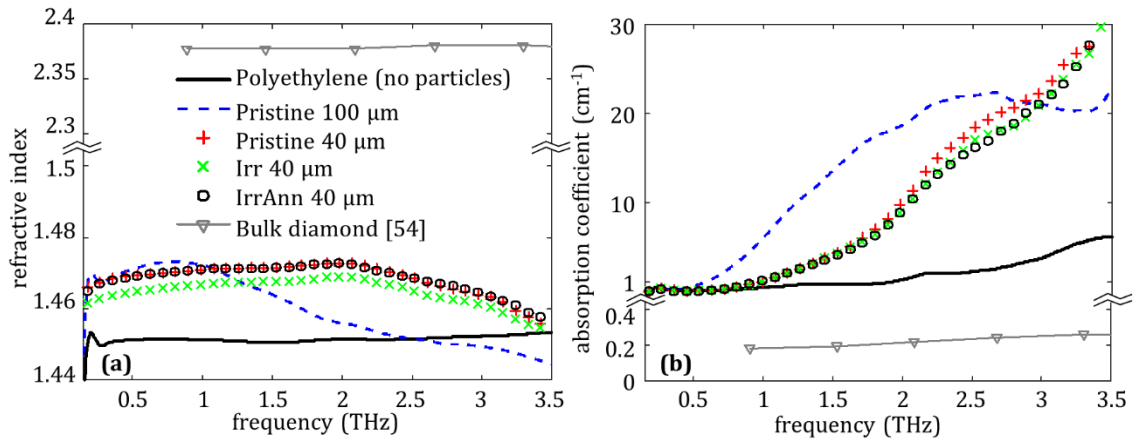


Figure 7. The average (a) refractive index and (b) absorption coefficient for polyethylene tablets containing 10% pristine 100 μm diamond, pristine 40 μm diamond, Irr 40 μm diamond or Irr-Ann 40 μm diamond.

3.3. OLC in Polyethylene

The OLC in powder form was tested in two sizes based on availability: 100 nm diameter and 200 nm diameter. Both sizes of OLC were implemented into polyethylene tablets in concentrations of 1% and 10% and were characterized with THz transmission spectroscopy as shown in Fig. 2a. The resulting sample THz properties are shown in Fig. 8.

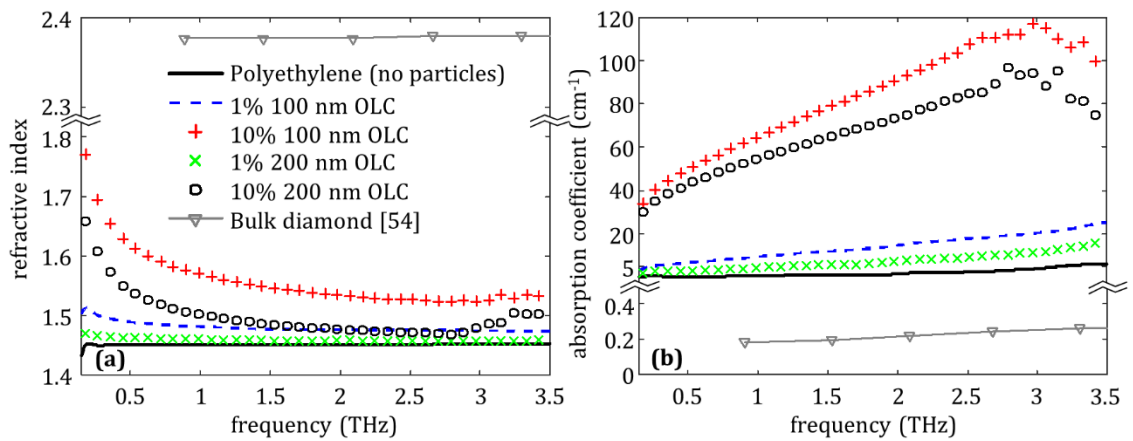


Figure 8. The average (a) refractive index and (b) absorption coefficient for polyethylene tablets containing 1% or 10% of either 100 nm or 200 nm OLC.

Fig. 8a shows that the 1% 100 nm OLC sample creates a uniform increase in the refractive index of the polyethylene tablet across the entire frequency range. Increasing the OLC to 10% shows a further shift in the refractive index from around 1.48 at 1 THz to roughly 1.57. On the other hand, there is very little increase provided by the 1% 200 nm OLC compared to the polyethylene alone. Increasing the amount to 10% shows a significant shift in the refractive index that follows the same trend as the 100 nm particles, but the increase is not as strong. Similar changes are seen in the absorption coefficient in Fig. 8b, with 100 nm OLC showing a larger uniform increase than 200 nm OLC. These results imply that as the size of the OLC decreases, its effect on the transmitted THz signal will increase. OLC can be generated in even smaller sizes than 100 nm, meaning that greater impact by the particles is possible as the size decreases. However, for the scope of this work, only 100 nm and 200 nm OLC particles could be tested due to availability of these particles.

The contrast between the OLC samples and pure polyethylene can also be compared to the properties of the polyethylene tablet with 40 μm or 100 μm microdiamonds at 10% concentration in Fig. 6. The OLC provides a greater and more uniform shift in both refractive index and absorption coefficient with a lower concentration than both microdiamond sample sizes. In Fig. 8, for 1% OLC the 100 nm particles show slightly higher absorption than the 200 nm particles. The results at 10% concentration are consistent, with 100 nm higher than 200 nm. Both 10% concentrations show higher absorption than the 1%, which is the anticipated result. The higher absorption in the smaller 100 nm particles could be explained due to the multiple reflections of the signal between the particles. For Fig. 6, the same consistency is seen between the smaller microdiamond sizes of 1 μm and 20 μm (1 μm shows slightly higher absorption than 20 μm). However, the results of the 100 μm and 40 μm particles are inconsistent with the above

observation. This could be explained by a resonance phenomenon. For example, the wavelength at 2.5 THz is roughly 83 μm in polyethylene which is close to the size of the 100 μm particles and consistent with the peak seen in the absorption coefficient. A peak for the 40 μm particles would be anticipated at a higher frequency which is not seen in the figure (out of range of the plotted data). Thus, while there is some shift in properties associated with microdiamonds in the tested THz band, OLC shows a much greater potential for the purpose of enhanced THz imaging.

3.4. *Microdiamonds and OLC in IDC Phantom*

So far, the particles were only characterized in relatively low-loss media to observe the THz interaction of the particles alone. To determine the effectiveness of these particles in a high-absorption environment, such as freshly excised breast tissues, the developed breast phantom IDC tissue (cancer-like tissue) is used as a medium here. In this case, since the 100 μm microdiamonds and 100 nm OLC show the most promise of the two particle types, they are investigated in greater detail. The weight of the IDC phantom recipe is calculated such that the particles could be introduced using a 10% concentration for the microdiamonds and a 1% or 10% concentration for the OLC. Each sample with these particles is measured at slices from 6 different locations in the breast phantom tissue in the spectroscopy setup shown in Fig. 2b to obtain an average set of values for these data. The results are shown in Fig. 9 and are compared to the phantom without particles. It should be noted that the frequency range for the spectroscopy in Fig. 9 was reduced to 2 THz maximum, instead of 3.5 THz used in the previous results, due to the high losses in the breast phantom tissues causing a significant attenuation of the signal beyond 2 THz. This frequency limit agrees with the reported spectroscopy data of freshly excised human breast tumor tissue [19].

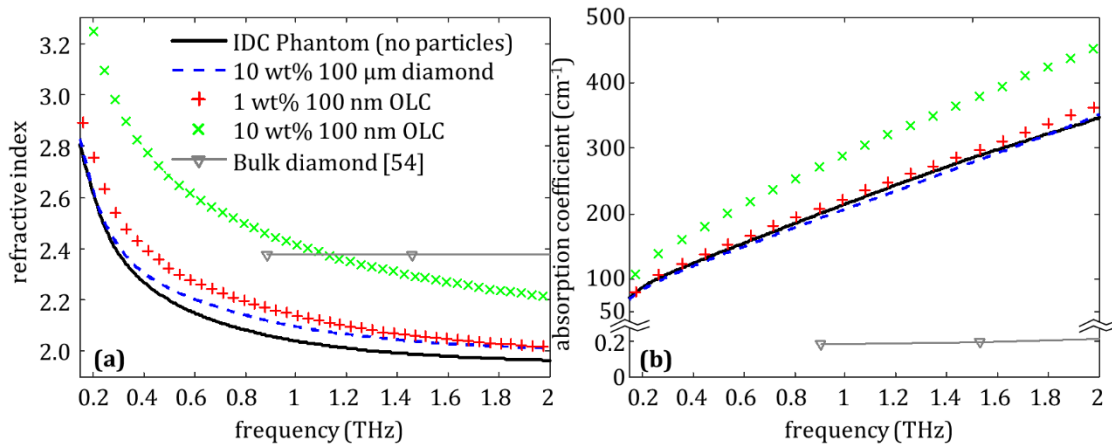


Figure 9. The average refractive index and absorption coefficient for IDC phantoms that contain either 10% of pristine 100 μm diamond, 1% of 100 nm OLC or 10% of 100 nm OLC.

Fig. 9a shows that the refractive index of the IDC phantom tissues increases slightly from the 100 μm microdiamonds at frequencies between 1 and 2 THz. However, the increase is minimal and not enough to provide a significant contrast. The 1% OLC shows a more uniform increase, although small, in the refractive index across the entire frequency range. On the other hand, the phantom with 10% OLC is seen to have a significantly higher refractive index than the IDC phantom alone. The absorption coefficient of the phantoms in Fig. 9b shows similar trends to refractive index in Fig. 9a. The results indicate that the 100 nm OLC shows the greatest potential for use as a contrast agent out of all the particles tested in this work, as it shows a noticeable change in the properties of the IDC phantom even in low concentrations.

It should be noted that there is a difference in refractive index between the 10% 100 nm OLC in the IDC phantom in Fig. 9a and the 10% 100 nm OLC in polyethylene in Fig. 8a, especially at lower frequencies. This is due to the nature of the background material, as the OLC is seen to provide a consistent increase over the pure polyethylene or over the IDC phantom without particles. For OLC, this shift in the refractive index is seen to be more significant at lower frequencies in Fig. 8a. This low frequency emphasis combined with the high refractive index at

low frequencies in the IDC phantom generates the very strong increase seen in the phantom with OLC added in Fig. 9a.

4. Results of Breast Phantom Tumor Imaging with and without OLC Particles

Due to the significant THz interaction observed for the 100 nm OLC in PDMS, polyethylene, and in IDC phantom background media, it is selected for use in a THz reflection mode imaging setup to examine the practical contrast improvement potential of these particles. The setup is similar to that of Fig. 1a but with the signal reflected from the sample as seen in Fig. 1b. As an initial test, four breast phantom tissues are developed following our recipe in [49] and [50] and compared in Fig. 10. The four samples are made as follows: one fibroglandular phantom without particles, one IDC phantom without particles, one IDC phantom with 1% 100 nm OLC, and one IDC phantom with 10% 100 nm OLC. Since OLC can be functionalized to selectively bind to cancer cells, only OLC implementation into the cancer phantom is investigated here. A THz raster scan is performed of each phantom at step size of 400 μm , and the results are shown in Fig. 10. All THz images are generated by taking the peak value of the reflected electric field signal at each pixel and normalizing by the peak value of the incident signal [23-25]. Fig. 10a shows the reflection for the fibro phantom. It should be noted that there is some amount of random noise present in the THz image despite being a solid phantom, which is primarily due to sample surface roughness creating small air pockets between the phantom and the polystyrene plate used for holding the sample. This roughness is a common challenge in fresh tissue as well, as an uneven tissue surface can result in air gaps with the polystyrene plate as was observed in our previous work [24]. While several attempts were made to minimize the roughness and associated noise in the phantom, thus far it has not been fully resolved and therefore appears in all phantom imaging in this work. Fig. 10b shows the THz image of the IDC phantom without the particles. It should

be noted that the reflected field from the IDC phantom inherently shows slightly higher values than the fibro phantom, as is indicated by the slight change of field color from light blue to yellow. This corresponds to a fibro reflection between 0.14 and 0.17 in arbitrary units of the electric field compared to the 0.17 to 0.2 seen in the IDC phantom, which is expected due to the challenging difference in the THz properties between the two tissue types. In all figures there is a rim of higher reflection seen in the red color surrounding each phantom that corresponds to a Teflon spacer used to contain the phantoms while they were being held down for imaging.

Fig. 10c shows a THz image of an IDC phantom with the same recipe as Fig. 10b but with 1% 100 nm OLC added. Here the reflected field is shown to increase to values closer to 0.2 units, which provides greater contrast against the fibro phantom than the IDC phantom alone, although the change in values is small. Finally, the THz image of the IDC phantom with 10% OLC is shown in Fig. 10d. In this case a significant increase in the reflection of the phantom is seen, with an improvement in reflected field of nearly 50% from the IDC phantom alone shown in Fig. 10b. The small area of higher reflection on the left side of the sample in Fig. 10d is most likely due to accumulated OLC that did not uniformly distribute in the phantom. The potential of OLC as an effective contrast agent in THz imaging is consistent with the increases observed in the refractive index and absorption coefficient seen in Fig. 9.

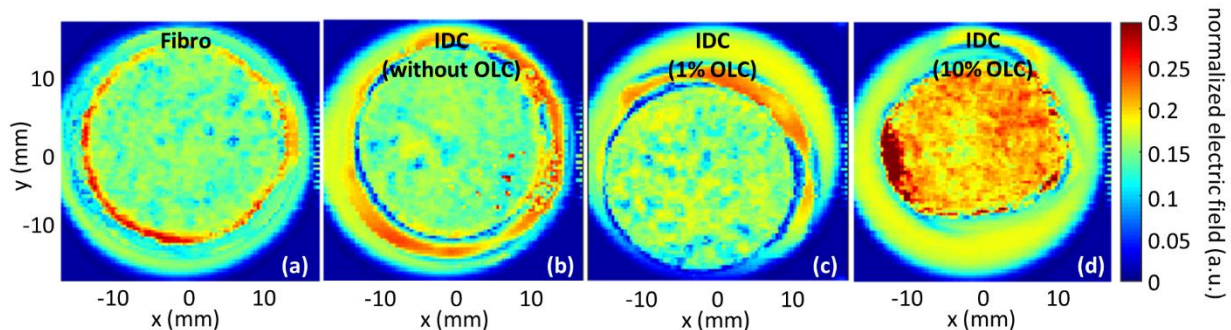


Figure 10. THz reflection images of single phantoms generated by taking the reflection peak normalized to the incident signal peak. (a) Fibro phantom with no OLC, (b) IDC phantom with no OLC, (c) IDC phantom with 1% 100 nm OLC, and (d) IDC phantom with 10% 100 nm OLC.

To investigate the effectiveness of the OLC as a contrast agent when dispersed through adjacent IDC and fibroglandular (fibro) tissues, a three-dimensional phantom tumor model is developed as shown in Fig. 11. IDC phantoms with and without OLC are generated (Fig. 11a) and wrapped in a fibroglandular phantom to simulate a highly fibrous margin as shown in Fig. 11b. For developing the phantom tumors with OLC, particles are added and mixed with the IDC phantom in either 1% or 10% concentrations. The phantom tumor bulk is then bisected to expose a surface with adjacent IDC and fibro phantom tissues for imaging as seen in Fig. 11c. Finally, the phantom is scanned in the reflection mode as shown in Fig. 11d. While the THz signal has experimentally shown penetration up to 300 μm in the fibro phantom for reflection imaging of hidden IDC phantoms, this application is focused on imaging just the surgical edge of excised tissue and not for scanning human bodies. Therefore, this setup is selected to emulate THz imaging of freshly excised tissues similar to our ongoing research using fresh animal and human excised tumors.

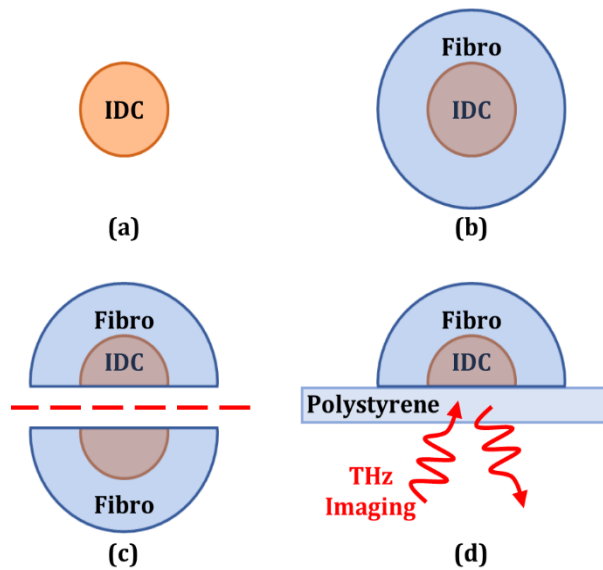


Figure 11. Steps in phantom tumor model formation with (a) IDC phantom core, (b) phantom fibro surrounding IDC, (c) tumor model bisection, and (d) THz reflection imaging setup where the emitter and detector are below the sample.

Figs. 12a-c show the photographs of the phantom tumors including the IDC phantom without OLC, the IDC phantom with 1% OLC, and the IDC phantom with 10% OLC, respectively. For these photos, the fibro phantom is dyed with green food coloring while the IDC phantom is dyed with red food coloring for comparison. These colors have no effect on THz signals. However, for the IDC phantoms containing OLC, the color of the carbon particles make the phantom appear grey or black instead. The THz images are given for the sample without OLC in Fig. 12d, with 1% OLC in Fig. 12e, and with 10% OLC in Fig. 12f. All images are produced using the same normalized reflection peak against the incident peak as described for Fig. 10. For each THz image, the outline of the IDC region in the photograph was superimposed as a dashed line to compare the regions of the phantom. The comparison between the IDC and fibro phantoms without OLC in Figs. 12a and 12d shows that there is some distinction between the two regions. However, the contrast is low, and the noise attributed to the surface roughness of the phantom causes dips in the IDC below the values of the fibro which serves as an additional challenge in interpreting the THz image. The sample with 1% OLC in Figs. 12b and 12e shows faint contrast between the two regions as well. This is expected from the 1% OLC showing a relatively small effect in the spectroscopy of the phantom in Fig. 9 and in the image in Fig. 10c. Finally, the sample with 10% OLC in Figs. 12c and 12f shows a drastically increased reflection for the IDC phantom compared to the surrounding fibro phantom and compared to the sample without OLC. This increase in reflection in Fig. 12f is consistent with spectroscopy of the phantom with 10% OLC in Fig. 9 due to the strong increase in the refractive index and absorption coefficient, which both increase the reflected signal. Here the reflection of the IDC phantom is almost doubled compared with that of the other two samples, while the fibro phantom is approximately the same. Therefore, the OLC in a 10% concentration is shown to be a potential contrast agent in THz imaging of breast cancer.

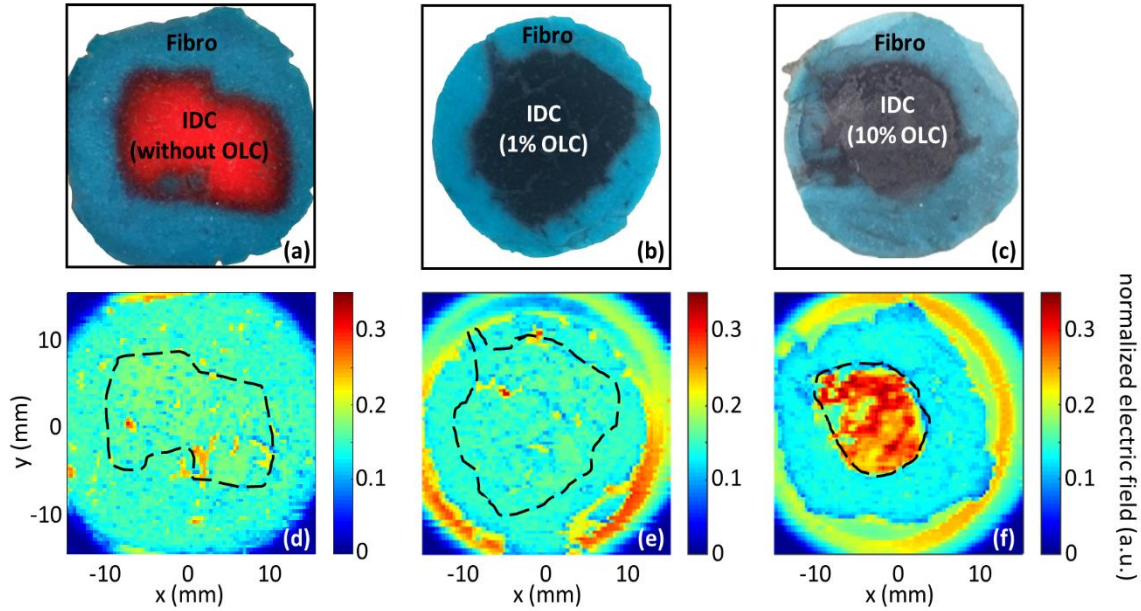


Figure 12. THz reflection imaging of combined phantoms shown in photographs for (a) photo of IDC phantom with no OLC, (b) photo of IDC phantom with 1% of 100 nm OLC, and (c) photo of IDC phantom with 10% of 100 nm OLC. THz images in (d-f) show the resulting THz reflection images for (d) no OLC in IDC, (e) 1% OLC in IDC, and (f) 10% OLC in IDC.

5. Conclusions

This work has investigated various carbon-based particles as potential contrast agents in THz imaging. Overall, OLC demonstrates the greatest interaction with the THz signal compared with microdiamonds and nanodiamonds investigated in the same background medium. Also THz imaging of 10% OLC in cancer phantoms shows greater enhancement of the THz response than other nanoparticles used in THz imaging without the need for external sources as reported in the literature [27-29]. Other works showed that OLC is suitable for functionalization that would cause them to selectively bind to cancer cells, making it promising for future investigations in THz margin assessment of breast cancer and possible other types of cancer [40]. The significance of the OLC 100 nm results presented here is that their size is a fraction of the THz wavelengths used in this work. The broadband interaction of OLC with electromagnetic waves, despite its sub-wavelength size, was attributed to its physical features at multiple sizes including defects in the

onion-like layers, the overall aggregate size of the particles, and the interaction of larger conglomerates of adjacent OLC particles due to the graphene-like structure of the outer layers [37], [39].

The use of OLC as a THz contrast agent primarily depends on the size and safety limitations of the particles [41], [42]. Thus far there is relatively little research into the biological safety of OLC. For higher concentrations reported in literature, 6 mg/L (0.6% by weight in water) of 30 nm OLC showed some concerns of gene damage but less than carbon nanotubes [42], and 3000 $\mu\text{g/mL}$ (0.3% by weight in water) showed only a minor reduction in cell viability [43]. Compared to the highest reported concentration of 0.6% 30 nm OLC, the same number of 100 nm OLC particles would be ~22% by weight in water. Thus, the concentrations reported in this work are feasible; however, additional research is needed. Trends in the spectroscopy of OLC imply that smaller sizes may provide even greater contrast than the 100 nm particles investigated here. As such, future work will focus on particle injection in animal model (murine) in vivo to investigate toxicity and safe particle concentration, and additional work is being conducted to measure the sensitivity and specificity of THz imaging in fresh tissue applications.

Acknowledgments

This work was funded in part by NSF/ECCS award #140800, NSF/DGE award #1450079, NIH award R15CA208798, and the University of Arkansas Distinguished Doctoral Fellowship. The pulsed THz system used in this work was funded by NSF/MRI award #1228958.

References

- [1] A. M. Hassan and M. El-Shenawee, "Review of Electromagnetic Techniques for Breast Cancer Detection," *IEEE Rev. Biomed. Eng.* **4**, 103–118 (2011). [doi:10.1109/RBME.2011.2169780]
- [2] A. J. Surowiec, S. S. Stuchly, J. R. Barr, and A. Swarup, "Dielectric Properties of Breast Carcinoma and the Surrounding Tissues," *IEEE Trans. Biomed. Eng.* **35**(4), 257–263 (1988). [doi:10.1109/10.1374]

- [3] W. T. Joines, Y. Zhang, C. Li, and R. L. Jirtle, "The measured electrical properties of normal and malignant human tissues from 50 to 900 MHz," *Med. Phys.* **21**(4), 547–550 (1994). [doi:10.1118/1.597312]
- [4] J. W. Choi, J. Cho, Y. Lee, J. Yim, B. Kang, K. K. Oh, W. H. Jung, H. J. Kim, C. Cheon, H. Lee, and Y. Kwon, "Microwave detection of metastasized breast cancer cells in the lymph node; potential application for sentinel lymphadenectomy," *Breast Cancer Res. Treat.* **86**(2), 107–115 (2004). [doi:10.1023/B:BREA.0000032979.52773.fb]
- [5] A. M. Campbell and D. V Land, "Dielectric properties of female human breast tissue measured in vitro at 3.2 GHz," *Phys. Med. Biol.* **37**(1), 193–210 (1992). [doi:10.1088/0031-9155/37/1/014]
- [6] M. Lazebnik, L. McCartney, D. Popovic, C. B. Watkins, M. J. Lindstrom, J. Harter, S. Sewall, A. Magliocco, J. H. Booske, M. Okoniewski, and S. C. Hagness, "A large-scale study of the ultrawideband microwave dielectric properties of normal breast tissue obtained from reduction surgeries," *Phys. Med. Biol.* **52**(10), 2637–2656 (2007). [doi:10.1088/0031-9155/52/10/001]
- [7] M. Lazebnik, D. Popovic, L. McCartney, C. B. Watkins, M. J. Lindstrom, J. Harter, S. Sewall, T. Ogilvie, A. Magliocco, T. M. Breslin, W. Temple, M. Daphne, J. H. Booske, M. Okoniewski, and S. C. Hagness, "A large-scale study of the ultrawideband microwave dielectric properties of normal, benign and malignant breast tissues obtained from cancer surgeries," *Phys. Med. Biol.* **52**(20), 6093–6115 (2007). [doi:10.1088/0031-9155/52/20/002]
- [8] V. G. Peters, D. R. Wymant, M. S. Patterson, and G. L. Frank, "Optical properties of normal and diseased human breast tissues in the visible and near infrared," *Phys. Med. Biol.* **35**(9), 1317–1334 (1990). [doi:10.1088/0031-9155/35/9/010]
- [9] G. M. Palmer and N. Ramanujam, "Monte Carlo-based inverse model for calculating tissue optical properties. Part II: Application to breast cancer diagnosis," *Appl. Opt.* **45**(5), 1072–1078 (2006). [doi:10.1364/AO.45.001072]
- [10] Q. R. J. G. Tummers, F. P. R. Verbeek, B. E. Schaafsma, M. C. Boonstra, J. R. van der Vorst, G.-J. Liefers, C. J. H. van de Velde, J. V Frangioni, and A. L. Vahrmeijer, "Real-time intraoperative detection of breast cancer using near-infrared fluorescence imaging and Methylene Blue," *Eur. J. Surg. Oncol.* **40**(7), 850–858 (2014). [doi:10.1016/j.ejso.2014.02.225]
- [11] S. Kumar, C. Desmedt, D. Larsimont, C. Sotiriou, and E. Goormaghtigh, "Change in the microenvironment of breast cancer studied by FTIR imaging," *Analyst* **138**(14), 4058–4065 (2013). [doi:10.1039/c3an00241a]
- [12] V. Sharma, S. Shivalingaiah, Y. Peng, D. Euhus, Z. Gryczynski, and H. Liu, "Auto-fluorescence lifetime and light reflectance spectroscopy for breast cancer diagnosis: potential tools for intraoperative margin detection," *Biomed. Opt. Express* **3**(8), 1825–1840 (2012). [doi:10.1364/BOE.3.001825]

- [13] D. M. Layfield, D. J. May, R. I. Cutress, C. Richardson, A. Agrawal, M. Wise, and C. Yiangou, "The effect of introducing an in-theatre intra-operative specimen radiography (IOSR) system on the management of palpable breast cancer within a single unit," *The Breast* **21**(4), p. 459-463 (2012). [doi:10.1016/j.breast.2011.10.010]
- [14] L. Bathla, A. Harris, M. Davey, P. Sharma, and E. Silva, "High resolution intra-operative two-dimensional specimen mammography and its impact on second operation for re-excision of positive margins at final pathology after breast conservation surgery," *Amer. J. Surg.* **202**(4), 387-394 (2011). [doi:10.1016/j.amjsurg.2010.09.031]
- [15] P. D. Britton, L. I. Sonoda, A. K. Yamamoto, B. Koo, E. Soh, and A. Goud, "Breast surgical specimen radiographs: How reliable are they?" *European Journal of Radiology* **79**(2), 245-249 (2011). [doi:10.1016/j.ejrad.2010.02.012]
- [16] C. Rua, P. Lebas, P. Michenet, and L. Ouldamer, "Evaluation of lumpectomy surgical specimen radiographs in subclinical, in situ and invasive breast cancer, and factors predicting positive margins," *Diagn. Interv. Imaging* **93**(11), 871-877 (2012). [doi:10.1016/j.diii.2012.07.010]
- [17] G. J. Wilmink and J. E. Grundt, "Invited Review Article: Current State of Research on Biological Effects of Terahertz Radiation," *J. Infrared Millim. Terahertz Waves* **32**(10), 1074–1122 (2011). [doi:10.1007/s10762-011-9794-5]
- [18] P. Y. Han, G. C. Cho, and X. C. Zhang, "Time-domain transillumination of biological tissues with terahertz pulses," *Opt. Lett.* **25**(4), 242–244 (2000). [doi:10.1364/OL.25.000242]
- [19] P. C. Ashworth, E. Pickwell-MacPherson, E. Provenzano, S. E. Pinder, A. D. Purushotham, M. Pepper, and V. P. Wallace, "Terahertz pulsed spectroscopy of freshly excised human breast cancer," *Opt. Express* **17**(15), 12444–12454 (2009). [doi:10.1364/OE.17.012444]
- [20] A. J. Fitzgerald, V. P. Wallace, M. Jimenez-linan, L. Bobrow, R. J. Pye, and A. D. Purushotham, "Terahertz Pulsed Imaging of human breast tumors," *Radiology* **239**(2), 533–540 (2006). [doi:10.1148/radiol.2392041315]
- [21] R. M. Woodward, V. P. Wallace, R. J. Pye, B. E. Cole, D. D. Arnone, E. H. Lin, and M. Pepper, "Terahertz Pulse Imaging of ex vivo Basal Cell Carcinoma," *J. Invest. Dermatol.* **120**(1), 72–78 (2003). [doi:10.1046/j.1523-1747.2003.12013.x]
- [22] S. Yamaguchi, Y. Fukushi, O. Kubota, T. Itsuji, T. Ouchi, and S. Yamamoto, "Brain tumor imaging of rat fresh tissue using terahertz spectroscopy," *Sci. Rep.* **6**, 1–6 (2016). [doi:10.1038/srep30124]
- [23] T. Bowman, M. El-Shenawee, and L. K. Campbell, "Terahertz transmission vs reflection imaging and model-based characterization for excised breast carcinomas," *Biomed. Opt. Express* **7**(9), 3756–3783 (2016). [doi:10.1364/BOE.7.003756]

- [24] T. C. Bowman, M. El-Shenawee, and L. K. Campbell, "Terahertz Imaging of Excised Breast Tumor Tissue on Paraffin Sections," *IEEE Trans. Antennas Propag.* **63**(5), 2088–2097 (2015). [doi:10.1109/TAP.2015.2406893]
- [25] T. Bowman, Y. Wu, J. Gauch, L. K. Campbell, M. El-Shenawee, "Terahertz Imaging of Three-Dimensional Dehydrated Breast Cancer Tumors," *Journal of Infrared, Millimeter, and Terahertz Waves*, **38**(6), 766–786 (2017). [doi:10.1007/s10762-017-0377-y]
- [26] Y. Miura, A. Kamataki, M. Uzuki, T. Sasaki, J. Nishizawa, and T. Sawai, "Terahertz-wave spectroscopy for precise histopathological imaging of tumor and non-tumor lesions in paraffin sections," *Tohoku J. Exp. Med.* **223**(4), 291–296 (2011). [doi:10.1620/tjem.223.291]
- [27] S. J. Oh, J. Kang, I. Maeng, J.-S. Suh, Y. M. Huh, S. Haam, and J.-H. Son, "Nanoparticle-enabled terahertz imaging for cancer diagnosis," *Opt. Express* **17**(5), 3469–3475, 2009. [doi:10.1364/OE.17.003469]
- [28] J. Y. Park, H. J. Choi, G. Nam, K. Cho, and J. Son, "In Vivo Dual-Modality Terahertz/Magnetic Resonance Imaging Using Superparamagnetic Iron Oxide Nanoparticles as a Dual Contrast Agent," *IEEE Trans. Terahertz Sci. Technol.* **2**(1), 93–98 (2012). [doi:10.1109/TTHZ.2011.2177174]
- [29] R. Zhang, L. Zhang, T. Wu, S. Zuo, R. Wang, J. Zhang, and J. Fang, "Contrast-enhanced continuous-terahertz-wave imaging based on superparamagnetic iron oxide nanoparticles for biomedical applications," *Opt. Express* **24**(8), 7915–7921 (2016). [doi:10.1364/OE.24.007915]
- [30] D. K. Lee, H. Kim, T. Kim, B. Cho, K. Lee, and J. H. Son, "Characteristics of gadolinium oxide nanoparticles as contrast agents for terahertz imaging," *J. Infrared Millim. Terahertz Waves* **32**(4), 506–512 (2011). [doi:10.1007/s10762-011-9776-7]
- [31] M. Ney and I. Abdulhalim, "Ultrahigh polarimetric image contrast enhancement for skin cancer diagnosis using InN plasmonic nanoparticles in the terahertz range," *J. Biomed. Opt.* **20**(12), 125007 (2015). [doi:10.1117/1.JBO.20.12.125007]
- [32] Y. Y. Hui and H.-C. Chang, "Recent Developments and Applications of Nanodiamonds as Versatile Bioimaging Agents," *J. Chinese Chem. Soc.* **61**(1), 67–76 (2014). [doi:10.1002/jccs.201300346]
- [33] S. Giordani, J. Bartelmess, M. Frasconi, I. Biondi, S. Cheung, M. Grossi, D. Wu, L. Echegoyen, and D. F. O'Shea, "NIR fluorescence labelled carbon nano-onions: synthesis, analysis and cellular imaging," *J. Mater. Chem. B* **2**, 7459–7463 (2014). [doi:10.1039/C4TB01087F]
- [34] V. Vaijayanthimala, P.-Y. Cheng, S.-H. Yeh, K.-K. Liu, C.-H. Hsiao, J.-I. Chao, and H.-C. Chang, "The long-term stability and biocompatibility of fluorescent nanodiamond as an in vivo contrast agent," *Biomaterials* **33**(31), 7794–7802 (2012). [doi:10.1016/j.biomaterials.2012.06.084]

- [35] Y. Xing, W. Xiong, L. Zhu, E. Osawa, S. Hussin, and L. Dai, "DNA Damage in Embryonic Stem Cells Caused by Nanodiamonds," *ACS Nano* **5**(3), 2376–2384 (2011). [doi:10.1021/nn200279k]
- [36] J. Bartelmess, S. J. Quinn, and S. Giordani, "Carbon nanomaterials: multi-functional agents for biomedical fluorescence and Raman imaging," *Chem. Soc. Rev.* **44**, 4672–4698 (2014). [doi:10.1039/C4CS00306C]
- [37] J. Macutkevic, J. Banys, S. Moseenkov, V. Kuznetsov, N. Nunn, and O. Shenderova, "Dielectric Properties of Onion-Like Carbon and Detonation Nanodiamond/Polydimethylsiloxane Composites," *Polym. Compos.* **36**(11), 1–9 (2014). [doi:10.1002/pc.23119]
- [38] I. Kranauskaite, J. Macutkevic, J. Banys, E. Talik, V. Kuznetsov, N. Nunn, and O. Shenderova, "Synergy effects in the electrical conductivity behavior of onion-like carbon and multiwalled carbon nanotubes composites," *Phys. Status Solidi B* **252**(8), 1–5 (2015). [doi:10.1002/pssb.201451745]
- [39] O. Shenderova, V. Grishko, G. Cunningham, S. Moseenkov, G. McGuire, and V. Kuznetsov, "Onion-like carbon for terahertz electromagnetic shielding," *Diam. Relat. Mater.* **17**(4-5), 462–466 (2008). [doi:10.1016/j.diamond.2007.08.023]
- [40] M. Frasconi, R. Marotta, L. Markey, K. Flavin, V. Spampinato, G. Ceccone, L. Echegoyen, E. M. Scanlan, and S. Giordani, "Multi-Functionalized Carbon Nano-onions as Imaging Probes for Cancer Cells," *Chem. Eur. J.* **21**(52), 19071–19080 (2015). [doi:10.1002/chem.201503166]
- [41] M. Yang, K. Flavin, I. Kopf, G. Radics, C. H. A. Hearnden, G. J. McManus, B. Moran, A. Villalta-Cerdas, L. A. Echegoyen, S. Giordani, and E. C. Lavelle, "Functionalization of Carbon Nanoparticles Modulates Inflammatory Cell Recruitment and NLRP3 Inflammasome Activation," *Small* **9**(24), 4194–4206 (2013). [doi:10.1002/smll.201300481]
- [42] L. Ding, J. Stilwell, T. Zhang, O. Elboudwarej, H. Jiang, J. P. Selegue, P. A. Cooke, J. W. Gray, and F. F. Chen, "Molecular Characterization of the Cytotoxic Mechanism of Multiwall Carbon Nanotubes and Nano-Onions on Human Skin Fibroblast," *Nano Lett.* **5**(12), 2448–2464 (2005). [doi:10.1021/nl051748o]
- [43] J. Luszczyn, M. E. Plonska-Brzezinska, A. Palkar, A. T. Dubis, A. Simionescu, D. T. Simionescu, B. Kalska-Szostko, K. Winkler, and L. Echegoyen, "Small noncytotoxic carbon nano-onions: First covalent functionalization with biomolecules," *Chem. - A Eur. J.* **16**(16), 4870–4880 (2010). [doi:10.1002/chem.200903277]
- [44] J. Bartelmess and S. Giordani, "Carbon nano-onions (multi-layer fullerenes): Chemistry and applications," *Beilstein J. Nanotechnol.* **5**(1), 1980–1998 (2014). [doi:10.3762/bjnano.5.207]

- [45] K. Ito, K. Furuya, Y. Okano, and L. Hamada, "Development and Characteristics of a Biological Tissue-Equivalent Phantom for Microwaves," *Electron. Commun. Japan Part I Commun.* **84**(4), 67–77 (2001). [doi:10.1002/1520-6424(200104)84:4<67::AID-ECJA8>3.0.CO;2-D]
- [46] M. Lazebnik, E. L. Madsen, G. R. Frank, and S. C. Hagness, "Tissue-mimicking phantom materials for narrowband and ultrawideband microwave applications," *Phys. Med. Biol.* **50**(18), 4245–4258 (2005). [doi:10.1088/0031-9155/50/18/001]
- [47] G. C. Walker, E. Berry, S. W. Smye, and D. S. Brettell, "Materials for phantoms for terahertz pulsed imaging," *Phys. Med. Biol.* **49**(21), N363–N369 (2004). [doi:10.1088/0031-9155/49/21/N01]
- [48] C. Reid, A. P. Gibson, J. C. Hebden, and V. P. Wallace, "An oil and water emulsion phantom for biomedical terahertz spectroscopy," *Proc. 4th IEEE-EMBS Intl. Summer School and Symposium on Medical Devices and Biosensors*, 25–28 (2007). [doi:10.1109/ISSMDBS.2007.4338284]
- [49] A. Walter, T. Bowman, and M. El-Shenawee, "Development of breast cancer tissue phantoms for terahertz imaging," *Proc. SPIE* **9700**, 970003 (2016). [doi:10.1117/12.2211176]
- [50] A. Walter, "Development of Breast Tissue Phantoms for Enhanced Terahertz Imaging Utilizing Microdiamond and Nano-Onion Particles," University of Arkansas (2017).
- [51] S. Tomita, M. Fujii, and S. Hayashi, "Optical extinction properties of carbon onions prepared from diamond nanoparticles," *Phys. Rev. B* **66**(25), 245424 (2002). [doi:10.1103/PhysRevB.66.245424]
- [52] K. Lal and R. Parshad, "The permittivity of heterogeneous mixtures," *J. Phys. D. Appl. Phys.* **6**(11), 1363–1368 (1973). [doi:10.1088/0022-3727/6/11/311]
- [53] J. Macutkevicius, I. Kranauskaite, J. Banys, S. Moseenkov, V. Kuznetsov, and O. Shenderova, "Metal-insulator transition and size dependent electrical percolation in onion-like carbon/polydimethylsiloxane composites," *J. Appl. Phys.* **115**(21), 213702 (2014). [doi:10.1063/1.4880995]
- [54] V. V. Kubarev, "Optical properties of CVD-diamond in terahertz and infrared ranges," *Nucl. Instr. Meth. Phys. Res. A*, **603**(1-2), 22-24 (2009). [doi:10.1016/j.nima.2008.12.121]

Chapter 6: Pulsed Terahertz Imaging of Breast Cancer in Freshly Excised Murine Tumors

© 2017 SPIE. Reprinted by permission from T. Bowman, T. Chavez, K. Khan, J. Wu, A. Chakraborty, N. Rajaram, K. Bailey, and M. El-Shenawee, “Pulsed terahertz imaging of breast cancer in freshly excised murine tumors,” *Journal of Biomedical Optics*, vol. 23, no. 2, pp. 026004, 2018. [doi: 10.1117/1.JBO.23.2.026004]

Abstract

This paper investigates terahertz imaging and classification of freshly excised murine xenograft breast cancer tumors. These tumors are grown via injection of E0771 breast adenocarcinoma cells into the flank of mice maintained on high-fat diet. Within one hour of excision, the tumor and adjacent tissues are imaged using a pulsed terahertz system in the reflection mode. The THz images are classified using a statistical Bayesian mixture model with unsupervised and supervised approaches. Correlation with digitized pathology images is conducted using classification images assigned by a modal class decision rule. The corresponding receiver operating characteristic (ROC) curves are obtained based on the classification results. A total of thirteen tumor samples obtained from nine tumors are investigated. The results show good correlation of THz images with pathology results in all samples of cancer and fat tissues. For tumor samples of cancer, fat, and muscle tissues, THz images show reasonable correlation with pathology where the primary challenge lies in the overlapping dielectric properties of cancer and muscle tissues. The use of a supervised regression approach shows improvement in the classification images although not consistently in all tissue regions. Advancing THz imaging of breast tumors from mice and the development of accurate statistical models will ultimately progress the technique for the assessment of human breast tumor margins.

1. Introduction

Terahertz (THz) imaging technology has been a growing area of interest for biomedical applications [1]. For example, pulsed THz systems have been used to conduct imaging of liver

cirrhosis [2], osseous tissue damage [3], and differentiation of cancerous tissues of the brain [4], stomach [5], colon [6] and breast [7]–[10], among others. However, imaging of breast and other cancers has been mostly limited to formalin-fixed, paraffin-embedded (FFPE) tissue to date, with only a few studies working with freshly excised tissue due to the challenges of obtaining fresh tissue outside of a surgical setting [4], [10]–[12]. One alternative to fresh human tissue, as used in this work, is tumors from mice. Mice have notably been used to generate xenograft brain tumors for THz imaging of fresh and FFPE tissue using either 9L/lacZ glioma cells [4] or 6C glioma cells [13]. They have also been used to obtain FFPE xenograft liver tumors from H22 liver cancer cells for THz imaging [14] and breast cancer tumors grown from MDA MB 231 cells imaged subcutaneously *in vivo* and fresh *ex vivo* [15]. This work makes use of E0771 mouse-derived breast adenocarcinoma to generate xenograft tumors for excision and THz imaging. Additionally, a high-fat diet is used to provide a sufficient fatty background for xenograft tumors to more closely resemble human excised tissue [16].

While a significant amount of THz imaging has been able to qualitatively compare produced images of tissue to pathology sections [8], [9], the quantification of THz image accuracy has been limited so far. This process generally requires some automatic classification or thresholding of THz image data and digitization of pathology information for comparison. Digitization of pathology in this work is obtained using a morphing algorithm, which enables a pixel-by-pixel comparison between the THz images and digitized pathology results [7], [17]. Of classification methods used for THz imaging of fresh tissue, the use of support vector machines (SVM) and principal component analysis (PCA) reported up to 92% accuracy for breast cancer when combined [18]. The techniques used separately showed a 96% sensitivity and 87% specificity for SVM and 92% sensitivity and 87% specificity for PCA of normal vs dysplastic

tissue in colon cancer imaging [19]. SVM also attained a 72% discrimination in 1.89 THz continuous wave imaging of breast cancer [7]. In applications not handling fresh tissue, SVM was used for FFPE tissue imaging and spectroscopy [5,20,21]. Only a few other methods have been used for fresh tissue imaging, such as PCA for murine brain glioma [4]. However, several classification methods have been applied to FFPE tissue applications and/or spectroscopy of tissues including: wavelet transformation for osteosarcoma [22], orthogonal signal correction and fuzzy rule-bending expert system for cervical cancer [23], multispectral classification of FFPE basal cell carcinoma [24], and PCA for potentially malignant skin nevi [25] and FFPE liver cancer [26], [27].

This work investigates a Bayesian mixture model utilizing a Markov chain Monte Carlo (MCMC) scheme for THz image classification of both fresh and FFPE murine breast tumors [28]. The current work is different from the authors' previous work where they performed qualitative THz imaging and characterization of FFPE breast cancer tissue [8,9] as well as THz imaging and image processing of three-dimensional FFPE breast cancer tissue and characterization of carbon nanoparticles for THz contrast enhancement [29], [30]. Preliminary results using the methods in this work on a frozen tissue sample have been published in conference proceedings [31], [32]. To the authors' knowledge, this is the first time the Bayesian mixture model has been applied to THz imaging applications, and it is also the first time that the E0771 breast adenocarcinoma cells have been used in THz imaging.

This work is organized as follows: methodology including mice tumor sample preparation, image acquisition, and the statistical model in Section 2; the results of THz image correlation with pathology in Section 3; and discussion and concluding remarks in Section 4.

2. Methodology

2.1. Terahertz Imaging Setup

This work makes use of the TPS Spectra 3000 THz pulsed imaging and spectroscopy system (TeraView, Ltd., UK) at the University of Arkansas. A diagram of the system can be seen in Fig. 1. The THz emitter is a biased bowtie antenna on a GaAs substrate excited by a femtosecond Ti:Sapphire laser pulse to generate the THz signal. The signal is then directed using mirrors to the sample as seen in Fig. 1a. For this work, two imaging setups are observed. For formalin-fixed, paraffin-embedded (FFPE) samples, the tissue block surface is imaged directly as seen in Fig. 1a. The setup in Fig. 1b is used in fresh tissue samples, where a polystyrene plate is placed between the tissue and the system to provide a consistent imaging plane and to prevent fluid leakage into the system optics. A second polystyrene plate is placed on top of the tissue to provide light pressure

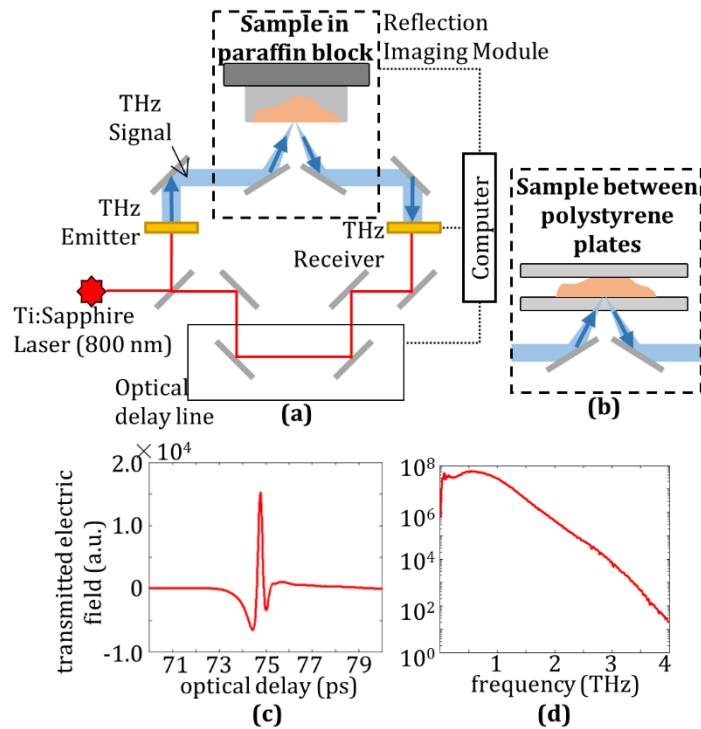


Figure 1. (a) Diagram of THz imaging system in reflection mode for FFPE tissue in paraffin block or for (b) fresh tissue between polystyrene plates. (c) Incident time domain signal and (d) incident spectrum following Fourier transform.

to keep the tissue interface flat with the imaging window. The incident THz time-domain signal is seen in Fig. 1c, and the Fourier transform of the signal is shown in Fig. 1d, demonstrating a frequency range from 0.1 to 4 THz. To generate the THz image, the stage holding the sample is scanned in steps (smallest step is 50 μm with 200 μm used in all results in this work). The reflected THz pulse is measured at each pixel. For FFPE samples, the THz image is obtained from the peak value of the reflected signal normalized against the incident signal peak obtained using a golden mirror. For fresh tissue samples, better image clarity was observed by taking the spectral power across a selected range, f_1 to f_2 , as [11]:

$$\text{spectral power} = \int_{f_1}^{f_2} |E_{\text{samp}}(f_{\text{THz}})|^2 / |E_{\text{ref}}(f_{\text{THz}})|^2 df_{\text{THz}}, \quad (1)$$

where E_{samp} is the magnitude of the reflected sample signal following Fourier transform, E_{ref} is a reference signal from the polystyrene plate interface with air at the same plane as the fresh tissue (to keep the signal focus the same), and f_{THz} is the frequency in THz. This calculation is only used for fresh tissue because the FFPE tissue is low-absorption and therefore subject to multiple reflections [29], which can cause frequency domain oscillations.

2.2. Mice Tumor Sample preparation

E0771 murine breast adenocarcinoma cells were grown in RPMI 1640 media supplemented with 10% fetal bovine serum (FBS), 1% L-Glutamine, and 1% penicillin-streptomycin. These cells were kept in a humidified incubator (5% CO_2 and 37°C) and cultured when the cells reached 75-90% confluence. This culturing involved passaging the cells by collecting and redistributing them into new petri dishes to prevent overcrowding and cell death. E0771 cells in this work were injected within the first 10 passages to prevent any deterioration in cell viability. For example, one mouse could be injected with cells after 3 passages, while another could be injected after 9 passages, depending on cell availability when each mouse reached its target weight. A group of 10

C57BL/6J mice were maintained on a high-fat diet (D12492 from Research Diets, Inc.) until they reached a target weight of 35g [16]. The mice were then injected in the flank with a subcutaneous bolus (3 million cells suspended in serum- and media-free saline) of E0771 murine breast cancer cells to grow tumor xenografts. Once tumors reached a diameter of 1 cm, tumors and adjacent fat were excised from the mice under anesthesia for terahertz imaging.

Excised samples were transferred in phosphate-buffered saline (PBS) for transfer from the excision site to the THz system and imaged within an hour of excision. Tumors were bisected to have a surface with both cancer and fat at a flat surface for imaging. Following THz imaging, the samples were placed in 10% buffered formalin and shipped to the Oklahoma Disease Diagnostic Laboratory (OADDL) for histopathology assessment.

Of the 10 injected mice, 9 grew sufficient tumors for this study while 1 mouse did not grow any tumors even after multiple injections. For the first 4 tumors only one half of the bisected tumor was imaged as a fresh sample, but as handling improved the latter 5 tumors had both bisected halves imaged, designated as section A and section B in the results presented in Section 3. Some bisections were discarded; for example, the sample designated as 6A was found to have an excessive amount of deterioration in the pathology assessment and was therefore not investigated further. This leaves a total of 13 samples used in this study. All animals received care in compliance with the guidelines outlined in the Guide for the Care and Use of Laboratory Animals. The procedures were approved by the University of Arkansas Institutional Animal Care and Use Committee (IACUC).

2.3. *Correlation Process of THz and Pathology images*

The goal of this work is to quantitatively assess the accuracy of THz images with respect to the pathology results. A pixel-by-pixel comparison is proposed for the generation of receiver

operating characteristic (ROC) curves [7]. Since a pathology photograph has inherently higher resolution than the THz imaging, two processes are implemented to compare the two images. First, a pathology morphing algorithm is used to digitize the histopathology slides and generate a pathology classification at the same resolution and orientation as the THz image, known as the morphed pathology mask. Second, a statistical model is implemented on the THz image to generate a probability-based classification of the different tissue regions in the sample. These two processes are then combined to obtain pixel-by-pixel correlation. The details of these schemes are given in the following sub-sections.

2.3.1. Pathology Morphing and Pathology Mask Generation

To make pixel-by-pixel comparison possible, the image morphing in this work reshapes a pathology image according to the external contour of the THz image to match their external shapes [17]. Although this technique is often used to create a sequence of intermediate images between the source and the target, in this case it is used only to match the pathology to the external contour of the THz image. The morphing algorithm is performed in MATLAB using the following five steps, which are demonstrated in Fig. 2: (i) Masking: a THz image mask (Fig. 2b) is

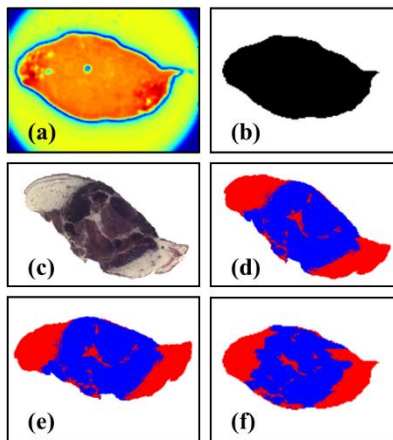


Figure 2. Pathology morphing process for Mouse Tumor 3. (a) THz reflection image of fresh tissue and (b) resulting THz image mask. (c) The low power pathology image, (d) pathology mask, (e) rotated pathology mask, and (f) final morphed pathology mask after resizing and reshaping with respect to the image mask in (b).

established by using the external contour of the original THz image (Fig. 2a). The algorithm uses only the external contour so that the morphed pathology is not affected by features in the THz image. (ii) Classification: low power microscope images of the pathology slide are stitched using a panorama editor, and the stitched image is converted into the Hue, Saturation, and Value (HSV) color model (Fig. 2c). Fat tissue is identified by differences in saturation while fibrous, muscle, and cancer regions are identified by different hue thresholds scaled to the brightness and contrast of the original pathology image. Each identified region is then assigned a value for the pathology results (Fig. 2d). (iii) Rotation: to account for differences in orientation between the THz image and pathology, the pathology mask is temporarily assigned values of 0 (outside) and 1 (inside) and is rotated in 1° iterations. For each rotation, the edges of the pathology and the THz masks are cropped, and the cropped pathology resolution is temporarily reduced to that of the THz mask. The cross-correlation between the two images is performed by using the sum-product operation [33], and the original pathology mask is rotated to the angle with the highest cross-correlation (Fig. 2e). (iv) Resizing: the pathology mask is down-sampled to match the THz mask resolution. (v) Reshaping: a reshaping operation is performed on each row or column of the pathology mask using cubic spline interpolation for stretching or down-sampling for shrinking until it matches the dimensions of THz mask (Fig. 2f) [34].

2.3.2. *Statistical Bayesian Mixture Model*

A statistical Bayesian mixture model is used to classify the THz scan data in a way that it can be compared to pathology. This method produces a vector of probabilities that each pixel in the THz image belongs to a region of tissue. This method provides a two-fold advantage over simple thresholding techniques: (i) the pixels that would be borderline between two different tissue regions can be represented by probability between those two regions, and (ii) a decision rule can

be applied to classify each pixel into individual regions. This work uses a modal class decision rule simply based on which region has the largest probability for each pixel, but additional decision rules can be applied without the need to modify the probability model. This work explores both unsupervised (e.g. Gaussian and t-distribution) and supervised (e.g. regression model) approaches.

The unsupervised approach considers the pixel-wise summarized intensities of the THz image as random variables that are independent but not identically distributed. Pixels from the same tissue region are assumed to follow the same probability distribution while pixels of different regions may have different probability distributions. Hence, the probability distribution for any pixel in the image can be thought of as a mixture model, a weighted sum of parametric probability distributions or mixture components. This work utilizes a Bayesian framework for implementing mixture models. A Markov chain Monte Carlo (MCMC) scheme is used to generate a large number of samples from the posterior joint distribution of mixture parameters and compute empirical summaries for these parameters [28]. To carry out the MCMC, the data augmentation technique in [35] is used. For a THz image of n pixels with x_i denoting the intensity of pixel i for $i = 1, 2, \dots, n$. A hierarchal structure for mixture distribution for x_i is proposed:

$$[x_i | \theta, z_i] \stackrel{ind}{\sim} f(\theta_{z_i}), z_i \sim \mathcal{Mult}(q_1, q_2, \dots, q_k), \pi(\theta) = \prod_{j=1}^k \pi(\theta_j), \pi(q_{1:k}) = \mathcal{Dir}(\alpha_{1:k}), (1)$$

Where z_i is a latent variable corresponding to pixel i that would indicate the tissue region of the pixel. If the image has k distinct tissue regions, $z_i \in \{1, 2, \dots, k\}$. The marginal model for x integrating out the z is a k -component mixture model with mixture weights given by $q_{1:k}$. \mathcal{Mult} and \mathcal{Dir} are abbreviations for multinomial and Dirichlet probability distributions, respectively. θ_j , the parameters for the probability distribution (mean, standard deviation, etc.) for pixels from region j , has a prior distribution $\pi(\theta_j)$ for $j = 1, 2, \dots, k$. $\alpha_{1:k}$ denotes the parameters in the Dirichlet prior for $q_{1:k}$. One can produce different types of mixture model by altering the choice

of the family of distributions for f and the associated set of parameters θ . The two specifications of f that used in this work are described below. Our first proposal is a Gaussian mixture model (Normal distribution):

$$[x_i|z_i = j] = \mathcal{N}(\mu_j, \sigma_j^2), \mu_j \sim \mathcal{N}(\mu_{0j}, c_{0j}), \sigma_j^2 \sim \frac{1}{\sigma_j^2} \quad (2)$$

Where μ_j, σ_j are the location and scale parameters of the Normal-distribution Gaussian function \mathcal{N} for component j . μ_{0j}, c_{0j} are hyper-parameters and assumed to be known. In absence of any reliable prior information, one can arbitrarily choose the c_{0j} to be large to diffuse the prior probability. The prior choice for σ_j^2 is known as the noninformative prior and is improper as well.

Our second proposal is a t -mixture model (t -distribution):

$$[x_i|z_i = j] = t_{d_j}(\mu_j, \sigma_j^2), \mu_j \sim \mathcal{N}(\mu_{0j}, c_{0j}), \sigma_j^2 \sim \frac{1}{\sigma_j^2} \quad (3)$$

Where $d_j \in N$, the degrees of freedom for the j -th component, characterizes the heaviness of the tail. A small value for d_j will produce a heavy tailed t -density curve whereas higher values of d_j will make the tails lighter and will eventually approach Gaussian tails. Hence, instead of using fixed d_j values, the model can be more flexible by learning the possible values of d_j from the data. However, employing the Gibbs sampling technique directly on a t -mixture density is difficult, so the t -density is instead viewed as a scale-mixture of Gaussian density [36]. Here the Gaussian and t -mixture models from (3-4) are employed on each sample. Additionally, skewed mixture models were also investigated as in [37], but the implementation of these models is more complex, and no case was found where they outperform the non-skewed models.

Following each iteration of the model, posterior updates of $\mu_j, \sigma_j^2, q_{1:k}$, and z_i (and d_j for t -mixture) were applied prior to the next iteration. Post-MCMC, posterior draws were collected

for each of z_1, z_2, \dots, z_n . The probability vectors p_t representing the classification uncertainty are empirically calculated as:

$$p_t(j) = \frac{\#z_i=j}{\#Iterations}, i = 1, 2, \dots, n \text{ and } j = 1, 2, \dots, k \quad (5)$$

For this work the number of iterations was set at 20000, while only the latter 10000 were considered for calculating the probability vectors to let the model converge. One important point to note is that the mixture model for the data as mentioned in (2) stays the same for any permutation of $\{\theta_1, \theta_2, \dots, \theta_k\}$, i.e., there is no natural ordering between mixture components. Thus, they must be labeled according to some criterion [38]. Here the mean intensity of the included points in each component is used to number them.

Three assumptions are required for this approach to work: (i) the value of k , the number of regions present in a tumor, is assumed prior to running the MCMC algorithm, (ii) the ordering of different regions in terms of increasing intensity values is also assumed, (iii) each component has a unimodal distribution. However, a multi-modal distribution for a region will work as well if the number of modes is known.

For cases where the assumptions for the classification model may not be met, a supervised stochastic learning model is investigated, which builds the model utilizing one or more training THz images and their corresponding pathologies [39]. For any pixel, the classification from pathology is considered a categorical response corresponding to the pixel intensity. As there is prior knowledge about the ordering of different regions based on pixel intensities, the problem is treated as an ordinal regression by numbering the categories in ascending or descending order. In a Bayesian framework, the data augmentation approach of [39] is used.

The correlation schemes discussed above are summarized in the flow chart of Fig. 3. The morphed pathology is used as the reference point for the statistical model in two ways. The first

method provides a visual comparison by taking the classification image following the decision rule applied to the probability maps of the model. The second method plots a ROC curve of the True and False Positive Ratios for different threshold values assigned to the probability maps. For some probability threshold of a given map (e.g. cancer or fat), a number of pixels will be assigned to the region in question. For example, the True Positive Ratio of the cancer region indicates the ratio between the pixels correctly assigned as cancer and the total number of pixels actually belonging to cancer in the morphed pathology. As another example, the False Positive Ratio of fat is the ratio between the pixels incorrectly assigned as fat and the total number of non-fat pixels in the pathology. A statistically effective technique should achieve a relatively high True Positive Ratio while maintaining a low False Positive Ratio.

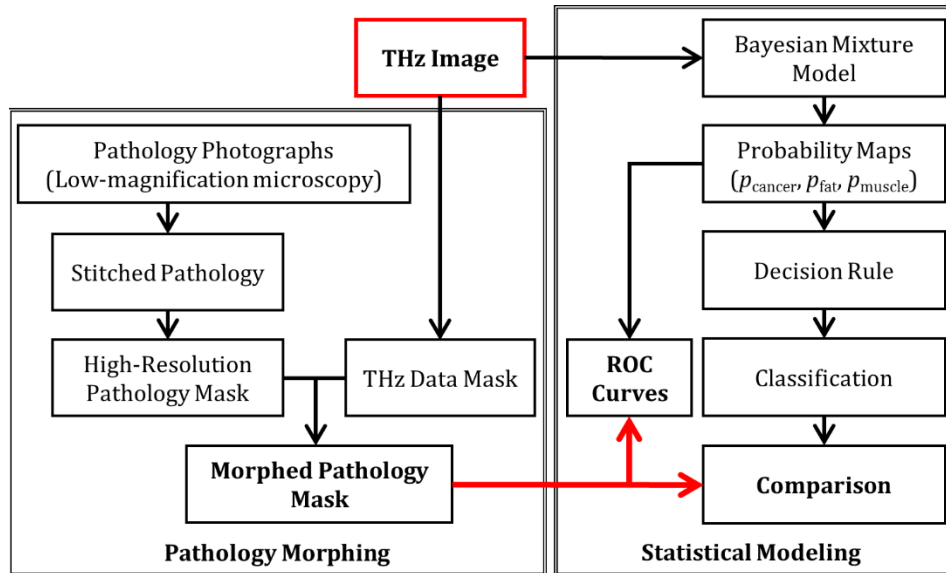


Figure 3. Correlation process flow chart for comparing THz images to pathology.

3. Experimental Results

3.1. Classification of samples with two tissue regions

In this work, thirteen samples obtained from nine murine xenograft breast cancer tumors are handled. Seven mice samples are selected here to compare the THz imaging, morphed pathology, and statistical model results, as summarized in Table 1.

Table 1. Selected Mice samples

Mouse #	2	4	7A	7B	8A	8B	9A
Details	2 regions	3 regions	3 regions				
	cancer, fat	cancer, muscle, fat	cancer, muscle, fat				

The images of fresh tissue samples are acquired as well the images of the FFPE samples of the same tissues following histopathology. The results from three samples (Sample 2, 4 and 7A) are shown in Fig. 4. The results of the fresh and FFPE tissues are presented for mouse tumor 2 in Figs. 4a-i, for mouse tumor 4 in Figs. 4j-r, and for mouse tumor 7A in Figs. 4s-z. The first row of each tumor sample corresponds to the fresh tissue, where Fig. 4a shows the pathology for mouse tumor 2 (rotated to the fresh tissue orientation) with regions of fat and cancer indicated. The morphed pathology mask in Fig. 4b shows the digitized assignment of the two regions with red color designating cancer and blue color designating fat. The THz reflected spectral power image calculated using (1) with $f_1 = 0.5$ THz and $f_2 = 1$ THz in all results, is shown in Fig. 4c. Here it can be seen that the cancer region shows a distinctly high reflection compared to the fat region. The result of the statistical model is shown in Fig. 4d for the t -distribution and is observed to correlate well to both the THz and the pathology images. The same process is shown for the FFPE tissue with the morphed pathology in Fig. 4f, THz time-domain peak image in Fig. 4g, and the model-based classification in Fig. 4h. Here the THz image can be seen to closely agree with the pathology, which is supported by the similarity between the morphed pathology and statistical model. The ROC curves for both fresh and FFPE tissue cases is given in Fig. 4i. Here it can be seen that the detection of cancer and fat regions is very good for both cases of tumor sample 2, with a greater area under the ROC curve indicating better correlation.

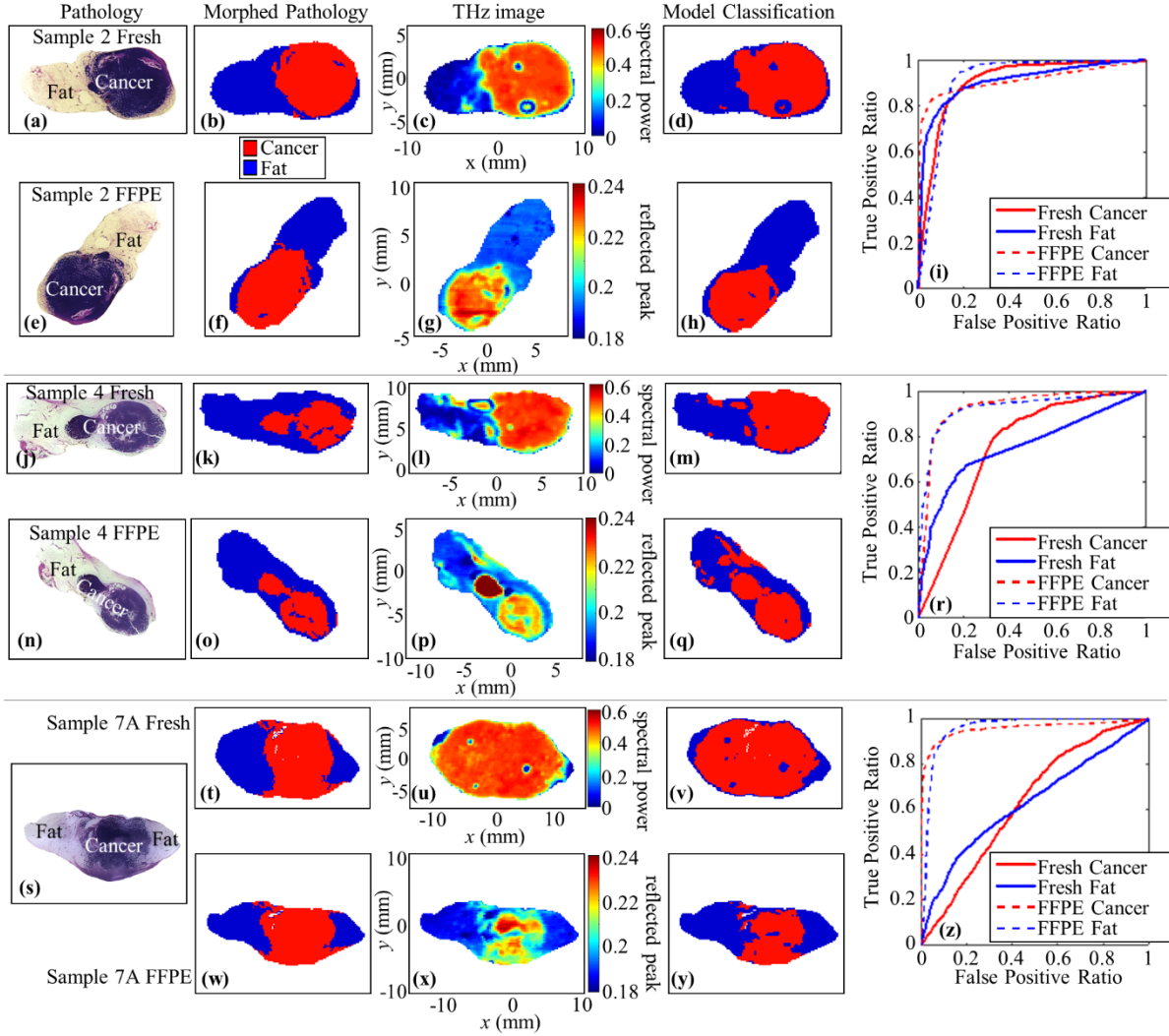


Figure 4. Correlation results for tumor samples 2, 4, and 7A. For tumor sample 2, images (b-d) for freshly excised tumor tissue and images (f-h) for FFPE tissue; (a) pathology image, (b) morphed pathology mask, (c) THz image, and (d) t-distribution model classification; the (e) pathology image (same as in (a)), (f) morphed pathology mask, (g) THz image, and (h) t-distribution model classification; and (i) the ROC curves. For tumor sample 4, images (k-m) for fresh tissue and images (o-q) for FFPE tissue; (j) pathology image, (k) morphed pathology mask, (l) THz image, and (m) t-distribution model classification; (n) pathology image, (o) morphed pathology mask, (p) THz image, and (q) t-distribution model classification; and (r) the ROC curves. For tumor sample 7A, images (t-v) for fresh tissue and images (w-y) for FFPE tissue; (s) pathology image; the (t) morphed pathology mask, (u) THz image, and (v) t-distribution model classification; the (w) morphed pathology mask, (x) THz image, and (y) t-distribution model classification; and (z) the ROC curves.

Similarly good indication of the THz imaging can be seen for tumor sample 4. Figs. 4k-m show the results for the fresh tissue imaging. Here it should be noted that the pathology in Fig. 4j

and mask in Fig. 4k reveal two primary regions of cancer, a larger area with cell density similar to other tumor cancer regions in this work and a smaller area (appearing as a cricle in Fig. 4j) with very dense cancer cells undergoing rapid growth (based on pathology assessment). This second cancer region is not seen in the fresh tissue image of Fig. 4l primarily due to the histopathology process that slices into the tissue 100 μm or more to get a good cross-section of the tissue. This difference between the imaging surface and the slice taken for pathology can result in different features being visible between fresh tissue and pathology. The FFPE tissue images in Figs. 4n-q show this second area of cancer clearly, with particularly high reflection due to the high density of the cancer cells. It should be noted that the pathology slice is taken from the same surface at which the FFPE tissue scan is performed. The ROC curves in Fig. 4r show good detection from the THz imaging of the FFPE tissue, with slightly less detection in the fresh tissue due to the difference in imaging surface discussed above.

For tumor sample 7A both fresh and FFPE tissues had similar orientation during imaging, so a single pathology image in Fig. 4s shows the central cancer tissue with fat on each side. In this case the morphed pathology in Fig. 4t designates much larger areas of fat than is seen in the THz image of the fresh tissue in Fig. 4u and subsequent classification in Fig. 4v. For this sample there was excess fluid pooled under the tissue when it was freshly excised. Additionally the tumor had grown large enough to undergo some necrosis in the center, leading to the loose cellular tissue and blood being spread across the tissue surface when bisecting the tumor. As a result, a higher reflection from this liquid was spread over the areas that would normally be fat. On the other hand, the images from the FFPE tissue in Fig. 4x and classification in Fig. 4y show much better agreement with the pathology mask in Fig. 4w because this fluid was removed in the process. Fig. 4x of THz image also shows the varying reflections in the cancer region, with more dense cancer

tissue reflecting more, agreeing with the pathology in Fig. 4s. Though due to some necrosis, captured in the THz image, the correlation with morphed pathology is not as consistent as in tumors 2 and 4. Fig. 4z shows that while the classification of the FFPE tissue is accurate, the fresh tissue poses a challenge due to the excess fluid. Note that THz images show clear visual differentiation between tissue regions especially in the FFPE cases, in agreement with previous work [9, 29-30].

Another challenge is that some tissue samples showed more significant shape distortion between THz images of fresh tissue and pathology fixation. Examples of this distortion are shown in Fig. 5 for tumor sample 7B (Figs. 5a-h) and tumor sample 8A (Figs. 5i-p). For sample 7B the tissue not only has some distortion due to the histopathology process but is also seen to have

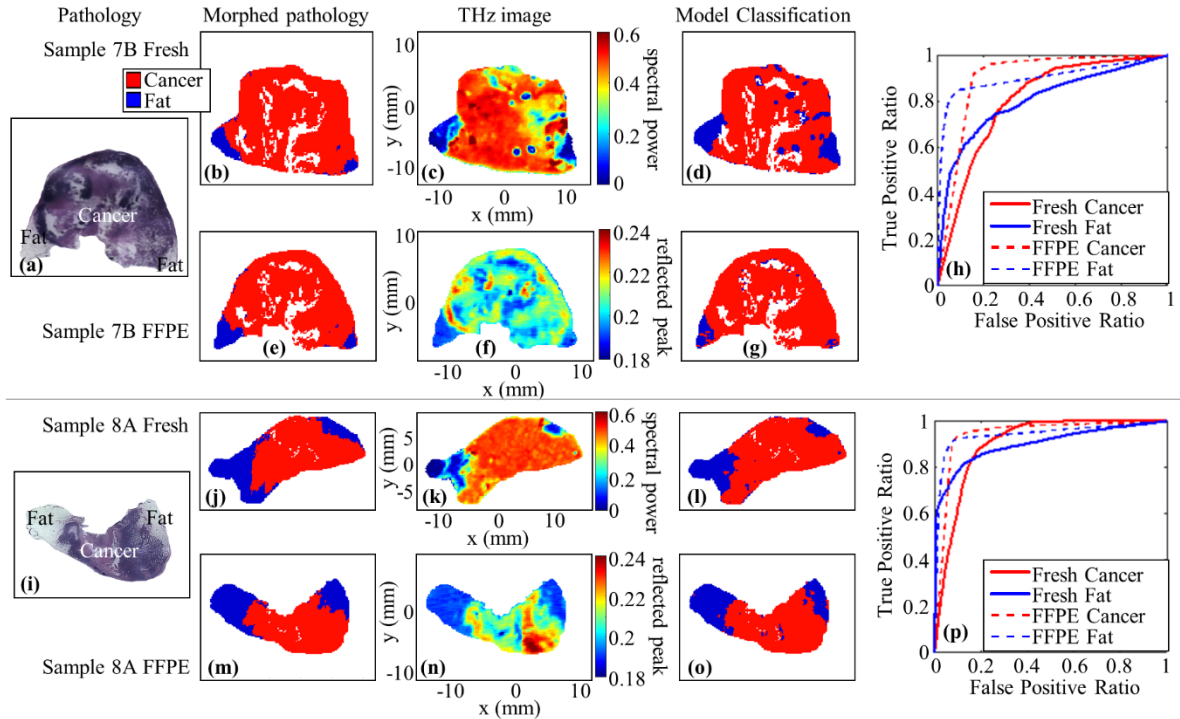


Figure 5. Correlation results for samples 7B and 8A. For tumor sample 7B, images (b-d) for freshly excised tumor and images (e-g) for FFPE tissue; (a) pathology image; the (b) morphed pathology mask, (c) THz image, and (d) t-distribution model classification; the (e) morphed pathology mask, (f) THz image, and (g) t-distribution model classification; and (h) the ROC curves. For tumor sample 8A, images (j-l) for freshly excised tissue and images (m-o) for FFPE tissue; (i) pathology image; the (j) morphed pathology mask, (k) THz image, and (l) t-distribution model classification; the (m) morphed pathology mask, (n) THz image, and (o) t-distribution model classification; and (p) the ROC curves.

several gaps as detailed in Fig. 5a. These gaps primarily arise due to the necrosis on the interior of larger tumors that fill with fluid during the fresh tissue imaging and paraffin for the FFPE tissue. These gaps are considered a separate region during pathology morphing to maintain their size and shape but considered background for the sake of correlation such that the points are disregarded from comparison. The morphed pathology for the fresh tissue outline in Fig. 5b shows these gaps clearly in the cancer, with some small regions of fat in the lower corners. These gaps are also imposed on the model results in each case to exclude those points from comparison. Shape distortion between the fresh tissue and pathology can be seen in the THz image and model classification in Figs. 5c and d, where the lower reflection regions in the corners of the tissue appear approximately the same size as the fat regions in the pathology but slightly shifted. This results in some challenge for lining up the pathology with the fresh tissue images. In contrast, for FFPE tissue the THz image in Fig. 5f show very good agreement with the morphed pathology in Fig. 5e and the model classification in Fig. 5g as well. The THz image of the FFPE tissue in Fig. 5f also shows the gaps of the pathology as areas of low reflection due to filling the gaps with paraffin. The image demonstrates good comparison with the original pathology in Fig. 5a. This is due to the pathology being taken from the surface of the FFPE tissue block as discussed previously. The ROC curves in Fig. 5h then show that the THz imaging of the FFPE tissue has good detection of tissue regions while the fresh tissue imaging classification is diminished due to the tissue distortion.

The ability for the current image morphing to account for shape change in the tissue is dependent on the specific tumor sample. As seen for tumor sample 8A, the pathology in Fig. 5i undergoes a significant change in shape compared to the morphed pathology for the fresh tissue in Fig. 5j. However, the THz image in Fig. 5k show good agreement with the pathology mask in Fig.

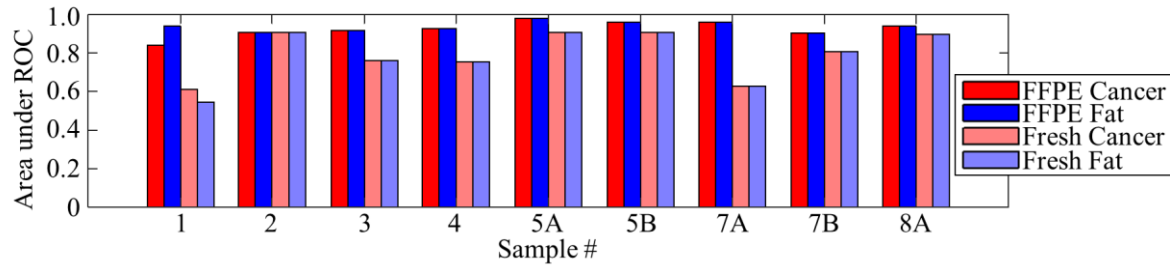


Figure 6. Area under ROC curve for nine samples with two regions.

5j and with the statistical model in Fig. 5l. Meanwhile the results for the FFPE tissue in Figs. 5m-o show good correlation similar to other FFPE tissue cases. The ROC curves in Fig. 5p indicate that both fresh and FFPE tissue have reasonable detection for the two regions of tissue.

For comparing the results across several samples, there are a few ways to quickly describe the ROC curve. These include the 5% or 10% false positive sensitivity (the true positive ratio when the false positive ratio is 0.05 or 0.1) or the area under the curve. To relate these two values, an ROC curve with a true positive ratio of 0.9 when the false positive ratio is 0.1 would generally have an area under the curve of 0.8 to 0.9, so a ROC area above 0.8 would be considered good correlation. The ROC area for all tumor samples with two regions is shown in Fig. 6. The FFPE tissue THz imaging can be seen to have a curve area above 0.8 in all cases, which is expected due to the pathology being taken from the exact surface imaged in the FFPE tissue blocks. THz imaging of fresh tissue can also be seen to have relatively good detection in most cases. There were some cases where the detection was lower, such as in tumor sample 1 where the tissue had been frozen. This was done in an optimal cutting temperature (OCT) medium that couldn't be cleared for imaging. Other cases of low detection were tumor samples 3 and 7A, where significant fluid had accumulated under the tissue, and tumor sample 4, where there was a difference in the scanned surface between the pathology and fresh tissue image (see Fig. 4). In general, THz imaging shows good detection between distinct regions of fat and cancer tissue in the freshly excised mice tumors, and the challenges in cases with lower correlation are clearly identified. For most cases the tissue

morphing was able to resolve differences in tissue shape between the fresh tissue and pathology, even for the severe case in sample 8A, though not all cases were corrected and there is a potential to improve the pathology correlation with a more robust morphing algorithm.

3.2. *Classification of samples with three tissue regions*

The excision of some larger tumors included muscle tissue from the abdominal wall of the mouse. Muscle is not anticipated in human breast cancer excisions, but arose in these samples due to the limited space for the tumors to grow in the fat deposits of the mice. As such they are examined here to test the statistical model. In this section, results of unsupervised (non-regression) and supervised (regression) approaches are shown in Fig. 7. The regression model used data from tumor sample 9B as an arbitrary training sample. The training used the regions defined in the morphed pathology to collect intensity distributions for each tissue type for building the model. The images of sample 9B are not shown here but its statistics are shown later in Fig. 11.

For tumor sample 8B, the pathology in Fig. 7a shows that the cancer is mostly along the center and the upper right part of the tissue. This sample was unique in that the center of the cancer had mostly fatty tissue with some cancer mixed in. The other fat deposits and muscles can be seen on the lower edge. These regions translate more or less directly into the morphed pathology in Fig. 7b, with a few small gaps represented in white color that are imposed to the morphed pathology and model classification. However, for the THz image of the fresh tissue in Fig. 7c the fat region at the core of the tissue cannot be seen, and there is a spot of very high reflection over the fat deposit on the left side. The latter is most likely fluid pooled beneath the fat, and the inability to see the cancer distributed through the fat could be from fluid and loose cells being distributed on the surface during bisection. There is also a possibility that the surface changed significantly between the fresh THz image and pathology. The classification model results using the Normal

distribution in Fig. 7d show a generally good assignment of fat and cancer regions, but for muscle regions it focuses on areas of borderline reflection between high and low regions rather than a separate broad region. The classification image is improved somewhat using the regression model in Fig. 7e. Here, all higher reflections are considered cancer while the region of fat is mostly unchanged. However, the region of muscle tissue in the pathology is still not indicated by the model. Therefore while there does appear to be some small difference in the THz image along the lower edge where the muscle is in pathology, it is not detected for correlation.

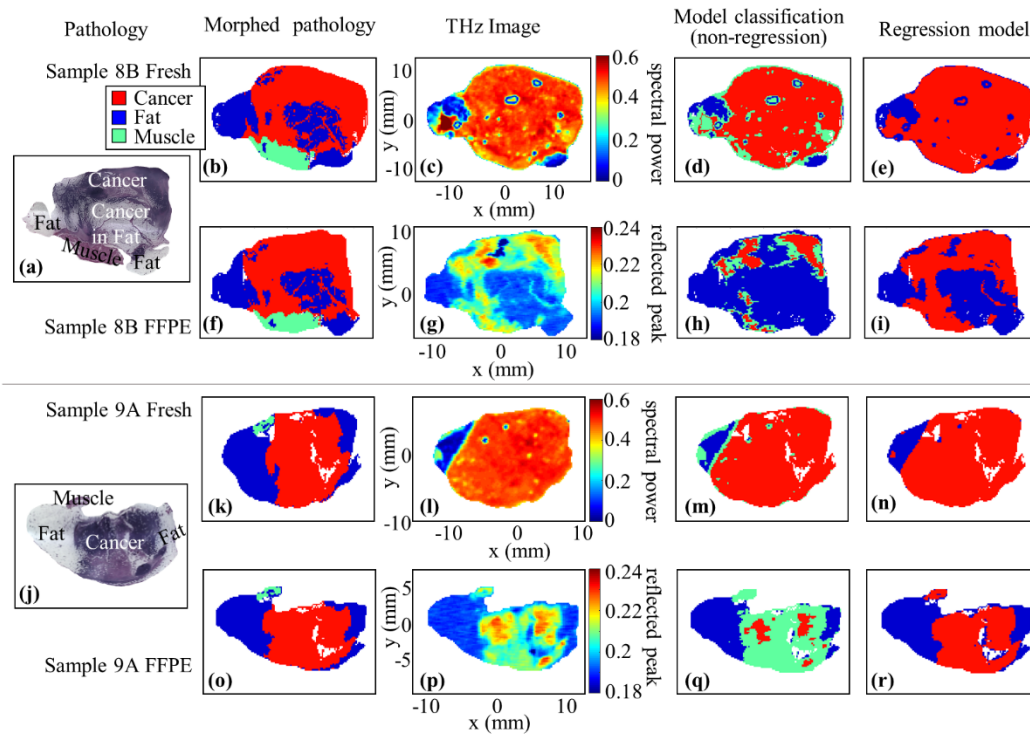


Figure 7. Correlation results for samples 8B and 9A. For tumor sample 8B, images (b-e) for freshly excised tissue and images (f-i) for FFPE tissue; (a) pathology image; the (b) morphed pathology mask, (c) THz image, (d) Normal distribution model classification, and (e) regression model classification; and the (f) morphed pathology mask, (g) THz image, and (h) Normal distribution model classification, and (i) regression model classification. For tumor sample 9A, images (k-n) for freshly excised tissue and images (o-r) for FFPE tissue; (j) pathology image; the (k) morphed pathology mask, (l) THz image, (m) t-distribution model classification, and (n) regression model classification; and the (o) morphed pathology mask, (p) THz image, and (q) t-distribution model classification, and (r) regression model classification.

The FFPE tissue results show a similar challenge. The morphed pathology in Fig. 7f and THz image in Fig. 7g both show very close agreement with the pathology in Fig. 7a. However, this sample involves both muscle tissue and necrotic cancer tissue (seen as faded areas in the cancer in pathology or low reflection spots in the cancer in the THz image), which both have reflection in between the cancer and fat and tend to overlap. The result in Fig. 7h indicates that the classification model classified almost all of the lower reflection areas as fat, with only the spots of highest reflection being classified as cancer and the small amount of midrange values considered as muscle. The regression model in Fig. 7i shows significant improvement in this case with accurate detection of the fat and mostly accurate detection of cancer, though once again the muscle tissue is not classified by the model.

Similar challenges are seen for tumor sample 9A, shown in Figs. 7j-r. In this sample the region of muscle is relatively small in the upper left part of the pathology image in Fig. 7j, leaving primarily cancer in the center and fat on the left and right sides. The morphed pathology in Fig. 7k is consistent with the pathology image in Fig. 7j. Meanwhile the THz image of the fresh tissue in Fig. 7l once again shows the challenge of clearing fluid from under the tissue. Here the high reflection of fluid in the tissue decreases the expected area of fat on the left and completely covers the fat on the right. As with the previous case, the classification (non-regression) model in Fig. 7m classifies the tissue regions of high and low reflection as cancer and fat, respectively, while the transition tissue region between them is classified as the muscle tissue. The regression model in Fig. 7n did not improve the results of Fig. 7m. The FFPE tissue results in Fig. 7o-r are similar to tumor sample 8A. Here the reflection of the muscle and some of the necrotic cancer tissue overlap in the THz image in Fig. 7p, resulting in most of the cancer region being classified as muscle in the classification (non-regression) model results in Fig. 7q. The regression model in Fig. 7r

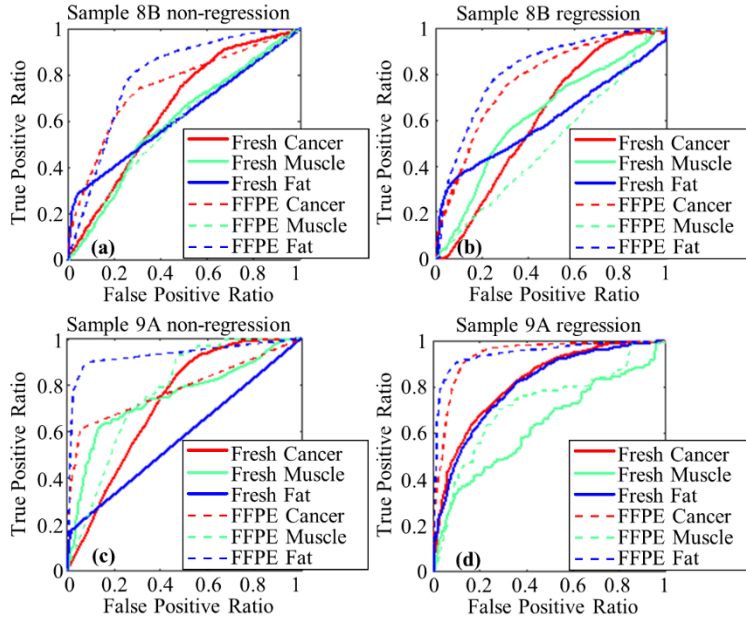


Figure 8. ROC curves for sample 8B using (a) Normal distribution model classification and (b) regression model classification, and for sample 9A using (c) t-distribution model classification and (d) regression model classification.

correctly defines most of the cancer region but does not classify any noticeable muscle region. In both samples shown here, the THz images show differentiation in heterogeneous regions of tissue that can be directly compared to the original pathology. However this heterogeneity is lost when reducing the morphed pathology and classification model to just three regions.

The ROC curves in Fig. 8 show the challenge for the current statistical model to classify the tissue when three regions are present (cancer, fat, muscle). For the fresh tissue images of tumor sample 8B, the ROC curves in Fig. 8a show relatively lower areas under the curves (0.6551 for cancer, 0.5967 for muscle, and 0.6244 for fat). This is due to the fact that even if a classification image meets the decision rule for the three regions, the certainty of the classified tissue type in the probability maps of the model may still be low. Meanwhile the FFPE tissue results in the same figure show that the cancer and fat are both reasonably detected while the muscle is not, which agrees with the visual correlation of the tissue. Using the regression model for sample 8B provides the ROC curves in Fig. 8b. The regression model is shown to not significantly change the results

of the fresh tissue (ROC areas of 0.616 for cancer, 0.6276 for muscle, and 0.6061 for fat), while it improves the classification of cancer and fat in the FFPE (increased from 0.7507 to 0.7793 for cancer and 0.796 to 0.8238 for fat). The classification of muscle tissue is decreased (down from 0.5849 to 0.4624). For tumor sample 9A the ROC curves in Fig. 8c denote some effective detection of the tissue regions in the fresh tissue but with low certainty, while the FFPE tissue has slightly better detection. The regression model results in Fig. 8d show notable improvement in the cancer and fat tissue regions for the fresh tissue imaging (areas increased from 0.7253 to 0.8272 for cancer and 0.5808 to 0.8121) with some decrease in muscle classification (down from 0.7512 to 0.6365). For FFPE tissue the classification for cancer increases significantly (up from 0.7874 to 0.9431), while classification of muscle decreases (ROC area down from 0.7762 to 0.7266) and fat marginally increases (from 0.9318 to 0.9531). As such, while the regression model improves some cases its usefulness is not consistent across all samples.

In all implementations of the regression model observed here the classification of cancer and fat tended to increase or stay the same while the classification of muscle tended to decrease. This is investigated more directly by observing the probability maps for sample 8B in Fig. 9. Although these probability maps are generated for every sample, only one is shown here for the sake of space. For each image the regions with higher values (dark red) indicate a larger probability

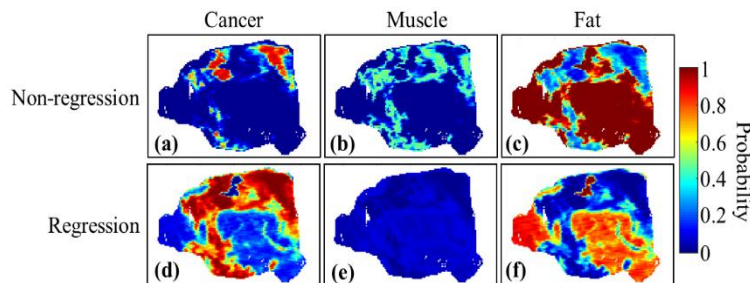


Figure 9. Probability maps generated by the statistical model for sample 8B FFPE. Maps using Normal distribution for regions of (a) cancer, (b) muscle, and (c) fat and using regression model for regions of (d) cancer, (e) muscle, and (f) fat.

that pixel being in the described region. For the Normal distribution model in Figs. 9a-c, a high probability of cancer (Fig. 9a) is assigned to the areas of highest reflection in the earlier THz image, while an increased probability of muscle (Fig. 9b) is given to the next highest reflections from muscle and necrotic cancer. It should be noted that the probability of muscle here is not particularly high, but the regions of higher values in Fig. 9b still possess a greater probability of muscle than cancer or fat and are therefore assigned as such in the classification image. Meanwhile the probability of fat in Fig. 9c shows good indication of the fat regions. By informing the regression model with existing data of cancer, muscle, and fatty tissue, the probability maps in Figs. 9d-f are generated. Here the full region of cancer is now shown to have a high probability for cancer in Fig. 9d, leading to the improvement seen in the ROC area of Fig. 8d. However, there is very little probability of muscle anywhere in Fig. 9e. This may be due to using only one image for training the model, the muscle in all cases being small, and/or the refractive index and absorption coefficients of muscle is close to cancer tissue in THz frequency, see Fig. 10 [40,41]. This same effect is the cause for the decreased ROC area for muscle in the samples in Fig. 8. Meanwhile the fat classification in Fig. 9f remains mostly unchanged.

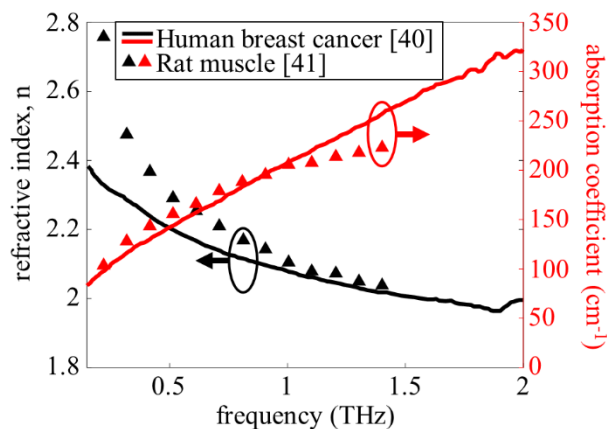


Figure 10. Published refractive index and absorption coefficient values for human breast cancer [40] and rat muscle [41].

The areas under the ROC curves for the four samples with three tissue regions are given in Fig. 11. In all cases the FFPE tissue continued to show good classification of cancer and fat areas, though the presence of the muscle region did make the detection of each region less accurate, where the detection of muscle in all cases was the lowest. For fresh tissue all samples investigated showed some challenge in detecting the three regions except for sample 9B where all ROC areas neared 0.8 except for the detection of muscle in the FFPE tissue (images not shown here). The accuracy across all fresh tissue samples was primarily affected by necrosis inside the larger tumors, which caused higher reflections in the THz imaging due to excess fluid and loose tissue.

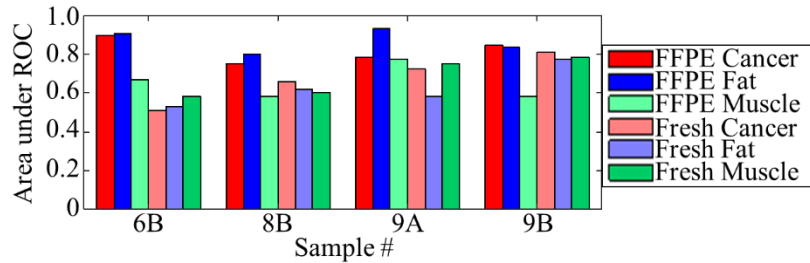


Figure 11. Area under ROC curve for four samples with three regions.

A summary of the areas under the ROC curves for all cases discussed in Figs. 6 and 11 is given in Table 2. Here the strong correlation can be shown in all FFPE cases, except the cases that involved muscle or moderate to advanced necrosis. The primary challenge in fresh tissue is clearing the fluid from the imaging surface, which is often compounded in cases with necrosis.

Table 2. Area under ROC curve results for all cases in Figs. 6 and 11.

Mouse #	FFPE			Fresh			Notes
	Cancer	Fat	Muscle	Cancer	Fat	Muscle	
1	0.84	0.94	N/A	0.61	0.55	N/A	Frozen in OCT before Fresh imaging
2	0.91	0.91	N/A	0.91	0.91	N/A	-
3	0.92	0.92	N/A	0.76	0.76	N/A	Excess fluid, minor necrosis
4	0.93	0.93	N/A	0.76	0.76	N/A	Difference in pathology surface
5A	0.98	0.98	N/A	0.91	0.91	N/A	-
5B	0.96	0.96	N/A	0.91	0.91	N/A	-
6B	0.90	0.91	0.67	0.51	0.53	0.58	Excess fluid, minor necrosis
7A	0.96	0.96	N/A	0.63	0.63	N/A	Excess fluid, minor necrosis
7B	0.90	0.90	N/A	0.81	0.81	N/A	Advanced necrosis
8A	0.94	0.94	N/A	0.90	0.90	N/A	Significant shape change in pathology
8B	0.75	0.80	0.58	0.66	0.62	0.60	Excess fluid, advanced necrosis
9A	0.79	0.93	0.78	0.73	0.58	0.75	Excess fluid, moderate necrosis
9B	0.85	0.84	0.58	0.81	0.78	0.78	Moderate necrosis

4. Discussion and Conclusion

Over the 13 samples handled in this work, THz images are seen to have statistically good discrimination between tissues with two regions (cancer and fat), with a few exceptions due to factors outside of imaging performance. The primary challenges in classifying THz images of tissue in this work are (i) the presence of fluids including water and necrotic blood on the underside of the fresh tissue, (ii) the correlation with pathology obtained after fixing the tissue in formalin and embedding it in paraffin, and (iii) the morphed pathology (digitized pathology) using an interpolation algorithm to reduce the resolution of the original pathology. The presence of fluid occurred to some extent in samples 3 and 7 and in all three-tissue region samples except sample

9B. This resulted in some cases of fat tissue being classified as cancer in the statistical model. In correlating the pathology to the THz images of fresh tissue, a change in tissue shape occurred going through histopathology processing. These concerns can be addressed in future work by drying the tissue thoroughly using a lint-free filter paper, using tissue marking ink for orienting tissue between imaging and pathology, and mounting tissue sections on a rigid surface (i.e. cardboard) for formalin fixation. Additional challenges in shape comparison of THz images of fresh tissue to pathology can be improved with more rigorous morphing techniques, such as adopting a mesh-based morphing (ongoing research) instead of the interpolation used in this work. However, there is still a need for a true comparison against THz imaging of fresh tissue to determine accuracy, and future work will look into other common imaging techniques (e.g. CT, radiography, etc) to have a direct comparison for fresh tissue imaging.

For the 4 samples where muscle tissue is present, overlap between muscle and cancer tissue reflections in the THz image creates some challenge in correctly classifying these regions. While muscle is unlikely to be present in surgical sections of human breast cancer, other kinds of fibrous tissue may be present and thus it requires investigating more advanced models for three tissue regions. Ongoing research is focusing on spontaneously generated breast cancer tumors from transgenic mice, which have natural tumor structures and fibrous tissue more comparable to human tissue for more accurate assessment of THz imaging. Another area in which the approach could be improved is the classification model. The statistical models used here show success when handling samples with two regions but tend to miss areas of a third region of tissue. In general the models presented here can classify three tissue regions if the reflection from the regions are distinct. It was observed in human tumors that the model was not able to fully classify cancer and fibroglandular tissue for the same reason where cancer and fibrous tissue have close properties [42]. Future work

will focus on new detection methods and advanced models to address this challenge. The obtained results demonstrate promise for THz imaging of freshly excised tumors and shed the light on the main challenges that need to be resolved before it can be implemented on human tissue.

Disclosures

The authors have no financial interests or conflicts of interests to disclose regarding this manuscript.

Acknowledgments

This work was funded by NIH award #R15CA208798. It was also funded in part by NSF award #1408007. Funding for the pulsed THz system was obtained through NSF/MRI award #1228958. The authors would like to thank Dr. L. Norian from the University of Alabama at Birmingham for feedback on the high-fat diet protocol for the mice. The authors would also like to thank the students M. Harper, D. Lee, and K. Alhallak in the Functional Optical Imaging and Spectroscopy laboratory for assistance in cell growth, injection, and tumor excision.

References

- [1] S. Fan, Y. He, B. S. Ung, and E. Pickwell-MacPherson, "The growth of biomedical terahertz research," *J. Phys. D. Appl. Phys.* **47**, 374009 (2014).
- [2] S. Sy, S. Huang, Y.-X. J. Wang, J. Yu, A. T. Ahuja, Y.-T. Zhang, and E. Pickwell-MacPherson, "Terahertz spectroscopy of liver cirrhosis: investigating the origin of contrast.," *Phys. Med. Biol.* **55**, 7587–7596 (2010).
- [3] W. E. Baughman, H. Yokus, S. Balci, D. S. Wilbert, P. Kung, and S. M. Kim, "Observation of hydrofluoric acid burns on osseous tissues by means of terahertz spectroscopic imaging," *IEEE J. Biomed. Heal. Informatics* **17**, 798–805 (2013).
- [4] S. J. Oh, S.-H. Kim, Y. Bin Ji, K. Jeong, Y. Park, J. Yang, D. W. Park, S. K. Noh, S.-G. Kang, Y.-M. Huh, J.-H. Son, and J.-S. Suh, "Study of freshly excised brain tissues using terahertz imaging," *Biomed. Opt. Express* **5**, 2837–42 (2014).
- [5] H. A. Kashanian, H. B. Ghaffary, N. C. Bagherzadeh, S. D. Roostaie, and H. E. Alidoost, "Gastric Cancer Diagnosis Using Terahertz Imaging," *Majlesi J. Multimed. Process.* **4**, 1–7 (2015).

- [6] F. Wahaia, G. Valusis, L. M. Bernardo, A. Almeida, J. A. Moreira, P. C. Lopes, J. Macutkevic, I. Kasalynas, D. Seliuta, R. Adomavicius, R. Henrique, and M. Lopes, "Detection of colon cancer by terahertz techniques," *J. Mol. Struct.* **1006**, 77–82 (2011).
- [7] B. St. Peter, S. Yngvesson, P. Siqueira, P. Kelly, A. Khan, S. Glick, and A. Karellas, "Development and Testing of a Single Frequency Terahertz Imaging System for Breast Cancer Detection," *IEEE J. Biomed. Heal. Informatics* **17**, 785–797 (2013).
- [8] T. Bowman, M. El-Shenawee, and L. K. Campbell, "Terahertz transmission vs reflection imaging and model-based characterization for excised breast carcinomas," *Biomed. Opt. Express* **7**, 3756–3783 (2016).
- [9] T. C. Bowman, M. El-Shenawee, and L. K. Campbell, "Terahertz Imaging of Excised Breast Tumor Tissue on Paraffin Sections," *IEEE Trans. Antennas Propag.* **63**, 2088–2097 (2015).
- [10] A. J. Fitzgerald, V. P. Wallace, M. Jimenez-Linan, L. Bobrow, R. J. Pye, and A. D. Purushotham, "Terahertz Pulsed Imaging of human breast tumors," *Radiology* **239**, 533–540 (2006).
- [11] C. B. Reid, A. Fitzgerald, G. Reese, R. Goldin, P. Tekkis, P. S. O’Kelly, E. Pickwell-MacPherson, A. P. Gibson, and V. P. Wallace, "Terahertz pulsed imaging of freshly excised human colonic tissues," *Phys. Med. Biol.* **56**, 4333–4353 (2011).
- [12] P. Doradla, K. Alavi, C. Joseph, and R. Giles, "Detection of colon cancer by continuous-wave terahertz polarization imaging technique," *J. Biomed. Opt.* **18**, 90504 (2013).
- [13] S. Yamaguchi, Y. Fukushi, O. Kubota, T. Itsuji, T. Ouchi, and S. Yamamoto, "Brain tumor imaging of rat fresh tissue using terahertz spectroscopy," *Sci. Rep.* **6**, 1–6 (2016).
- [14] C. H. Zhang, G. F. Zhao, B. B. Jin, Y. Y. Hou, H. H. Jia, J. Chen, and P. H. Wu, "Terahertz Imaging on Subcutaneous Tissues and Liver Inflamed by Liver Cancer Cells," *Terahertz Sci. Technol.* **5**, 114–123 (2012).
- [15] H. Chen, T.-H. Chen, T.-F. Tseng, J.-T. Lu, C.-C. Kuo, S.-C. Fu, W.-J. Lee, Y.-F. Tsai, Y.-Y. Huang, E. Y. Chuang, Y.-J. Hwang, and C.-K. Sun, "High-sensitivity in vivo THz transmission imaging of early human breast cancer in a subcutaneous xenograft mouse model," *Opt. Express* **19**, 21552–21562 (2011).
- [16] S. K. Boi, C. M. Buchta, N. A. Pearson, M. B. Francis, D. K. Meyerholz, J. L. Grobe, and L. A. Norian, "Obesity alters immune and metabolic profiles: New insight from obese-resistant mice on high-fat diet," *Obesity* **24**, 2140–2149 (2016).
- [17] M. T. Rahman, Al-Amin, M. A. J. Bin Bakkre, A. R. Chowdhury, and M. A.-A. Bhuiyan, "A Novel Approach of Image Morphing Based on Pixel Transformation," *Proc. of 2007 10th Int. Conf. Comput. Inf. Technol. ICCIT*, December 2007. [doi: 10.1109/ICCITECHN.2007.4579398]

- [18] A. J. Fitzgerald, S. Pinder, A. D. Purushotham, P. O'Kelly, P. C. Ashworth, and V. P. Wallace, "Classification of terahertz-pulsed imaging data from excised breast tissue," *J. Biomed. Opt.* **17**, 16005 (2012).
- [19] L. H. Eadie, C. B. Reid, A. J. Fitzgerald, and V. P. Wallace, "Optimizing multi-dimensional terahertz imaging analysis for colon cancer diagnosis," *Expert Syst. Appl.* **40**, 2043–2050 (2013).
- [20] N. Qi, Z. Zhang, Y. Xiang, Y. Yang, X. Liang, and P. D. B. Harrington, "Terahertz time-domain spectroscopy combined with support vector machines and partial least squares-discriminant analysis applied for the diagnosis of cervical carcinoma," *Anal. Methods* **7**, 2333–2338 (2015).
- [21] D. Hou, X. Li, J. Cai, Y. Ma, X. Kang, P. Huang, and G. Zhang, "Terahertz spectroscopic investigation of human gastric normal and tumor tissues," *Phys. Med. Biol.* **59**, 5423–5440 (2014).
- [22] D. Ng, F. T. Wong, W. Withayachumnankul, D. Findlay, B. Ferguson, and D. Abbott, "Classification of osteosarcoma T-ray responses using adaptive and rational wavelets for feature extraction," *Proc. SPIE 6802, Complex Systems II* (2007), Vol. 6802, p. 680211.
- [23] N. Qi, Z. Zhang, Y. Xiang, Y. Yang, and P. de B. Harrington, "Terahertz time-domain spectroscopy combined with fuzzy rule-building expert system and fuzzy optimal associative memory applied to diagnosis of cervical carcinoma," *Med. Oncol.* **32**, 383 (2015).
- [24] E. Berry, J. W. Handley, A. J. Fitzgerald, W. J. Merchant, R. D. Boyle, N. N. Zinov'ev, R. E. Miles, J. M. Chamberlain, and M. A. Smith, "Multispectral classification techniques for terahertz pulsed imaging: An example in histopathology," *Med. Eng. Phys.* **26**, 423–430 (2004).
- [25] K. I. Zaitsev, N. V. Chernomyrdin, K. G. Kudrin, I. V. Reshetov, and S. O. Yurchenko, "Terahertz Spectroscopy of Pigmentary Skin Nevi in Vivo," *Opt. Spectrosc.* **119**, 404–410 (2015).
- [26] F. Formanek, M.-A. Brun, and A. Yasuda, "Contrast improvement of terahertz images of thin histopathologic sections.," *Biomed. Opt. Express* **2**, 58–64 (2010).
- [27] S. Nakajima, H. Hoshina, M. Yamashita, C. Otani, and N. Miyoshi, "Terahertz imaging diagnostics of cancer tissues with chemometrics technique," *Appl. Phys. Lett.* **90**, 41102 (2007).
- [28] W. R. Gilks, S. Richardson, and D. J. Spiegelhalter, eds., *Markov Chain Monte Carlo in Practice*, Chapman and Hall (1995).
- [29] T. Bowman, Y. Wu, J. Gauch, L. K. Campbell, and M. El-Shenawee, "Terahertz Imaging of Three-Dimensional Dehydrated Breast Cancer Tumors," *J. Infrared, Millimeter, Terahertz Waves* **38**, 766–786 (2017).

- [30] T. Bowman, A. Walter, O. Shenderova, N. Nunn, G. McGuire, and M. El-Shenawee, "A phantom study of terahertz spectroscopy and imaging of micro- and nano-diamonds and nano-onions as contrast agents for breast cancer," *Biomed. Phys. Eng. Express* **3**, 55001 (2017).
- [31] T. Bowman, N. Rajaram, A. Chakraborty, K. Bailey, and M. El-Shenawee, "Terahertz Imaging and Segmentation of Freshly Excised Xenograft Mouse Tumors," *Proc. of XXXII International Union of Radio Science 2017 URSI General Assembly and Scientific Symposium, (K7P Electromagnetic Biomedical Imaging)*, August 2017.
- [32] T. Bowman, K. Alhallak, T. Esparza, M. K. Khan, D. Lee, N. Rajaram, J. Wu, A. Chakraborty, K. Bailey, and M. El-Shenawee, "Terahertz Imaging of Freshly Excised Breast Cancer using Mouse Model," *Proc. of 42nd International Conference on Infrared, Millimeter and Terahertz Waves*, August 2017. [doi: 10.1109/IRMMW-THz.2017.8067153]
- [33] K. Sharma and A. Goyal, "Classification Based Survey of Image Registration Methods," *Proc. of 2013 Fourth Int. Conf. Comput. Commun. Netw. Technol.* 1–7 (2013). [doi: 10.1109/ICCCNT.2013.6726741]
- [34] W. Dos Passos, *Numerical Methods, Algorithms and Tools in C#* (CRC Press, 2009).
- [35] J. Diebolt and C. P. Robert, "Estimation of Finite Mixture Distributions through Bayesian Sampling," *J. R. Stat. Soc. Ser. B* **56**, 363–375 (1994).
- [36] C. Fernández and M. F. J. Steel, "Bayesian Regression Analysis With Scale Mixtures of Normals," *Econom. Theory* **16**, 80–101 (2000).
- [37] S. Frühwirth-Schnatter and S. Pyne, "Bayesian inference for finite mixtures of univariate and multivariate skew-normal and skew-t distributions," *Biostatistics* **11**, 317–336 (2010).
- [38] M. Stephens, "Dealing with Label Switching in Mixture Models," *J. R. Stat. Soc. Ser. B Statistical Methodol.* **62**, 795–809 (2000).
- [39] J. H. Albert and S. Chib, "Bayesian Analysis of Binary and Polychotomous Response Data," *J. Am. Stat. Assoc.* **88**, 669–679 (1993).
- [40] P. C. Ashworth, E. Pickwell-MacPherson, E. Provenzano, S. E. Pinder, A. D. Purushotham, M. Pepper, and V. P. Wallace, "Terahertz pulsed spectroscopy of freshly excised human breast cancer.," *Opt. Express*, vol. 17, no. 15, pp. 12444–12454, 2009.
- [41] G. J. Wilmink, B. L. Ibey, T. Tongue, B. Schulkin, N. Laman, X. G. Peralta, C. C. Roth, C. Z. Cerna, B. D. Rivest, J. E. Grundt, and W. P. Roach, "Development of a compact terahertz time-domain spectrometer for the measurement of the optical properties of biological tissues.," *J. Biomed. Opt.*, vol. 16, no. 4, p. 47006, 2011.

- [42] M. El-Shenawee, T. Bowman, T. Esparza, K. Khan, J. Wu, A. Chakraborty, and K. Bailey, "Statistical Signal Processing for Quantitative Assessment of Pulsed Terahertz Imaging of Human Breast Tumors," Proc. of 42nd International Conference on Infrared, Millimeter and Terahertz Waves, Cancun, Mexico, August 2017. [doi:10.1109/IRMMW-THz.2017.8067265]

Chapter 7: Conclusions

Over the course of this work, THz has proven effective in distinguishing between breast cancer tissue and healthy tissues in both FFPE and fresh tissue applications. The first experimental THz imaging of FFPE breast cancer tissue showed good contrast between infiltrating ductal carcinoma and healthy tissue with strong correlation to pathology, even for subwavelength sample thicknesses of 10, 20, and 30 μm [1]. It also showed that this contrast exists even for dehydrated tissue, showing that water content of the tissue is not the sole reason for THz differentiation between tissue types. While inherent contrast had been shown independent of water for other tissue types, such as cirrhotic liver [2], this was, to the authors' knowledge, the first published indication of this trend in breast cancer tissue. It has further been shown for brain cancer that the presence of water in fresh tissue can further increase the contrast between cancer and healthy tissue [3], which is still under investigation for breast cancer tissue. The work in [1] further showed that THz can reach reasonable resolution for distinguishing between small regions of tissue when compared to pathology, though it obviously cannot distinguish individual cells like optical techniques.

The work in [4] expanded the THz imaging applications with the use of transmission imaging, as well as investigating both lobular carcinoma and infiltrating ductal carcinoma. The results showed excellent comparison to pathology for both reflection and transmission imaging setups for 20 and 30 μm tissue on polystyrene slides. Furthermore, spectroscopy algorithms were developed in order to characterize the tissue from imaging in transmission or reflection. While transmission imaging was shown to have lower resolution than reflection due to the additional focusing mirrors in the reflection setup, transmission spectroscopy was shown to have far less susceptibility to phase distortions from slide thickness or poor tissue adhesion. Meanwhile reflection imaging is better for imaging fresh tissue in the future due to its improved resolution and the high absorption of fresh tissue, which agrees with observations made in literature as well

[5]. The development of reflection models also allowed for polarization approximation of an arbitrarily polarized beam via experimental methods, which was necessary for reflection spectroscopy using THz images in the future [4].

The progression of samples from flat sections to three-dimensional blocks of tissue showed increasingly good differentiation between cancer and noncancerous tissue for both lobular and infiltrating ductal carcinoma in [6]. Upper and lower boundaries of the tissue were clearly seen throughout the paraffin blocks without the need to physically section the tissue, with a THz reflection occurring at each change in interface at depth. The 3D datasets could be segmented to look at different planes of the data as well, with a developed time of flight algorithm providing depth information based on the time delay between peaks. Finally, several image processing techniques showed enhancement of THz imaging of flat sections. Most methods did not appreciably improve the imaging of the three-dimensional blocks, save for unsharp masking and edge detection using a Sobel operator. While manual image processing continues to be effective for producing THz images, successful image generation here does set a precedent for automated techniques in the future [6].

THz investigation of carbon-based particles using phantoms in [7] showed the potential of onion-like carbon for increasing the contrast in fresh breast cancer tissue. OLC showed improved interactions above other similar carbon particles in PDMS, polyethylene tablets, and the cancer phantoms, despite being much smaller than the wavelength of the THz frequency range. Furthermore, this was done without the need for external sources or excitations as part of the imaging setup [8]. Since OLC can be functionalized to attach selectively to cancer and has been seen to have low toxicity, it possesses strong potential as a contrast agent in future work [9], [10].

However, some additional investigation is needed into the toxicity and reasonable concentrations in a surgical setting to truly model the contrast enhancement [7].

Expanding THz imaging to fresh tissue in the form of xenograft mouse tumors was effectively shown in [11]. This included pathology morphing and a Bayesian mixture model for statistical analysis that had yet to be applied to THz imaging. Investigation across 13 samples showed statistically significant discrimination between tissue regions when two regions were present (cancer and fat). The challenges identified for this work were: (1) excess fluid in and around the tissue, including water and necrotic blood, (2) correlation of fresh tissue to pathology following changes in tissue shape and position in the histopathology process, and (3) the algorithm used to interpolate the digitized pathology to a small resolution. These are being addressed by a more thorough method for drying the tissue, mounting the tissue on a rigid surface (cardboard) for formalin fixation to maintain tissue structure, and more rigorous morphing algorithms. Additional challenges included overlapping properties of muscle and necrotic cancer causing similar reflection. Future work is transitioning toward spontaneously generated transgenic mice tumors, which have more naturally occurring vasculature and are therefore less prone to necrosis. Meanwhile muscle is not anticipated in human breast cancer tissue, but is still of interest due to its similarity to other fibrous or connective tissues. Finally, more powerful classification models are being investigated to provide better automatic assessment of THz images in the future [11].

In all cases of THz imaging seen in the published works of this dissertation, THz has been shown to provide inherent contrast between cancer and healthy tissues with strong agreement with pathology, especially for FFPE tissue where water content is not a critical concern. For THz imaging of fresh tissue there is good contrast between cancer and fatty tissue, but the primary challenge is in determining and enhancing the contrast between fibrous and cancerous tissue.

While these regions are seen to be clearly distinct in spectroscopy [12], this represents a single group's work and other supporting spectroscopy does not exist. As such one area in which THz applications for breast cancer can expand is with spectroscopy of freshly excised human samples for healthy fat and fibrous tissue as well as breast cancer to validate the contrast seen between tissue types. In this way the existing spectroscopy in literature can be supported by a second set of data. The spectroscopy results can be further implemented to produce more accurate tissue phantoms and propagation models in future work. For the final objective of human tissue applications, freshly excised surgical tissue from biobanks has been examined already but has yet to be published [13]-[15]. The tissue handling methodology and model-based THz imaging in this work are already in place to conduct human tissue spectroscopy and imaging, and can serve as a strong basis for to develop an intraoperative breast cancer application.

References

- [1] T. C. Bowman, M. El-Shenawee, and L. K. Campbell, "Terahertz Imaging of Excised Breast Tumor Tissue on Paraffin Sections," *IEEE Trans. Antennas Propag.* 63, 2088–2097 (2015).
- [2] S. Sy, S. Huang, Y.-X. J. Wang, J. Yu, A. T. Ahuja, Y.-T. Zhang, and E. Pickwell-MacPherson, "Terahertz spectroscopy of liver cirrhosis: investigating the origin of contrast.," *Phys. Med. Biol.* 55, 7587–7596 (2010).
- [3] S. J. Oh, S.-H. Kim, Y. Bin Ji, K. Jeong, Y. Park, J. Yang, D. W. Park, S. K. Noh, S.-G. Kang, Y.-M. Huh, J.-H. Son, and J.-S. Suh, "Study of freshly excised brain tissues using terahertz imaging," *Biomed. Opt. Express* 5, 2837–42 (2014).
- [4] T. Bowman, M. El-Shenawee, and L. K. Campbell, "Terahertz transmission vs reflection imaging and model-based characterization for excised breast carcinomas," *Biomed. Opt. Express* 7, 3756–3783 (2016).
- [5] R. M. Woodward, B. E. Cole, V. P. Wallace, R. J. Pye, D. D. Arnone, E. H. Linfield, and M. Pepper, "Terahertz pulse imaging in reflection geometry of human skin cancer and skin tissue," *Phys. Med. Biol.* 47, 3853 (2002).
- [6] T. Bowman, Y. Wu, J. Gauch, L. K. Campbell, and M. El-Shenawee, "Terahertz Imaging of Three-Dimensional Dehydrated Breast Cancer Tumors," *J. Infrared, Millimeter, Terahertz Waves* 38, 766–786 (2017).

- [7] T. Bowman, A. Walter, O. Shenderova, N. Nunn, G. McGuire, and M. El-Shenawee, "A phantom study of terahertz spectroscopy and imaging of micro- and nano-diamonds and nano-onions as contrast agents for breast cancer," *Biomed. Phys. Eng. Express*, vol. 3, no. 5, p. 55001, 2017.
- [8] S. J. Oh, J. Kang, I. Maeng, J.-S. Suh, Y. M. Huh, S. Haam, and J.-H. Son, "Nanoparticle-enabled terahertz imaging for cancer diagnosis," *Opt. Express*, vol. 17, no. 5, pp. 3469–3475, 2009.
- [9] M. Frascioni, R. Marotta, L. Markey, K. Flavin, V. Spampinato, G. Ceccone, L. Echegoyen, E. M. Scanlan, and S. Giordani, "Multi-Functionalized Carbon Nano-onions as Imaging Probes for Cancer Cells," *Chem. Eur. J.*, vol. 21, pp. 19071–19080, 2015.
- [10] L. Ding, J. Stilwell, T. Zhang, O. Elboudwarej, H. Jiang, J. P. Selegue, P. A. Cooke, J. W. Gray, and F. F. Chen, "Molecular Characterization of the Cytotoxic Mechanism of Multiwall Carbon Nanotubes and Nano-Onions on Human Skin Fibroblast," *Nano Lett.*, vol. 5, no. 12, pp. 2448–2464, 2005.
- [11] T. Bowman, T. Chavez, K. Khan, J. Wu, A. Chakraborty, N. Rajaram, K. Bailey, and M. El-Shenawee, "Pulsed terahertz imaging of breast cancer in freshly excised murine tumors," *J. Biomed. Opt.*, vol. 23, no. 2, 2018.
- [12] P. C. Ashworth, E. Pickwell-MacPherson, E. Provenzano, S. E. Pinder, A. D. Purushotham, M. Pepper, and V. P. Wallace, "Terahertz pulsed spectroscopy of freshly excised human breast cancer.," *Opt. Express*, vol. 17, no. 15, pp. 12444–12454, 2009.
- [13] M. El-Shenawee, T. Bowman, T. Esparza, K. Khan, J. Wu, A. Chakraborty, and K. Bailey, "Statistical Signal Processing For Quantitative Assessment Of Pulsed Terahertz Imaging Of Human Breast Tumors," 42nd International Conference on Infrared, Millimeter and Terahertz Waves, Cancun, Mexico, 27 August – 1 September 2017.
- [14] T. Bowman, K. Bailey, and M. El-Shenawee, "Pulsed Terahertz Imaging of Fresh and Fixed Human Breast Cancer Tissue," 42nd International Conference on Infrared, Millimeter and Terahertz Waves, Cancun, Mexico, 27 August – 1 September 2017.
- [15] T. Bowman, K. Bailey, and M. El-Shenawee, "Terahertz Imaging of Freshly Excised Invasive Ductal Carcinoma Breast Tumors," 2017 URSI General Assembly and Scientific Symposium, Montreal, Quebec, Canada, 19-26 August 2017.

Appendix A: Additional Published Work

In addition to the published works in this dissertation, the author has also published another peer-reviewed journal paper outside of the experimental terahertz work and based instead on scattered fields and as follows:

T. C. Bowman, A. M. Hassan, and M. El-Shenawee, "Imaging 2D Breast Cancer Tumor Margin at Terahertz Frequency using Numerical Field Data based on DDSCAT," *Applied Computational Electromagnetics Society Journal*, vol. 28, no. 11, pp. 1017-1024, November 2013.

In this work, the discrete dipole approximation (DDSCAT) was first used to computationally generate numerical field data from a breast cancer model. This work was based on the spectroscopy results showing differentiation at THz frequencies between cancer and healthy tissue in [1] and inspired by preliminary THz imaging of FFPE tissue on slides. DDSCAT was selected for this purpose due to its proven effectiveness in generating scattered fields from heterogeneous objects in both two and three dimensions [2], [3]. Breast cancer tumor models were generated with comedo and papillary-type structures using the tumor growth models developed in [4]. A Rytov approximation was used to convert the scattered field data into a THz image and calculate the dielectric properties of the scattering tumor. The results showed effective reconstruction of the tissue regions when using lower permittivity values than fresh tissue while maintaining the same permittivity ratio between cancer or fibrous tissue and the fatty tissue background. This method provided sufficient contrast to show the promise of THz imaging. The same concept was later expanded to similar inverse scattering algorithms such as the Linear Sampling Method [5].

References

- [1] P. C. Ashworth, E. Pickwell-MacPherson, E. Provenzano, S. E. Pinder, A. D. Purushotham, M. Pepper, and V. P. Wallace, "Terahertz pulsed spectroscopy of freshly excised human breast cancer.," *Opt. Express*, vol. 17, no. 15, pp. 12444–12454, 2009.
- [2] B. T. Draine and P. J. Flatau, "Discrete-Dipole Approximation For Scattering Calculations," *J. Opt. Soc. Am. A*, vol. 11, no. 4, p. 1491, 1994.
- [3] P. J. Flatau and B. T. Draine, "Fast near field calculations in the discrete dipole approximation for regular rectilinear grids," *Opt. Express*, vol. 20, no. 2, pp. 1247–1252, 2012.
- [4] S. C. Ferreira, M. L. Martins, and M. J. Vilela, "Reaction-diffusion model for the growth of avascular tumor," *Phys. Rev. E. Stat. Nonlin. Soft Matter Phys.*, vol. 65, no. 2, p. 21907, 2002.
- [5] T. Bowman, A. Hassan, and M. El-Shenawee, "Terahertz imaging of breast cancer margin using the Linear Sampling Method," in 2013 IEEE Antennas and Propagation Society International Symposium (APSURSI) (IEEE, 2013), pp. 538–539, 2013.

Appendix B: MATLAB Codes

Liquid Sample Holder Transmission Spectroscopy

```
clear all

tic

mag=csvread('ExampleTxnh.csv'); %Datafile for Transmittance, header removed
pha=csvread('ExamplePhnh.csv'); %Datafile for Transmission Phase, header
    removed
numpoints=1; %Number of Points (Measurements) for which to run the solution

Glass=load('QuartzBHRefnNew.mat'); %Quartz Reference File
Glassn=Glass.n;
Glassalph=Glass.alph;

nmin=0; % Minimum for swept refractive index
nmax=10; % Maximum for swept refractive index
nsteps=400; % Number of refractive index steps
alphamin=0; % Minimum for swept absorption coefficient (1/cm)
alphamax=800; % Maximum for swept absorption coefficient (1/cm)
alphasteps=1500; % Number of absorption coefficient steps
refinesteps=50; % Number of refinements in second step
freqsteps=700; % Number of frequencies investigated
unwraptol=pi; % Unwrapping tolerance (default pi)

dglass=3.065; % Thickness of glass sublayer in mm
dsample=[0.100 0.100 0.100]; % Thickness of tissue sample in mm

nbg=1+j*0; % Refractive index of background material (air)
c=3e8;

clear n alph

for point=1:numpoints

waven=mag(:,1);
magfreq=mag(:,point+1);
phasefreq=-1*pha(:,point+1);
phasefrequn=unwrap(phasefreq,unwraptol);

display(point);

L=length(waven);

clear Enorm internal1 internal2 internalref reflect23 reflect12 reflect232

for ii=1:L
    Enorm(ii)=sqrt(magfreq(ii))*exp(j*phasefreq(ii));
end

for stat=1:freqsteps

    if mod(stat,50)==0
        display(stat)
    end
end
```

```

end

nrange=nmin:(nmax-nmin)/(nsteps):nmax;
alpharange=alphamin:(alphamax-alphamin)/(alphasteps):alphamax;

clear tx1 phasediff transmitted zerobalance
clear zerobalancereal zerobalanceimag2 zerobalancetotal

nglass=Glassn(stat)-j*1/(2*2*pi*waven(stat))*Glassalph(stat);

zeromin=1;
refnindex=1;
alphindex=1;

clear phasediff phasenorm cn

[a3 n3]=meshgrid(alpharange,nrange);

clear tx1 phasediff transmitted zerobalance
clear zerobalancereal zerobalanceimag2 zerobalancetotal

zeromin=1;
refnindex=1;
alphindex=1;

clear phasediff phasenorm cn num den num2 den2 w

f=waven(stat)*3e-2;
w=2*pi*f*1e12;

nbg=w/c;
nglass=w/c*Glassn(stat)-j*Glassalph(stat)*100/2;
cn=w/c*n3-j*a3*100/2;

gamma1=j*nbg;
gamma2=j*nglass;
gamma3=j*cn;
% exglass=exp(-2*gamma2*dglass*1e-3);
exglass=0;
exsample=exp(-2*gamma3*dsample(point)*1e-3);

num=4*nglass*cn*((nbg+nglass)^2-(nbg-nglass)^2*exglass);

den=(nglass+nbg).^2*(nglass+cn).^2+...
2*(cn.^2-nglass^2).*(nglass^2-nbg^2).*exglass.*(1-exsample)+...
(cn-nglass).^2*(nglass-nbg)^2*exglass*exglass-...
(cn-nglass).^2*(nglass+nbg)^2.*exsample-...
(nglass-nbg)^2*(cn+nglass).^2*exglass*exglass.*exsample;

transmitted=num./den;

phasenorm=(-1*(gamma3-gamma1)*dsample(point)*1e-3);

zerobalancereal=real(log(transmitted))+real(phasenorm)-
log(sqrt(magfreq(stat)));
zerobalanceimag=imag(log(transmitted))+imag(phasenorm)-
phasefrequn(stat);

```

```

        zerobalancetotal=zerobalancereal+i*zerobalanceimag;

[minrange ntemp]=min(abs(zerobalancetotal));
[minval aval]=min(minrange);
nval=ntemp(aval);
refnindex=nval;
alphindex=aval;

if
    (refnindex~=1) && (refnindex~=nsteps+1) && (alphindex~=1) && (alphindex~=alphas
    teps+1)

nrange2=nrange(refnindex-1):(nrange(refnindex+1)-nrange(refnindex-
    1))/refinesteps:nrange(refnindex+1);
alphanrange2=alphanrange(alphindex-1):(alphanrange(alphindex+1)-
    alphanrange(alphindex-1))/refinesteps:alphanrange(alphindex+1);
refnindex2=26;
alphindex2=26;

clear phasediff phasenorm cn

[a3b n3b]=meshgrid(alphanrange2,nrange2);

cnb=w/c*n3b-j*a3b*100/2;

    gamma3b=j*cnb;
    exsampleb=exp(-2*gamma3b*dsample(point)*1e-3);

    num2=4*nnglass*cnb*((nbg+nnglass)^2-(nbg-nnglass)^2*exglass);

    den2=(nnglass+nbg).^2*(nnglass+cnb).^2+...
        2*(cnb.^2-nnglass^2)*(nnglass^2-nbg^2)*exglass.*(1-exsampleb)+...
        (cnb-nnglass).^2*(nnglass-nbg)^2*exglass*exglass-...
        (cnb-nnglass).^2*(nnglass+nbg)^2.*exsampleb-...
        (nnglass-nbg)^2*(cnb+nnglass).^2*exglass*exglass.*exsampleb;

    transmitted2=num2./den2;

    phasenormb=(-1*(gamma3b-gamma1)*dsample(point)*1e-3);

        zerobalancereal2=real(log(transmitted2))+real(phasenormb)-
        log(sqrt(magfreq(stat)));
        zerobalanceimag2=imag(log(transmitted2))+imag(phasenormb)-
        phasefrequn(stat);
        zerobalancetotal2=zerobalancereal2+i*zerobalanceimag2;

[minrange2 ntemp2]=min(abs(zerobalancetotal2));
[minval2 aval2]=min(minrange2);
nval2=ntemp2(aval2);

    n(stat,point)=nrange2(nval2);
    alph(stat,point)=alphanrange2(aval2);
    waven(stat);

else
    n(stat,point)=nrange(nval);
    alph(stat,point)=alphanrange(aval);

```

```

    waven(waven(stat));

end
end
end

wave=waven(1:stat);

clearvars -except n alph wave mag pha

toc

```

Reflection Imaging Magnitude and Phase Calculation

```

clear all

tvldata=TVLread('Rx Scan 4 Fly.tvl','raw');
BuildImageFly1half;
% reference(1:1024)=Imagespace(40,50,1:1024); %Use a scan point reference
reference=tvldata.Ref.'/2;
% ref2(1:1024)=Imagespace(40,50,1:1024); %Use a scan point reference
ref2=reference;
[peak1 pos1]=max(reference);
[peak2 pos2]=max(ref2);
[peakadj posadj]=min(reference(1:150));
[peakall posall]=min(Imagespace(:, :, 1:150), [], 3);
fil=ones(5,5)/25;
% posall2=round(imfilter(posall,fil)); %Apply shift
posall2=posadj+0*round(imfilter(posall,fil)); %Apply no shift

xmin=1;
xmax=length(xrange);
ymin=1;
ymax=length(yrange);

sampledelay=0.0;

timerange=tvldata.tt;
points=length(timerange);
points2=2000;
timestepmm=(timerange(points)-timerange(1))/(points-1)*2*1e-3;
freqmax=1/(timestepmm/3e8)/2;
freqstep=freqmax/4096;
freqrange=(1:8192).*freqstep;
freq=freqrange(1:points2);
waven=freq/3e8/100;

[refpeak refpos]=min(reference);
% temp=blackmanharris(2*refpos); %Applying Weighting to Signal
% reframpup=temp(1:refpos);
% temp=blackmanharris(2*(1024-refpos));
% reframpdown=temp((length(temp)/2+1):length(temp));
% refadop=[reframpup; reframpdown];
% refweight=reference.*refadop.';

refbigstep=reference(1024)-reference(1);

```

```

refsmallstep=refbigstep/(8192-1024+1);
reframp=reference(1024)-(1:(8192-1024))*refsmallstep;
refnew1=( [reference reframp] );
refnew=circshift(refnew1,[0 (pos2-pos1)]);

reftemp=fft(refnew,8192);

for ypt=1:(ymax-ymin+1)
    yrow=yrange(ypt-1+ymin);
    for xpt=1:(xmax-xmin+1)
        xcol=xrange(xpt-1+xmin);

        sample(1:1024)=Imagespace(ypt-1+ymin,xpt-1+xmin,1:1024);
        [sampeak sampos]=max(sample);
        % temp=blackmanharris(2*sampos); %Applying Weighting to Signal
        % samrampup=temp(1:sampos);
        % temp=blackmanharris(2*(1024-sampos));
        % samrampdown=temp((length(temp)/2+1):length(temp));
        % % samadop=[samrampup; samrampdown];
        % samadop=circshift(refadop,[posall2(ypt-1+ymin,xpt-1+xmin)-posadj 0]);
        % samweight=sample.*samadop.';

        sampbigstep=sample(1024)-sample(1);
        sampsmallstep=sampbigstep/(8192-1024+1);
        sampramp=sample(1024)-(1:(8192-1024))*sampsmallstep;
        sampnew1=( [sample sampramp] );
        % sampnew=circshift(sampnew1,[0 round(sampdelay/((timerange(points)-
        timerange(1))/(points-1)))]);
        sampnew=circshift(sampnew1,[0 posadj-posall2(ypt-1+ymin,xpt-1+xmin)]);

        temp1=fft(sampnew,8192);

        for jj=1:(points2)
            diff(jj)=temp1(jj)/reftemp(jj);
        end

        mag(ypt,xpt,:)=abs(diff).^2;
        temppha=-1*angle(diff);
        temppha(1)=0;
        pha(ypt,xpt,:)=unwrap(temppha);

        magmat(ypt,xpt,:)=abs(temp1).^2;
        phamat(ypt,xpt,:)= -1*unwrap(angle(temp1));

        phanorm(ypt,xpt,:)= -1*angle(temp1);

    end
end

save('MagPhaTestNoFilter1half.mat','magmat','phamat','xmin','xmax','ymin','ym
ax','xrange','yrange','freqrange','waven','-mat');
save('MagPhaLoadNoFilter1half.mat','mag','pha','xmin','xmax','ymin','ymax','x
range','yrange','freqrange','waven','-mat');

clear diff freq freqmax freqstep indexstart jj n offset points
clear points2 refadop refbigstep reference refnew refpeak refpos reframp
clear reframpdown reframpup refsmallstep reftemp refweight rowindex samadop

```

```
clear sampeak sample sampledelay sampnew
```

Reflection Imaging Spectroscopy

```
clear all
```

```
tic
```

```
Outfile='TETM_PhantomScan.mat'; % Output file
```

```
tvldata=TVLread('Meat 14 Scan 2 Fly.tvl','raw'); %
```

```
    Load TVL file
```

```
display(['TVL file loaded: ' num2str(round(toc*100)./100) 's']); %
```

```
    Time Stamp
```

```
load('MagPhaLoadShiftZ.mat'); %
```

```
    Load Magnitude and Phase File
```

```
display(['Magnitude/Phase file loaded: ' num2str(round(toc*100)./100) 's']);
```

```
    % Time Stamp
```

```
Glass=load('PSPlate.mat'); %
```

```
    Load slide material file
```

```
display(['Background file loaded: ' num2str(round(toc*100)./100) 's']); %
```

```
    Time Stamp
```

```
xmin=1; % Set range of x-axis data from Magnitude and Phase  
    File
```

```
xmax=length(xrange);
```

```
ymin=1; % Set range of y-axis data from Magnitude and Phase  
    File
```

```
ymax=length(yrange);
```

```
nmin=1; % Minimum for swept refractive index
```

```
nmax=5; % Maximum for swept refractive index
```

```
nsteps=600; % Number of refractive index steps
```

```
alphamin=0; % Minimum for swept absorption coefficient (1/cm)
```

```
alphamax=1000; % Maximum for swept absorption coefficient (1/cm)
```

```
alphasteps=1000; % Number of absorption coefficient steps
```

```
refinesteps=50; % Number of refinements in second step
```

```
freqsteps=540; % Number of frequencies
```

```
fstar=540; % Start frequency
```

```
fstop=540; % Stop frequency
```

```
dglass=3.000; % Thickness of glass sublayer in mm
```

```
dsample=10.000; % Thickness of tissue sample in mm
```

```
sampdelay=0.0; % Delay line adjustment in measurements
```

```
relativeerror=1e-6; % Relative error of refinement
```

```
polarpsi=60; % Polarization rotation of incident (from TE)
```

```
% Universal constants
```

```
c=3e8; % Speed of light in vacuum
```

```
relperm=8.854187817e-12; % Vacuum permittivity
```

```
% Clear solution variables
```

```
n=zeros(ymax-ymin+1,xmax-xmin+1,freqsteps); % Refractive index
```

```
alph=n; % Absorption Coefficient
```

```
epsr=n; % Relative permittivity (real)
```

```
epsi=n; % Relative permittivity (imag)
```

```

errcheck=n; % Error handling

% Find frequency domain units
timerange=tvldata.tt;
points=length(timerange);
points2=2000;
timestepmm=(timerange(points)-timerange(1))/(points-1)*2*1e-3;
freqmax=1/(timestepmm/3e8)/2;
freqstep=freqmax/4096;
freqrange=(1:8192).*freqstep;
freq=freqrange(1:points2);
waven=freq/3e8/100;

% Adjust slide properties to frequency range in scan
Glassn=interp1(Glass.wave,Glass.n,waven);
Glassalph=interp1(Glass.wave,Glass.alph,waven);

% Initialize f-independent calculation space variables
nrange=nmin:(nmax-nmin)/(nsteps):nmax;
alpharange=alphamin:(alphamax-alphamin)/(alphasteps):alphamax;
[a3 n3]=meshgrid(alpharange,nrange);

% Build initial calculated solution space
for stat=1:freqsteps
% for stat=fstar:fstop
    % Define frequency
    f=waven(stat)*3e-2;
    w=2*pi*f*1e12;

    % Complex refractive index
    na0=Glassn(stat)-j*c/w*Glassalph(stat)*100/2;
    na2=1;
    na1=n3 -j*c/w*a3*100/2;
    na3=1;

    % Propagation angles
    ctheta0=cos(asin(sin(pi/6)./na0));
    ctheta1=cos(asin(sin(pi/6)./na1));
    ctheta2=cos(asin(sin(pi/6)./na2));
    ctheta3=cos(asin(sin(pi/6)./na3));

    % Propagation coefficients (gamma)
    gam2=j*w/c*na2;
    gam1=j*w/c*na1;
    gam0=j*w/c*na0;

    % Propagation shift
    psi2=dglass *1e-3.*gam2.*ctheta2;
    psi1=dsample*1e-3.*gam1.*ctheta1;
    psi0=0;

    % Exponential propagation
%     exglass =exp(-2*psi2);
    exglass =0; % No internal Glass reflections
%     exsample=exp(-2*psi1);
    exsample=0; % No internal sample reflections

```

```

% Fresnel Reflection Coefficients (TE Mode)
rho01TE=(na0.*ctheta0-na1.*ctheta1)./(na0.*ctheta0+na1.*ctheta1);
rho10TE=-1*rho01TE;
rho12TE=(na1.*ctheta1-na2.*ctheta2)./(na1.*ctheta1+na2.*ctheta2);
rho21TE=-1*rho12TE;
rho23TE=(na2.*ctheta2-na3.*ctheta3)./(na2.*ctheta2+na3.*ctheta3);
rho32TE=-1*rho23TE;

% Fresnel Reflection Coefficients (TM Mode)
rho01TM=(na0./ctheta0-na1./ctheta1)./(na0./ctheta0+na1./ctheta1);
rho10TM=-1*rho01TM;
rho12TM=(na1./ctheta1-na2./ctheta2)./(na1./ctheta1+na2./ctheta2);
rho21TM=-1*rho12TM;
rho23TM=(na2./ctheta2-na3./ctheta3)./(na2./ctheta2+na3./ctheta3);
rho32TM=-1*rho23TM;

Reflect23TE=rho23TE;
Reflect12TE=(rho12TE+Reflect23TE.*exglass
)./(1+rho12TE.*Reflect23TE.*exglass );

Reflect01TE=(rho01TE+Reflect12TE.*exsample)./(1+rho01TE.*Reflect12TE.*ex
sample);

Reflect23TM=rho23TM;
Reflect12TM=(rho12TM+Reflect23TM.*exglass
)./(1+rho12TM.*Reflect23TM.*exglass );

Reflect01TM=(rho01TM+Reflect12TM.*exsample)./(1+rho01TM.*Reflect12TM.*ex
sample);

% Sample Reflection
LambSamPerpTE=Reflect01TE;
LambSamPerpTM=Reflect01TM;

% Propagation shift difference in Reference/Sample
psiG1=dsample*1e-3.*gam0.*ctheta0;
psiG1array(stat)=psiG1;

% Glass Reflections
rho12GTE=(na0.*ctheta0-na2.*ctheta2)./(na0.*ctheta0+na2.*ctheta2);      % TE
Mode
rho12GTM=(na0./ctheta0-na2./ctheta2)./(na0./ctheta0+na2./ctheta2);      % TM
Mode

Reflect12GTE=(rho12GTE+Reflect23TE.*exglass)./(1+rho12GTE.*Reflect23TE.*e
xglass);

Reflect12GTM=(rho12GTM+Reflect23TM.*exglass)./(1+rho12GTM.*Reflect23TM.*e
xglass);
%   Reflect01GTE=Reflect12GTE*exp(-2*psiG1);
%   Reflect01GTM=Reflect12GTM*exp(-2*psiG1);

% Reference reflection
LambRefPerpTE=Reflect12GTE;
LambRefPerpTM=Reflect12GTM;

```



```

ReflectGrid(:, :, stat)=reflected;
% ReflectSign(:, :, stat)=refltsign;

% A2/B2 values for refinement
R23TEarray(stat)=Reflect23TE;
R23TMarray(stat)=Reflect23TM;
% toc
end
display(['Constructed          calculated          solution          matrix:          '
num2str(round(toc*100)./100) 's']);

% Unwrap reflection phase in solutions
UnwrapGrid=unwrap(imag(log(ReflectGrid)), [], 3);
display(['Unwrapped          phase          from          calculated          solutions:          '
num2str(round(toc*100)./100) 's']);

% Compare and refine
for stat=fstar:fstop
% Define frequency
f=waven(stat)*3e-2;
w=2*pi*f*1e12;

% Load passed f-dependent values
reflected=ReflectGrid(:, :, stat);
na0=Glassn(stat)-j*c/w*Glassalph(stat)*100/2;
ctheta0=cos(asin(sin(pi/6)./na0));
gam0=j*w/c*na0;

psiG1=psiG1array(stat);
Reflect23TE=R23TEarray(stat);
Reflect23TM=R23TMarray(stat);

for ypt=ymin:ymax
% for ypt=60:60
% yrow=yrange(ypt-1+ymin);
for xpt=xmin:xmax
% for xpt=60:60
% xcol=xrange(xpt-1+xmin);

% Define measurement mag/pha for comparison
magfreq=mag(ypt, xpt, stat);
phasefreq(1:length(pha))=-1*pha(ypt, xpt, 1:length(pha));
phasefrequn=unwrap(phasefreq);

% Evaluate error function
zerobalancereal=real(log(reflected))-log(sqrt(magfreq));
% zerobalanceimag=UnwrapGrid(:, :, stat)-phasefrequn(stat);
zerobalanceimag=imag(log(reflected))-angle(exp(j*phasefreq(stat)));
zerobalancetotal=zerobalancereal+i*zerobalanceimag;

% Find minimum error location
[minrange ntemp]=min(abs(zerobalancetotal));
[minval aval]=min(minrange);
nval=ntemp(aval);
refnindex=nval;
alphindex=aval;
errprev=minval;

```

```

% Prep refinement space
nrangespec=nrange;
alphanrangespec=alpharange;

% Set refinement parameters and enter loop
errorspec=1;
loopct=0;
loopmax=10;
flag1=true;
flag2=true;
flag3=true;
while (flag3)
    clear nrange2 alpharange2
    % Set refractive index refinement
    if (refnindex==1)
        nrange2=nrangespec(refnindex):(nrangespec(refnindex+1)-
            nrangespec(refnindex))/(refinesteps/2):nrangespec(refnindex+1);
    else if (refnindex==length(nrangespec))
        nrange2=nrangespec(refnindex-1):(nrangespec(refnindex)-
            nrangespec(refnindex-1))/(refinesteps/2):nrangespec(refnindex);
    else
        nrange2=nrangespec(refnindex-1):(nrangespec(refnindex+1)-
            nrangespec(refnindex-1))/refinesteps:nrangespec(refnindex+1);
    end
end
% Set absorption coefficient refinement
if (alphindex==1)
    alpharange2=alphanrangespec(1):(alphanrangespec(2)-
        alphanrangespec(1))/(refinesteps/2):alphanrangespec(2);
else if (alphindex==length(alphanrangespec))
    alpharange2=alphanrangespec(alphindex-1):(alphanrangespec(alphindex)-
        alphanrangespec(alphindex-1))/(refinesteps/2):alphanrangespec(alphindex);
else
    alpharange2=alphanrangespec(alphindex-1):(alphanrangespec(alphindex+1)-
        alphanrangespec(alphindex-1))/refinesteps:alphanrangespec(alphindex+1);
end
end

% Set refinement solution variables
[a3b n3b]=meshgrid(alpharange2,nrange2);

nalb=n3b-j*c/w*a3b*100/2;
cthetalb=cos(asin(sin(pi/6)./nalb));
gam1b=j*w/c*nalb;
psilb=dsample*1e-3.*gam1b.*cthetalb;

% Exponential propagation
%   exglass =exp(-2*psi2 );
exglass =0;      % No internal Glass reflections
%   exsample=exp(-2*psilb);
exsample=0;     % No internal Sample reflections

rho01TEb=(na0 .*ctheta0 -nalb.*cthetalb)./(na0 .*ctheta0 +nalb.*cthetalb);
rho12TEb=(nalb.*cthetalb-na2 .*ctheta2 )./(nalb.*cthetalb+na2 .*ctheta2 );

rho01TMb=(na0 ./ctheta0 -nalb./cthetalb)./(na0 ./ctheta0 +nalb./cthetalb);

```

```

rho12TMb=(nalb./ctheta1b-na2 ./ctheta2 )./(nalb./ctheta1b+na2 ./ctheta2 );

Reflect12TEb=(rho12TEb+Reflect23TE .*exglass )./(1+rho12TEb.*Reflect23TE
.*exglass );

Reflect01TEb=(rho01TEb+Reflect12TEb.*exsample)./(1+rho01TEb.*Reflect12TEb
.*exsample);

Reflect12TMb=(rho12TMb+Reflect23TM .*exglass )./(1+rho12TMb.*Reflect23TM
.*exglass );

Reflect01TMb=(rho01TMb+Reflect12TMb.*exsample)./(1+rho01TMb.*Reflect12TMb
.*exsample);

% Sample Reflection
LambSamPerpTEb=Reflect01TEb;
LambSamPerpTMb=Reflect01TMb;

clear PhaShiftSb

combomagSb=sqrt(abs(LambSamPerpTEb*cos(polarpsi*pi/180)).^2+abs(LambSamPerpTMb*
sin(polarpsi*pi/180)).^2);
PhaShiftSb(:, :, 1)=angle(LambSamPerpTEb);
PhaShiftSb(:, :, 2)=angle(LambSamPerpTMb);
PhatempSb=unwrap(PhaShiftSb, [], 3);

combophaSb=angle(LambSamPerpTEb)*cos(polarpsi*pi/180)^2+PhatempSb(:, :, 2)*
sin(polarpsi*pi/180).^2;

%
reflectedb=sqrt((LambSamPerpTEb*cos(polarpsi*pi/180)).^2+(LambSamPerpTMb*
sin(polarpsi*pi/180)).^2)./...
%
LambRefGrid(stat);
reflectedb=combomagSb.*exp(i*combophaSb)./LambRefGrid(stat);

clear PhaseGrid shifted shifted2

% Adjust refinement solutions to agree with phase shift
PhaseGrid=UnwrapGrid(nval,aval,stat)+(imag(log(reflectedb))-
imag(log(reflected(nval,aval)))));

% Refinement error calculations
zerobalancereal2=real(log(reflectedb))-log(sqrt(magfreq));
%
zerobalanceimag2=PhaseGrid-phasefrequn(stat);
zerobalanceimag2=angle(exp(j*PhaseGrid))-angle(exp(j*phasefrequn(stat)));
zerobalancetotal2=zerobalancereal2+i*zerobalanceimag2;

% Find minimum error
[minrange2 ntemp2]=min(abs(zerobalancetotal2));
[minval2 aval2]=min(minrange2);
nval2=ntemp2(aval2);
errorspec=minval2;
refnindex=nval2;
alphindex=aval2;

% Set range for next refinement loop

```

```

nrangespec=nrange2;
alphanrangespec=alphanrange2;
loopct=loopct+1;

% Check loop parameters
flag1=errorspec>relativeerror;
flag2=loopct<loopmax;
flag3=flag1&flag2;

% Loop outputs
if stat==14
if loopct==10
    loopct;
end
end
end

n(ypt,xpt,stat)=nrangespec(refnindex);
alph(ypt,xpt,stat)=alphanrangespec(alphanindex);
compn=nrangespec(refnindex)-
    j*alphanrangespec(alphanindex)/(4*pi*waven(stat));
epsr(ypt,xpt,stat)=real(compn^2);
epsi(ypt,xpt,stat)=-1*imag(compn^2);
waven(stat);

errcheck(ypt,xpt,stat)=abs(zerobalancereal2(nval2,aval2)/log(sqrt(magfreq
))+i*zerobalanceimag2(nval2,aval2)/phasefrequn(stat));

end
end
display(['Solved frequency #' num2str(stat) ' (' num2str(round(waven(stat)*3e-
2*1000)/1000) ' THz): ' num2str(round(toc*100)./100) 's']);
end
wave=waven(1:stat);
save(Outfile,'n','alph','epsr','epsi','wave','errcheck','-mat');
display(['Results saved: ' num2str(round(toc*100)./100) 's']);

clearvars -except n alph epsr epsi wave errcheck mag pha xrange yrange

```